A whirlwind journey of wavelet turbulent flux mapping : estimation of spatialized turbulent flux on tall towers and its uncertainties

Pedro Henrique Herig Coimbra

THESE DE DOCTORAT

NNT : 2024UPASJ011

A Whirlwind Journey of Wavelet Turbulent Flux Mapping: Estimation of spatialized turbulent flux on tall towers and its uncertainties

Estimation des flux de CO_2 par covariances turbulentes à l'échelle de plusieurs km^2

Thèse de doctorat de l'université Paris-Saclay

École doctorale n° 129, sciences de l'environnement d'Île-de-France (SEIF)
Spécialité de doctorat : Géosciences
Graduate School : Géosciences, climat, environnement et planètes
Référent : Université de Versailles-Saint-Quentin-en-Yvelines

Thèse préparée dans la unité de recherche **ECOSYS** (Université Paris Saclay, INRAE, AgroParisTech), sous la direction de **Benjamin LOUBET**, directeur de recherche, INRAE, AgroParisTech, Université Paris-Saclay (ECOSYS), le co-encadrement de **Olivier LAURENT**, ingénieur chercheur, CEA, Université Paris-Saclay (LSCE)

Thèse soutenue à Paris-Saclay, le 17 mai 2024, par

Pedro Henrique HERIG COIMBRA

Composition du Jury

Membres du jury avec voix délibérative

Valerie GROS Directrice de recherche, CNRS, Université Paris Saclay (LSCE)	Présidente
Andreas IBROM Professeur, Technical University of Denmark (DTU)	Rapporteur & Examinateur
Matthias CUNTZ Directeur de recherche, INRAE, Université de Lorraine, AgroParisTech (SILVA)	Rapporteur & Examinateur
Solène TURQUETY Professeur, Sorbonne Université (LATMOS)	Examinatrice
Thomas LAUVAUX Professeur, Université of Reims Champagne Ardenne (GSMA)	Examinateur

université PARIS-SACLAY
ÉCOLE DOCTORALE
Sciences de l'Environnement d'Île-de-France (SEIF)

Titre : Estimation des flux de CO_2 par covariances turbulentes à l'échelle de plusieurs km^2

Mots clés : CO_2 flux; covariance turbulente; grande tour; ondelettes; images satellitaires; inversion bayésienne.

Résumé : Le climat et l'activité humaine sont étroitement liés. Les émissions de gaz à effet de serre (GES) impactent la dynamique climatique et la qualité de l'air, affectant des millions de personnes dans le monde. La surveillance efficace des GES est essentielle pour des décisions politiques éclairées, mais elle est complexe en raison de la variabilité des sources et puits, ainsi que du transport atmosphérique. Les réseaux de surveillance abordent cette variabilité en déployant des capteurs dans des lieux géographiques divers, échantillonnant en continu sur le temps.

Les zones urbaines sont des points d'émission clés. Cependant, directement surveiller les changements de GES sur > 5 km2 avec des sources variées et des zones végétalisées manque d'une méthode standard. La méthode de covariance turbulente (eddy covariance, EC) offre une surveillance directe et continue du flux net de GES. L'EC basée sur les ondelettes fonctionne sur les mêmes principes mais ne nécessite pas de stationnarité, laissant plus de données exploitables pour l'analyse, ce qui est particulièrement bénéfique dans les environnements urbains complexes.

Démêler les composantes anthropiques et biogéniques d'un flux net de CO2 est reconnu comme un problème clé à résoudre dans les zones urbanisées. Les modèles écosystémiques conventionnels utilisés pour partitionner la productivité primaire brute (GPP) et la respiration de l'écosystème (Reco) ne sont pas appropriés pour les zones urbanisées. La partition directe en utilisant des corrélations haute fréquence entre les gaz traceurs peut aider à surmonter les limitations des méthodes de partitionnement standard.

Bien que l'EC reste la norme pour les études locales, l'estimation des flux de surface à plus grande échelle implique souvent d'assimiler des mesures de concentration de fond à des estimations antérieures à l'aide de modèles de transport. Les méthodes d'inversion utilisant les données de flux de tour sont encore rares et il serait intéressant de les tester dans les zones urbanisées.

L'objectif de cette thèse était d'évaluer l'EC basée sur les ondelettes combinée à des méthodes d'inversion bayésiennes pour la cartographie des flux de CO2. Au cours de la thèse, j'ai découvert une nouvelle méthode de partitionnement direct qui a été utilisée pour améliorer l'inversion globale dans la zone suburbaine du plateau de Saclay.

Dans le premier article de la thèse, nous avons proposé la nouvelle méthode de partitionnement direct basée sur l'analyse en quadrants des flux décomposés en fréquence de CO2 et de vapeur d'eau. Nous avons montré que cette méthode pouvait fournir des estimations impartiales de GPP et Reco. Nous avons également constaté que l'EC basée sur les ondelettes a gardé jusqu'à ~30% plus des données exploitables.

Dans le deuxième article, nous avons utilisé une grande tour équipée d'analyseurs à haute précision mais lents. Malgré des fréquences d'acquisition plus lentes, l'atténuation était limitée à ~20 % par une plus faible contribution de hautes fréquences à cette hauteur. Les résultats encouragent une collaboration entre les réseaux atmosphériques et écosystémiques.

Dans le troisième article, nous avons combiné la méthode de partitionnement proposée dans le premier article avec les instruments d'une tour atmosphérique du deuxième article. Le flux de CO2 partionné en biogéniques et anthropiques ont été assimilé dans des estimations spatialisées des flux à quelques km2. Les cartes de flux obtenues offrent l'avantage de reposer sur des mesures de flux directes à l'échelle du paysage et peuvent être utilisées pour informer les inversions à grande échelle à des échelles plus larges.

Les résultats centrés sur la région parisienne fournissent des bases pour les mesures de flux à l'échelle du paysage et à definir des stratégies de surveillance des émissions. Ces avancées contribuent à la compréhension et à la résolution des défis environnementaux aux échelles temporelles et spatiales où les décisions sont prises.

Title : A Whirlwind Journey of Wavelet Turbulent Flux Mapping: Estimation of spatialized turbulent flux on tall towers and its uncertainties

Keywords : CO_2 flux; eddy covariance; tall tower; wavelets; satellite; Bayesian inversion.

Abstract : Climate and human activity are closely linked. Greenhouse gas (GHGs) emissions impact climate dynamics and air quality, affecting millions globally. Effective GHG monitoring is essential for informed policy decisions, yet it is complex due to spatial and temporal variability of sources and sinks, and atmospheric transport. Monitoring networks address this variability by deploying sensors across diverse geographic locations sampling continuously over time.

Urban areas are key emission points, driving climate change. However, monitoring direct GHG changes over > 5 km2 with varied sources and vegetated areas lacks a standard method. Eddy Covariance (EC) offers direct, continuous GHG net flux monitoring. Wavelet-based EC operates on the same principles as the standard method but calculates covariance using frequency decomposed time series. This approach does not require stationarity, leaving more data available for analysis, particularly beneficial in complex urban environments where non-stationary fluxes are common.

Disentangling anthropogenic and biogenic components of a net CO2 flux is recognised as a key issue yet to be resolved in urbanised areas. Conventional ecosystem models used to partition gross primary productivity (GPP) and ecosystem respiration (Reco) are not appropriate for urbanised areas. Direct partitioning using high-frequency correlations between tracer gases may help overcoming the limitations of standard partitioning methods.

While Eddy Covariance remains standard for local studies, estimating larger-scale surface fluxes often involves assimilating background concentration measurements to prior estimations using transport models. The progress in satellite imagery and detailed inventories provides a new basis that helps improve these methods. However, inversion methods using tower flux data are still sparse and would be interesting to test in urbanised areas.

The objective of this PhD was to evaluate wavelet-based EC combined with Bayesian inversion methods for CO2 flux mapping.

During the course of the PhD I discovered a new direct partitioning method that was used with a combination of CH4 and CO to improve the overall inversion in the suburban area of the Saclay plateau.

In the first paper of the PhD, we hypothesised that decomposing concentration and wind signals by frequency can capture individual "gusts" within each frequency, typically mixed in the original signal. We leveraged this feature to propose a new parameter-free direct partitioning method based on quadrant analysis of CO2 and water vapour frequency decomposed fluxes. We showed that this method could indeed provide unbiased estimates of GPP and Reco at a crop and a forest ecosystem site near Paris. We also found that wavelet eddy covariance further saved up to ~30% of the non-stationary data in these sites.

In the second paper, we proposed using tall towers equipped with high-precision but slow analysers for measuring fluxes. Despite slower acquisition frequencies, attenuation was limited to ~20 % by a lower contribution of high frequencies at this height. Results encourage further collaboration between atmospheric and ecosystem networks for in-situ measurements.

In the third paper, we combined the partitioning method proposed in the first paper with the flux from the second paper, including now more gases measured to partition CO2 fluxes in biogenic and anthropogenic components and assimilate them in previous spatially-explicit estimations of fluxes at few km2. The obtained flux maps offer the advantage of relying on direct flux measurements at the landscape scale and may be used to informing large-scale inversions at broader scales.

Results focused on the Parisian region provide valuable insights for flux measurements at the landscape scale and beyond, and contributing to emission monitoring strategies. These advancements contribute to understanding and addressing environmental challenges at the temporal and spatial scales where decisions are made.

RESUME

Le climat et l'activité humaine sont étroitement liés. Les émissions de gaz à effet de serre (GES) impactent la dynamique climatique et la qualité de l'air, affectant des millions de personnes dans le monde. La surveillance efficace des GES est essentielle pour des décisions politiques éclairées, mais elle est complexe en raison de la variabilité des sources et puits, ainsi que du transport atmosphérique. Les réseaux de surveillance abordent cette variabilité en déployant des capteurs dans des lieux géographiques divers, échantillonnant en continu sur le temps.

Les zones urbaines sont des points d'émission clés. Cependant, directement surveiller les changements de GES sur > 5 km^2 avec des sources variées et des zones végétalisées manque d'une méthode standard. La méthode de covariance turbulente (eddy covariance, EC) offre une surveillance directe et continue du flux net de GES. L'EC basée sur les ondelettes fonctionne sur les mêmes principes mais ne nécessite pas de stationnarité, laissant plus de données exploitables pour l'analyse, ce qui est particulièrement bénéfique dans les environnements urbains complexes.

Démêler les composantes anthropiques et biogéniques d'un flux net de CO2 est reconnu comme un problème clé à résoudre dans les zones urbanisées. Les modèles écosystémiques conventionnels utilisés pour partitionner la productivité primaire brute (GPP) et la respiration de l'écosystème (Reco) ne sont pas appropriés pour les zones urbanisées. La partition directe en utilisant des corrélations haute fréquence entre les gaz traceurs peut aider à surmonter les limitations des méthodes de partitionnement standard.

Bien que l'EC reste la norme pour les études locales, l'estimation des flux de surface à plus grande échelle implique souvent d'assimiler des mesures de concentration de fond à des estimations antérieures à l'aide de modèles de transport. Les méthodes d'inversion utilisant les données de flux de tour sont encore rares et il serait intéressant de les tester dans les zones urbanisées.L'objectif de cette thèse était d'évaluer l'EC basée sur les ondelettes combinée à des méthodes d'inversion bayésiennes pour la cartographie des flux de CO2. Au cours de la thèse, j'ai découvert une nouvelle méthode de partitionnement direct qui a été utilisée pour améliorer l'inversion globale dans la zone suburbaine du plateau de Saclay.

Dans le premier article de la thèse, nous avons proposé la nouvelle méthode de partitionnement direct basée sur l'analyse en quadrants des flux décomposés en fréquence de CO_2 et de vapeur d'eau. Nous avons montré que cette méthode pouvait fournir des estimations impartiales de GPP et Reco. Nous avons également constaté que l'EC basée sur les ondelettes a gardé jusqu'à ~30% plus des données exploitables.

Dans le deuxième article, nous avons utilisé une grande tour équipée d'analyseurs à haute précision mais lents. Malgré des fréquences d'acquisition plus lentes, l'atténuation était limitée à ~20 % par une plus faible contribution de hautes fréquences à cette hauteur. Les résultats encouragent une collaboration entre les réseaux atmosphériques et écosystémiques.

Dans le troisième article, nous avons combiné la méthode de partitionnement proposée dans le premier article avec les instruments d'une tour atmosphérique du deuxième article. Le flux de CO_2 partionné en biogéniques et anthropiques ont été assimilé dans des estimations spatialisées des flux à quelques km2. Les cartes de flux obtenues offrent l'avantage de reposer sur des mesures de flux directes à l'échelle du paysage et peuvent être utilisées pour informer les inversions à grande échelle à des échelles plus larges.

Les résultats centrés sur la région parisienne fournissent des bases pour les mesures de flux à l'échelle du paysage et à definir des stratégies de surveillance des émissions. Ces avancées contribuent à la compréhension et à la résolution des défis environnementaux aux échelles temporelles et spatiales où les décisions sont prise.

A Whirlwind Journey of Wavelet Turbulent Flux Mapping:

Estimation of spatialized turbulent flux on tall towers and its uncertainties

Estimation des flux de CO_2 par covariances turbulentes à l'échelle de plusieurs km^2

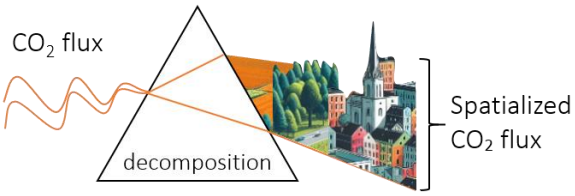

Pedro Henrique Herig Coimbra

Directed by Benjamin Loubet, co-supervised by Olivier Laurent

A collaboration between the laboratory *Écologie fonctionnelle et écotoxicologie des agroécosystèmes* (ECOSYS) at the French National Research Institute for Agriculture, Food, and Environment (INRAE) and the *Laboratoire de Sciences du Climat et de l'Environement* (LSCE) at the French Alternative Energies and Atomic Energy Commission (CEA) with support from the Euopean network for greenhouse gas monitoring, Integrated Carbon Observation System (ICOS), and Université Paris Saclay

Defence 17th May 2024

Bigger whirls have little whirls

Which feed on their velocity,

And little whirls have lesser whirls

And so on to viscosity.

Lewis F. Richardson

Big whirls and little whirls, through decomposition unfold,

Time and frequency unveil, each eddy's tale told.

At high frequencies, processes linger unmixed,

Measuring distinct swirls, helps us partition.

Pedro H. H. Coimbra

ACKNOWLEDGEMENTS

Thanks to collaborative work and initiatives that provide free and unrestricted access to all scientific knowledge and foster open-coded science for all,

TABLE OF MATTERS

LIST OF FIGURES

LIST OF ABBREVIATIONS

Abbreviation	Definition
CO2e	CO2 equivalents = total effect of all GHG normalized to CO2
EC	Eddy Covariance method
GPP	Gross Primary Product
R_{eco}	Ecosystem respiration
aCO_2	Anthropogenic emissions
VPRM	Vegetation Photosynthesis and Respiration Model. It is a model that estimates CO_2 fluxes spatialized using satellite reflectance data.

1. INTRODUCTION

The need to reduce anthropogenic pressure on climate, air quality, and ecosystems is now shared in Europe and most democracies, with debates focusing mainly on the means and trajectory for doing it. The international scientific community is mobilized and expected on its capacity to produce predictions and propose means of mitigation and adaptation. To this end, earth system models represent continental surfaces from local scales (air quality, diversity) to global scales (warming) now and predict the future. A key element in evaluating these models lies in reliably monitoring greenhouse gases (GHG) at these different scales.

Thanks to new technology from the '90s, we have high-frequency measurements of GHG concentrations and microclimate. This technological progress led to networks of flux towers being set up worldwide. Each station simultaneously measures GHG surface fluxes and relevant soil and atmospheric variables (Pastorello et al., 2020). The continuous monitoring allowed unceasing scientific progress and the flourishing of a new scientific branch, bioclimatology, from its roots in plant physiology and climate physics. We now understand better the ecosystem response to temperature (Duffy et al., 2021), climate extremes (Ciais et al., 2005; Gourlez de la Motte et al., 2020), and, more broadly, the evolution of climate and its impacts on different ecosystems thanks to this collective effort.

In parallel, technical progress has also allowed atmospheric scientists to measure and monitor GHGs in the atmosphere accurately. Ground-based monitoring stations have been the foundation for studying greenhouse gases' composition and behaviour in the atmosphere (Keeling, 1960). Now, atmospheric tower large-scale networks allow GHG emissions mapping (Storm et al., 2023). Improving emissions inventories (McGrath et al., 2023) and satellite technology have also made mapping possible. Satellite technology has dramatically evolved in measuring new radiation bands and increasing resolution over the years (Harris and Jastrow, 1958; Hansen et al., 2013), continuously improving (Brown et al., 2022)

The combination of these methods has allowed us to predict the evolution of greenhouse gas (GHG) (Vuichard et al., 2019), pollutant emissions (Messina et al., 2016) and carbon storage (Camino-Serrano et al., 2018) by continental surfaces in a context of climate change, land-use change (bioenergy), and changes in practices (lower inputs). It also enhanced our capacity to represent the response of ecosystems (Yue et al., 2018) (eutrophication, acidification, biodiversity) to climate change, uses, and inputs of pollutants and nutrients (Goll et al., 2017) from atmospheric sources.

Much of these accomplishments have only been possible thanks to established existing networks that work regionally but contribute to worldwide science. Large zones without measurements still exist, especially in southern countries, and even in denser regions such as Europe, not all ecosystems are represented equally. Combining efforts can help expand both networks while still preserving high-quality standards. Urban areas, in particular, represent a significant source of GHG emissions, as they are demographically dense, making them one of the targets for mitigating climate change. Many northern countries' cities have ambitious GHG

emission reduction plans over the next 2 decades. There arises an imperative for robust monitoring of urban areas' emissions reduction.

Conventionally, inventories are used, given their scalability. However, they have limits: temporal profiles may have spatial variability neglected, and reliability on the inputs is necessary. These inventories are sometimes adjusted by assimilating atmospheric data (Lian et al., 2023). The emission maps are often evaluated at departmental or cantonal scales (Ramanantenasoa et al., 2018). A current weakness lies in the inability to validate biogeochemical models and inventories at the spatial scales at which they are used. For biogeochemical models and remote sensing products, validation is based on observation sites on homogeneous ecosystems of a few hectares (Vuichard et al., 2016; Kountouris et al., 2018) or atmospheric inversions at scales of 1°×1° (Kountouris et al., 2018). However, in mosaic landscapes, local data for validation or calibration on kilometric grids leads to systematic flux biases that can reach 40% (Ran et al., 2016).

Therefore, hard checks are needed on model results and inventories, and underestimations of nitrogen oxide emissions have already been found compared to direct measurements (Drysdale et al., 2022). This discrepancy leads us to believe that mapping surface fluxes from direct measurements can be a significant step towards accurate spatialized surface fluxes at finer scales. Nonetheless, it remains a scientific challenge. Indeed, research addressing spatial variability has been done by whether a dense flux tower network (Ran et al., 2016; Xiao et al., 2011), inversion on light-efficiency model (Xiao et al., 2011) or statistical methods (Crawford and Christen, 2015; Metzger et al., 2013; Xu et al., 2017). The need to partition net flux remains when mapping gases with considerable sources and sinks and different processes involved, such as CO_2. In particular for urban and peri-urban areas where flux measurement exists (Velasco et al., 2009; Bergeron and Strachan, 2011; Ueyama and Takano, 2022), but is nonetheless not trivial as they have to deal with heterogeneous surfaces, uneven canopy and strong point sources.

This concise overview highlights that while we possess valuable insights, a critical element is still missing from our understanding. We lack a comprehensive framework that systematically utilises direct flux measurements to monitor greenhouse gas surface fluxes in heterogeneous landscapes, including urban and peri-urban mosaics. Developing such a framework is essential for enhancing our ability to accurately assess and mitigate the impacts of greenhouse gas emissions in diverse environments. To achieve this goal, firstly, we need to deal with non-stationary fluxes, which are expected in these landscapes as shifts from one land use to another, and in particular, point sources can cause sudden shifts in flux measurements with changes in the wind. Secondly, tall towers allow us to expand the footprint and make measurements representative of a larger area. However, we need to guarantee flux can be measured on these towers despite using longer tubes and setups not made for eddy covariance. Using these setups might also be a mid-ground between the atmospheric and ecosystem communities, where possible synergies on setup and scale can appear. Thirdly, a framework to assimilate these new direct measurements as a map and be able to attribute flux to individual pieces in this landscape mosaic is required.

This PhD aims to propose and evaluate such a framework to map CO_2 surface fluxes in a landscape of several km^2 using direct tall-tower flux measurements, satellite-driven biogenic flux model, inventories and footprint models bound by a Bayesian inference method.

The thesis manuscript is organised as follows: Chapter 1 overviews in-situ measurements, briefly introduces surface fluxes and processes, details the eddy-covariance method, and presents existing mapping techniques to estimate surface fluxes. Chapter 2 dives into wavelet-based eddy covariance, briefly explaining its origins, use in the flux community and novelty introduced by this thesis, including a new direct method for partitioning the fluxes into upward and downward components. Chapter 3 focuses on testing the wavelet framework to calculate the CO_2 flux and partition it into respiration and photosynthesis in a crop and a forest ICOS ecosystem site. Chapter 4 explores the synergy between atmospheric and ecosystem networks, using the instruments from an ICOS atmospheric tall tower coupled with a 3D anemometer to calculate surface fluxes and address the technical and height-induced challenges. Using high precision but slow-response (~3s) analysers has the advantage of expanding the network geographically and including more trace gases. Chapter 5 serves as a proof-of-concept for a framework based on Bayesian inference to assimilate tall tower partitioned fluxes in model estimations to map surface fluxes of CO_2 in the peri-urban environment of the Saclay ICOS tall tower. A short conclusion and perspectives chapter closes the document.

References

Bergeron, O. and Strachan, I. B.: CO2 sources and sinks in urban and suburban areas of a northern mid-latitude city, Atmos. Environ., 45, 1564–1573, https://doi.org/10.1016/j.atmosenv.2010.12.043, 2011.

Brown, C. F., Brumby, S. P., Guzder-Williams, B., Birch, T., Hyde, S. B., Mazzariello, J., Czerwinski, W., Pasquarella, V. J., Haertel, R., Ilyushchenko, S., Schwehr, K., Weisse, M., Stolle, F., Hanson, C., Guinan, O., Moore, R., and Tait, A. M.: Dynamic World, Near real-time global 10 m land use land cover mapping, Sci. Data, 9, 251, https://doi.org/10.1038/s41597-022-01307-4, 2022.

Camino-Serrano, M., Guenet, B., Luyssaert, S., Ciais, P., Bastrikov, V., De Vos, B., Gielen, B., Gleixner, G., Jornet-Puig, A., Kaiser, K., Kothawala, D., Lauerwald, R., Peñuelas, J., Schrumpf, M., Vicca, S., Vuichard, N., Walmsley, D., and Janssens, I. A.: ORCHIDEE-SOM: modeling soil organic carbon (SOC) and dissolved organic carbon (DOC) dynamics along vertical soil profiles in Europe, Geosci. Model Dev., 11, 937–957, https://doi.org/10.5194/gmd-11-937-2018, 2018.

Ciais, P., Reichstein, M., Viovy, N., Granier, A., Ogée, J., Allard, V., Aubinet, M., Buchmann, N., Bernhofer, C., Carrara, A., Chevallier, F., De Noblet, N., Friend, A. D., Friedlingstein, P., Grünwald, T., Heinesch, B., Keronen, P., Knohl, A., Krinner, G., Loustau, D., Manca, G., Matteucci, G., Miglietta, F., Ourcival, J. M., Papale, D., Pilegaard, K., Rambal, S., Seufert, G., Soussana, J. F., Sanz, M. J., Schulze, E. D., Vesala, T., and Valentini, R.: Europe-wide reduction in primary productivity caused by the heat and drought in 2003, Nature, 437, 529–533, https://doi.org/10.1038/nature03972, 2005.

Crawford, B. and Christen, A.: Spatial source attribution of measured urban eddy covariance CO2 fluxes, Theor. Appl. Climatol., 119, 733–755, https://doi.org/10.1007/s00704-014-1124-0, 2015.

Drysdale, W. S., Vaughan, A. R., Squires, F. A., Cliff, S. J., Metzger, S., Durden, D., Pingintha-Durden, N., Helfter, C., Nemitz, E., Grimmond, C. S. B., Barlow, J., Beevers, S., Stewart, G., Dajnak, D., Purvis, R. M., and Lee, J. D.: Eddy Covariance Measurements Highlight Sources of Nitrogen Oxide Emissions Missing from Inventories for Central London, Atmospheric Chem. Phys. Discuss., 1–35, https://doi.org/10.5194/acp-2021-982, 2022.

Duffy, K. A., Schwalm, C. R., Arcus, V. L., Koch, G. W., Liang, L. L., and Schipper, L. A.: How close are we to the temperature tipping point of the terrestrial biosphere?, Sci. Adv., 7, eaay1052, https://doi.org/10.1126/sciadv.aay1052, 2021.

Goll, D. S., Vuichard, N., Maignan, F., Jornet-Puig, A., Sardans, J., Violette, A., Peng, S., Sun, Y., Kvakic, M., Guimberteau, M., Guenet, B., Zaehle, S., Penuelas, J., Janssens, I., and Ciais, P.: A representation of the phosphorus cycle for ORCHIDEE (revision 4520), Geosci. Model Dev., 10, 3745–3770, https://doi.org/10.5194/gmd-10-3745-2017, 2017.

Gourlez de la Motte, L., Beauclaire, Q., Heinesch, B., Cuntz, M., Foltýnová, L., Šigut, L., Kowalska, N., Manca, G., Ballarin, I. G., Vincke, C., Roland, M., Ibrom, A., Lousteau, D., Siebicke, L., Neiryink, J., and Longdoz, B.: Non-stomatal processes reduce gross primary productivity in temperate forest ecosystems during severe edaphic drought, Philos. Trans. R. Soc. Lond. B. Biol. Sci., 375, 20190527, https://doi.org/10.1098/rstb.2019.0527, 2020.

Hansen, M. C., Potapov, P. V., Moore, R., Hancher, M., Turubanova, S. A., Tyukavina, A., Thau, D., Stehman, S. V., Goetz, S. J., Loveland, T. R., Kommareddy, A., Egorov, A., Chini, L., Justice, C. O., and Townshend, J. R. G.: High-Resolution Global Maps of 21st-Century Forest Cover Change, Science, 342, 850–853, https://doi.org/10.1126/science.1244693, 2013.

Harris, I. and Jastrow, R.: Upper Atmosphere Densities from Minitrack Observations on Sputnik I, Science, 127, 471–472, https://doi.org/10.1126/science.127.3296.471.b, 1958.

Keeling, C. D.: The Concentration and Isotopic Abundances of Carbon Dioxide in the Atmosphere, Tellus, 12, 200–203, https://doi.org/10.1111/j.2153-3490.1960.tb01300.x, 1960.

Kountouris, P., Gerbig, C., Rödenbeck, C., Karstens, U., Koch, T. F., and Heimann, M.: Atmospheric CO_2 inversions on the mesoscale using data-driven prior uncertainties: quantification of the European terrestrial CO_2 fluxes, Atmospheric Chem. Phys., 18, 3047–3064, https://doi.org/10.5194/acp-18-3047-2018, 2018.

Lian, J., Lauvaux, T., Utard, H., Bréon, F.-M., Broquet, G., Ramonet, M., Laurent, O., Albarus, I., Chariot, M., Kotthaus, S., Haeffelin, M., Sanchez, O., Perrussel, O., Denier van der Gon, H. A., Dellaert, S. N. C., and Ciais, P.: Can we use atmospheric CO_2 measurements to verify emission trends reported by cities? Lessons from a 6-year atmospheric inversion over Paris, Atmospheric Chem. Phys., 23, 8823–8835, https://doi.org/10.5194/acp-23-8823-2023, 2023.

Messina, P., Lathière, J., Sindelarova, K., Vuichard, N., Granier, C., Ghattas, J., Cozic, A., and Hauglustaine, D. A.: Global biogenic volatile organic compound emissions in the ORCHIDEE and MEGAN models and sensitivity to key parameters, Atmospheric Chem. Phys., 16, 14169–14202, https://doi.org/10.5194/acp-16-14169-2016, 2016.

Metzger, S., Junkermann, W., Mauder, M., Butterbach-Bahl, K., Trancón y Widemann, B., Neidl, F., Schäfer, K., Wieneke, S., Zheng, X. H., Schmid, H. P., and Foken, T.: Spatially explicit regionalization of airborne flux measurements using environmental response functions, Biogeosciences, 10, 2193–2217, https://doi.org/10.5194/bg-10-2193-2013, 2013.

Pastorello, G., Trotta, C., Canfora, E., Chu, H., Christianson, D., Cheah, Y.-W., Poindexter, C., Chen, J., Elbashandy, A., Humphrey, M., Isaac, P., Polidori, D., Reichstein, M., Ribeca, A., van Ingen, C., Vuichard, N., Zhang, L., Amiro, B., Ammann, C., Arain, M. A., Ardö, J., Arkebauer, T., Arndt, S. K., Arriga, N., Aubinet, M., Aurela, M., Baldocchi, D., Barr, A., Beamesderfer, E., Marchesini, L. B., Bergeron, O., Beringer, J.,

Bernhofer, C., Berveiller, D., Billesbach, D., Black, T. A., Blanken, P. D., Bohrer, G., Boike, J., Bolstad, P. V., Bonal, D., Bonnefond, J.-M., Bowling, D. R., Bracho, R., Brodeur, J., Brümmer, C., Buchmann, N., Burban, B., Burns, S. P., Buysse, P., Cale, P., Cavagna, M., Cellier, P., Chen, S., Chini, I., Christensen, T. R., Cleverly, J., Collalti, A., Consalvo, C., Cook, B. D., Cook, D., Coursolle, C., Cremonese, E., Curtis, P. S., D'Andrea, E., da Rocha, H., Dai, X., Davis, K. J., Cinti, B. D., Grandcourt, A. de, Ligne, A. D., De Oliveira, R. C., Delpierre, N., Desai, A. R., Di Bella, C. M., Tommasi, P. di, Dolman, H., Domingo, F., Dong, G., Dore, S., Duce, P., Dufrêne, E., Dunn, A., Dušek, J., Eamus, D., Eichelmann, U., ElKhidir, H. A. M., Eugster, W., Ewenz, C. M., Ewers, B., Famulari, D., Fares, S., Feigenwinter, I., Feitz, A., Fensholt, R., Filippa, G., Fischer, M., Frank, J., Galvagno, M., et al.: The FLUXNET2015 dataset and the ONEFlux processing pipeline for eddy covariance data, Sci. Data, 7, 225, https://doi.org/10.1038/s41597-020-0534-3, 2020.

Ramanantenasoa, M. M. J., Gilliot, J.-M., Mignolet, C., Bedos, C., Mathias, E., Eglin, T., Makowski, D., and Génermont, S.: A new framework to estimate spatio-temporal ammonia emissions due to nitrogen fertilization in France, Sci. Total Environ., 645, 205–219, https://doi.org/10.1016/j.scitotenv.2018.06.202, 2018.

Ran, Y., Li, X., Sun, R., Kljun, N., Zhang, L., Wang, X., and Zhu, G.: Spatial representativeness and uncertainty of eddy covariance carbon flux measurements for upscaling net ecosystem productivity to the grid scale, Agric. For. Meteorol., 230–231, 114–127, https://doi.org/10.1016/j.agrformet.2016.05.008, 2016.

Storm, I., Karstens, U., D'Onofrio, C., Vermeulen, A., and Peters, W.: A view of the European carbon flux landscape through the lens of the ICOS atmospheric observation network, Atmospheric Chem. Phys., 23, 4993–5008, https://doi.org/10.5194/acp-23-4993-2023, 2023.

Ueyama, M. and Takano, T.: A decade of CO2 flux measured by the eddy covariance method including the COVID-19 pandemic period in an urban center in Sakai, Japan, Environ. Pollut., 304, 119210, https://doi.org/10.1016/j.envpol.2022.119210, 2022.

Velasco, E., Pressley, S., Grivicke, R., Allwine, E., Coons, T., Foster, W., Jobson, B. T., Westberg, H., Ramos, R., Hernández, F., Molina, L. T., and Lamb, B.: Eddy covariance flux measurements of pollutant gases in urban Mexico City, Atmospheric Chem. Phys., 9, 7325–7342, https://doi.org/10.5194/acp-9-7325-2009, 2009.

Vuichard, N., Ciais, P., Viovy, N., Li, L., Ceschia, E., Wattenbach, M., Bernhofer, C., Emmel, C., Grünwald, T., Jans, W., Loubet, B., and Wu, X.: Simulating the net ecosystem CO2 exchange and its components over winter wheat cultivation sites across a large climate gradient in Europe using the ORCHIDEE-STICS generic model, Agric. Ecosyst. Environ., 226, 1–17, https://doi.org/10.1016/j.agee.2016.04.017, 2016.

Vuichard, N., Messina, P., Luyssaert, S., Guenet, B., Zaehle, S., Ghattas, J., Bastrikov, V., and Peylin, P.: Accounting for carbon and nitrogen interactions in the global terrestrial ecosystem model ORCHIDEE (trunk version, rev 4999): multi-scale evaluation of gross primary production, Geosci. Model Dev., 12, 4751–4779, https://doi.org/10.5194/gmd-12-4751-2019, 2019.

Xiao, J., Davis, K. J., Urban, N. M., Keller, K., and Saliendra, N. Z.: Upscaling carbon fluxes from towers to the regional scale: Influence of parameter variability and land cover representation on regional flux estimates, J. Geophys. Res. Biogeosciences, 116, https://doi.org/10.1029/2010JG001568, 2011.

Xu, K., Metzger, S., and Desai, A. R.: Upscaling tower-observed turbulent exchange at fine spatio-temporal resolution using environmental response functions, Agric. For. Meteorol., 232, 10–22, https://doi.org/10.1016/j.agrformet.2016.07.019, 2017.

Yue, C., Ciais, P., Luyssaert, S., Li, W., McGrath, M. J., Chang, J., and Peng, S.: Representing anthropogenic gross land use change, wood harvest, and forest age dynamics in a global vegetation model ORCHIDEE-MICT v8.4.2, Geosci. Model Dev., 11, 409–428, https://doi.org/10.5194/gmd-11-409-2018, 2018.

2. OVERVIEW OF IN-SITU MEASUREMENT TECHNIQUES FOR SURFACE TURBULENT FLUX

This first chapter overviews the processes and measurement techniques for retrieving surface fluxes. In the first part, we introduce briefly the main processes governing the surface-atmosphere fluxes and the existing measurement techniques at the local scale. In the second part, we detail the eddy-covariance method and related equations, and we conclude with a short overview of existing mapping techniques to estimate surface fluxes.

2.1 Short overview of surface-atmosphere exchange processes and measurement techniques

2.1.1 The atmospheric boundary layer: the surface-atmosphere interface

The atmospheric boundary layer is a critical region where the atmosphere directly interacts with the Earth's surface. It is the layer of air closest to the ground, and its height varies depending on terrain and weather conditions, but it typically extends over a few hundred meters. Within this layer, various physical, chemical, and biological processes govern the exchange of heat and gases between the surface and atmosphere (Seinfeld, Pandis, et Noone 1998).

The diel pattern is intricately shaped by momentum, heat, and water vapour exchanges with the Earth's surface (Kaimal and Finnigan, 1994). Solar radiation warms the ground and the adjacent air throughout the day, fuelling convective motions that generate buoyant plumes and larger eddies in an unstable surface layer. These larger turbulent elements transfer their energy to smaller elements through a cascade process. Conversely, with no solar input and colder ground temperatures at night, kinetic energy dissipates, leading to the collapse of turbulent motions and the onset of stable conditions.

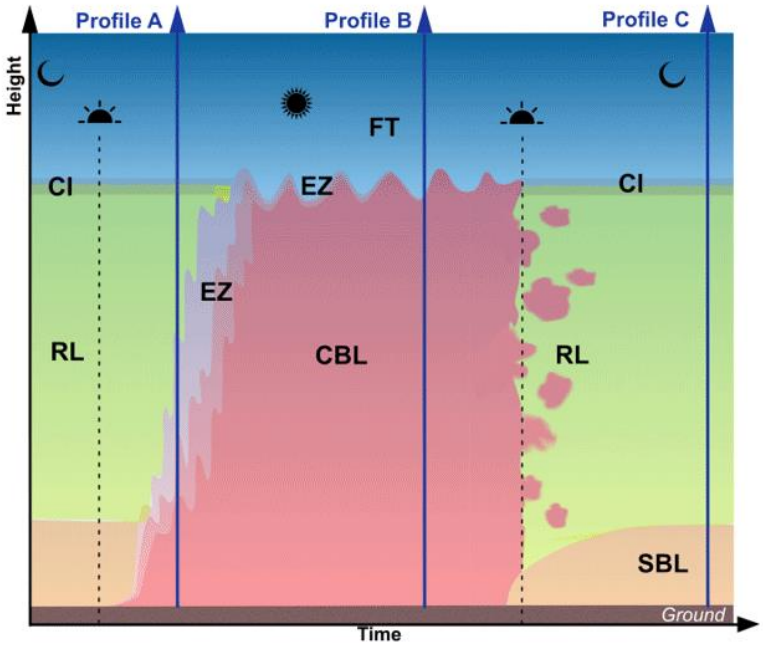

Figure 2.1. Idealised diurnal atmospheric boundary layer (ABL) evolution over flat terrain on a cloud-free day. Morning growth of the convective boundary layer (CBL; pink shading); nocturnal conditions with a residual layer (RL; green shading) above the stable boundary layer (SBL; orange shading) near the surface. A capping inversion (CI) separates the ABL from the free troposphere (FT; blue shading) above. The entrainment zone (EZ) is a region of enhanced exchange between the CBL and the RL or FT, respectively. Source: (Kotthaus et al. 2023).

Atmospheric turbulence dominates transport mechanisms within the convective boundary layer, and surface-driven processes dominate (Kotthaus et al., 2023). With certain conditions of surface homogeneity, the vertical fluxes within this layer remain relatively constant with height, making measurements taken in this region representative of surface-level fluxes. This characteristic justifies using the eddy covariance approach for measuring surface fluxes (Foken 2008).

Surface-driven processes govern boundary layer dynamics, with biological processes playing a significant role. Vegetation, encompassing forests, grasslands, wetlands and crops, influences gas exchange, such as CO_2, water vapour, and CH_4, through photosynthesis, transpiration, and respiration. Soil respiration similarly contributes to these exchanges. These biological activities impact atmospheric composition and regulate surface energy, including heat and water fluxes, thereby shaping local and regional climate patterns (Monteith et Unsworth, 2013).

2.1.2 The Earth's surface energy budget

The Earth's energy budget represents the balance between incoming solar radiation and outgoing thermal radiation. Solar energy is absorbed by the Earth's surface, heating it and driving various processes such as evaporation, photosynthesis, and, at larger scales, atmospheric circulation (Forster et al. 2021).

The fraction of solar and atmospheric radiation absorbed by the Earth's surface is called net radiation and is primarily driven by the surface albedo, the ratio of reflected to absorbed solar radiation, and the surface temperature. The net radiation is dissipated to the soil via conduction and the air through convection (H, sensible heat flux) and by latent heat (LE, latent heat flux), associated with evaporation and transpiration (Seinfeld, Pandis et Noone 1998). In dry conditions, most of the energy absorbed by the surface is dissipated as sensible heat and soil conduction, leading to high surface temperatures, whereas in humid ecosystems, latent heat predominates, tempering surface temperature. At larger scales, local energy fluxes impact cloud formation and regional climate (Forster et al. 2021).

Transpiration, a fundamental facet of the hydrological cycle, represents the release of water vapour through plant stomata, which modulates surface temperature and humidity levels. This process is regulated by stomatal aperture, a dynamic gateway controlled by environmental factors such as light intensity, temperature, humidity, and atmospheric CO_2 concentration. The stomatal aperture regulates water vapour fluxes and all gas exchanges at the leaf scale, including CO_2 sequestration by photosynthesis. Thus, the stomatal aperture dictates transpiration, as does plant water status and photosynthetic activity (Farineau et Morot-Gaudry 2017).

2.1.3 Greenhouse gas exchange at the surface-atmosphere interface

The exchange of gases between the Earth's surface and the atmosphere happens locally, and they play a crucial role on larger scales by regulating atmospheric composition, influencing climate, and notably driving climate change through the greenhouse effect. Fossil fuel and industrial CO_2 and CH_4 are the two main contributors to the warming of the planet (Dhakal et al., 2022).

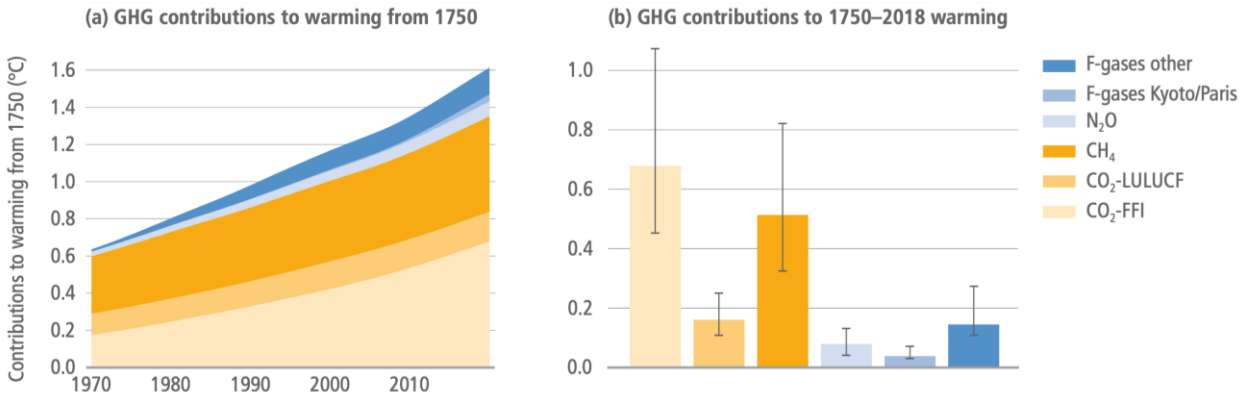

Figure 2.2. Contribution of different GHGs to global warming over the period 1750 to 2018. CO_2 from fossil fuel combustion and industrial processes (FFI); net CO_2 from land use, land use change and forestry (LULUCF); methane (CH_4); nitrous oxide (N_2O); fluorinated gases (F-gases: HFCs, PFCs, SF6, NF3). Major GHGs and aggregates of minor gases as a time series in (a) and as a total warming bar chart with a 90% confidence interval added in (b). F-Kyoto/Paris includes the gases covered by the Kyoto Protocol and Paris Agreement,

while F-other includes those covered by the Montreal Protocol but excludes the HFCs. Source: (Dhakal et al. 2022).

In the CO_2 budget, while natural processes such as photosynthesis and respiration drive substantial flux exchanges, net fluxes are comparatively smaller than anthropogenic fluxes (Figure 2.3). Indeed, fossil fuel and cement production emissions alone are approximately three times larger than the net land fluxes (Canadell et al. 2021).

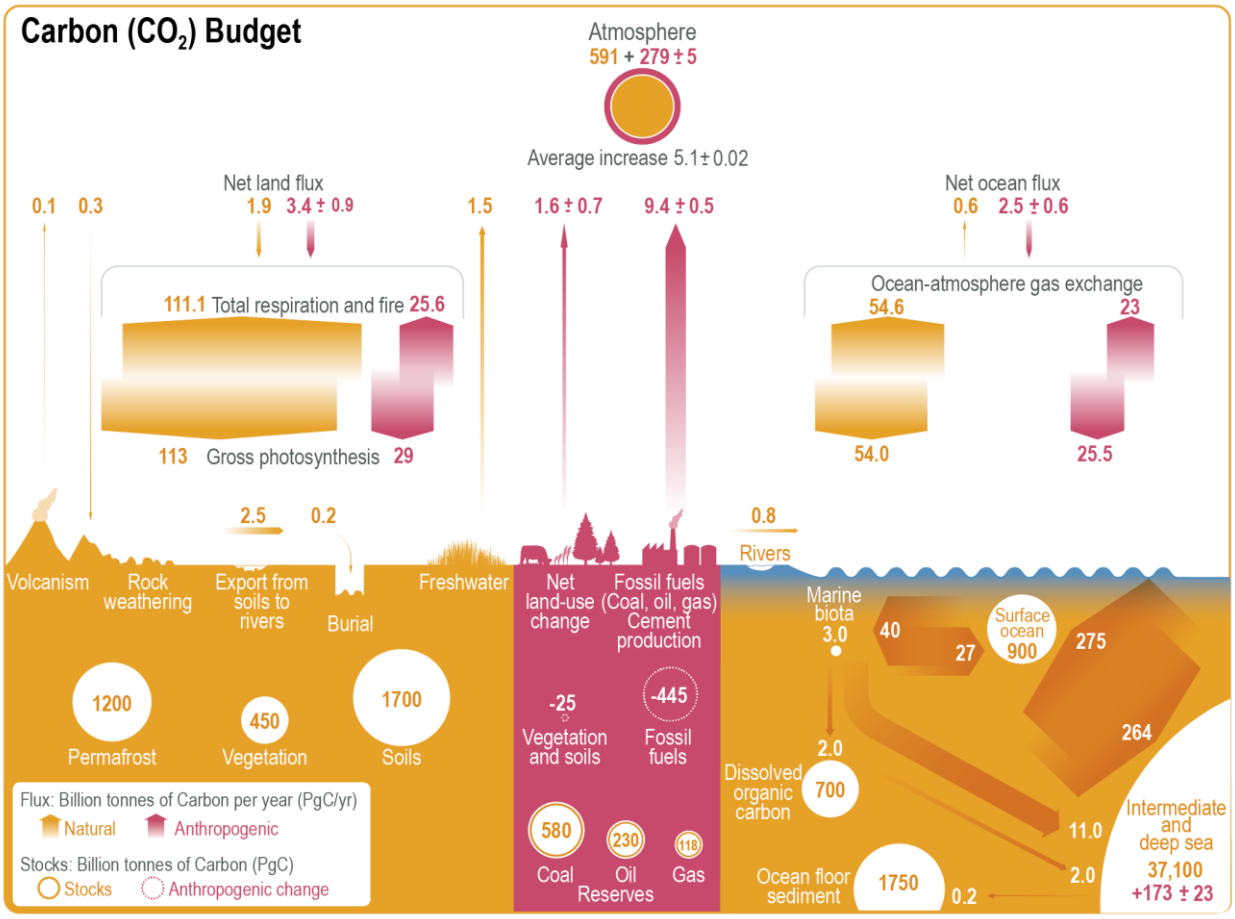

Figure 2.3. Global carbon (CO2) budget (2010–2019). Yellow arrows represent annual carbon fluxes (in PgC yr–1) associated with the natural carbon cycle, estimated for the time prior to the industrial era, around 1750. Pink arrows represent anthropogenic fluxes averaged over the period 2010–2019. Circles with yellow numbers represent pre-industrial carbon stocks in PgC. Circles with pink numbers represent anthropogenic changes to these stocks (cumulative anthropogenic fluxes) since 1750. Values, data sources and methodology in Canadell et al. (2021). Source: (Canadell et al. 2021).

Land and sea vegetation plays a vital role in the exchange of gases at the Earth's surface. Through photosynthesis, they absorb CO_2 and water, converting them into carbohydrates and oxygen in sunlight. External factors, such as light intensity, CO_2 concentration, temperature, nutrients and water availability, and internal factors, such as enzyme activity, collectively regulate the rate of photosynthesis, ultimately impacting growth and productivity (Farineau et Morot-Gaudry 2017).

On land, photosynthesis has been shown to have optimal temperature ranges for functioning, where conditions warmer than a threshold (17°C globally) can become a limiting factor (Duffy et al. 2021). Besides temperature, water stress, due to elevated vapour pressure deficit in the air or low soil water content, regulates stomata closure so that the plant can preserve internal equilibrium during dry conditions, limiting photosynthesis (Medlyn et al. 2011).

Conversely, plants and soil release CO2 back into the atmosphere during respiration. It is well-established that respiration responds to temperature (Lloyd et Taylor 1994). No threshold was found for temperatures observed in the sites across the globe (FLUXNET) and under heatwaves, and respiration kept increasing with temperature (Anjileli et al. 2021; Duffy et al. 2021). Soil respiration also responds to low soil water content due to microbial community metabolism. Note that for soil respiration, surface moisture levels often correlate more strongly with soil respiration rates on the surface than deeper soil layers (Fu et al. 2020).

In the methane budget, natural processes play a significant role in driving substantial flux exchanges, particularly emissions from wet environments like freshwater bodies and wetlands, as well as methane consumption through atmospheric oxidation. Anthropogenic CH_4 emissions are also comparable in magnitude to these natural processes. For example, fossil fuel and livestock emissions are approximately equivalent to natural emissions in freshwater bodies and wetlands (Figure 2.4) (Canadell et al. 2021).

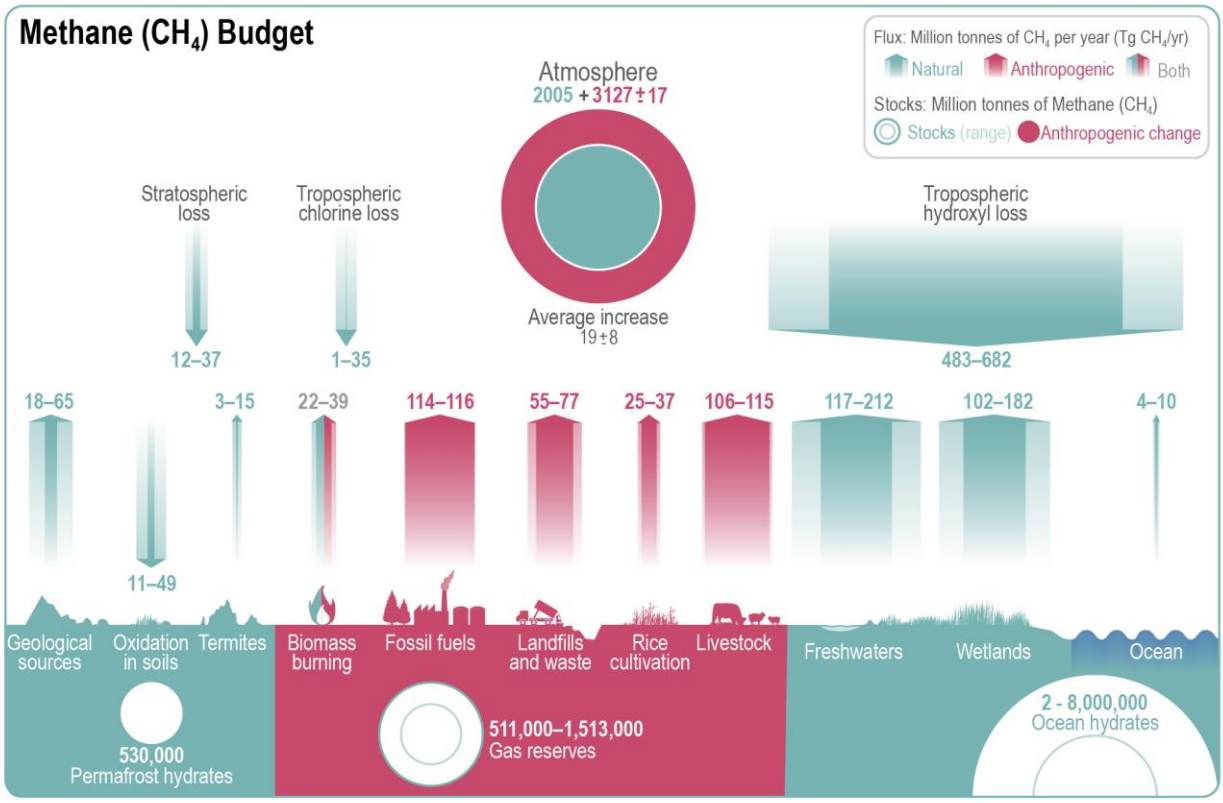

Figure 2.4. A Global methane (CH4) budget (2008–2017). Values, data sources and methodology in (Canadell et al. 2021). Source: (Canadell et al. 2021).

Soils both produce and consume CH_4. The net soil-atmosphere CH_4 flux arises from the equilibrium between these opposing processes. Organisms responsible for the consumption rely on molecular O_2 in soil. On the contrary, methanogenesis (CH_4 production) occurs in anaerobic conditions. Anaerobic conditions are often found in wetland soils and rice paddies; however, methanogenesis can also occur in upland soils within anaerobic "microsites" inside soil aggregates. Nonetheless, methanotrophy (consumption or oxidation) predominates in upland soils, resulting in a net sink of CH_4 (Dutaur et Verchot 2007).

Nitrous oxide (N_2O) is the third most emitted GHG by anthropogenic activities, emitted mainly by agricultural fertilised land (Tian et al. 2020). Despite not being key contributors to climate change, many other compounds are essential for climate, air quality and ecosystem functioning. In particular, short-lived species, among which nitrogen oxides (NO_x) and volatile organic compounds (VOC) are crucial to aerosol and ozone formation, both playing an essential role in air quality and climate (Fowler et al. 2015). These compounds are exchanged between the surface and the atmosphere and play a crucial role in the ecosystem's functioning (Brosset et Blande, 2022; M. Sutton, Howard, et Erisman, 2011).

2.1.4 In-situ measurement techniques for surface flux

Over the past four decades, significant advancements have been made in developing and refining in-situ measurement techniques for surface flux (Seinfeld, Pandis, et Noone 1998). Advances in observational techniques, such as eddy covariance flux measurements (Baldocchi 2003; Pastorello et al. 2020), remote sensing (Jung et al. 2020), and stable isotope analysis (Worthy et al. 2023), have provided invaluable insights into the spatiotemporal variability of surface-atmosphere gas exchanges. These observations, numerical models and theoretical frameworks have enhanced our understanding of the underlying mechanisms driving biogeochemical fluxes and their role in shaping Earth's climate system (Friedlingstein et al., 2020). All measurement techniques rely in one way or another on the mass balance equations of the compound (see next Section).

The enclosure method (or chamber) is the simplest and first employed method to measure surface fluxes (Lundegårdh 1927; Kanemasu, Powers, et Sij 1974). The closed chamber technique, which is the simplest, involves sealing a chamber over the surface of interest and monitoring changes in gas concentration over time to quantify fluxes as proportional to its time derivative. A slightly more complex method consists of open chambers where the flux is, in this case, proportional to the change in concentration between the inlet and the outlet of the chamber (Loubet et al. 1999; Pape et al. 2009). Chambers are particularly useful for investigating small-scale processes like leaf-, plant- or soil-atmosphere exchanges, including photosynthesis and respiration. Closed chambers offer simplicity, ease of deployment, and direct measurement of fluxes at specific locations, and they are well-suited for studying photosynthesis and respiration. Automated systems to control chamber closure and gas sampling enable continuous monitoring of surface fluxes over extended periods, providing insights into environmental changes' effects on ecosystem functioning (e.g. Griffis et al. 2004). The limitation of the chamber method is its small sampling surface and the fact that it modifies environmental conditions.

Another method that was employed early is the aerodynamic gradient method, which relies on measuring the vertical gradient of the target scalar or gas concentration profile within the

atmospheric boundary layer (Monteith et Unsworth, 2013). This approach involves deploying sensors at multiple heights above the surface to capture the concentration variations. By applying the gradient diffusion theory, the surface fluxes can be inferred from the rate of change in gas concentration with height, considering factors such as atmospheric stability and turbulent mixing in the diffusivity term (Bethenod et al. 1991). Aerodynamic gradient methods are still used for reactive gases such as ammonia (M. A. Sutton et al. 2009) or HONO (Laufs et al. 2017).

One of the fundamental methods employed in this field nowadays is the Eddy Covariance (EC) technique. This approach directly measures the exchange of mass and energy between the Earth's surface and the atmosphere by continuously monitoring the vertical wind speed and the concentration of the target scalar or gas (e.g., temperature, water vapour, carbon dioxide) within the atmospheric boundary layer (Brutsaert 1982). EC systems typically utilize fast-response sensors, such as ultrasonic anemometers and infrared gas analysers, to capture the turbulent fluctuations in these variables. By integrating the product of the fluctuations in vertical wind speed and gas concentration over time, the turbulent fluxes can be accurately quantified (Foken, Aubinet, et Leuning 2012). The eddy covariance technique is at the core of this PhD; it is detailed in the next section.

Integrating several measurement techniques, like eddy covariance or gradient methods, and chambers contributes to understanding surface flux dynamics at various spatial scales. These techniques evaluated larger than 350 Pg CO_2e global annual net soil emissions (Oertel et al. 2016).

2.2 Eddy Covariance's conventional framework

As climate change has put ecosystem carbon exchanges at the focal point, assessing them has become essential in recent years. Traditional tools such as leaf cuvettes and chambers have long provided flux data that can be used to define environmental response functions. The downsides include the small sampling area and the instrument's bias (light scattering and modification of canopy microclimate). On a plot or landscape scale, biomass inventories have been used. In a forest, they “rely on allometric relations to scale incremental changes in tree diameters at breast height to net primary production”, which can ignore other tree aspects (multi-age, species, small size classes), and they also do not consider soil carbon (Baldocchi 2003).

The technological progress in the last century, coupled with a maturation of the theoretical framework, allowed surface flux measurements on towers with a new approach, named eddy covariance, allowing long-term direct flux measurements at the ecosystem scale (Kaimal et Finnigan 1994). After some criticism and continuous development, the methodology became the standard method for measuring flux at the plot scales (Baldocchi 2003).

2.2.1 Background theory

Eddy covariance is a method for measuring mass, momentum, and energy exchange between the surface and the atmosphere. This exchange can be described using conservation equations of mass, momentum, and energy. This sub-section is primarily based on Foken, Aubinet, et Leuning (2012). For further reading and in-depth information, refer to their work.

The equation describing the conservation of any scalar or quantity ζ in the atmosphere can be written as:

$$\underbrace{\frac{\partial \rho_d \zeta}{\partial t}}_{I} + \underbrace{\vec{\nabla}(\vec{u}\rho_d\zeta)}_{II} + \underbrace{K_\zeta \Delta(\rho_d \zeta)}_{III} - \underbrace{S_\zeta}_{IV} = 0 \qquad 2.1$$

Where t is time, ρ_d is the dry air density, $\vec{u}$ is the wind velocity vector, K_ζ is the molecular diffusivity of ζ, S_ζ is the source/sink strength, $\vec{\nabla}$ and Δ are the divergence and Laplacian operators. This equation states that "the rate of change of the quantity (I) can be due to its atmospheric transport (II) molecular diffusion (III) or its production by a source/absorption by a sink into the infinitesimal volume (IV)" (Foken, Aubinet, et Leuning 2012). Applying these equations to the surface boundary layer requires the application of the Reynolds decomposition rules.

2.2.2 Reynolds decomposition and the ergodicity requirement

Reynolds decomposition is a technique that separates the mean from the turbulent fluctuations of a quantity ζ in a fluid flow. In this technique, the velocity or any other property of the fluid is divided into two components: a mean component ($\bar{\zeta}$) and a fluctuating component (ζ').

$$\zeta = \bar{\zeta} + \zeta' \qquad 2.2$$

Reynolds decomposition enables studying these components individually. For instance, the mean flow aids in calculating mass, momentum, and energy transport, while turbulent fluctuations help study mixing and diffusion processes.

Reynolds decomposition is fundamental for understanding turbulence and is widely utilised in fluid mechanics and aerodynamics. Breaking down the flow into mean and fluctuation parts allows for solving Navier-Stokes equations for large scales by reducing computational costs, although it requires an additional closure hypothesis to solve the problem. In *stricto sensu*, the relations are valid only for "ensemble" averaging (i.e., averaging over many realizations under identical conditions). However, since this is never possible in in-situ measurements, its application relies on ergodic conditions when time averaging approximates "ensemble" averages (Foken, Aubinet, et Leuning 2012).

2.2.3 Main equations

Turbulent motions mix air in the boundary layer, stimulating surface and atmosphere interactions. The eddy covariance method relies on measuring air parcels at a certain height. In most cases, it can give a reliable measurement of the net exchange surface flux using high-frequency measurements of the vertical component of the wind and a scalar, usually gas concentration or temperature.

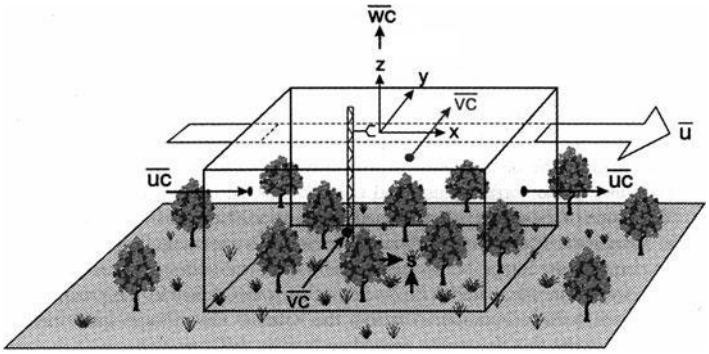

Figure 2.5. Schematic image of integration of Eq. 2.3 on a control volume inhomogeneous terrain (Finnigan et al. 2003)

This method relies on the conservation of mass or energy. Thus, retrieving surface flux from eddy covariance needs some assumptions.

$$F_s = \rho_d \frac{1}{4L^2} \int_{-L}^{L} \int_{-L}^{L} \int_{0}^{h_m} \left[\underbrace{\frac{\partial \overline{\chi_s}}{\partial t}}_{I} + \underbrace{\bar{u}\frac{\partial \overline{\chi_s}}{\partial x} + \bar{v}\frac{\partial \overline{\chi_s}}{\partial y} + \bar{w}\frac{\partial \overline{\chi_s}}{\partial z}}_{II} + \underbrace{\frac{\partial \overline{u'\chi_s'}}{\partial x} + \frac{\partial \overline{v'\chi_s'}}{\partial y}}_{III} + \underbrace{\frac{\partial \overline{w'\chi_s'}}{\partial z}}_{IV} \right] dz\, dx\, dy \qquad 2.3$$

Equation 2.3 describes the surface flux of a scalar (χ_s) and its constituent parts. It involves a 3D integration up to the measurement height (h_m) of stock (I), advection (II), and turbulent fluxes (III and IV). Stock represents the temporal variation of the scalar, while advection and turbulent fluxes denote transport across space (*x*, *y*, *z*) by bulk motion or turbulent eddies, respectively. Advection typically occurs over large spatial scales due to inhomogeneities of the scalar concentrations.

Measuring all these components with a single measuring point is not possible. Thus, assumptions are often made for simplification, assuming negligible advection and horizontal turbulent fluxes. These assumptions are justified under conditions of horizontal homogeneity, where there is no mixing with fluxes arising from a different surface. They allow the simplification of equation 2.3 into equation 2.4.

$$F_s = \underbrace{F_s^{STO}}_{I} + \underbrace{F_s^{EC}}_{IV} \qquad 2.4$$

Equation 2.4 presumes surface flux to be equal to stock, F_s^{STO}, and vertical turbulent flux, F_s^{EC}. The stock can be measured with a vertical profile of the scalar. For small towers, it is frequently assumed to be negligible due to the limited volume of bellow instruments (Moureaux et al. 2012). Vertical turbulent flux can be measured at a single point, and as standard, it is calculated by the eddy covariance technique.

The eddy covariance flux is the covariance between the vertical component of wind (*w*) and a scalar, namely $\overline{w'\chi_s'}$. The covariance sign indicates the direction of the flux, while the absolute value indicates the sink or source strength. By convention, a positive sign means that upwind brings air that is richer in the scalar or that downwind brings air that is poorer in the scalar. Conversely, a negative sign suggests the opposite relationship.

For the covariance calculation, an averaging period must be chosen. This choice is not trivial because it is funded in a dilemma: on the one hand, shorter periods include fewer frequencies; on the other hand, the longer, the harder it is to get stationary conditions necessary to respect the ergodic assumption. Shorter periods have also shown wider gaps in the energy balance closure (Finnigan et al. 2003). Considering a typical turbulent spectrum in the atmospheric boundary layer (Figure 2.6), 30 minutes is usually preferred for eddy covariance measurements.

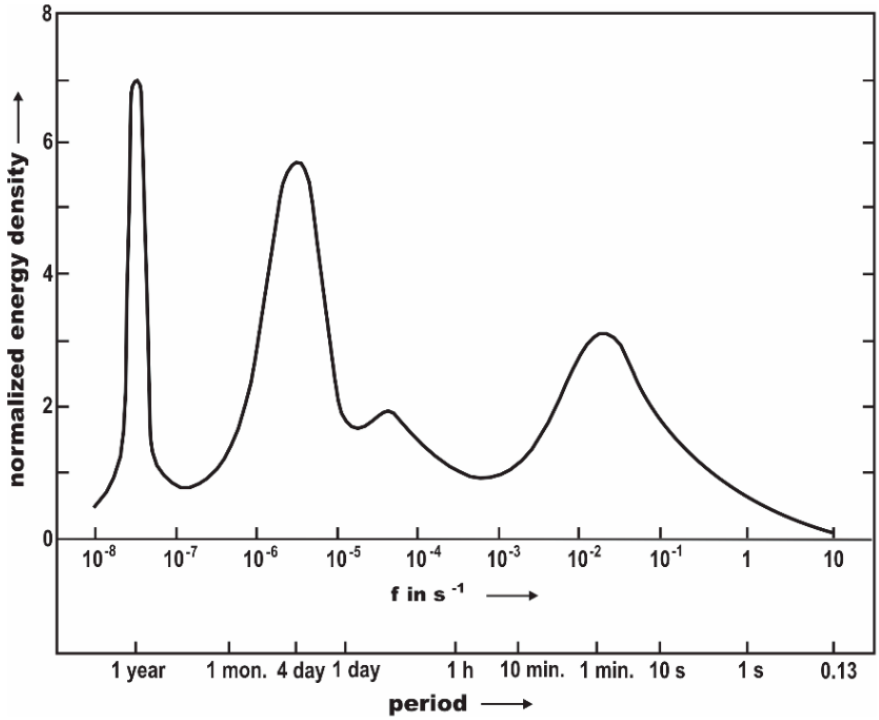

Figure 2.6. Schematic plot of the turbulence spectra. Source: (Foken 2008).

2.2.4 Spectral analysis

Energy spectra and co-spectra help identify a signal's integrity and, inversely, its possible attenuation at specific frequencies. Spectral analysis aims to identify and characterize the frequency components contributing to signal variability. Fourier transform is a common method to analyse the frequency distribution of a signal. This method decomposes a signal into sinusoidal components of different frequencies, thus assuming that the signal is periodic or extends to infinity. Using the Fourier transform is valid because of Parseval's or Plancherel's theorem.

Plancherel theorem, sometimes loosely referred to as Parseval's theorem, establishes a fundamental relationship between the energy or power of a signal in the time domain and its frequency-domain representation (Plancherel et Leffler 1910). According to this theorem, the

integral of a function's $f(x)$ squared modulus is equal to the integral of the squared modulus of its frequency transform, $f(\xi)$:

$$\int_{-\infty}^{\infty} |f(x)|^2 \, d_x = \int_{-\infty}^{\infty} |f(\xi)|^2 \, d_\xi \qquad 2.5$$

In other words, the theorem states that the variance, a measure of the total energy of a signal, is equal to the sum of the squared magnitudes of its Fourier coefficients, or put in another way, variance in the time and frequency domains are equal. This theorem allows further use of the Fourier transform for spectral analysis as it links the time and frequency domains.

Based on this framework, several studies have focused on characterizing turbulent spectra in the atmospheric boundary layer and how it is modified by instrumentation. Parameterizations of the momentum and sensible heat co-spectra have been proposed (Kaimal et al. 1972). Other authors have shown that instruments and measurement setups may induce energy loss or gain in the signal that biases their variance or covariance measurements: Low acquisition frequency or tube attenuation can work as a low pass filter, damping high-frequency contribution (Figure 2.7b). Removing trends in measured signals can work oppositely, damping low-frequency (Figure 2.7a) (William J. Massman 1991; W. J. Massman 2000).

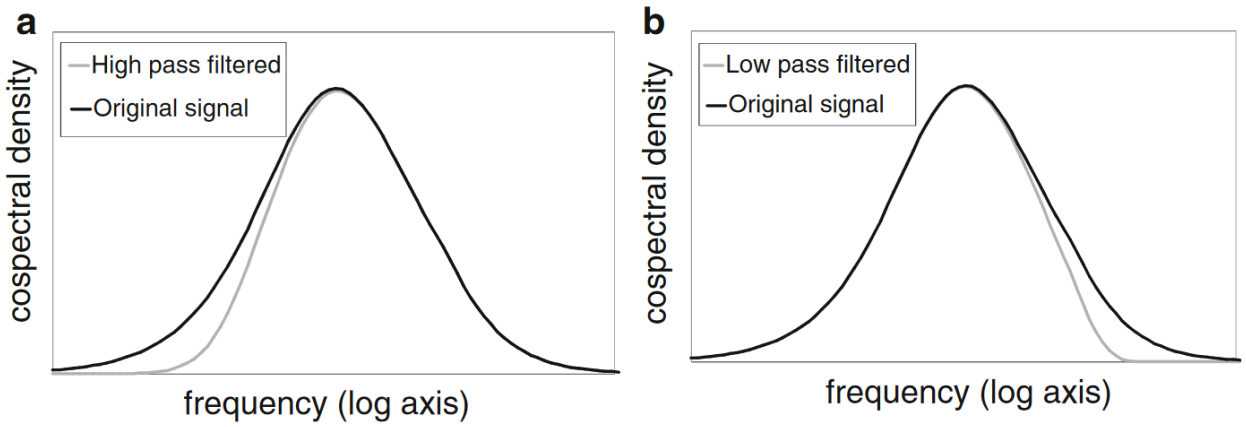

Figure 2.7. Typical atmospheric cospectrum (black curve) with effects of high pass filtering (a grey curve) and low pass filtering (b, grey curve). Source: (Foken, Aubinet, et Leuning 2012, figure 1.3).

The turbulent spectra also depend on measurement height, so at lower heights, systems would be more sensitive to high-frequency losses (Figure 2.8a), while systems placed at higher heights would be more sensitive to low-frequency losses (Figure 2.8b).

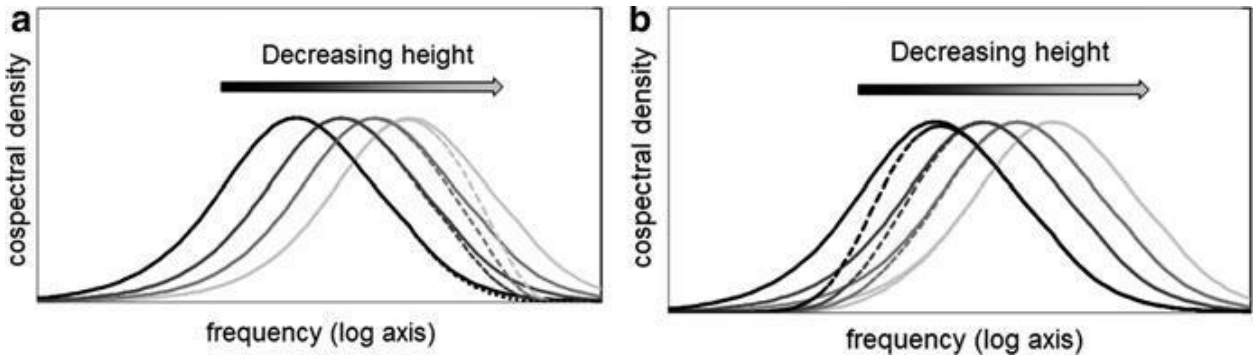

Figure 2.8. (a) Undamped (full line) and low pass filtered (dotted line) co-spectra; (b) Undamped (full line) and high pass filtered (dotted line) co-spectra. Source: (Foken, Aubinet, et Leuning 2012, figure 1.4).

General aspects of spectral correction

For accurate flux measurements, spectral attenuations due to tube, sensor low sampling frequency or high-pass filtering must be accounted for; thus, corrections are necessary. In the following part, the foundations of spectral corrections are laid down, and measurements are compared to the idealized 'true' spectra or co-spectra. A true, so-called original spectra Sp_{true} is, however, not measurable, so it is not usable. Options are to solve it analytically, replacing it with a parametrized spectrum, or experimentally, assuming similarity between scalars and using an unattenuated unbiassed spectra, which is commonly set to be the sonic temperature (Ibrom et al. 2007; Fratini et al. 2012; Peltola et al. 2021).

In all cases, a damped signal spectrum $Sp_{measured}$ can be expressed as a function of the true spectra through the use of a transfer function, *H*:

$$fSp_{measured}(f) = fSp_{true}(f) \times H(f) \qquad 2.6$$

Where *f* is the frequency (Hz), since *H* describes the attenuation of a scalar measurement due to a given setup (e.g., tube, pumps), it can be considered fixed for a single measuring setup and can be calculated using the average spectrum over the best-defined measurement periods (Sabbatini et al. 2018). However, any change in flow rate or filter dirtiness may lead to changes in *H*. In any case, it can be computed as:

$$H(f) = {F_n}^{-1} \frac{Sp_{measured}(f)/\sigma_{measured}}{Sp_{true}(f)/\sigma_{true}} \qquad 2.7$$

Where F_n is a normalisation factor to account for any inaccuracies in the covariance (Ibrom et al. 2007) and $\sigma_{measured}$ and σ_{true} are the standard deviation of the true and measured signal.

The empirical transfer function for the co-spectra (*TF*) can be further approximated using a first-order system, as the product of a transfer function *H* accounting for a filter's time constant,

τ_c (s), representing the system response time (as in eq. 2.7), and a transfer function H_p accounting for a generic phase shift φ between the scalar and the vertical velocity as (Massman, 2000):

$$H = \frac{1}{1 + (2\pi f \tau_c)^2} \quad 2.8$$

$$H_p = cos\varphi - 2\pi f \tau_c sin\varphi \quad 2.9$$

Note that the cut-off frequency, f_c equals $(2\pi\tau_c)^{-1}\ in\ Hz$. Frequently $TF = H$ is used, and H_p is not considered (Sabbatini et al., 2018; Ibrom et al., 2007). However, not accounting for the phase shift (e.g., using cross-covariance maximisation for lag correction and solely H for spectra correction) can bias TF (Peltola et al., 2021). Fortunately, in usual conditions, $H_p \approx 1/\sqrt{H}$ which leads to $TF = HH_p \sim \sqrt{H}$ (Peltola et al., 2021).

From *TF*, we can deduce a correction factor, *CF*, found as the ratio of the undisturbed covariance to itself attenuated by *TF*:

$$CF = \frac{\int Co_{undisturbed}(f)df}{\int Co_{undisturbed}(f) \times TF(f)df} \quad 2.10$$

$$F_{corrected} = CF \times F_{measured} \quad 2.11$$

Note that *H* is determined using only spectra, but *TF* incorporates phase shifts. Note also that the *w* transfer function and spatial sensor separation are not considered but may be applied as multiplicative transfer functions (W. J. Massman 2000).

2.2.5 Footprint analysis

Footprint analysis aims to determine the source area of measured scalars at a specific time. It is an essential analysis to ensure the measured flux is representative of a given biome or, on the contrary, to determine the proportion of differentiated sources and sinks contributing to the flux in the footprint (Chu et al. 2021). Footprints for fluxes are much smaller (typically < 1 km^2) in area than footprints for concentrations due to mixing. Flux footprint is also essential in airborne measurement to attribute the flux measured at a specific time to a given region (Desjardins et al. 2018).

Flux footprint models are scalar dispersion models that can either be Eulerian or Lagrangian, and among Eulerian, large eddy simulations (LES), Reynolds averaging numerical solutions (RANS) or pseudo analytical solutions (Vesala et al. 2008). Among various methods, the backward Lagrangian Stochastic Particle Dispersion Model, LPDM-B, stands out for its computational efficiency and simplicity. It is well-suited for long-time series within the boundary layer and remains valid across different boundary layer conditions and measurement heights (Kljun et al. 2015). Typically, footprints exhibit symmetry in the crosswind direction, although variables like wind shear and lateral wind variance can influence the shape.

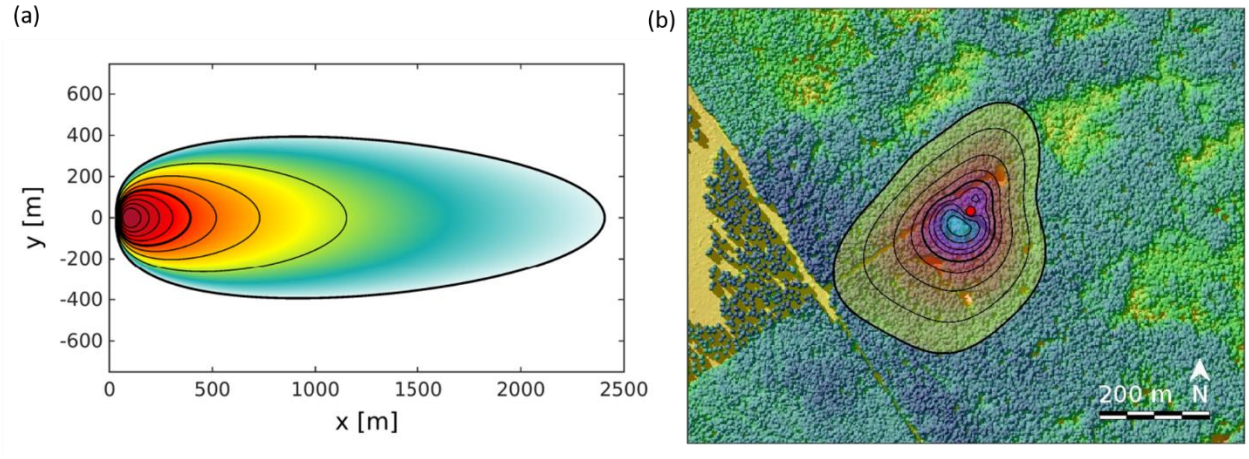

Figure 2.9. Example footprint estimate. (a) Convective scenario, with a measurement height of 20 m and roughness length of 0.01 m. The receptor is located at (0/0) m, and the x-axis points towards the main wind direction. (b) Footprint climatology for the ICOS flux tower Norunda, Sweden, for 1–31 May 2011. The red dot depicts the tower location with a receptor mounted 12 m above displacement height. The background map is tree height derived from an airborne lidar survey. In (a) and (b), footprint contour lines are shown in steps of 10 % from 10% to 90 %. Source: Modified from (Kljun et al. 2015).

2.2.6 CO_2 flux partitioning into respiration and photosynthesis

Eddy covariance measures net flux. However, in the case of CO_2, ecosystem respiration (Reco) and gross primary productivity (GPP) are often required to compare to models, validate satellite data, and understand ecosystem response to climate (e.g. Xia et al. 2015; Jung et al. 2020; van der Woude et al. 2023).

Modelling approaches

Different model-based partitioning methods are widely available and commonly used. Amidst the process-based models, night-time partitioning assumes that GPP is zero at night, so nocturnal NEE should equal R_{eco} (Reichstein et al. 2005). An Arrhenius-type temperature response model (Lloyd et Taylor 1994) is fitted using nocturnal observations and extrapolated into the day-yielding Reco. GPP is then deducted from $GPP = NEE - R_{eco}$.

Relying on night-time data alone can bias partitioning due to less developed turbulence and advective fluxes, unmeasured by conventional EC systems (Aubinet 2008). Therefore, corrections are necessary to detect these conditions, usually determined below a threshold u_* (Sabbatini et al. 2018). Another common method involves estimating respiration by extrapolating from light-response curves based on daytime data. However, this approach often overlooks variations in NEE caused by factors such as temperature (primarily affecting Reco) and vapour pressure deficit (which impacts GPP via stomatal regulation), among others (Lasslop et al. 2010).

Inhibition of leaf respiration in the light may also be a source of mismatch between Reco derived from EC measurements and independent R_{eco} from chamber measurements (Wehr et al. 2016), later included in a partitioning method (Keenan et al. 2019). Several process-based

partitioning methods are widely used thanks to a publicly available REddyProc module for R (Wutzler et al. 2018).

Statistical models, such as artificial neural networks (ANNs), have also been used to retrieve Reco (Tramontana et al., 2020). Diel results from the ANN differ from common model-based Reco but have similarities with independent R_{eco} chamber measurements (Wehr et al. 2016).

Direct partitioning methods

Even with a thorough understanding of the physical, biological, and chemical processes involved in respiration and photosynthesis, partitioning models still require simplifications, whether using proxy measurements or partial causal relations. Directly measuring partitioned flux would offer a promising solution to avoid these simplifications and give insights into the underlying processes.

At the leaf scale, CO_2 sequestration and transpiration are anticipated to co-occur, as they are primarily regulated by the same physiological mechanism: stomatal opening. Over a timescale of several minutes, it is expected that CO_2 and H_2O fluxes covary negatively. On the contrary, the soil is expected to emit CO2 while evaporating, so CO_2 and H_2O fluxes should covary positively over the soil. Furthermore, it can be assumed that a parcel of air from the soil or the vegetated part of an ecosystem is not entirely mixed before reaching the EC sensors. Based on this assumption, raw EC data can be conditionally sampled based on CO_2 and H_2O concentrations before calculating the covariance to partition soil and vegetation fluxes (Scanlon et Albertson, 2001; Scanlon et Sahu, 2008; Thomas et al., 2008; Scanlon et Kustas, 2010; Klosterhalfen et al., 2019; Zahn et al., 2022). A comparison between Thomas et al. (2008) and Scanlon et Kustas (2010) in Klosterhalfen et al. (2019) reported consistent and comparable soil-vegetation partitioned fluxes for H_2O and CO_2.

2.2.7 Systemic biases associated with Eddy Covariance

In the early stages of eddy covariance measurements, limitations in sensor performance or acquisition systems restricted the duration of data collection campaigns (R. Leuning et al. 1982). However, thanks to technological and methodological advancements, we can now gather decades of continuous surface flux data even in remote locations (Butterworth et Else 2018), using systematic and reproducible methods (Sabbatini et al. 2018; Pastorello et al. 2020). Nonetheless, two systematic errors persist: the lack of energy balance closure and the underestimation of nocturnal ecosystem fluxes when the turbulence is insufficient (Baldocchi 2003).

The lack of energy balance closure is a persistent challenge in eddy covariance measurements. It refers to the discrepancy between the incoming and outgoing energy fluxes at the Earth's surface, where the sum of all radiations (short and long wave incoming and outgoing radiations) does not match the sum of all energy transfer by convection (sensible and latent heat fluxes) and conduction in the soil (ground heat flux). This imbalance can arise due to various factors and is significant at half-hourly time steps, mainly due to heat storage in the ecosystem. At the daily time step, the small residual energy imbalance is explicable by horizontal advection, contamination of vertical covariance by horizontal covariance due to incorrect coordinate

rotations, and adjustment of radiation measurements over inclined surfaces (Ray Leuning et al. 2012). Vertical convection due to non-zero averaged vertical wind speed and horizontal advection in areas with variable surface water content are also identified causes of energy imbalance (Mauder et al. 2010). It is important to note that many of these issues would also affect the CO_2 flux and may lead to systematic biases on cumulated NEE.

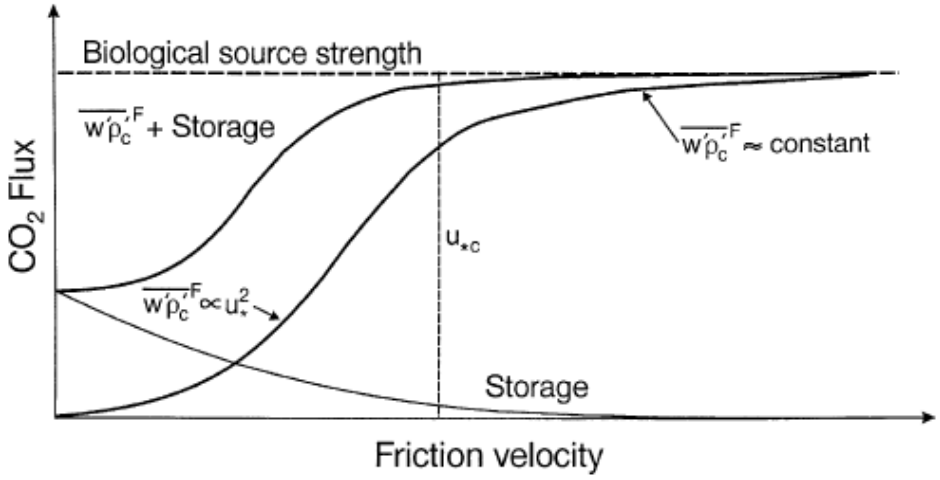

Figure 2.10. Schematic diagram showing nighttime CO2 eddy flux and air storage as a function of friction velocity. The F superscript indicates that the fluxes include the WPL term. Source: (W. J. Massman et Lee 2002)

During night-time, when solar radiation is absent, ecosystems exchange energy with the atmosphere through radiation cooling soil heat flux. CO_2 is also emitted to the atmosphere by respiration. However, eddy covariance measurements often underestimate these nocturnal fluxes due to turbulence breakdown, leading to a biased or incomplete (if data are filtered out) representation of ecosystem dynamics (Aubinet, Heinesch, et Longdoz 2002). Night-time data are, therefore, usually filtered out and gap-filled by identifying a u_* threshold value below which turbulent fluxes are considered biased (W. J. Massman et Lee 2002).

Another systematic bias may be encountered is decoupling, which occurs when the relationship between turbulent motions in the atmosphere and surface fluxes becomes weakened or disrupted (Wyngaard 1985). This decoupling can occur under certain meteorological conditions, such as stable atmospheric stratification or very low wind speeds, which inhibit the vertical exchange of momentum, heat, and moisture between the surface and the atmosphere. As a result, the measured surface fluxes may not accurately reflect the underlying ecosystem processes. Decoupling may be necessary for tall towers that expand over the mixing layer during stable conditions.

Finally, the accumulation of gases or other substances within the nocturnal boundary layer or inside the canopy during night-time leads to an additional term in the flux equations (eq. 2.3 and 2.4). In the absence of turbulent mixing and with reduced atmospheric ventilation, gases emitted by the surface, such as carbon dioxide or methane, can accumulate near the ground, leading to elevated concentrations. These accumulated fluxes, called storage fluxes, can be measured through profile measurements (Montagnani et al. 2018) but may be underestimated

due to advection (Aubinet, Heinesch, et Longdoz 2002). More so, turbulent flux during the destocking in the early hours may be flagged as unreliable due to non-stationarity.

Despite these limitations in Eddy Covariance measurements, the expansion of flux towers has happened on less than conventional terrain (uneven, mixed vegetation and non-vegetated land types).

2.3 Mapping techniques

2.3.1 Data assimilation

Data assimilation involves combining observational data with model estimations to generate optimal estimates while considering uncertainties in both data and models. For instance, this concept is used every day for weather prediction so that the previous model forecast is compared with newly received observations and updated accordingly. We start from the real state of the system of interest, which is assumed to be represented by a continuous state vector, x_c, and which results in a real signal, y_c, through a causality relationship defined by a function h (Tarantola 2005), such that:

$$y_c = h(x_c) \tag{2.12}$$

This equation cannot be used as such because y_c and x_c are not directly "accessible": y_c is affected by instrumental errors, ε_μ; and x_c is represented by a discrete state vector X or $\Pi(x_c)$ where Π represents the discretization. Also, even if the causality h, which represents the ensemble of processes explaining the relationship between x_c and y_c, could be known, in practice, h is represented by a numerical model H. Thus, the observed data, Y, can be expressed as:

$$Y = H(X) + \underbrace{h(x_c) - H\big(\Pi(x_c)\big)}_{\varepsilon_r} + \varepsilon_\mu \tag{2.13}$$

Here, ε_r represents the representativity error, accounting for errors in representing the physics in H and due to the projection of the real state x_c onto the discrete state space. The sum of ε_r and ε_μ, denoted as ε_o, is the observation error. The equation that links the state to the observation result is the observation equation:

$$Y = H(X) + \varepsilon_o \tag{2.14}$$

Typically, for data assimilation purposes, the statistics of the observation error ε_o are assumed to be known and Gaussian distributed with a mean 0 and with a covariance matrix denoted as R.

The analysis incorporates observational data into a numerical model to update the system's state estimate x of the discrete state X: the value of x is searched based on a prior estimation, x^b. A covariance matrix B is introduced to represent the errors on x^b, similarly to R for Y. The analysis

step formally consists of minimizing a cost function, J, where J increases the more $H(x)$ differs from Y and x^b from x. Both differences are weighted by the inverse of their error terms, namely R^{-1} and B^{-1}. A standard formulation is to average both sides of the equation:

$$\begin{aligned} J(x) &= \frac{1}{2}\left\|x - x^b\right\|_B^2 + \frac{1}{2}\|H(x) - Y\|_R^2 \\ &= \frac{1}{2}\left[\left(x - x^b\right)^T B^{-1}\left(x - x^b\right) + (H(x) - Y)^T R^{-1}(H(x) - Y)\right] \end{aligned} \quad 2.15$$

Where $\| \quad \|_B^2$ is the norm weighed by the covariance B and $(\quad)^T$ stands for transpose. Once the cost function is formalized, the solution of the analysis step is defined. Assuming Gaussian probability, the value of x that minimises J, the so-called analysis or posterior, x^a, can be computed by adding to the prior state x^b, an "innovation" part, $y - H(x^b)$, weighted by K (Tarantola, 2005).

$$x^a = x^b + K\left(Y - H(x^b)\right) \quad 2.16$$

Where $K = BH^T(HBH^T + R)^{-1}$, also referred to as Kalman gain. The posterior uncertainty matrix, A, can then be computed as:

$$\begin{aligned} A &= [B^{-1} + H^T R^{-1} H]^{-1} \\ &= B - BH^T(HBH^T + R)^{-1}HB \\ &= (I - KH)B \end{aligned} \quad 2.17$$

Where I is the identity matrix. Note that A is always smaller than B and R, which is the goal of the analysis, assimilating observations to improve estimations.

2.3.2 Surface flux mapping from atmospheric concentrations and flux tower

The Bayesian framework is extensively employed for assimilating atmospheric mixing ratio measurements into prior flux estimations to estimate surface fluxes on the global (Philippe Bousquet et al. 2000; Chevallier et al. 2010), continental (Kountouris et al. 2018) and regional (Lauvaux et al. 2012) scales.

Following section 2.3.1, the observations, y, are generally a network of towers and airborne measurements. The prior state, x^b, comprises direct simulations or previously optimized flux map estimations, while H is a transport model that provides estimations comparable to observations. The output of the inversion process, x^a, is a spatially resolved flux map. The analysis x^a and prior x^b are directly comparable (Figure 2.11), and the optimisation process implies that $H(x^a)$ should be closer to y than $H(x^b)$ (P. Bousquet et al. 1999).

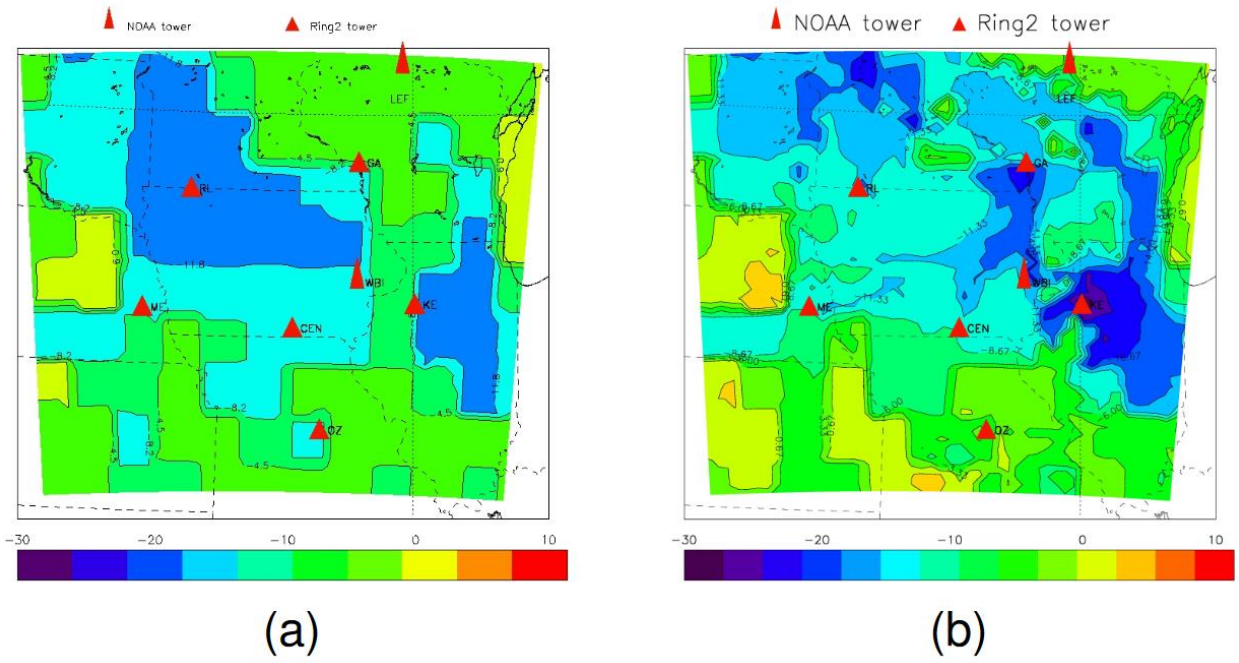

Figure 2.11. Map of the CO_2 fluxes accumulated from June to December in $TgC.degree^{-2}$. (a) prior and (b) posterior fluxes. Source: (Lauvaux et al. 2012).

A recommended approach is to validate the inversion using independent observations. Additionally, using a benchmark such as the *poor man's inversion* allows for assessing the superiority of the inversion over a simpler approach (Chevallier et al. 2010).

Flux towers provide direct flux measurements but were not always used to validate inversions because of their representativeness compared to the grid size used in the inversion (Chevallier et al. 2010). Efforts, however, have been made to upscale the Eddy flux observations to obtain global-scale estimates of biosphere-atmosphere CO_2 exchanges (Jung et al. 2020) that have been compared positively to atmospheric inversion.

With the advent of higher-resolution geospatial data, there has been a subsequent improvement in the spatial resolution of flux map estimations. On one side, atmospheric inversions can estimate fluxes at grid sizes smaller than the footprint of a flux tower; on the other side, footprint analysis from flux observations brings new knowledge on a site's heterogeneity (Barcza et al. 2009; Chen et al. 2009). Consequently, these developments have fostered communication between top-down and bottom-up approaches in flux estimation (Wolfe et al., 2018).

Achieving high-resolution and accurate local flux maps from atmospheric inversions would require a denser measurement network and more sophisticated transport models. However, since these models primarily aim to provide reliable estimates at larger scales, their effectiveness may remain uncertain for smaller areas at a few meters resolution.

The increased resolution of geospatial data has spurred researchers to explore the direct utilization of flux measurements for creating high-resolution flux maps (Figure 2.12). This progress

enables the generation of flux maps at resolutions as fine as a few meters using a single tower and remote sensing techniques combined with statistical methods (Crawford et Christen 2015; Stefan Metzger 2018). These methods use the patchy and variable source area to distinguish individual emissions processes. The development of these methods can enhance both local and larger-scale estimations, potentially serving as a means for cross-validating atmospheric inversions as their accuracy improves.

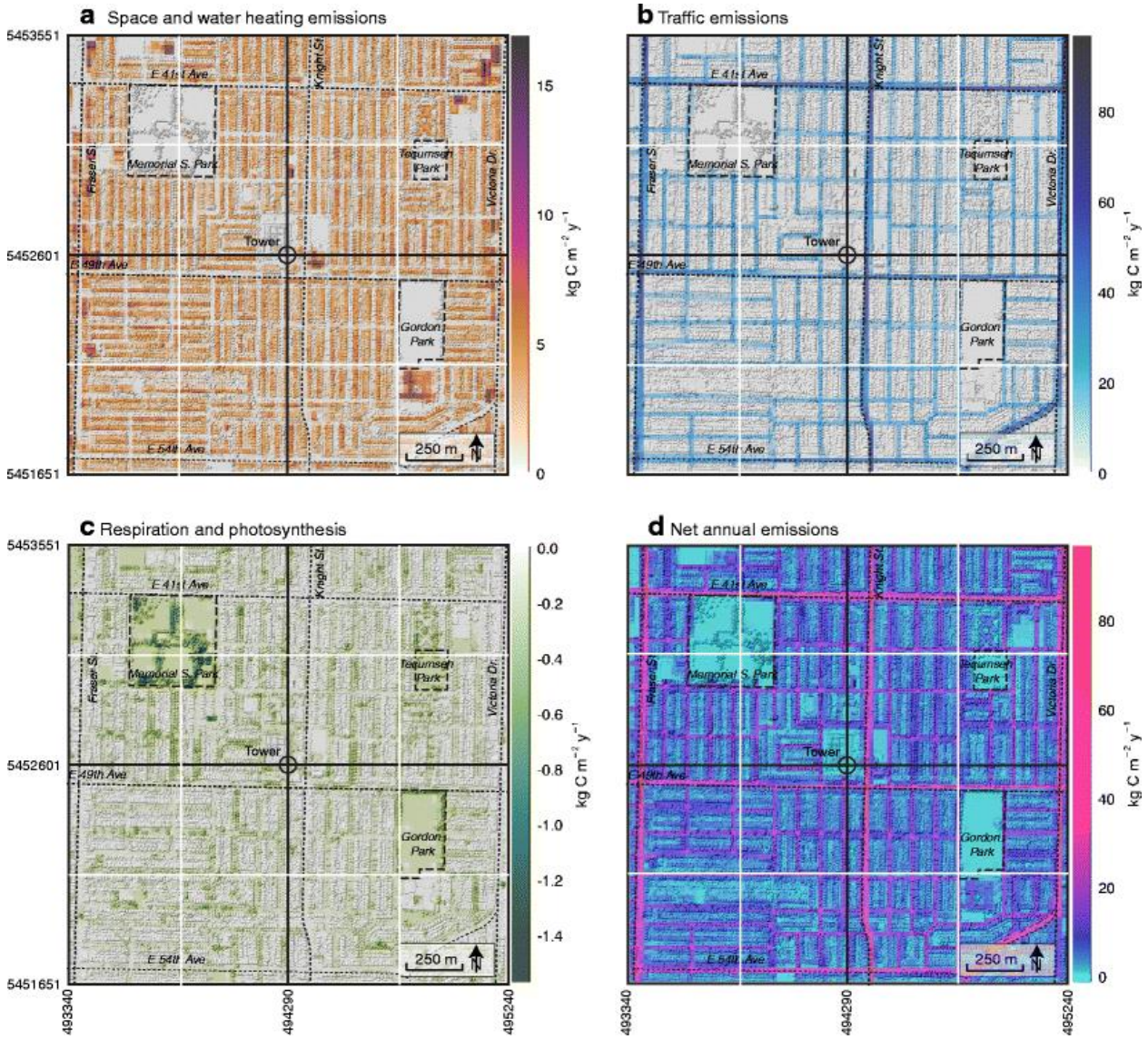

Figure 2.12. Maps of total annual emissions at 20-m resolution for space and water heating from buildings, b vehicle emissions, c respiration (human, soil, and vegetation) and photosynthesis, and d total annual emissions from all processes. Source: (Crawford et Christen 2015).

2.4 References

Anjileli, Hassan, Laurie S. Huning, Hamed Moftakhari, Samaneh Ashraf, Ata Akbari Asanjan, Hamid Norouzi, et Amir AghaKouchak. 2021. « Extreme Heat Events Heighten Soil Respiration ». *Scientific Reports* 11 (1): 6632. https://doi.org/10.1038/s41598-021-85764-8.

Aubinet, Marc. 2008. « Eddy Covariance Co2 Flux Measurements in Nocturnal Conditions: An Analysis of the Problem ». *Ecological Applications* 18 (6): 1368-78. https://doi.org/10.1890/06-1336.1.

Aubinet, Marc, Bernad Heinesch, et Bernad Longdoz. 2002. « Estimation of the Carbon Sequestration by a Heterogeneous Forest: Night Flux Corrections, Heterogeneity of the Site and Inter-Annual Variability ». *Global Change Biology* 8 (11): 1053-71. https://doi.org/10.1046/j.1365-2486.2002.00529.x.

Baldocchi, Dennis D. 2003. « Assessing the Eddy Covariance Technique for Evaluating Carbon Dioxide Exchange Rates of Ecosystems: Past, Present and Future ». *Global Change Biology* 9 (4): 479-92. https://doi.org/10.1046/j.1365-2486.2003.00629.x.

Barcza, Z., A. Kern, L. Haszpra, et N. Kljun. 2009. « Spatial Representativeness of Tall Tower Eddy Covariance Measurements Using Remote Sensing and Footprint Analysis ». *Agricultural and Forest Meteorology* 149 (5): 795-807. https://doi.org/10.1016/j.agrformet.2008.10.021.

Bergeron, Onil, et Ian B. Strachan. 2011. « CO2 sources and sinks in urban and suburban areas of a northern mid-latitude city ». *Atmospheric Environment* 45 (8): 1564-73. https://doi.org/10.1016/j.atmosenv.2010.12.043.

Bethenod, O., N. Katerji, P. Cellier, et P. Quetin. 1991. « Determination of carbon balance of a potato (Solanum tuberosum L.) crop by a simplified aerodynamic method. » https://www.cabidigitallibrary.org/doi/full/10.5555/19920754862.

Bousquet, P., P. Ciais, P. Peylin, M. Ramonet, et P. Monfray. 1999. « Inverse Modeling of Annual Atmospheric CO2 Sources and Sinks: 1. Method and Control Inversion ». *Journal of Geophysical Research: Atmospheres* 104 (D21): 26161-78. https://doi.org/10.1029/1999JD900342.

Bousquet, Philippe, Philippe Peylin, Philippe Ciais, Corinne Le Quéré, Pierre Friedlingstein, et Pieter P. Tans. 2000. « Regional Changes in Carbon Dioxide Fluxes of Land and Oceans Since 1980 ». *Science* 290 (5495): 1342-46. https://doi.org/10.1126/science.290.5495.1342.

Brosset, Agnès, et James D Blande. 2022. « Volatile-mediated plant–plant interactions: volatile organic compounds as modulators of receiver plant defence, growth, and reproduction ». *Journal of Experimental Botany* 73 (2): 511-28. https://doi.org/10.1093/jxb/erab487.

Brown, Christopher F., Steven P. Brumby, Brookie Guzder-Williams, Tanya Birch, Samantha Brooks Hyde, Joseph Mazzariello, Wanda Czerwinski, et al. 2022. « Dynamic World, Near Real-Time Global 10 m Land Use Land Cover Mapping ». *Scientific Data* 9 (1): 251. https://doi.org/10.1038/s41597-022-01307-4.

Brunet, Yves, et Serge Collineau. 1994. « Wavelet Analysis of Diurnal and Nocturnal Turbulence Above a Maize Crop ». In *Wavelet Analysis and Its Applications*, édité par Efi Foufoula-Georgiou et Praveen Kumar, 4:129-50. Wavelets in Geophysics. Academic Press. https://doi.org/10.1016/B978-0-08-052087-2.50011-6.

Brutsaert, Wilfried. 1982. « Methods Based on Turbulence Measurements ». In *Evaporation into the Atmosphere: Theory, History and Applications*, édité par Wilfried Brutsaert, 190-96. Dordrecht: Springer Netherlands. https://doi.org/10.1007/978-94-017-1497-6_8.

Butterworth, Brian J., et Brent G. T. Else. 2018. « Dried, Closed-Path Eddy Covariance Method for Measuring Carbon Dioxide Flux over Sea Ice ». *Atmospheric Measurement Techniques* 11 (11): 6075-90. https://doi.org/10.5194/amt-11-6075-2018.

Camino-Serrano, Marta, Bertrand Guenet, Sebastiaan Luyssaert, Philippe Ciais, Vladislav Bastrikov, Bruno De Vos, Bert Gielen, et al. 2018. « ORCHIDEE-SOM: Modeling Soil Organic Carbon (SOC) and Dissolved Organic Carbon (DOC) Dynamics along Vertical Soil Profiles in Europe ». *Geoscientific Model Development* 11 (3): 937-57. https://doi.org/10.5194/gmd-11-937-2018.

Canadell, J.G., P.M.S. Monteiro, M.H. Costa, L. Cotrim da Cunha, P.M. Cox, A.V. Eliseev, S. Henson, et al. 2021. « Global Carbon and other Biogeochemical Cycles and Feedbacks ». Édité par V. Masson-Delmotte, P. Zhai, A. Pirani, S.L. Connors, C. Péan, S. Berger, N. Caud, et al. *Climate Change 2021: The Physical Science Basis. Contribution of Working Group I to the Sixth Assessment Report of the Intergovernmental Panel on Climate Change*. Cambridge, United Kingdom and New York, NY, USA: Cambridge University Press. https://doi.org/10.1017/9781009157896.007.

Chen, Baozhang, T. Andrew Black, Nicholas C. Coops, Thomas Hilker, J. A. (Tony) Trofymow, et Kai Morgenstern. 2009. « Assessing Tower Flux Footprint Climatology and Scaling Between Remotely Sensed and Eddy Covariance Measurements ». *Boundary-Layer Meteorology* 130 (2): 137-67. https://doi.org/10.1007/s10546-008-9339-1.

Chevallier, F., P. Ciais, T. J. Conway, T. Aalto, B. E. Anderson, P. Bousquet, E. G. Brunke, et al. 2010. « CO2 Surface Fluxes at Grid Point Scale Estimated from a Global 21 Year Reanalysis of Atmospheric Measurements ». *Journal of Geophysical Research: Atmospheres* 115 (D21). https://doi.org/10.1029/2010JD013887.

Chu, Housen, Xiangzhong Luo, Zutao Ouyang, W. Stephen Chan, Sigrid Dengel, Sébastien C. Biraud, Margaret S. Torn, et al. 2021. « Representativeness of Eddy-Covariance Flux Footprints for Areas Surrounding AmeriFlux Sites ». *Agricultural and Forest Meteorology* 301-302 (mai): 108350. https://doi.org/10.1016/j.agrformet.2021.108350.

Ciais, Ph, M. Reichstein, N. Viovy, A. Granier, J. Ogée, V. Allard, M. Aubinet, et al. 2005. « Europe-Wide Reduction in Primary Productivity Caused by the Heat and Drought in 2003 ». *Nature* 437 (7058): 529-33. https://doi.org/10.1038/nature03972.

Crawford, B., et A. Christen. 2015. « Spatial Source Attribution of Measured Urban Eddy Covariance CO2 Fluxes ». *Theoretical and Applied Climatology* 119 (3): 733-55. https://doi.org/10.1007/s00704-014-1124-0.

Desjardins, R. L., D. E. Worth, E. Pattey, A. VanderZaag, R. Srinivasan, M. Mauder, D. Worthy, C. Sweeney, et S. Metzger. 2018. « The Challenge of Reconciling Bottom-up Agricultural Methane Emissions Inventories with Top-down Measurements ». *Agricultural and Forest Meteorology* 248 (janvier): 48-59. https://doi.org/10.1016/j.agrformet.2017.09.003.

Dhakal, S., J.C. Minx, F.L. Toth, A. Abdel-Aziz, M.J. Figueroa Meza, K. Hubacek, I.G.C. Jonckheere, et al. 2022. « Emissions Trends and Drivers ». Édité par P.R. Shukla, J. Skea, R. Slade, A. Al Khourdajie, R. van Diemen, D. McCollum, M. Pathak, et al. *Climate Change 2022: Mitigation of Climate Change. Contribution of Working Group III to the Sixth Assessment Report of the Intergovernmental Panel on Climate Change*. Cambridge, UK and New York, NY, USA: Cambridge University Press. https://doi.org/10.1017/9781009157926.004.

Drysdale, Will S., Adam R. Vaughan, Freya A. Squires, Sam J. Cliff, Stefan Metzger, David Durden, Natchaya Pingintha-Durden, et al. 2022. « Eddy Covariance Measurements Highlight Sources of Nitrogen Oxide Emissions Missing from Inventories for Central London ». *Atmospheric Chemistry and Physics Discussions*, janvier, 1-35. https://doi.org/10.5194/acp-2021-982.

Duffy, Katharyn A., Christopher R. Schwalm, Vickery L. Arcus, George W. Koch, Liyin L. Liang, et Louis A. Schipper. 2021. « How Close Are We to the Temperature Tipping Point of the Terrestrial Biosphere? » *Science Advances* 7 (3): eaay1052. https://doi.org/10.1126/sciadv.aay1052.

Dutaur, Laure, et Louis V. Verchot. 2007. « A Global Inventory of the Soil CH4 Sink ». *Global Biogeochemical Cycles* 21 (4). https://doi.org/10.1029/2006GB002734.

Farineau, Jack, et Jean-François Morot-Gaudry. 2017. *La photosynthèse: processus physiques, moléculaires et physiologiques*. Quae.

Finnigan, J. J., R. Clement, Y. Malhi, R. Leuning, et H.A. Cleugh. 2003. « A Re-Evaluation of Long-Term Flux Measurement Techniques Part I: Averaging and Coordinate Rotation ». *Boundary-Layer Meteorology* 107 (1): 1-48. https://doi.org/10.1023/A:1021554900225.

Foken, Thomas. 2008. *Micrometeorology*. Berlin Heidelberg: Springer-Verlag. https://doi.org/10.1007/978-3-540-74666-9.

Foken, Thomas, Marc Aubinet, et Ray Leuning. 2012. « The Eddy Covariance Method ». In *Eddy Covariance: A Practical Guide to Measurement and Data Analysis*, édité par Marc Aubinet, Timo Vesala, et Dario Papale, 1-19. Springer Atmospheric Sciences. Dordrecht: Springer Netherlands. https://doi.org/10.1007/978-94-007-2351-1_1.

Forster, P., T. Storelvmo, K. Armour, W. Collins, J.-L. Dufresne, D. Frame, D.J. Lunt, et al. 2021. « The Earth's Energy Budget, Climate Feedbacks, and Climate Sensitivity ». Édité par V. Masson-Delmotte, P. Zhai, A. Pirani, S.L. Connors, C. Péan, S. Berger, N. Caud, et al. *Climate Change 2021: The Physical Science Basis. Contribution of Working Group I to the Sixth Assessment Report of the Intergovernmental Panel on Climate Change*. Cambridge, United Kingdom and New York, NY, USA: Cambridge University Press. https://doi.org/10.1017/9781009157896.009.

Fowler, D., C. E. Steadman, D. Stevenson, M. Coyle, R. M. Rees, U. M. Skiba, M. A. Sutton, et al. 2015. « Effects of Global Change during the 21st Century on the Nitrogen Cycle ». *Atmospheric Chemistry and Physics* 15 (24): 13849-93. https://doi.org/10.5194/acp-15-13849-2015.

Fratini, Gerardo, Andreas Ibrom, Nicola Arriga, George Burba, et Dario Papale. 2012. « Relative humidity effects on water vapour fluxes measured with closed-path eddy-covariance systems with short sampling lines ». *Agricultural and Forest Meteorology* 165 (novembre): 53-63. https://doi.org/10.1016/j.agrformet.2012.05.018.

Friedlingstein, Pierre, Michael O'Sullivan, Matthew W. Jones, Robbie M. Andrew, Judith Hauck, Are Olsen, Glen P. Peters, et al. 2020. « Global Carbon Budget 2020 ». *Earth System Science Data* 12 (4): 3269-3340. https://doi.org/10.5194/essd-12-3269-2020.

Fu, Zheng, Philippe Ciais, Ana Bastos, Paul C. Stoy, Hui Yang, Julia K. Green, Bingxue Wang, et al. 2020. « Sensitivity of gross primary productivity to climatic drivers during the summer drought of 2018 in Europe ». *Philosophical Transactions of the Royal Society B: Biological Sciences* 375 (1810): 20190747. https://doi.org/10.1098/rstb.2019.0747.

Goll, Daniel S., Nicolas Vuichard, Fabienne Maignan, Albert Jornet-Puig, Jordi Sardans, Aurelie Violette, Shushi Peng, et al. 2017. « A Representation of the Phosphorus Cycle for ORCHIDEE (Revision 4520) ». *Geoscientific Model Development* 10 (10): 3745-70. https://doi.org/10.5194/gmd-10-3745-2017.

Gourlez de la Motte, Louis, Quentin Beauclaire, Bernard Heinesch, Mathias Cuntz, Lenka Foltýnová, Ladislav Šigut, Natalia Kowalska, et al. 2020. « Non-Stomatal Processes Reduce Gross Primary Productivity in Temperate Forest Ecosystems during Severe Edaphic Drought ». *Philosophical Transactions of the Royal Society of London. Series B, Biological Sciences* 375 (1810): 20190527. https://doi.org/10.1098/rstb.2019.0527.

Griffis, T. J., T. A. Black, D. Gaumont-Guay, G. B. Drewitt, Z. Nesic, A. G. Barr, K. Morgenstern, et N. Kljun. 2004. « Seasonal Variation and Partitioning of Ecosystem Respiration in a Southern Boreal Aspen Forest ». *Agricultural and Forest Meteorology* 125 (3): 207-23. https://doi.org/10.1016/j.agrformet.2004.04.006.

Hansen, M. C., P. V. Potapov, R. Moore, M. Hancher, S. A. Turubanova, A. Tyukavina, D. Thau, et al. 2013. « High-Resolution Global Maps of 21st-Century Forest Cover Change ». *Science* 342 (6160): 850-53. https://doi.org/10.1126/science.1244693.

Harris, I., et R. Jastrow. 1958. « Upper Atmosphere Densities from Minitrack Observations on Sputnik I ». *Science* 127 (3296): 471-72. https://doi.org/10.1126/science.127.3296.471.b.

Ibrom, Andreas, Ebba Dellwik, Henrik Flyvbjerg, Niels Otto Jensen, et Kim Pilegaard. 2007. « Strong low-pass filtering effects on water vapour flux measurements with closed-path eddy correlation systems ». *Agricultural and Forest Meteorology* 147 (3): 140-56. https://doi.org/10.1016/j.agrformet.2007.07.007.

Jung, Martin, Christopher Schwalm, Mirco Migliavacca, Sophia Walther, Gustau Camps-Valls, Sujan Koirala, Peter Anthoni, et al. 2020. « Scaling Carbon Fluxes from Eddy Covariance Sites to Globe:

Synthesis and Evaluation of the FLUXCOM Approach ». *Biogeosciences* 17 (5): 1343-65. https://doi.org/10.5194/bg-17-1343-2020.

Kaimal, J. C., et J. J. Finnigan. 1994. *Atmospheric Boundary Layer Flows: Their Structure and Measurement*. Oxford University Press.

Kaimal, J. C., J. C. Wyngaard, Y. Izumi, et O. R. Coté. 1972. « Spectral Characteristics of Surface-Layer Turbulence ». *Quarterly Journal of the Royal Meteorological Society* 98 (417): 563-89. https://doi.org/10.1002/qj.49709841707.

Kanemasu, E. T., W. L. Powers, et J. W. Sij. 1974. « FIELD CHAMBER MEASUREMENTS OF CO2 FLUX FROM SOIL SURFACE ». *Soil Science* 118 (4): 233.

Keeling, Charles D. 1960. « The Concentration and Isotopic Abundances of Carbon Dioxide in the Atmosphere ». *Tellus* 12 (2): 200-203. https://doi.org/10.1111/j.2153-3490.1960.tb01300.x.

Keenan, Trevor F., Mirco Migliavacca, Dario Papale, Dennis Baldocchi, Markus Reichstein, Margaret Torn, et Thomas Wutzler. 2019. « Widespread Inhibition of Daytime Ecosystem Respiration ». *Nature Ecology & Evolution* 3 (3): 407-15. https://doi.org/10.1038/s41559-019-0809-2.

Kljun, N., P. Calanca, M. W. Rotach, et H. P. Schmid. 2015. « A Simple Two-Dimensional Parameterisation for Flux Footprint Prediction (FFP) ». *Geoscientific Model Development* 8 (11): 3695-3713. https://doi.org/10.5194/gmd-8-3695-2015.

Klosterhalfen, Anne, Alexander Graf, Nicolas Brüggemann, Clemens Drüe, Odilia Esser, María P. González-Dugo, Günther Heinemann, et al. 2019. « Source Partitioning of H_2O and CO_2 Fluxes Based on High-Frequency Eddy Covariance Data: A Comparison between Study Sites ». *Biogeosciences* 16 (6): 1111-32. https://doi.org/10.5194/bg-16-1111-2019.

Kotthaus, Simone, Juan Antonio Bravo-Aranda, Martine Collaud Coen, Juan Luis Guerrero-Rascado, Maria João Costa, Domenico Cimini, Ewan J. O'Connor, et al. 2023. « Atmospheric Boundary Layer Height from Ground-Based Remote Sensing: A Review of Capabilities and Limitations ». *Atmospheric Measurement Techniques* 16 (2): 433-79. https://doi.org/10.5194/amt-16-433-2023.

Kountouris, Panagiotis, Christoph Gerbig, Christian Rödenbeck, Ute Karstens, Thomas F. Koch, et Martin Heimann. 2018. « Atmospheric CO_2 Inversions on the Mesoscale Using Data-Driven Prior Uncertainties: Quantification of the European Terrestrial CO_2 Fluxes ». *Atmospheric Chemistry and Physics* 18 (4): 3047-64. https://doi.org/10.5194/acp-18-3047-2018.

Lasslop, Gitta, Markus Reichstein, Dario Papale, Andrew D. Richardson, Almut Arneth, Alan Barr, Paul Stoy, et Georg Wohlfahrt. 2010. « Separation of Net Ecosystem Exchange into Assimilation and Respiration Using a Light Response Curve Approach: Critical Issues and Global Evaluation ». *Global Change Biology* 16 (1): 187-208. https://doi.org/10.1111/j.1365-2486.2009.02041.x.

Laufs, Sebastian, Mathieu Cazaunau, Patrick Stella, Ralf Kurtenbach, Pierre Cellier, Abdelwahid Mellouki, Benjamin Loubet, et Jörg Kleffmann. 2017. « Diurnal Fluxes of HONO above a Crop

Rotation ». *Atmospheric Chemistry and Physics* 17 (11): 6907-23. https://doi.org/10.5194/acp-17-6907-2017.

Lauvaux, T., A. E. Schuh, M. Uliasz, S. Richardson, N. Miles, A. E. Andrews, C. Sweeney, et al. 2012. « Constraining the CO_2 Budget of the Corn Belt: Exploring Uncertainties from the Assumptions in a Mesoscale Inverse System ». *Atmospheric Chemistry and Physics* 12 (1): 337-54. https://doi.org/10.5194/acp-12-337-2012.

Leuning, R., O. T. Denmead, A. R. G. Lang, et E. Ohtaki. 1982. « Effects of Heat and Water Vapor Transport on Eddy Covariance Measurement of CO2 Fluxes ». *Boundary-Layer Meteorology* 23 (2): 209-22. https://doi.org/10.1007/BF00123298.

Leuning, Ray, Eva van Gorsel, William J. Massman, et Peter R. Isaac. 2012. « Reflections on the surface energy imbalance problem ». *Agricultural and Forest Meteorology* 156 (avril): 65-74. https://doi.org/10.1016/j.agrformet.2011.12.002.

Lian, Jinghui, Thomas Lauvaux, Hervé Utard, François-Marie Bréon, Grégoire Broquet, Michel Ramonet, Olivier Laurent, et al. 2023. « Can We Use Atmospheric CO_2 Measurements to Verify Emission Trends Reported by Cities? Lessons from a 6-Year Atmospheric Inversion over Paris ». *Atmospheric Chemistry and Physics* 23 (15): 8823-35. https://doi.org/10.5194/acp-23-8823-2023.

Lloyd, J., et J. A. Taylor. 1994. « On the Temperature Dependence of Soil Respiration ». *Functional Ecology* 8 (3): 315-23. https://doi.org/10.2307/2389824.

Loubet, B., P. Cellier, S. Génermont, et D. Flura. 1999. « An Evaluation of the Wind-tunnel Technique for Estimating Ammonia Volatilization from Land: Part 2. Influence of the Tunnel on Transfer Processes ». *Journal of Agricultural Engineering Research* 72 (1): 83-92. https://doi.org/10.1006/jaer.1998.0349.

Lundegårdh, Henrik. 1927. « CARBON DIOXIDE EVOLUTION OF SOIL AND CROP GROWTH ». *Soil Science* 23 (6): 417.

Mahrt, L., et J. F. Howell. 1994. « The Influence of Coherent Structures and Microfronts on Scaling Laws Using Global and Local Transforms ». *Journal of Fluid Mechanics* 260 (février): 247-70. https://doi.org/10.1017/S0022112094003502.

Massman, W. J. 2000. « A simple method for estimating frequency response corrections for eddy covariance systems ». *Agricultural and Forest Meteorology* 104 (3): 185-98. https://doi.org/10.1016/S0168-1923(00)00164-7.

Massman, W. J., et X. Lee. 2002. « Eddy Covariance Flux Corrections and Uncertainties in Long-Term Studies of Carbon and Energy Exchanges ». *Agricultural and Forest Meteorology*, FLUXNET 2000 Synthesis, 113 (1): 121-44. https://doi.org/10.1016/S0168-1923(02)00105-3.

Massman, William J. 1991. « The Attenuation of Concentration Fluctuations in Turbulent Flow through a Tube ». *Journal of Geophysical Research: Atmospheres* 96 (D8): 15269-73. https://doi.org/10.1029/91JD01514.

Mauder, Matthias, Raymond L. Desjardins, Elizabeth Pattey, et Devon Worth. 2010. « An Attempt to Close the Daytime Surface Energy Balance Using Spatially-Averaged Flux Measurements ». *Boundary-Layer Meteorology* 136 (2): 175-91. https://doi.org/10.1007/s10546-010-9497-9.

McGrath, Matthew J., Ana Maria Roxana Petrescu, Philippe Peylin, Robbie M. Andrew, Bradley Matthews, Frank Dentener, Juraj Balkovič, et al. 2023. « The Consolidated European Synthesis of CO_2 Emissions and Removals for the European Union and United Kingdom: 1990–2020 ». *Earth System Science Data* 15 (10): 4295-4370. https://doi.org/10.5194/essd-15-4295-2023.

Medlyn, Belinda E., Remko A. Duursma, Derek Eamus, David S. Ellsworth, I. Colin Prentice, Craig V. M. Barton, Kristine Y. Crous, Paolo De Angelis, Michael Freeman, et Lisa Wingate. 2011. « Reconciling the Optimal and Empirical Approaches to Modelling Stomatal Conductance ». *Global Change Biology* 17 (6): 2134-44. https://doi.org/10.1111/j.1365-2486.2010.02375.x.

Messina, Palmira, Juliette Lathière, Katerina Sindelarova, Nicolas Vuichard, Claire Granier, Josefine Ghattas, Anne Cozic, et Didier A. Hauglustaine. 2016. « Global Biogenic Volatile Organic Compound Emissions in the ORCHIDEE and MEGAN Models and Sensitivity to Key Parameters ». *Atmospheric Chemistry and Physics* 16 (22): 14169-202. https://doi.org/10.5194/acp-16-14169-2016.

Metzger, S., W. Junkermann, M. Mauder, K. Butterbach-Bahl, B. Trancón y Widemann, F. Neidl, K. Schäfer, et al. 2013. « Spatially Explicit Regionalization of Airborne Flux Measurements Using Environmental Response Functions ». *Biogeosciences* 10 (4): 2193-2217. https://doi.org/10.5194/bg-10-2193-2013.

Metzger, Stefan. 2018. « Surface-Atmosphere Exchange in a Box: Making the Control Volume a Suitable Representation for in-Situ Observations ». *Agricultural and Forest Meteorology*, Honoring W.J. Massman's Discoveries: Bringing Physics to Agriculture, 255 (mai): 68-80. https://doi.org/10.1016/j.agrformet.2017.08.037.

Montagnani, Leonardo, Thomas Grünwald, Andrew Kowalski, Ivan Mammarella, Lutz Merbold, Stefan Metzger, Pavel Sedlák, et Lukas Siebicke. 2018. « Estimating the Storage Term in Eddy Covariance Measurements: The ICOS Methodology ». *International Agrophysics* 32 (4): 551-67. https://doi.org/10.1515/intag-2017-0037.

Monteith, John L., et Mike H. Unsworth, éd. 2013. « Principles of Environmental Physics ». In *Principles of Environmental Physics (Fourth Edition)*, i. Boston: Academic Press. https://doi.org/10.1016/B978-0-12-386910-4.00018-4.

Moureaux, Christine, Eric Ceschia, Nicola Arriga, Pierre Béziat, Werner Eugster, Werner L. Kutsch, et Elizabeth Pattey. 2012. « Eddy Covariance Measurements over Crops ». In *Eddy Covariance: A Practical Guide to Measurement and Data Analysis*, édité par Marc Aubinet, Timo Vesala, et Dario Papale, 319-31. Springer Atmospheric Sciences. Dordrecht: Springer Netherlands. https://doi.org/10.1007/978-94-007-2351-1_12.

Oertel, Cornelius, Jörg Matschullat, Kamal Zurba, Frank Zimmermann, et Stefan Erasmi. 2016. « Greenhouse gas emissions from soils—A review ». *Geochemistry* 76 (3): 327-52. https://doi.org/10.1016/j.chemer.2016.04.002.

Pape, L., C. Ammann, A. Nyfeler-Brunner, C. Spirig, K. Hens, et F. X. Meixner. 2009. « An Automated Dynamic Chamber System for Surface Exchange Measurement of Non-Reactive and Reactive Trace Gases of Grassland Ecosystems ». *Biogeosciences* 6 (3): 405-29. https://doi.org/10.5194/bg-6-405-2009.

Pastorello, Gilberto, Carlo Trotta, Eleonora Canfora, Housen Chu, Danielle Christianson, You-Wei Cheah, Cristina Poindexter, et al. 2020. « The FLUXNET2015 Dataset and the ONEFlux Processing Pipeline for Eddy Covariance Data ». *Scientific Data* 7 (1): 225. https://doi.org/10.1038/s41597-020-0534-3.

Peltola, Olli, Toprak Aslan, Andreas Ibrom, Eiko Nemitz, Üllar Rannik, et Ivan Mammarella. 2021. « The High-Frequency Response Correction of Eddy Covariance Fluxes – Part 1: An Experimental Approach and Its Interdependence with the Time-Lag Estimation ». *Atmospheric Measurement Techniques* 14 (7): 5071-88. https://doi.org/10.5194/amt-14-5071-2021.

Plancherel, Michel, et Mittag Leffler. 1910. « Contribution À ĽÉtude de la reprÉsentation D'une fonction arbitraire par des intÉgrales dÉfinies ». *Rendiconti del Circolo Matematico di Palermo (1884-1940)* 30 (1): 289-335. https://doi.org/10.1007/BF03014877.

Ramanantenasoa, Maharavo Marie Julie, Jean-Marc Gilliot, Catherine Mignolet, Carole Bedos, Etienne Mathias, Thomas Eglin, David Makowski, et Sophie Génermont. 2018. « A New Framework to Estimate Spatio-Temporal Ammonia Emissions Due to Nitrogen Fertilization in France ». *Science of The Total Environment* 645 (décembre): 205-19. https://doi.org/10.1016/j.scitotenv.2018.06.202.

Ran, Youhua, Xin Li, Rui Sun, Natascha Kljun, Lei Zhang, Xufeng Wang, et Gaofeng Zhu. 2016. « Spatial Representativeness and Uncertainty of Eddy Covariance Carbon Flux Measurements for Upscaling Net Ecosystem Productivity to the Grid Scale ». *Agricultural and Forest Meteorology*, Oasis-desert system, 230-231 (décembre): 114-27. https://doi.org/10.1016/j.agrformet.2016.05.008.

Reichstein, Markus, Eva Falge, Dennis Baldocchi, Dario Papale, Marc Aubinet, Paul Berbigier, Christian Bernhofer, et al. 2005. « On the Separation of Net Ecosystem Exchange into Assimilation and Ecosystem Respiration: Review and Improved Algorithm ». *Global Change Biology* 11 (9): 1424-39. https://doi.org/10.1111/j.1365-2486.2005.001002.x.

Sabbatini, Simone, Ivan Mammarella, Nicola Arriga, Gerardo Fratini, Alexander Graf, Lukas Hörtnagl, Andreas Ibrom, et al. 2018. « Eddy Covariance Raw Data Processing for CO2 and Energy Fluxes Calculation at ICOS Ecosystem Stations ». *International Agrophysics* 32 (4): 495-515. https://doi.org/10.1515/intag-2017-0043.

Scanlon, Todd M., et John D. Albertson. 2001. « Turbulent Transport of Carbon Dioxide and Water Vapor within a Vegetation Canopy during Unstable Conditions: Identification of Episodes Using

Wavelet Analysis ». *Journal of Geophysical Research: Atmospheres* 106 (D7): 7251-62. https://doi.org/10.1029/2000JD900662.

Scanlon, Todd M., et William P. Kustas. 2010. « Partitioning Carbon Dioxide and Water Vapor Fluxes Using Correlation Analysis ». *Agricultural and Forest Meteorology* 150 (1): 89-99. https://doi.org/10.1016/j.agrformet.2009.09.005.

Scanlon, Todd M., et Parameswar Sahu. 2008. « On the Correlation Structure of Water Vapor and Carbon Dioxide in the Atmospheric Surface Layer: A Basis for Flux Partitioning ». *Water Resources Research* 44 (10). https://doi.org/10.1029/2008WR006932.

Seinfeld, John H., Spyros N. Pandis, et Kevin Noone. 1998. « *Atmospheric Chemistry and Physics: From Air Pollution to Climate Change* ». *Physics Today* 51 (10): 88-90. https://doi.org/10.1063/1.882420.

Storm, Ida, Ute Karstens, Claudio D'Onofrio, Alex Vermeulen, et Wouter Peters. 2023. « A View of the European Carbon Flux Landscape through the Lens of the ICOS Atmospheric Observation Network ». *Atmospheric Chemistry and Physics* 23 (9): 4993-5008. https://doi.org/10.5194/acp-23-4993-2023.

Sutton, M. A., E. Nemitz, C. Milford, C. Campbell, J. W. Erisman, A. Hensen, P. Cellier, et al. 2009. « Dynamics of Ammonia Exchange with Cut Grassland: Synthesis of Results and Conclusions of the GRAMINAE Integrated Experiment ». *Biogeosciences* 6 (12): 2907-34. https://doi.org/10.5194/bg-6-2907-2009.

Sutton, Mark, Clare Howard, et Jan Willem Erisman. 2011. « The European Nitrogen Assessment: Sources, Effects and Policy Perspectives ». https://doi.org/10.1017/CBO9780511976988.

Tarantola, Albert. 2005. *Inverse Problem Theory and Methods for Model Parameter Estimation*. Other Titles in Applied Mathematics. Society for Industrial and Applied Mathematics. https://doi.org/10.1137/1.9780898717921.

Thomas, C., J. G. Martin, M. Goeckede, M. B. Siqueira, T. Foken, B. E. Law, H. W. Loescher, et G. Katul. 2008. « Estimating Daytime Subcanopy Respiration from Conditional Sampling Methods Applied to Multi-Scalar High Frequency Turbulence Time Series ». *Agricultural and Forest Meteorology* 148 (8): 1210-29. https://doi.org/10.1016/j.agrformet.2008.03.002.

Tian, Hanqin, Rongting Xu, Josep G. Canadell, Rona L. Thompson, Wilfried Winiwarter, Parvadha Suntharalingam, Eric A. Davidson, et al. 2020. « A Comprehensive Quantification of Global Nitrous Oxide Sources and Sinks ». *Nature* 586 (7828): 248-56. https://doi.org/10.1038/s41586-020-2780-0.

Torrence, Christopher, et Gilbert P. Compo. 1998. « A Practical Guide to Wavelet Analysis ». *Bulletin of the American Meteorological Society* 79 (1): 61-78. https://doi.org/10.1175/1520-0477(1998)079<0061:APGTWA>2.0.CO;2.

Tramontana, Gianluca, Mirco Migliavacca, Martin Jung, Markus Reichstein, Trevor F. Keenan, Gustau Camps-Valls, Jerome Ogee, Jochem Verrelst, et Dario Papale. 2020. « Partitioning Net

Carbon Dioxide Fluxes into Photosynthesis and Respiration Using Neural Networks ». *Global Change Biology* 26 (9): 5235-53. https://doi.org/10.1111/gcb.15203.

Ueyama, Masahito, et Tsugumi Takano. 2022. « A decade of CO2 flux measured by the eddy covariance method including the COVID-19 pandemic period in an urban center in Sakai, Japan ». *Environmental Pollution* 304 (juillet): 119210. https://doi.org/10.1016/j.envpol.2022.119210.

Velasco, E., S. Pressley, R. Grivicke, E. Allwine, T. Coons, W. Foster, B. T. Jobson, et al. 2009. « Eddy Covariance Flux Measurements of Pollutant Gases in Urban Mexico City ». *Atmospheric Chemistry and Physics* 9 (19): 7325-42. https://doi.org/10.5194/acp-9-7325-2009.

Vuichard, Nicolas, Philippe Ciais, Nicolas Viovy, Longhui Li, Eric Ceschia, Martin Wattenbach, Christian Bernhofer, et al. 2016. « Simulating the Net Ecosystem CO2 Exchange and Its Components over Winter Wheat Cultivation Sites across a Large Climate Gradient in Europe Using the ORCHIDEE-STICS Generic Model ». *Agriculture, Ecosystems & Environment* 226 (juin): 1-17. https://doi.org/10.1016/j.agee.2016.04.017.

Vuichard, Nicolas, Palmira Messina, Sebastiaan Luyssaert, Bertrand Guenet, Sönke Zaehle, Josefine Ghattas, Vladislav Bastrikov, et Philippe Peylin. 2019. « Accounting for Carbon and Nitrogen Interactions in the Global Terrestrial Ecosystem Model ORCHIDEE (Trunk Version, Rev 4999): Multi-Scale Evaluation of Gross Primary Production ». *Geoscientific Model Development* 12 (11): 4751-79. https://doi.org/10.5194/gmd-12-4751-2019.

Wehr, R., J. W. Munger, J. B. McManus, D. D. Nelson, M. S. Zahniser, E. A. Davidson, S. C. Wofsy, et S. R. Saleska. 2016. « Seasonality of Temperate Forest Photosynthesis and Daytime Respiration ». *Nature* 534 (7609): 680-83. https://doi.org/10.1038/nature17966.

Wolfe, Glenn M., S. Randy Kawa, Thomas F. Hanisco, Reem A. Hannun, Paul A. Newman, Andrew Swanson, Steve Bailey, et al. 2018. « The NASA Carbon Airborne Flux Experiment (CARAFE): Instrumentation and Methodology ». *Atmospheric Measurement Techniques* 11 (3): 1757-76. https://doi.org/10.5194/amt-11-1757-2018.

Worthy, Douglas E. J., Michele K. Rauh, Lin Huang, Felix R. Vogel, Alina Chivulescu, Kenneth A. Masarie, Ray L. Langenfelds, et al. 2023. « Results of a Long-Term International Comparison of Greenhouse Gas and Isotope Measurements at the Global Atmosphere Watch (GAW) Observatory in Alert, Nunavut, Canada ». *Atmospheric Measurement Techniques* 16 (23): 5909-35. https://doi.org/10.5194/amt-16-5909-2023.

Woude, Auke M. van der, Wouter Peters, Emilie Joetzjer, Sébastien Lafont, Gerbrand Koren, Philippe Ciais, Michel Ramonet, et al. 2023. « Temperature Extremes of 2022 Reduced Carbon Uptake by Forests in Europe ». *Nature Communications* 14 (1): 6218. https://doi.org/10.1038/s41467-023-41851-0.

Wutzler, Thomas, Antje Lucas-Moffat, Mirco Migliavacca, Jürgen Knauer, Kerstin Sickel, Ladislav Šigut, Olaf Menzer, et Markus Reichstein. 2018. « Basic and Extensible Post-Processing of Eddy Covariance Flux Data with REddyProc ». *Biogeosciences* 15 (16): 5015-30. https://doi.org/10.5194/bg-15-5015-2018.

Wyngaard, John C. 1985. « Structure of the Planetary Boundary Layer and Implications for Its Modeling ». *Journal of Applied Meteorology and Climatology* 24 (11): 1131-42. https://doi.org/10.1175/1520-0450(1985)024<1131:SOTPBL>2.0.CO;2.

Xia, Jianyang, Shuli Niu, Philippe Ciais, Ivan A. Janssens, Jiquan Chen, Christof Ammann, Altaf Arain, et al. 2015. « Joint control of terrestrial gross primary productivity by plant phenology and physiology ». *Proceedings of the National Academy of Sciences* 112 (9): 2788-93. https://doi.org/10.1073/pnas.1413090112.

Xiao, Jingfeng, Kenneth J. Davis, Nathan M. Urban, Klaus Keller, et Nicanor Z. Saliendra. 2011. « Upscaling Carbon Fluxes from Towers to the Regional Scale: Influence of Parameter Variability and Land Cover Representation on Regional Flux Estimates ». *Journal of Geophysical Research: Biogeosciences* 116 (G3). https://doi.org/10.1029/2010JG001568.

Xu, Ke, Stefan Metzger, et Ankur R. Desai. 2017. « Upscaling Tower-Observed Turbulent Exchange at Fine Spatio-Temporal Resolution Using Environmental Response Functions ». *Agricultural and Forest Meteorology* 232 (janvier): 10-22. https://doi.org/10.1016/j.agrformet.2016.07.019.

Yue, Chao, Philippe Ciais, Sebastiaan Luyssaert, Wei Li, Matthew J. McGrath, Jinfeng Chang, et Shushi Peng. 2018. « Representing Anthropogenic Gross Land Use Change, Wood Harvest, and Forest Age Dynamics in a Global Vegetation Model ORCHIDEE-MICT v8.4.2 ». *Geoscientific Model Development* 11 (1): 409-28. https://doi.org/10.5194/gmd-11-409-2018.

Zahn, Einara, Elie Bou-Zeid, Stephen P. Good, Gabriel G. Katul, Christoph K. Thomas, Khaled Ghannam, James A. Smith, et al. 2022. « Direct partitioning of eddy-covariance water and carbon dioxide fluxes into ground and plant components ». *Agricultural and Forest Meteorology* 315 (mars): 108790. https://doi.org/10.1016/j.agrformet.2021.108790.

3. EDDY COVARIANCE IN A WAVELET FRAMEWORK

Due to significant contributions during this work, we have decided to allocate a separate chapter to delve into the intricacies of wavelets. The background theory incorporates existing knowledge as an extension of section 2.2 on the conventional framework and then describes novelties developed during this work, namely on main equations and flux partitioning.

2.1. Background theory

Wavelet transform originated in the late 1970s and early 1980s as an alternative to Fourier methods for analysing non-stationary signals. Pioneered by Morlet, Grossmann, Meyer, and Daubechies, wavelet theory evolved rapidly in the late 1980s and 1990s, with Daubechies' orthogonal bases laying the groundwork for practical applications (Daubechies 1988). Its adaptability to capture both high and low-frequency details made wavelet transform indispensable in various fields, including image compression, denoising, and feature extraction, solidifying its status as a standard signal and image processing tool.

Wavelet transform finds diverse applications across multiple fields. For instance, biomedical signal processing detects anomalies in electrocardiography, ECG, electroencephalography, EEG, and signals. Image processing benefits from wavelets for compression, edge detection, and enhancement. Wavelet analysis aids in efficient video compression and enhances communication systems, particularly in wireless channels. Geophysical signal processing benefits from wavelets for analysing seismic data and detecting earthquakes or oil reservoirs.

While wavelets are relatively new in flux calculation (Mahrt et Howell 1994; Brunet et Collineau 1994), where spectral analysis has traditionally been conducted using Fourier methods, other fields of science have also explored the comparability of these two methods. For heart period detection, both methods showed minor differences (<1%) (Houtveen et Molenaar 2001). Wavelets were preferred for video and image compression, where sharp edges are important for better definition (Strang 1993).

The comparison between wavelets and Fourier analysis is natural, considering the widespread use of Fourier analysis and the potential of wavelets to offer not only frequency decomposition but also time-domain information. Wavelets can thus be loosely taken as an intermediate yet enriched case between a series defined in time and its spectra only defined in the frequency domain (Figure 3.1).

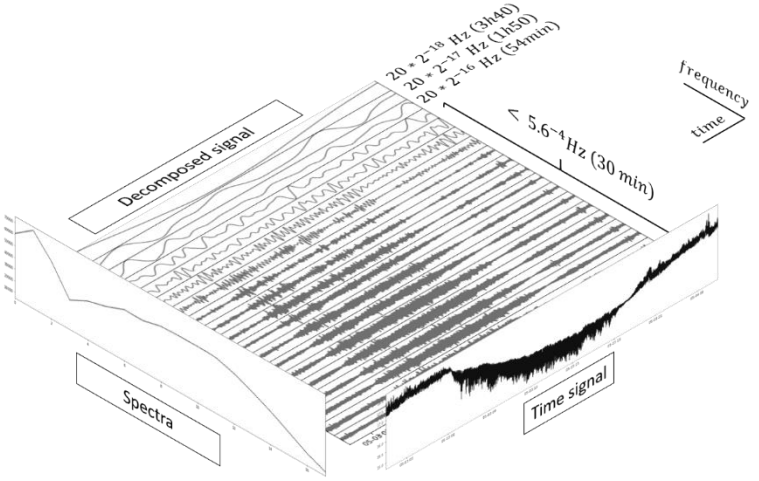

Figure 3.1. An illustrative example of the decomposition of a series in time and frequency domains.

By decomposing the time series of flux measurements into different scales and frequencies, wavelet transform allows researchers to identify transient events, periodic fluctuations, and long-term trends in the flux data. The decomposition evades the need for stationary conditions. This multi-resolution analysis is precious for understanding turbulent flows, as natural processes such as the opening and closing of leaf stomata, periodic bursts, heterogeneous landscapes, and shifting wind directions introduce non-stationarity to the system (Torrence et Compo 1998).

Wavelets are commonly employed in eddy covariance studies for flux calculation from aircraft measurements (Mauder, Desjardins, et MacPherson 2007; Metzger et al. 2013). They have also captured short-term turbulent events for CH_4 (Schaller, Göckede, et Foken 2017; Göckede, Kittler, et Schaller 2019). These studies utilize wavelets to calculate the covariance of the turbulent term (Eq. 2.3). Note, however, that Plancherel or Parseval's theorem applies to wavelets (Lewalle 1994), allowing wavelets to define a local instantaneous energy spectrum. This theorem states that the integral of a function's $f(x)$, squared modulus is equal to the integral of the squared modulus of its time and frequency wavelet decomposition, $\tilde{f}(x,j)$.

$$\int_{-\infty}^{\infty} |f(x)|^2 \, d_x = \int_0^{\infty} \int_{-\infty}^{\infty} \left|\tilde{f}(x,j)\right|^2 d_j d_x \qquad 3.1$$

Researchers had previously reformulated the Navier-Stokes Equations using wavelet form (Lewalle 1994). Even predating the establishment of wavelet theory, the three-dimensional Navier-Stokes equation had undergone projection onto a quasi-orthogonal basis using functions localized in both space and scale (Zimin 1981 *apud* Farge, 1992). A hierarchy of eddies was considered in constructing this basis, assuming large eddies advected small ones. Interestingly, the phase-space segmentation of Zimin's hierarchical basis is the same as that of wavelets (Marie Farge 1992).

3.1.1 Frequency decomposition

Wavelet transform is a bandpass filter allowing the decomposition of a time series into sub-series defined for a given frequency. The following steps briefly explain how to perform a frequency-resolved covariance using wavelets. More details can be found in (Marie Farge 1992; Torrence et Compo 1998; M. Farge et Schneider 2001).

Any signal *f*(t) can be decomposed into different scales, which results in the signal itself once added up. The simplest example is the Reynolds decomposition that separates a time series into its mean and its instantaneous deviation:

$$f(t) = f'(t) + \overline{f(t)} \qquad 3.2$$

In Eq. 3, the mean, $\overline{f(t)}$, is the low-frequency component, with a frequency representative of 1/T, where T is the averaging period. Similarly, a time series can be decomposed into J sub-series, each representative of a band of frequencies j:

$$f(t) = \sum_{j=0}^{J} f(t,j) \qquad 3.3$$

The wavelet transform is a way to decompose the signal using a mother wavelet ψ, a finite wave function. Considering N discrete observations with a sampling period δ_t, so that $t = n\,\delta_t$ where n is the time index, we can generate a family of wavelets normalized in L^2-norm:

$$\psi_{n,j}(n') = s_j^{-1/2}\psi\left[\frac{(n'-n)\delta_t}{s_j}\right] \qquad 3.4$$

Where s_j is the scaling factor, usually defined using a geometric progression with a maximum limited by the total sampling period $N\delta t$: $s_j = s_0 2^{j\delta_j}$, for $j = 0,1,\ldots J$. Here, J is the size of the set of scales, s_0 is the smallest resolvable scale, approximately $2\delta_t$, and δ_j is the scale factor. The convolution of the signal *f*(n) with a scaled mother wavelet ψ yields *W*(n,j), the high pass wavelet coefficient for time series *f*(n):

$$W(n,j) = \sum_{n'=0}^{N-1} f(n')\psi_{n,j}(n') \qquad 3.5$$

W is also named details to differentiate from the approximation coefficient, resulting from a low pass filter. From W, we can reconstruct the signal by first normalizing it:

$$\tilde{f}(n,j) = \frac{\delta j \delta t^{0.5}}{C_\delta \psi_0(0)} \Re\{W(n,j)\} \qquad 3.6$$

C_δ is a scale-independent reconstruction factor depending on the chosen mother wavelet function (Table 3.1) and $\tilde{f}(n,j)$ is the decomposed signal defined in both time and frequency. The fully reconstructed signal is then found by summing to infinity the different frequencies:

$$f(n) = \sum_{j=0}^{\infty} \tilde{f}(n,j) \qquad 3.7$$

We can avoid summing to infinite by acknowledging the low pass filter, which yields an approximation coefficient which can be normalized to the low pass part of the signal named A:

$$f(n) = \sum_{j=0}^{J} \tilde{f}(n,j) + A_J \qquad 3.8$$

At the highest frequency $\sum_{j=0}^{0} \tilde{f}(n,j) = 0$ and $A_J = f(n)$. It becomes clear that eq. (6) is a particular case for infinity. In the intermediate cases, *f*(n) is the sum of all its components, A is similar to a time average, and a finite sum of $\tilde{f}(n,j)$ is close to an instantaneous deviation.

$$f(n) - \frac{\sum_{n=0}^{T} f(n)}{T} \approx \sum_{f=\infty}^{1/T} \tilde{f}(n,f) \qquad 3.9$$

T is the averaging time (e.g., seconds), and f is the frequency (sj−1, e.g., Hz).

3.2 Main equations

Here, we explain the changes in the covariance calculation when using discrete or continuous wavelets compared to standard approaches. For variance, consider the two variables to be the same. For unidimensional variables, covariance calculation is straightforward; it is the mean product of two instantaneous deviations, $Cov_{x,y} = \overline{(x-\bar{x})(y-\bar{y})}$. The frequency decomposition renders each variable bidimensional in time and frequency, $\tilde{x}_j(t)$ and $\tilde{y}_j(t)$, and as such, their product should account for cross-covariance in time and frequency, namely:

$$Cov_{x,y} = \sum\nolimits_{j=0}^{J} \overline{\tilde{x}_j \tilde{y}_j} + \sum\nolimits_{k \neq j} \overline{\tilde{x}_j \tilde{y}_k} \qquad 3.10$$

The orthogonality of discrete wavelets implies independent frequencies, yielding $Cov_{x,y} = \sum_{j=0}^{J} \overline{\tilde{x}_j \tilde{y}_j}$. Thus, the cross-covariance problem only appears when using continuous wavelets. In this latter case, a correction factor needs to be introduced to account for the covariance terms $\overline{\tilde{x}_j \tilde{y}_k}$. Some authors propose not to use decomposed signals, $\tilde{x}_j(t)$ and $\tilde{y}_j(t)$, but directly calculating the covariance using the following equation, which directly accounts for the cross-correlation terms (Torrence et Compo 1998):

$$Cov_{x,y} = \frac{\delta j \delta t}{C_\delta N} \sum_{n=0}^{N-1} \sum_{j=0}^{J} W_x(n,j) W_y(n,j) \qquad 3.11$$

Note that the equation (2.11) cannot be retrieved from (2.5).

By postulating that the cross-covariance ($\sum_{k \neq j} \overline{\tilde{x}_j \tilde{y}_k}$) is proportional to the direct part ($\sum_{j=0}^{J} \overline{\tilde{x}_j \tilde{y}_j}$) at a factor determined by the mother wavelet, we can find an empirical factor named C_φ that corrects the covariance in the case of continuous wavelets.

$$Cov_{x,y} = C_\varphi \sum_{j=0}^{J} \overline{\tilde{x}_j \tilde{y}_j} \qquad 3.12$$

Note that C_φ, like C_δ, is only required for continuous wavelet decompositions in which the wavelet function is not an orthogonal base. The covariance correction factor C_φ empirically found for Morlet and DOG wavelets (Coimbra et al., 2023) can be seen in Table 3.1.

Table 3.1: Mother wavelets used in this study. Mother wavelet formula, $\boldsymbol{\psi(\eta)}$, empirically derived factors, Cδ and $\psi_0(0)$, from (Farge, 1992) and Cφ (Coimbra et al., 2023).

Name	Decomposition	$\psi(\eta)$	Cδ	$\psi_0(0)$	Cφ
Morlet (kψ= 6)	Continuous	$e^{ik_\psi \eta} e^{-\frac{\eta^2}{2}}$	0.776	$\pi^{-1/4}$	5.271
DOG (m=2), also known as Marr or Mexican Hat	Continuous	$-1^m \frac{d^m}{d\eta^m}(e^{-\frac{\eta^2}{2}})$	3.541	0.867	16.568
Daubechies (k=6)	Discrete	$(-1)^k a_{N-1-k}$	1	1	1

3.3 Direct partitioning

In Chapter 1, we have presented the existing direct partitioning methods consisting of conditional sampling concentrations before eddy-covariance computation. This chapter presents a novel method inspired by conditional sampling that uses wavelet decomposed signals.

3.3.1 Partitioning of turbulent flux using wavelets

The method was built on the empirical assumption that wavelet decomposition should capture positive and negative "gusts" at each frequency, mixed up in the original signal. Based on this assumption, partitioning was made by simply separating the frequency decomposed covariances (e.g.: $\tilde{w}\tilde{\chi}_s(t,j)$) Before any averaging is performed into positive (sources) and negative (sinks) components. In its basic form, this conditional sampling can be used with vertical wind, *w*, and a scalar, *s*. The sampling should yield two groups:

$$\tilde{w}\tilde{\chi}_s = \tilde{w}\tilde{\chi}_s^+ + \tilde{w}\tilde{\chi}_s^- \qquad 3.13$$

Where x^+ (x^-) stands for conditional sampling of variable x when x is positive (negative), and the frequency ranges index j have been omitted for readability. For CO_2, $\widetilde{w}\widetilde{\chi}_s^+$ would correspond to respiration and $\widetilde{w}\widetilde{\chi}_s^-$ to photosynthesis. By incorporating an additional, conditional sampling based on other scalar fluxes in which emission or absorption processes are correlated with s, we can better attribute $\widetilde{w}\widetilde{\chi}_s^+$ and $\widetilde{w}\widetilde{\chi}_s^-$ to a given process. For instance, in the case of CO_2, conditional sampling based on H_2O fluxes helps to attribute respiration and photosynthesis. Each term in Eq. (15) can then be further divided based on conditional sampling on the other scalar flux, as in the following example for $\widetilde{w}\widetilde{\chi}_s^+$:

$$\widetilde{w}\widetilde{\chi}_s^+ = \widetilde{w}\widetilde{\chi}_s^+|\widetilde{w}\widetilde{\chi}_v^+ + \widetilde{w}\widetilde{\chi}_s^+|\widetilde{w}\widetilde{\chi}_v^- \qquad 3.14$$

Where $\widetilde{\chi}_v$ is the mixing ratio of another gas (e.g., H_2O, CO) and $x|y$ stands for sampling x when y is true. The method is very flexible and allows for employing any variable split into positive and negative (or above and below a threshold). Figure 2 summarises it.

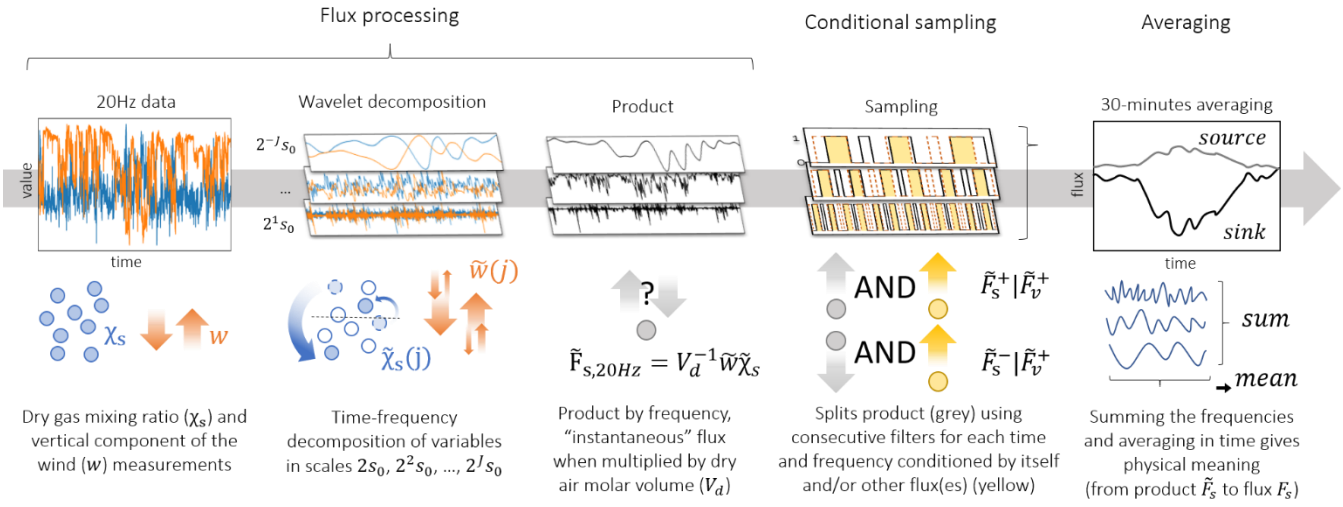

Figure 3.2: Conceptual scheme showing the main wavelet-based eddy covariance processing steps: time and frequency decomposition; the product of instantaneous deviation; partitioning by conditional sampling; and frequency integration and time averaging. Where w is the vertical component of the wind velocity, $\boldsymbol{\chi_s}$ is the mixing ratio of a gas, j represents the frequency scale. Bars are for averaging, and quotation marks are deviations from the mean.

Conditional sampling does not change observations in any way and is simply a way of splitting observations to see them differently. In other words, the sum of all components of a conditionally sampled flux returns the original flux. The partitioning comes from attributing each conditionally sampled flux to an environmental exchange process.

For example, for water vapour and CO_2, we can formalize this H_2O-CO_2 partitioning as:

$$\widetilde{w}\widetilde{\chi}_{CO_2}^{GPP} = \widetilde{w}\widetilde{\chi}_{CO_2}^-|\widetilde{w}\widetilde{\chi}_{H_2O}^+|D^+ + 0.5 \times \widetilde{w}\widetilde{\chi}_{CO_2}^-|\widetilde{w}\widetilde{\chi}_{H_2O}^-|D^+ \qquad 3.15$$

$$\widetilde{w}\tilde{\chi}_{CO_2}^{Reco} = \widetilde{w}\tilde{\chi}_{CO_2}^{+}|\widetilde{w}\tilde{\chi}_{H_2O}^{+} + 0.5 \times \widetilde{w}\tilde{\chi}_{CO_2}^{-}|\widetilde{w}\tilde{\chi}_{H_2O}^{-}|D^{+} + \widetilde{w}\tilde{\chi}_{CO_2}^{-}|D^{-} \quad 3.16$$

Where D is 1 when day (PPFD>10 μmol m−2 s −1) and −1 otherwise and $GPP = \sum_{j=0}^{J} V_a \overline{\widetilde{w}\tilde{\chi}_{CO_2}^{GPP}}$, $R_{eco} = \sum_{j=0}^{J} V_a \overline{\widetilde{w}\tilde{\chi}_{CO_2}^{Reco}}$ (Figure 3.3).

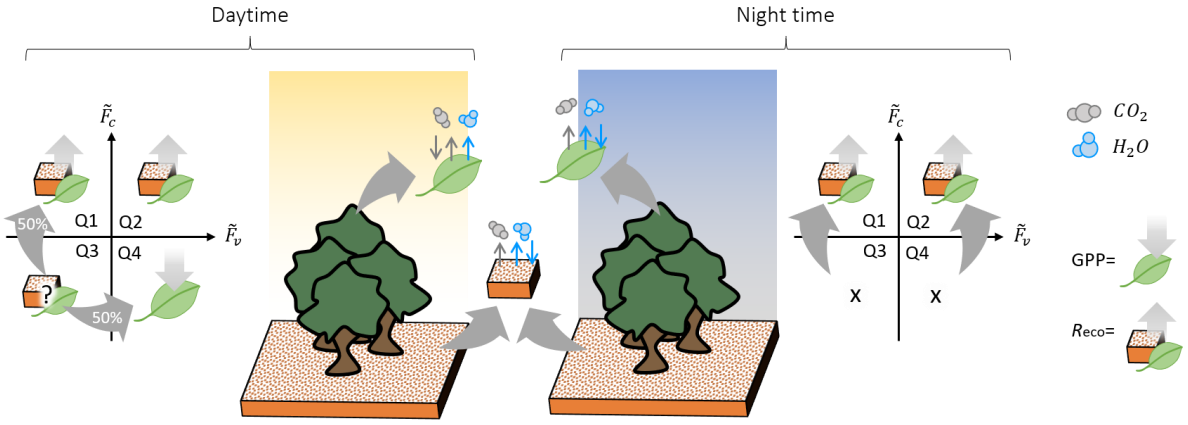

Figure 3.3: Conceptual scheme for wavelet-based NEE flux partitioning. Quadrants and arrows in the figure show conceivable fluxes during day and night. In quadrants, grey arrows show reallocation from unlikable (question mark) and unreasonable ("x") fluxes towards the most probable actual flux.

When anthropogenic emissions are not negligible, partitioning should also be used to consider them as a separate set of sources. Using tracers specific to anthropogenic emissions as filters in the conditional sampling (Figure 3.2), we could ideally further partition sources into ecosystem respiration and fossil fuel emissions, as conceptually shown in Figure 3.4 when CO is used as a tracer of fossil fuel combustion.

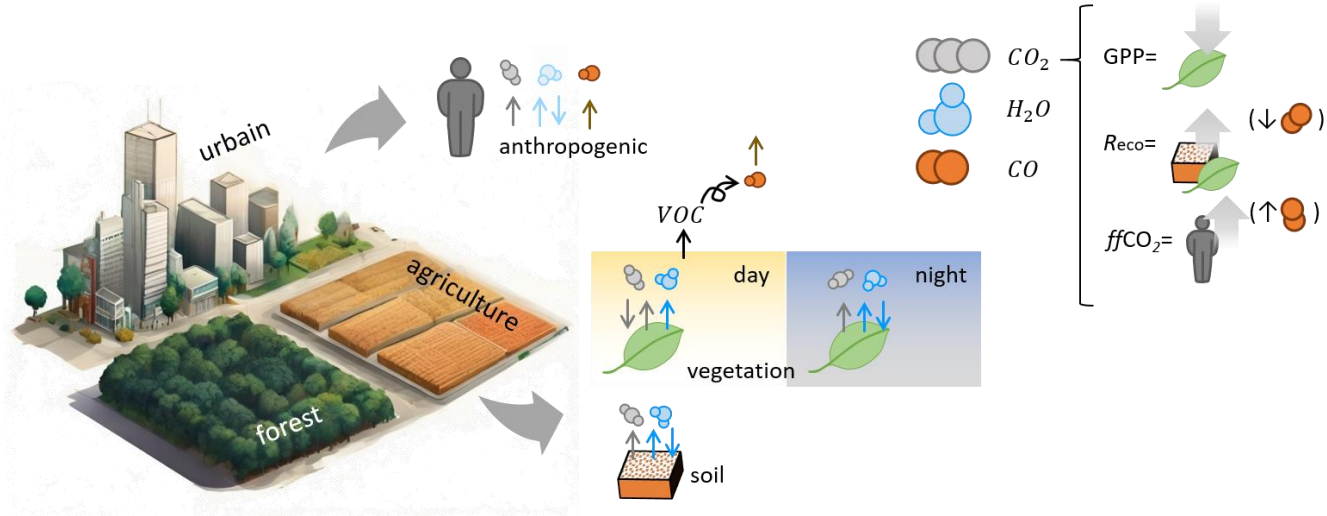

Figure 3.4. Conceptual schemes of correlations between CO2, H2O, and CO flux directions are based on the physical source or sink. GPP is gross primary productivity (photosynthesis); Reco is ecosystem respiration, which

includes leaves and soil. aCO_2 is an anthropogenic emission. VOC stands for volatile organic compounds, which are sources of CO. The figure was partially generated using artificial intelligence (DALL-E3).

This CO-CO_2 partitioning, similarly to H_2O-CO_2, can be further formalized as:

$$\widetilde{w}\tilde{\chi}_{CO_2}^{Reco} = \left(\widetilde{w}\tilde{\chi}_{CO_2} - \widetilde{w}\tilde{\chi}_{CO_2}^{GPP}\right)|\widetilde{w}\tilde{\chi}_{CO}^{-} \quad 3.17$$

$$\widetilde{w}\tilde{\chi}_{CO_2}^{aCO_2} = \left(\widetilde{w}\tilde{\chi}_{CO_2} - \widetilde{w}\tilde{\chi}_{CO_2}^{GPP}\right)|\widetilde{w}\tilde{\chi}_{CO}^{+} \quad 3.18$$

From which the partitioned fluxes can be calculated as before, $GPP = \sum_{j=0}^{J} V_a \overline{\widetilde{w}\tilde{\chi}_{CO_2}^{GPP}}$, $R_{eco} = \sum_{j=0}^{J} V_a \overline{\widetilde{w}\tilde{\chi}_{CO_2}^{Reco}}$ and $aCO_2 = \sum_{j=0}^{J} V_a \overline{\widetilde{w}\tilde{\chi}_{CO_2}^{aCO_2}}$ (Figure 3.3).

3.3.2 Attributing the storage term in partitioned fluxes

Note that the partitioning so far only considers the turbulent term, while the surface flux F_s is the sum of a turbulent F_s^{EC} and a storage F_s^{STO} flux (eq. 2.4), which can be considerable for tall towers, as we target in this work. However, distributing the storage term into each partitioned flux is not trivial. The closure of our system constrains the options, and the net flux must equal its partitioned parts. A possibility is to arbitrarily set coefficients α (α_{GPP}, α_{Reco}, α_{aCO2}, …) and add a storage term αF_s^{STO} for each of the partitioned fluxes (eq. 3.16-3.18). In this case, all α must sum to one, but each α can be chosen individually, for example, based on the amount of data used.

3.3.3 Sensitivity to noise of the partitioning

While random noise is expected to have minimal impact on covariance, the partitioning process of $\widetilde{w}\tilde{\chi}_s$ may wrongly attribute a noisy flux to positive and negative components $\widetilde{w}\tilde{\chi}_s^{+}$and $\widetilde{w}\tilde{\chi}_s^{-}$, similar to noise in vertical wind speed, which can lead to wrongness in Relaxed Eddy Accumulation methods (Ammann and Meixner, 2002). To demonstrate this noise sensibility, we selected one week of data and contaminated CO_2 measurements with Gaussian white noise, which has equally distributed spectral densities across all frequencies. We added 4 noise levels with variances corresponding to 10, 20, 40, and 90 % of the signal's variance. As a result, we obtained a signal-to-noise ratio (SNR) of 10.0, 5.0, 2.5 and 1.1.

We tested the effect of the noising on the partitioning using a few days of data (Figure 3.5). We compared noised and original values for the spectra, co-spectra and partitioned co-spectra. In Figure 3.5.d, to demonstrate a denoising effect, we fitted a 1:1 curve, and during partitioning, we only filtered as positive and negative when values were higher than this 1:1 curve. This filtering yielded values closer to the original partitioning.

Random noise does not covariate with an independent variable; thus, the effect of noise on the covariance is expected to be minimal. In Figure 3.5 and Figure 3.6, we show that adding white noise strongly affects CO_2 spectrum (a) but has no apparent effect on w and CO_2 co-spectrum (b). The strong high-frequency contribution, however, reappears when the co-spectrum is split into its positive and negative counterparts (c) as is performed during conditional sampling. The correction, removing a fitted *fb* curve in CO_2 spectra, yields the corrected co-spectra much closer

to the unnoisy signal (d). Note that a low-frequency contribution can be seen in (c) but not in (b); however, it does not seem to be affected by noise.

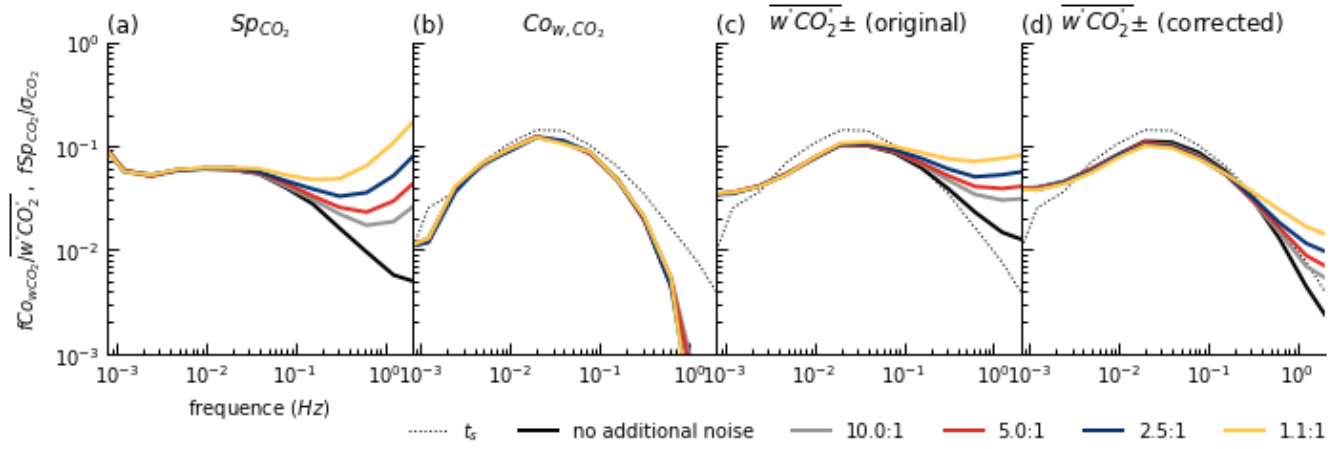

Figure 3.5. Noise imputation and the (co)spectra. (a) CO2 spectra, (b) w CO2 co-spectra, (c) mean between positive and negative decomposed co-spectra, (d) the same as (c) but after noise removal. Colours indicate the imputed noise. Data from 23/07/2023 to 31/07/2023 for FR-SAC (Saclay ICOS tower).

The diel pattern (Figure 3.6) confirms that noise imputation had minimal impact in $\overline{w'CO_2'}$, but appears in the decomposition (b) and is successfully corrected in (c). The noise (d) is very close to zero, varying between −0.07 and 0.12 (−0.29 and 0.70) µmol m^{-2} s^{-1} in the original (1.1:1 added noise) covariance.

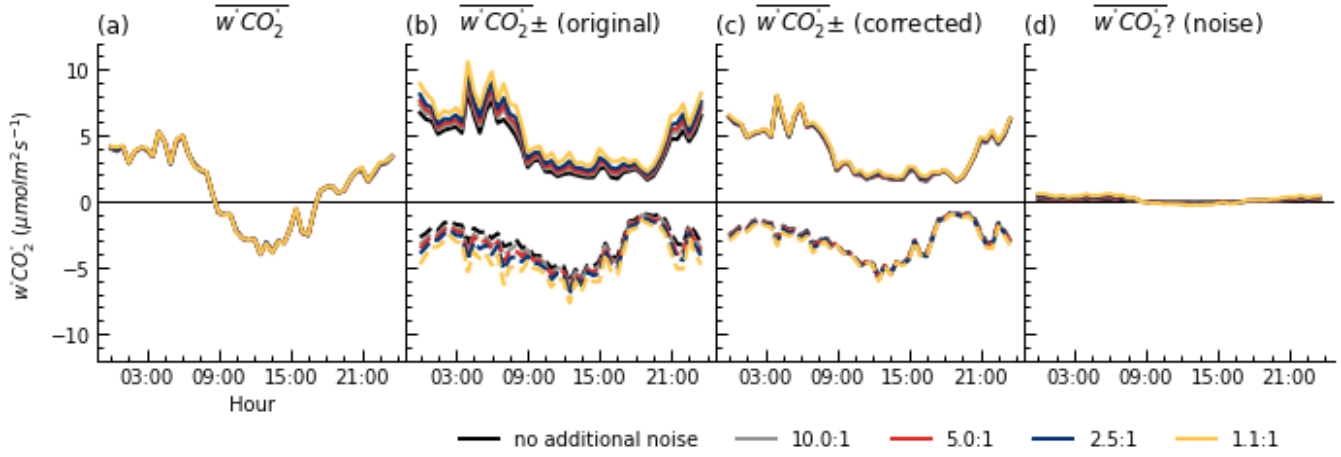

Figure 3.6. Noise imputation and the diel pattern. (a) w CO_2 covariance, (b) positive (solid) and negative (dashed) original decomposed counterparts, (c) the same as (b) but after noise removal, and (c) the noise removed. Colours indicate the imputed noise. Data from 23/07/2023 to 31/07/2023 for FR-SAC (Saclay ICOS tower).

3.3.4 Ongoing challenges

In specific conditions, the method may underestimate partitioned fluxes. If we imagine measuring a flux in a location with no sinks or sources, high-frequency measurements may detect

differences in high-frequency fluxes, even though the half-hourly flux should be null. Since it is not zero, the instantaneous deviation may add up separately into negative and positive fluxes partitioning groups. The consequence is that the direct partitioning, in this case, may generate unrealistic positive and negative partitioned fluxes.

Such amplification can happen with noisy instruments (gas analyser or ultrasonic anemometer) or when the scalar or wind variations are smaller than the instrument's capacity to measure it (called amplitude resolution problem). A possible solution would be to create a "dead band", such as in the REA approaches (Ammann and Meixner, 2002), where absolute values of the scalar flux not high enough to be considered as actual fluxes should be attributed to an uncertainty band. Since the partition is done in the time-frequency domain, the dead band should also be defined in frequency and time. For this, Allan deviation seems to be an appropriate metric. The deviation could be considered fixed over time if no significant change in the instrumental setup happens. The partitioning considering noisy measurements can be rewritten from eq. 3.13 as:

$$\widetilde{w}\tilde{\chi}_s = \widetilde{w}\tilde{\chi}_s^+ + \widetilde{w}\tilde{\chi}_s^- + \widetilde{w}\tilde{\chi}_s^0 \qquad 3.19$$

Note the inclusion of a new group, $\widetilde{w}\tilde{\chi}_s^0$. This group should include values where the partitioning of a group is not contemplated. In the case of a fixed dead band, it can be determined by a threshold, ξ, such as if $|s - \bar{s}| < \xi$, then that $\tilde{\chi}_s^0 = \tilde{\chi}_s$ and $\tilde{\chi}_s^+ = \tilde{\chi}_s^- = 0$ in all frequencies. The use of a frequency-defined threshold, such as Allan deviation, works similarly, but the condition is determined in the frequency domain and becomes $\tilde{\chi}_s < \xi_j$.

Finally, storage flux may also be a concern. For periods with significant storage, the turbulent flux might not provide information from the surface flux but rather from the "pool" of gases previously emitted and stored below the tower. In this case, the direct partitioning method may provide partitioned fluxes dampening or closer to net flux.

In any case, the method is expected to yield better results, as the more significant the source/sink is, the smaller the instrument's noise and storage terms are.

3.4 References

Ammann, C. and Meixner, F.X., 2002. Stability dependence of the relaxed eddy accumulation coefficient for various scalar quantities. J. Geophys. Res.-Atmos., 107(D7-8). 10.1029/2001jd000649

Daubechies, Ingrid. 1988. « Orthonormal Bases of Compactly Supported Wavelets ». *Communications on Pure and Applied Mathematics* 41 (7): 909-96. https://doi.org/10.1002/cpa.3160410705.

Farge, M., et K. Schneider. 2001. « Analysing and Computing Turbulent Flows Using Wavelets ». In *New Trends in Turbulence Turbulence: Nouveaux Aspects: 31 July – 1 September 2000*, édité par M. Lesieur, A. Yaglom, et F. David, 449-504. Les Houches - Ecole d'Ete de Physique Theorique. Berlin, Heidelberg: Springer. https://doi.org/10.1007/3-540-45674-0_9.

Farge, Marie. 1992. « Wavelet transforms and their applications to turbulence ». *Annual review of fluid mechanics* 24 (1): 395-458.

Göckede, Mathias, Fanny Kittler, et Carsten Schaller. 2019. « Quantifying the Impact of Emission Outbursts and Non-Stationary Flow on Eddy-Covariance CH_4 Flux Measurements Using Wavelet Techniques ». *Biogeosciences* 16 (16): 3113-31. https://doi.org/10.5194/bg-16-3113-2019.

Houtveen, Jan H., et Peter C.M. Molenaar. 2001. « Comparison between the Fourier and Wavelet Methods of Spectral Analysis Applied to Stationary and Nonstationary Heart Period Data ». *Psychophysiology* 38 (5): 729-35. https://doi.org/10.1111/1469-8986.3850729.

Lewalle, J. 1994. « Wavelet Transforms of Some Equations of Fluid Mechanics ». *Acta Mechanica* 104 (1): 1-25. https://doi.org/10.1007/BF01170275.

Mauder, Matthias, Raymond L. Desjardins, et Ian MacPherson. 2007. « Scale Analysis of Airborne Flux Measurements over Heterogeneous Terrain in a Boreal Ecosystem ». *Journal of Geophysical Research: Atmospheres* 112 (D13). https://doi.org/10.1029/2006JD008133.

Metzger, S., W. Junkermann, M. Mauder, K. Butterbach-Bahl, B. Trancón y Widemann, F. Neidl, K. Schäfer, et al. 2013. « Spatially Explicit Regionalization of Airborne Flux Measurements Using Environmental Response Functions ». *Biogeosciences* 10 (4): 2193-2217. https://doi.org/10.5194/bg-10-2193-2013.

Schaller, Carsten, Mathias Göckede, et Thomas Foken. 2017. « Flux Calculation of Short Turbulent Events – Comparison of Three Methods ». *Atmospheric Measurement Techniques* 10 (3): 869-80. https://doi.org/10.5194/amt-10-869-2017.

Strang, Gilbert. 1993. « Wavelet Transforms versus Fourier Transforms ». *Bulletin of the American Mathematical Society* 28 (2): 288-305. https://doi.org/10.1090/S0273-0979-1993-00390-2.

Torrence, Christopher, et Gilbert P. Compo. 1998. « A Practical Guide to Wavelet Analysis ». *Bulletin of the American Meteorological Society* 79 (1): 61-78. https://doi.org/10.1175/1520-0477(1998)079<0061:APGTWA>2.0.CO;2.

Zimin, Vd. 1981. « Hierarchic Model of Turbulence ». *Izvestiya. Atmospheric and Oceanic Physics* 17 (12): 1265-73.

4. AN INNOVATIVE APPROACH FOR MEASURING SURFACE FLUXES USING WAVELETS

At high resolution, in-situ observations are of crucial importance. When studying surface fluxes, these observations often come from the Eddy Covariance (EC) method. This method is widely recognized for its ability to provide direct, continuous, and reliable monitoring of greenhouse gas fluxes. For CO_2, Gross Primary Productivity (GPP) and Ecosystem Respiration (Reco) are commonly derived from Net Ecosystem Exchange (NEE). For this, a simple model of ecosystem respiration response to temperature is usually fitted to night-time data and then extrapolated to daytime.

Direct covariance calculation makes the standard EC method unreliable in non-stationary conditions, reducing the amount of available data and thus possibly impacting the annual carbon balance. Furthermore, standard partitioning methods implicitly rely on strong assumptions about ecosystem respiration response to environmental conditions.

In this first article, we propose a new processing framework based on wavelets for Eddy Covariance. Wavelets are unaffected by non-stationarity, allowing for more exploitable data, which should benefit the annual carbon balance. A new direct partitioning method was also developed, applying conditional sampling of wavelet-decomposed signals. This empirical method separates the positive and negative parts of the wavelet-decomposed product of the vertical wind component (w) and the dry molar fraction of CO_2, conditioned by the water vapour flux, to compute GPP and Reco. This direct partitioning may be less prone to model assumptions. This new framework was tested over multiple years of data on two French ICOS ecosystem sites, a mixed oak forest (FR-Fon) and an agricultural site (FR-Gri).

The results show that between 17 and 29% of non-stationary data lost with the standard EC method were usable with the wavelet-based method. Furthermore, a good correlation of NEE calculated by both methods was observed during turbulent and stationary periods (R^2=0.99). The new direct partitioning based on wavelets provided daily by GPP and Reco is very similar to standard partitioning methods. Our method also mitigated common model errors, such as positive nocturnal GPP and showed consistency with management practices on the agricultural site. In croplands during abrupt changes, such as harvest or manure application, standard methods, dependent on calibration, may not accurately capture these patterns.

The diurnal cycle of Reco was notably different from the standard methods: While standard methods respond only to temperature, ours exhibited a bimodal diurnal cycle correlated with solar radiation and soil temperature. This cycle is similar to some results based on chamber measurements on low vegetation (including the plant), suggesting a plausible outcome.

The wavelet and partitioning framework developed in this Chapter will be used in Chapters 4 and 5 to compute turbulent fluxes and partition them into Reco, GPP and anthropogenic fluxes.

4.1 Article: Improvement of CO_2 Flux Quality Through Wavelet-Based Eddy Covariance

Citation: Coimbra, P. H. H., Loubet, B., Laurent, O., Mauder, M., Heinesch, B., Bitton, J., Delpierre, N., Depuydt, J., and Buysse, P.: Improvement of CO_2 Flux Quality Through Wavelet-Based Eddy Covariance: A New Method for Partitioning Respiration and Photosynthesis, https://doi.org/10.2139/ssrn.4642939, 24 November 2023.

Submitted to Agricultural and Forest Meteorology on 17 October 2023. No review has been received so far.

Preprint available here: https://doi.org/10.2139/ssrn.4642939, 24 November 2023.

Please note that the wavelet method described in this chapter follows the procedures outlined in 3. Any differences in nomenclature between the two may arise from variations in formalization but are duly addressed in the Materials and Methods section of the chapter. In doubt, please refer to the Materials and Methods section of the current chapter for clarification.

Improvement of CO_2 flux quality through wavelet-based Eddy Covariance: a new method for partitioning respiration and photosynthesis

Pedro Henrique H. Coimbra[1*], Benjamin Loubet[1], Olivier Laurent[2], Matthias Mauder[3,4], Bernard Heinesch[5], Jonathan Bitton[5], Nicolas Delpierre[6,7], Jérémie Depuydt[1], Pauline Buysse[1]

[1] ECOSYS, INRAE, AgroParisTech, Université Paris-Saclay, Palaiseau, France
[2] Laboratoire des Sciences du Climat et de l'Environnement, CEA, CNRS, Université Paris-Saclay, Gif-sur-Yvette, France
[3] Institute of Meteorology and Climate Research - Atmospheric Environmental Research (IMK-IFU), Karlsruhe Institute of Technology, Garmisch-Partenkirchen, Germany
[4] Institute of Hydrology and Meteorology, Technische Universität Dresden, Dresden, Germany
[5] Faculté des Sciences Agronomiques de Gembloux, Unité de Physique, Gembloux, Belgium
[6] Ecologie Systématique Evolution, CNRS, AgroParisTech, Université Paris-Saclay, Gif-sur-Yvette, France
[7] Institut Universitaire de France, France

* corresponding author: pedro-henrique.herig-coimbra@inrae.fr

Abstract

Eddy Covariance (EC) is praised for producing direct, continuous, and reliable flux monitoring for greenhouse gases. For CO_2, the method has been commonly used to derive gross primary productivity (GPP) and ecosystem respiration (R_{eco}) from net ecosystem exchange (NEE).

However, standard EC is impacted by non-stationarity, reducing data quality and consequently impacting standard partitioning methods constructed on simplistic assumptions.

This work proposes a new wavelet-based processing framework for EC tested over two French ICOS ecosystem sites, a mixed forest (FR-Fon) and cropland (FR-Gri), over several years. A new direct partitioning method was also developed, applying conditional sampling in wavelet decomposed signals. This new empirical method splits positive and negative parts of the wavelet decomposed product of the wind vertical component and CO_2 dry molar fraction, conditioned by water vapour flux, to compute GPP and R_{eco}.

Results show 17 to 29 % fewer gaps in wavelet-based than with standard EC, varying between sites, day and night. A good correlation between methods was observed during turbulent and stationary periods (R^2=0.99). However, wavelet-based NEE was 9% lower than in standard EC, likely related to low-frequency attenuation led by the detrending nature of wavelet transform.

The new wavelet-based direct partitioning provided daily GPP and R_{eco}, which are very similar to night- and day-time model-based partitioning methods, with the difference between our method and these standard methods smaller than between them. Our method did not produce positive GPP, a common error in the night-time method. It also showed R_{eco} seasonal patterns coherent with management practices at the crop site (growing season, harvest, manure application), which was not always the case for the standard methods. The R_{eco} diel cycle was noticeably different, whereas the standard methods are temperature-driven; our method had a daily pattern correlated to solar radiation and a night-time pattern correlated to soil temperature.

Eddy-covariance; wavelet; CO2 flux; partitioning; photosynthesis; respiration;

4.2 Introduction

Global surface temperature is 1.1 °C warmer compared with the pre-industrial era, even more significant on land (1.6 °C) (IPCC, 2021). Climate change leads to widespread adverse impacts and related losses and damages to nature and people (IPCC, 2022b). Projections show more than 2°C warming in 2100 due to mismatches between implemented policies and long-term goals (IPCC, 2022a). The warming results from the increase in greenhouse gas (GHG) concentration in the atmosphere, which is, in turn, the result of anthropogenic emissions (IPCC, 2021). The largest share of these emissions (86%) comes from fossil fuel CO_2 emissions (9.6 ± 0.5 Pg C yr−1) (Canadell et al., 2021). While stopping these emissions should remain the first objective, mitigating climate change will require decreasing all GHG sources. Agriculture, forestry and other land use (AFOLU) is a significant source of GHG (12.0 ± 2.9 GtCO2eq yr−1) (Jia et al., 2019). However, it has the potential to remove CO_2 from the atmosphere. Indeed, carbon uptake by vegetation has increased over the past decades, but uncertainties remain about whether this trend will continue (Canadell et al., 2021). Considering these uncertainties, soil carbon sequestration in croplands and grasslands has a considerable potential for removing CO2 from the atmosphere (0.4–8.6 GtCO2eq yr−1) (Jia et al., 2019). Measuring and separating the different processes of land-atmosphere carbon flux is crucial to advise and monitor policies and goals effectively. Doing it, however, is not trivial.

The international scientific community is leveraging advanced techniques to produce reliable surface-atmosphere GHG flux monitoring. Eddy Covariance (EC) is praised for directly and continuously measuring surface turbulent fluxes. Since the early measurements, the method has been applied to different gases, including water vapour, CO2, CH4 and N2O (Valentini et al., 1996; Moncrieff et al., 1997; Fowler et al., 1995). Active development of instrumentation and standardization of the methods and networks has made it the reference measurement for terrestrial ecosystem GHG fluxes (Pastorello et al., 2020).

Continuity is essential to compute annual GHG budgets and long-term soil carbon balance. Despite the attempt to have near-continuous observations, a fraction of the observation is either missing or non-reliable, resulting in data gaps. These gaps can sometimes be due to technical reasons but, most importantly, related to underdeveloped turbulence and non-stationarity of the flow, both required to compute reliable fluxes with the standard EC method (Aubinet et al., 2012; Pastorello et al., 2020). In FLUXNET2015 (Pastorello et al., 2020), with more than 1500 site-years of data worldwide, 60 % of the CO2 flux is gap-filled. Filling these short gaps is problematic because it can significantly bias the annual GHG budgets (Du et al., 2014; Vekuri et al., 2023).

Efforts have been mobilized to find defensible methods to fill CO2 flux gaps (Falge et al., 2001) and make it part of the standard post-processing (Wutzler et al., 2018; Pastorello et al., 2020). From various methods, artificial neural networks (ANN) (Papale and Valentini, 2003; Moffat, 2012) and look-up tables (Falge et al., 2001; Reichstein et al., 2005) seem more promising than processed-based ones (Moffat et al., 2007). Ensuring enough high-quality data for gap-filling is crucial during night-time for less stationary surface fluxes (CH_4, N_2O) (Irvin et al., 2021; Mishurov and Kiely, 2011) and heterogeneous sites (Aubinet et al., 2002).

Methods that resolve surface flux in time and frequency do not require stationarity. Continuous Wavelet Transform (CWT) (Torrence and Compo, 1998) and Discrete Wavelet Transform (DWT) (Mallat, 1989) are two of these methods that decompose a signal in time and per scale (Farge, 1992; Farge and Schneider, 2001). These methods are sought in airborne campaigns when short-time resolution is needed (Strunin and Hiyama, 2004; Mauder et al., 2007; Desjardins et al., 2018; Metzger et al., 2013) and to retrieve outbursts and non-stationary flux (Schaller et al., 2017; Göckede et al., 2019). By not requiring stationarity, they yield high-quality data with fewer gaps, hence, more available data for analysis to feed gap-filling algorithms and further partitioning.

EC measurements provide the net turbulent surface flux, which is often the primary information we are interested in. However, often enough, we need to partition CO_2 flux (Net Ecosystem Exchange, NEE) into gross primary productivity (GPP) and ecosystem respiration (R_{eco}). The need comes because they are modelled in surface models, which we desire to calibrate under varying environmental forcing variables, mainly temperature, radiation, soil and air humidity (Duffy et al., 2021).

Standard methods for NEE partitioning involve using photosynthetically non-active periods to estimate R_{eco} and further extrapolate it (night-time method) or use a light-response model for GPP (day-time method) (Reichstein et al., 2012). Alternative partitioning methods involve filtering raw EC data based on the correlation sign between CO_2 and H_2O mixing ratios before calculating

the eddy covariance (Thomas et al., 2008; Scanlon and Kustas, 2010; Klosterhalfen et al., 2019; Zahn et al., 2022). These methods are called conditional sampling. The Thomas et al. (2008) method assumes that, during the daytime, CO_2 and H_2O ecosystem fluxes have opposite signs when a parcel of air is coming from the plant crown, which is dominated by photosynthesis and has similar signs when air is coming from the ground where respiration dominates. This method has been developed and evaluated over a range of canopies and showed an excellent ability to separate plants (net primary production, NPP) from soil sources (soil respiration R_{soil}) (Zeeman et al., 2013; Zahn et al., 2022). A similar method was developed by (Scanlon and Albertson, 2001 Scanlon and Sahu, 2008; Scanlon and Kustas, 2010), which uses the same concept and additional considerations on correlations between H_2O and CO_2 to partition between stomatal and non-stomatal CO_2 and H_2O fluxes. This method also showed consistent H_2O and CO_2 partitioned fluxes (Scanlon and Kustas, 2012; Sulman et al., 2016; Wang et al., 2016; Perez-Priego et al., 2018; Rana et al., 2018; Scanlon et al., 2019). A comparison between Thomas et al. (2008) and Scanlon and Kustas (2010) (Klosterhalfen et al., 2019) showed that the latter provided overall larger soil flux components than the former.

This study presents a wavelet-based framework for turbulent flux calculation. It also proposes a new partitioning method inspired by the conditional sampling concept but uses frequency-resolved fluxes to provide GPP and R_{eco}. We first evaluate how many gaps are generated by each flux computing method and how these impact half-hourly statistics, annual carbon cycles and standard partitioning. We then evaluate the new partitioning method by comparing it to the standard methods (Reichstein et al., 2005). We use CO_2 flux measured in two contrasted ecosystems ICOS sites in a single climatic region, with four years (2019-2022) from a deciduous mixed forest site (FR-Fon) and two years (2021-2022) from a crop site (FR-Gri).

4.3 Material and methods

In this work, we processed EC data from two ICOS sites. Both sites were treated equally and passed the same steps (Figure 4.1).

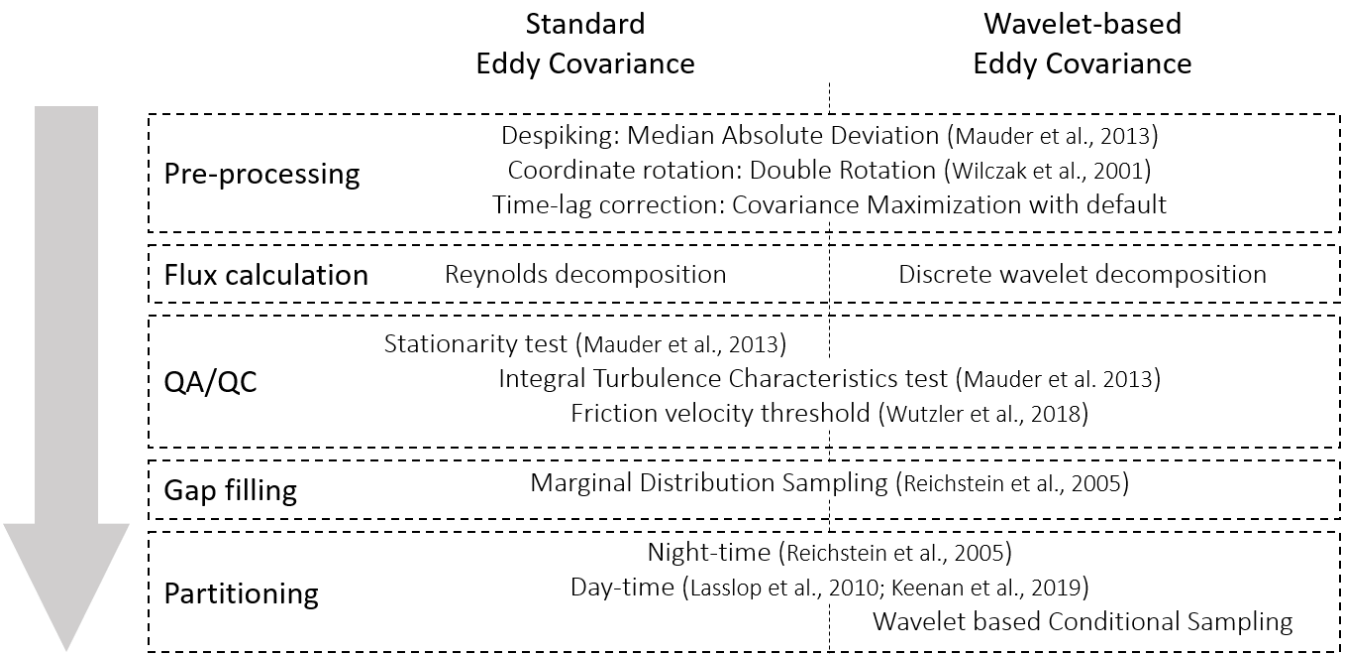

Figure 4.1. Processing steps in standard and wavelet-based Eddy Covariance in this work.

4.3.1 Site description

The study uses data from two French sites in the Parisian region and part of the ICOS network (https://www.icos-cp.eu) and FLUXNET. Climatically, the area can be described as oceanic with mild temperatures (11.2-11.5°C annual mean) and moderately wet (677-700 mm annual precipitation).

The first site, FR-Gri, is a 19-hectare crop site (Loubet et al., 2011), rotating between maize, wheat, barley, and rapeseed with intermediate crops. The measuring system is set up on a short tower that moves from 2 to 4 meters according to the crop growth. We used data from January 2021 to December 2022, consisting of winter rapeseed until 31 July 2021, winter wheat from 7 October 2021 to 5 July 2022, and barley seeded on 11 October 2022. The second site, FR-Fon, is a deciduous broadleaf mixed forest mainly composed of oak and a dominant height of 25 meters at the age of 100 (Delpierre et al., 2016). The eddy covariance setup is located at 37 meters. From this site, we used data from January 2019 to December 2022.

In both sites, the Eddy Covariance setup consisted of a closed-path infrared gas analyzer (LI-7200; Li-Cor Inc., Lincoln, NE, USA) and a three-dimensional sonic anemometer (Gill HS; Gill Instruments Ltd, Lymington, Hampshire, UK). Both instruments and acquisition setups followed ICOS guidelines and protocols (Sabbatini et al., 2018).

4.3.2 EC flux processing

To compute the atmosphere-biosphere flux, we consider a virtual rectangle box extending from the ground to the location of the eddy-covariance setup of width W, length L and height h_m. The mass balance of a scalar in the virtual box is used to retrieve the expression of the overall

ecosystem flux F_{eco} (g m^{-2} s^{-1}). The mass balance includes a storage term (I), an advection transport term (II) and a turbulent diffusion term (III), which, when integrated over the three dimensions of the virtual box, equals (Foken et al., 2012; Metzger, 2018; Aubinet et al., 2005; van Gorsel et al., 2009):

$$0 = \int_{-L}^{L}\int_{-W}^{W}\int_{0}^{h_m}\left[-S + \underbrace{\overline{\rho_d}\frac{\partial\overline{\chi_s}}{\partial t}}_{I} + \underbrace{\overline{\rho_d u}\frac{\partial\overline{\chi_s}}{\partial x} + \overline{\rho_d v}\frac{\partial\overline{\chi_s}}{\partial y} + \overline{\rho_d w}\frac{\partial\overline{\chi_s}}{\partial z}}_{II} + \underbrace{\frac{\partial\overline{\rho_d}\,\overline{u'\chi'_s}}{\partial x} + \frac{\partial\overline{\rho_d}\,\overline{v'\chi'_s}}{\partial y} + \frac{\partial\overline{\rho_d}\,\overline{w'\chi'_s}}{\partial z}}_{III}\right] dz\,dx\,dy \quad (4.1)$$

Where S is the ecosystem volumetric flux (g m^{-3} s^{-1}), ρ_d the dry air density, χ_s the scalar dry mole fraction (mol mol^{-1}), t the time (s), while u, v and w are the upwind, crosswind and vertical component of the windspeed (m s^{-1}). Overbars indicate time averaging; quotation marks the instantaneous deviation from the mean. Assuming a horizontally homogeneous ecosystem (homogeneity in ecosystem functioning and structure over x and y) allows suppressing the horizontal derivatives and integrals in eq. (1) (Finnigan et al., 2003; Metzger, 2018). This assumption also leads to a zero dry air vertical flux due to continuity $\overline{\rho_d w} = 0$ (Webb et al., 1980). Then, recognising that the integral of S over the height z is $F_{eco} - F_{soil}$ and that, similarly, the integral of $\frac{\partial\overline{\rho_d}\,\overline{w'\chi'_s}}{\partial z}$ over z is $\overline{\rho_d}\,\overline{w'\chi'_s} - F_{soil}$, eq. (1) leads to:

$$F_{eco} = \overline{\rho_d}.\left(\int_0^{h_m}\frac{\partial\overline{\chi_s}}{\partial t}dz + \overline{w'\chi_s{}'}\right) \quad (4.2)$$

Where $\overline{w'\chi'_s}$ is the turbulent flux at h_m. The ecosystem flux can hence be evaluated from $\overline{w'\chi_s{}'}$ and the storage term ($\int_0^{h_m}\frac{\partial\overline{\chi_s}}{\partial t}dz$), which may be significant in medium and tall towers but can be neglected in small ones. In practice, $\overline{w'\chi_s{}'}$ is computed from a time series of w and χ_s and sampled at a frequency typically higher than 5 Hz to capture the smallest eddies contributing to the flux (Gu et al., 2012).

In this study, we use three methods to evaluate $\overline{w'\chi_s{}'}$: the standard eddy covariance method (EC_S), and two frequency resolved methods, one using a Continuous Wavelet Transform (CW-EC) and the other using a Discrete Wavelet Transform (DW-EC).

From w and χ_s, the standard method consists of calculating the product of the instantaneous deviations of both variables from their respective means (covariance); frequency-resolved methods work the same, using, however, a priory decomposed instantaneous deviation (Figure 3.2).

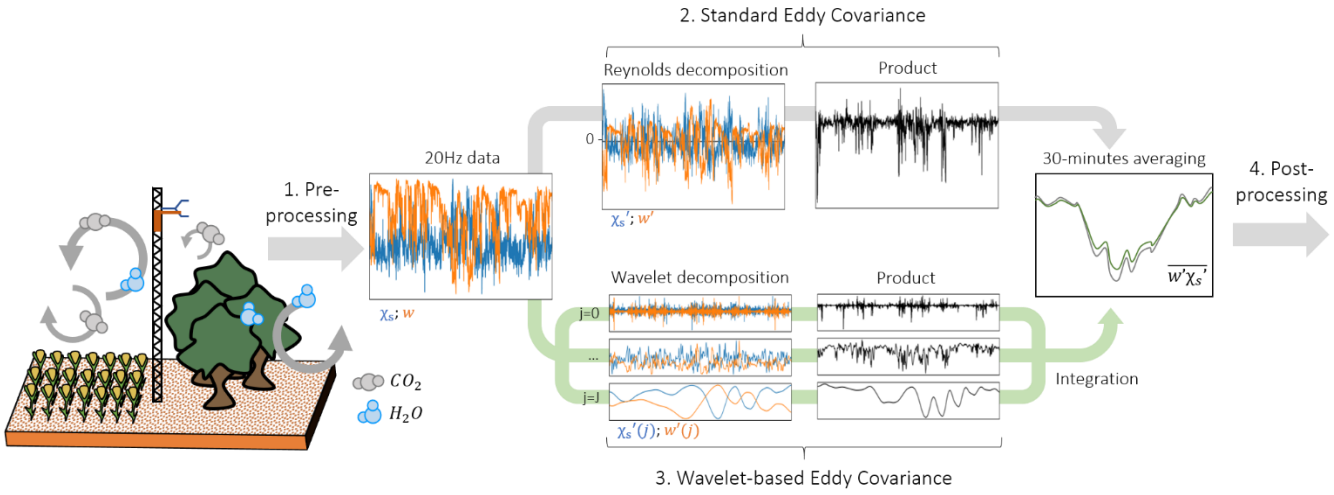

Figure 4.2: Conceptual scheme showing the main processing steps: data pre-processing (1); covariance calculation consisting of Reynolds decomposition and product of instantaneous deviation (2) and using frequency decomposition (3); post-processing (4). w is the vertical component of the wind velocity, χ is the mixing ratio, j represents the frequency scale, bars are for averaging and quotation marks are deviations from the mean.

Data pre-processing

In this study, data flux pre-processing was done using EddyPro 7.0.9. For all flux calculations, we applied de-spiking (Mauder et al., 2013), covariance maximization for time lag correction, and double rotation for tilt correction (Wilczak et al., 2001). The time lag default was set to 0.08 s for a 71.1 cm tube with a 5.3 mm inner diameter and 15 L/min flow rate, and it was allowed to vary in its vicinity. Using closed path systems and dry mixing ratios for gas avoids compensating for density fluctuations (Kowalski and Serrano-Ortiz, 2007). No detrending was applied. Standard flux calculations require further corrections to address low and high-frequency losses (Massman and Lee, 2002). These spectral corrections are usually applied after flux calculation. Here, for simplicity's sake and since we are focusing on comparing the flux calculation, gap filling and partitioning methods rather than interpreting the fluxes themselves, these corrections were omitted.

Standard Eddy covariance (EC_S)

The eddy covariance method consists of calculating the covariance $\overline{w'\chi_s'}$ (step 2 in Figure 3.2). Typically, the time average for fluxes is 30 minutes to 1 hour (Rebmann et al., 2018; Pastorello et al., 2020; Aubinet et al., 1999). Turbulent fluctuations χ_s' and w' are formally defined as deviations from an ensemble average and not from a time average. The ergodic assumption is required to make the ensemble and time average equivalent. In sum, the averaging period should thus be stationary and sufficiently long to gather enough data to get a low random error (Lumley and Panofsky, 1964; Kaimal and Finnigan, 1994). In general, a 30-minute period satisfies these requirements.

Wavelet Transform methods

Wavelet transform is a bandpass filter allowing the decomposition of a time series into sub-series defined for a given frequency. The following steps explain how to perform a frequency-resolved covariance using wavelets (Figure 3.2, panel 3). More details can be found in (Farge, 1992; Torrence and Compo, 1998; Farge and Schneider, 2001).

Any signal *f*(*t*) can be decomposed into different scales, which results in the signal itself once added up. The simplest example is the Reynolds decomposition that separates a time series into its mean and its instantaneous deviation:

$$f(t) = f'(t) + \overline{f(t)} \tag{4.3}$$

In Eq. 3, the mean, $\overline{f(t)}$, is the low-frequency component, with a frequency representative of 1/T, where T is the averaging period. Similarly, a time series can be decomposed into *J* sub-series, each representative of a frequency *j*:

$$f(t) = \sum_{j=0}^{J} f(t,j) \tag{4.4}$$

The wavelet transform is a way to decompose the signal using a mother wavelet ψ, a wave function with finite support (Eq. 5). Unlike removing an average, wavelet transform yields stationary sub-series (Torrence and Compo, 1998). Considering N discrete observations with a sampling period δ_t, so that $t = n\ \delta_t$ where *n* is the time index, we can generate a family of wavelets normalized in L^2-norm:

$$\psi_{n,j}(n') = s_j^{-1/2}\psi\left[\frac{(n'-n)\delta_t}{s_j}\right] \tag{4.5}$$

Where s_j is the scaling factor, usually defined using a geometric progression with a maximum limited by the total sampling period $N\delta t$: $s_j = s_0 2^{j\delta_j}$, for $j = 0,1, \ldots J$. Here, *J* is the size of the set of scales, s_0 is the smallest resolvable scale, approximately $2\delta t$, and δj is the scale factor. The convolution of the signal $f(n)$ with a scaled mother wavelet ψ, yields the $\tilde{f}(n,j)$, the wavelet coefficient for time series $f(n)$:

$$\tilde{f}(n,j) = \sum_{n'=0}^{N-1} f(n')\psi_{n,j}(n') \tag{4.6}$$

From which one can reconstruct the signal:

$$f(n) = \frac{\delta j \delta t^{0.5}}{C_\delta \psi_0(0)} \sum_{j=0}^{\infty} \Re\{\tilde{f}(n,j)\} \quad (4.7)$$

C_δ is a scale-independent reconstruction factor depending on the chosen mother wavelet function. Note that $f(n)$ is the sum of all its components; however, at any specific frequency, the wavelet transform works such that the decomposed signal $f(n,j)$ averages to zero and should be interpreted as its instantaneous deviation. Note that C_δ is only required for continuous wavelet decompositions in which the wavelet function is not an orthogonal base. Although this allows an arbitrary set of scales to be chosen, providing a more resolved signal spectrum (Arts and van den Broek, 2022; Torrence and Compo, 1998), a correction factor C_δ is required to compensate for these overlaps, not required in discrete wavelet decomposition. Applying equations 4.5 and 4.6 to w and χ_s we can calculate the total flux as follows:

$$F_c = \overline{\rho_d}\overline{w'\chi_s'} = \overline{\rho_d} C_\varphi \sum_j \overline{w'\chi_s'}(j) \quad (4.8)$$

Where $\overline{w'\chi_s'}(j)$ is the mean of the product between w and χ_s decomposed signals at frequency j (frequency-resolved covariance), C_φ is the reconstruction factor depending on the chosen mother wavelet function and determined empirically by comparing $\overline{w'\chi_s'}(j)$ *to* $\overline{w'\chi_s'}$, where averaging is done over the time index n. When continuous wavelet decomposition is used since it is not an orthogonal base, the sum of the $\overline{w'\chi_s'}(j)$ for all j is not strictly equal to $\overline{w'\chi_s'}$ as cross-correlations between scales are not zero. The empirical factor C_φ is used to correct for this effect (see Supp. Mat. A). When discrete decomposition is used, C_φ = 1, since the orthogonality of the wavelet functions, which characterizes DWT, implies that total energy is conserved and yields independent frequencies; hence, cross-correlations between scales are zero. The orthogonal base also forces the set of scales to be discrete, $\delta_j = 1$ and $s_j = 2^j$, for $j = 0,1, \ldots J$ (Farge, 1992). The wavelet coefficients are then:

$$\psi_{n,j}(n') = 2^{j/2}\psi\left(2^j n' - n\right) \quad (4.9)$$

A great interest in the DWT is that the orthogonality and progressively smaller decomposition make it far cheaper computationally than CWT at the expense of a coarser resolution in frequency (Mallat, 1989), making it a good candidate for time series longer than a couple of weeks without significant difference (see Figure S 4.1 for a brief comparison).

Commonly used wavelet functions are the Morlet and the Mexican Hat for continuous decomposition, for they are well-defined in the frequency and time domain (Schaller et al., 2017), and the Daubechies 6 for the discrete decomposition (Table 3.1).

This study used the discrete decomposition and the Daubechies (k=6) wavelet (Daubechies, 1988). For comparisons with the standard eddy covariance method, we compute the covariance by summing scales s_j smaller than 1800 seconds (30 min) in eq. (4.8). Calculations were done using

the *PyWavelets* module (Lee et al., 2019). Despiking (Mauder et al., 2013) was used in each sub-series to eliminate any unrealistic values identified.

Cone of influence

Wavelet coefficients calculated with the convolution product in eq. (6) are subject to the influence of neighbours, resulting in a time "influence cone" that grows with decreasing frequency (Torrence and Compo, 1998). This cone renders the reconstruction unusable at the edges of the dataset and for scaling factors close to the dataset duration. The cone of influence (COI) is the boundary of the wavelet spectrum, which, exterior to its edge, effects become important. It is defined as:

$$COI = f\ \delta t\ n\ , n = 0, 1, \dots, N-1, N, N+1, \dots, 1, 0 \qquad (4.10)$$

f is the Fourier factor specific to each wavelet.

We extended the dataset over periods larger than the period of interest for every averaging time to avoid the cone of influence.

4.3.3 Timeseries flagging and gap-filling

Previous steps allowed us to calculate $\overline{w'c'}$. We must still verify the EC's assumptions through a quality check (Figure 4.1). Non-stationarity data for standard EC and periods lacking turbulence for both standard and wavelet-based EC are considered unreliable and thus flagged and further gap-filled.

Quality flags

Quality flags followed the standard 0-1-2 flag system used in FLUXNET (Mauder and Foken, 2011). The system is based on two tests, one for stationarity and another to verify that turbulence is fully developed (Foken and Wichura, 1996). It is important to recall that standard EC cannot be used during non-stationary moments, but wavelet decomposition yields stationary sub-series that allow skipping this step.

The stationarity test (STA) calculates the absolute relative deviation between the mean of the covariances computed over 5-min intervals and the covariance computed over a 30-min period:

$$STA = \left| \frac{\frac{1}{6}\sum_{i=1}^{6} \overline{(w'c')_i^{5-mn}} - \overline{(w'c')^{30-mn}}}{\overline{(w'c')^{30-mn}}} \right| \qquad (4.11)$$

The turbulence test, or integral turbulence characteristics (ITC) test, identifies if eddies are fully developed by calculating the absolute relative deviation between the measured and modelled integral turbulent characteristic σ_w/u_*. The model is calculated as

$$\left(\sigma_w/u_*\right)^{model} = \begin{cases} 0.21\, ln\left(\frac{z_+ f}{u_*}\right) + 3.1, & if\ -0.2 < z/L < 0.4 \\ 2\left(\frac{z}{L}\right)^{1/8}, & else \end{cases} \quad (4.12)$$

Where f is Coriolis parameter (s^{-1}), u_* friction velocity (m/s), z is the height (m), L Obukhov length (-), and z+ is set to 1 meter for a mathematical convention so that $\frac{z_+ f}{u_*}$ is dimensionless (Thomas and Foken, 2002).

$$ITC = \left| \frac{\left(\sigma_w/u_*\right)^{model} - \left(\sigma_w/u_*\right)^{measurement}}{\left(\sigma_w/u_*\right)^{measurement}} \right| \quad (4.13)$$

A detailed description of the quality control procedures can be found in Foken and Wichura (1996) and Mauder and Foken (2011). Data is considered high-quality when this deviation is below 30% for all applicable tests, as shown in Table 4.1.

Table 4.1: Quality flag categories proposed by Mauder and Foken (2011), based on stationarity and integral turbulence characteristics (ITC) tests presented by Foken and Wichura (1996).

Quality flag	Stationarity test (STA)	Integral turbulence characteristics test (ITC)
0 (High)	< 30 %	< 30 %
1 (Medium)	31 – 100 %	31 – 100 %
2 (Low)	> 100 %	> 100 %

u∗ filtering

Further screening is necessary to discard observations below a friction velocity threshold ($u*_{crit}$) (Wutzler et al., 2018; Papale et al., 2006). Under stable stratified atmospheric conditions, the EC technique has been shown to underestimate nocturnal CO_2 respiration (Goulden et al., 1996; Baldocchi, 2003). The reason is that the turbulence is attenuated by the positive air density gradient (Kaimal and Finnigan, 1994). As biotic flux is not expected to depend on turbulence, we can define a threshold value for friction velocity ($u*_{crit}$) below which the measured ecosystem CO_2 flux starts to decrease. Below $u*_{crit}$ turbulence is not developed enough to mix the surface layer and the EC to perform well. This method provides an alternative way to determine the turbulent requirement based on an ecosystem function instead of using a physical-based one, as with ITC.

Once a threshold is defined, observations below this threshold are dropped and gap-filled (Gu et al., 2005; Aubinet et al., 2012). The u_* threshold was determined using the *REddyProc* library in R and was free to vary among seasons (Wutzler et al., 2018).

Gap-filling

Gap-filling was performed on data flagged for medium (1) and low (2) quality or below u*crit for EC_S (stationary and turbulence flag considered) and DW-EC (only turbulence flag considered).

We used the Marginal Distribution Sampling (MDS) method, the most commonly used gap-filling method (Pastorello et al., 2020). MDS consists of sampling data in the temporal vicinity of the data to be gap filled, usually a 15-day window, with similar meteorological conditions defined by the income shortwave, the air temperature, and the vapour pressure deficit. This subset yields a distribution function used to fill the gap, exploiting both the meteorological drivers and the temporal auto-correlation structure of NEE (Reichstein et al., 2005). For the calculations, we used the *REddyProc* library in R (Wutzler et al., 2018).

4.3.4 NEE partitioning

Flux partitioning refers to the division of the Net Ecosystem Exchange (NEE) into the ecosystem respiration (R_{eco}) and the gross primary productivity (GPP). Ecosystem respiration refers to the release of CO_2 by organisms during their metabolic activities, including autotrophic respiration by plants and heterotrophic respiration by micro- and macro-organisms in soil and the ecosystem. GPP represents the uptake of CO_2 by plants through photosynthesis:

$$NEE = GPP + R_{eco} \tag{4.14}$$

GPP is a flux directed from the atmosphere to the ground (negative), while R_{eco} is from the ground to the atmosphere (positive). In standard practice, partitioning relies on the presumed responses of GPP and Reco to light, water, and temperature. We applied the known night- and day-time methods on both standard and wavelet-based CO2 fluxes and proposed a new method for the wavelet-based flux here.

Night-time partitioning method

Night-time (NT) partitioning assumes that GPP is zero at night, so NEE equals R_{eco} (Reichstein et al., 2005). Reference respiration rate is then parametrized using an Arrhenius-type temperature response model for nocturnal measurements and projected into the day (Lloyd and Taylor, 1994).

$$R_{eco} = R_{ref} . e^{E_0\left(\frac{1}{T_{ref}-T_0}-\frac{1}{T_{air}-T_0}\right)} \tag{4.15}$$

Where R_{ref} (μmol·m−2·s−1) is the reference respiration rate at the reference temperature (T_{ref} = 15ºC), T_{air} is air temperature, T_0 is fixed at −46.02°C, E_0 (°C) is the temperature sensitivity, a free parameter. A constant value is estimated for E_0 for the whole year, while R_{ref} is estimated every five days using a 15-day window (Reichstein et al., 2005).

Further references to NT estimations use the terms NT-GPP and NT-R_{eco}. The R code implementation for NT is available to download from https://github.com/bgctw/REddyProc (Wutzler et al., 2018).

Day-time partitioning method

Day-time (DT) partitioning differs from NT in that a light response curve (Lasslop et al., 2010) is parametrized using day-time measurements. NEE is estimated as follows:

$$NEE = \frac{\alpha\beta R_g}{\alpha R_g + \beta} + R_{eco} \quad (4.16)$$

Where R_{eco} is a respiration model eq. (4.15), R_g is the global radiation (Wm−2), α (μmol·C·J−1) is the initial slope of the light response curve, and β (μmol·m−2·s−1) is the maximum rate of CO_2 uptake of the canopy at light saturation. β is estimated using an exponentially decreasing function of atmospheric vapour pressure deficit of air (VPD):

$$\beta = \begin{cases} \beta_0 e^{-k(VPD-VPD_0)}, & VPD > VPD_0 \\ \beta_0, & VPD < VPD_0 \end{cases} \quad (4.17)$$

Note that what is physiologically more relevant in β is the leaf-to-air VPD, which can vary from atmospheric VPD in the same direction as leaf temperatures vary from air temperature. However, flux sites measure atmospheric rather than leaf-to-air VPD.

The standard calibration procedure is done in two steps. First, E_0 and R_{ref} are estimated using night-time observations. The remaining parameters (α, β_0, k, and VPD_0) and R_{ref} (now using previous estimation as a prior) are fitted using Eq. (4.16) on day-time data.

Recent studies have proposed the inhibition of leaf respiration in the light as a source of mismatch between EC and independent R_{eco} measurements (Wehr et al., 2016). A modified version of standard partitioning has been proposed to include this mechanism (Keenan et al., 2019). The modified DT version preserves the structure of the original DT but uses R_{ref} prior, fitted during night-time, for nocturnal partitioning while estimating daytime as usual. The R code implementation for DT's original and modified versions can be downloaded from https://github.com/bgctw/REddyProc (Wutzler et al., 2018). Unless specified otherwise, DT estimations follow the modified version (Keenan et al., 2019) and are referred to as DT-GPP and DT-R_{eco}.

A new direct wavelet-based partitioning method

Direct observations of gross primary productivity (GPP) and ecosystem respiration (R_{eco}) are not feasible at the field scale, thus justifying the necessity of model-based partitioning. Thomas et al. (2008) and Scanlon and Kustas (2010) have proposed ingenious ways of incorporating prior knowledge of co-processes to compute a model-free partitioning of soil respiration (R_{soil}) and plant net primary productivity (NPP).

In this study, we take advantage of the frequency decomposition of $w'\chi_s'$ using wavelets to go beyond what Thomas et al. (2008) did; thus, discrete-wavelet-based conditional sampling (DW-CS). In an empirical approach, we conditionally sample the frequency-decomposed products

$w'(t,j) * \chi_s{}'(t,j)$ to separate positive and negative components of the CO_2 and H_2O fluxes in each frequency j. The underlying empirical assumption is that wavelet decomposition should allow the trapping of the positive and negative "gusts" in each frequency, which are mixed up in the original signal. For simplicity $w'\chi_s{}'(t,j)$ is replaced by φ_s in the following equations:

$$\varphi_c = \varphi_c^+ + \varphi_c^- = \varphi_c^+|\varphi_v^+ + \varphi_c^+|\varphi_v^- + \varphi_c^-|\varphi_v^+ + \varphi_c^-|\varphi_v^- \quad (4.18)$$

Where c and v stand for CO_2 and H_2O, x^+ stands for sampling x when x is positive and the opposite for x^-, and $x|y$ stands for sampling x when y is true. We could assume that positive CO_2 flux (φ_c^+) is R_{eco} and negative (φ_c^-) is GPP. However, to guarantee the physical meaning of GPP, we took advantage of GPP's dependency on light, more precisely, photosynthetic photon flux density (PPFD), and set GPP to zero during the night (PPFD ≤ 10 µmol m^{-2} s^{-1}). We further considered that the daytime (PPFD > 10 µmol m^{-2} s^{-1}) negative CO2 fluxes conditioned by negative water vapour fluxes ($\varphi_c^-|\varphi_v^-$) as non-realistic and therefore attributed it equally to R_{eco} and GPP (see Figure 3.3), which leads to the following definition of R_{eco} and GPP:

$$PPFD \leq 10\ \mu mol\ m^{-2}\ s^{-1} \begin{cases} Reco = \varphi_c^+ + \varphi_c^- \\ GPP = 0 \end{cases}$$
$$PPFD > 10\ \mu mol\ m^{-2}\ s^{-1} \begin{cases} Reco = \varphi_c^+ + 0.5 \times \varphi_c^-|\varphi_v^- \\ GPP = \varphi_c^-|\varphi_v^+ + 0.5 \times \varphi_c^-|\varphi_v^- \end{cases} \quad (4.19)$$

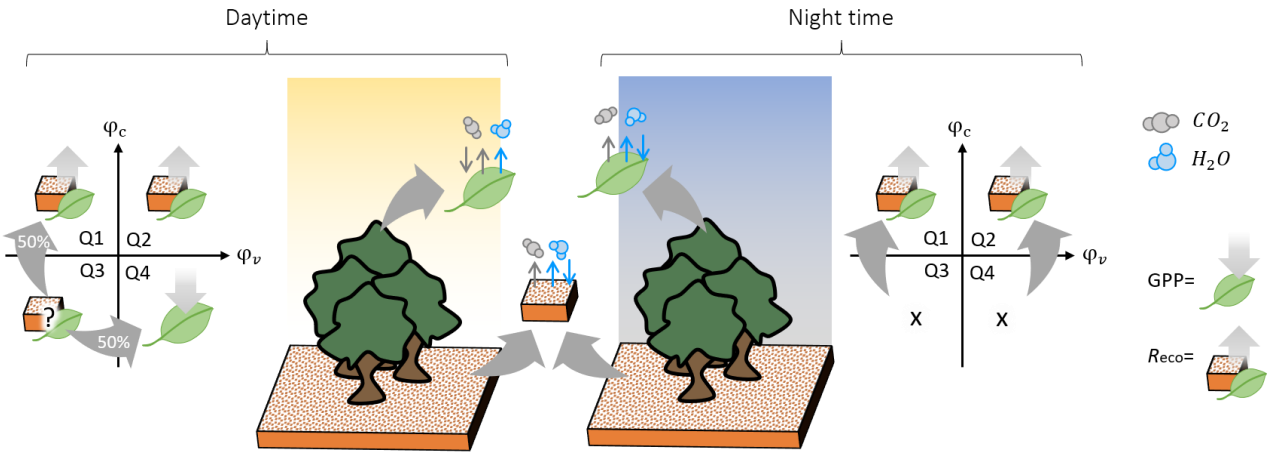

Figure 4.3: Conceptual scheme for wavelet-based NEE flux partitioning. $\boldsymbol{\varphi_c}$ stands for $\boldsymbol{w'\chi_{CO_2}{}'(t,j)}$ and $\boldsymbol{\varphi_v}$ for $\boldsymbol{w'\chi_{H_2O}{}'(t,j)}$. Quadrants and arrows in the figure show conceivable fluxes during day and night. In quadrants, grey arrows show reallocation from unlikable (question mark) and unreasonable ("x") fluxes towards the most probable actual flux.

4.3.5 Performance measurements

Comparisons between methods were carried out using mean bias and the annual gap-filled CO2 flux balance error. Defined as:

$$Mean\ Error\ (bias) = \frac{1}{N}\sum_{n=1}^{N}(NEE_{x,n} - NEE_{y,n}) \quad (4.20)$$

$$Mean\ Absolute\ Error = \frac{1}{N}\sum_{n=1}^{N}\left|NEE_{x,n} - NEE_{y,n}\right| \quad (4.21)$$

Where *N* equals the amount of data, $NEE_{x,n}$ is the Net Ecosystem Exchange calculated using one of the *x* methods among EC_S and DW-EC at a time *n*.

4.4 Results

4.4.1 CO_2 flux computed by EC and DW-EC

In this section, we compare the CO_2 flux (or NEE) computed by EC_S and DW-EC and then analyse the additional information on DW-EC's co-spectra. During the photosynthetically active months (warmer months for FR-Fon and crop seasons for FR-Gri), the two sites were carbon sinks with a negative NEE (Figure 4.4). During winter, when the trees have lost their leaves and crop sites are bare soil, the lack of GPP transforms sites into sources with a positive NEE. As a consequence, NEE in FR-Fon showed a clear seasonality, while FR-Gri showed a more variable pattern. We observe a substantial decrease in absolute value in the NEE for short periods during summers and springs for all years. Some relate to cloudy days, others to high vapour pressure deficit, which indicates air dryness. In June and July 2019, France was hit by short heat waves (Sousa et al., 2020; Pohl et al., 2023). In the crop site (FR-Gri), we identify the crop season in the spring of both years and the intercrop in Autumn 2021 by the decrease in NEE. We can also notice that harvest is done long after NEE has become positive; this is to bring the crop to maturity after senescence. Finally, the crop site also showed an earlier growth compared to the forest site, which is expected as the trees at this site are 100 years old on average and have, therefore, a late foliar development during the year while the crops were winter crops, which are in their growth stage early during the year.

Overall, the NEE ranged from −10 to 6 µmol m−2 s−1, with stronger respiration during winter and spring at the crop site compared to the forest site. Daily mean NEE estimated by EC_S and DW-EC were very close to each other (R^2= 0.97 (0.98), ME= 0.1 (0.05) µmol m-2 s-1, MAE= 0.33 (0.38) µmol m-2 s-1, ECS=1.08 (1.12) ×DW linear fit for FR-Fon (FR-Gri)).

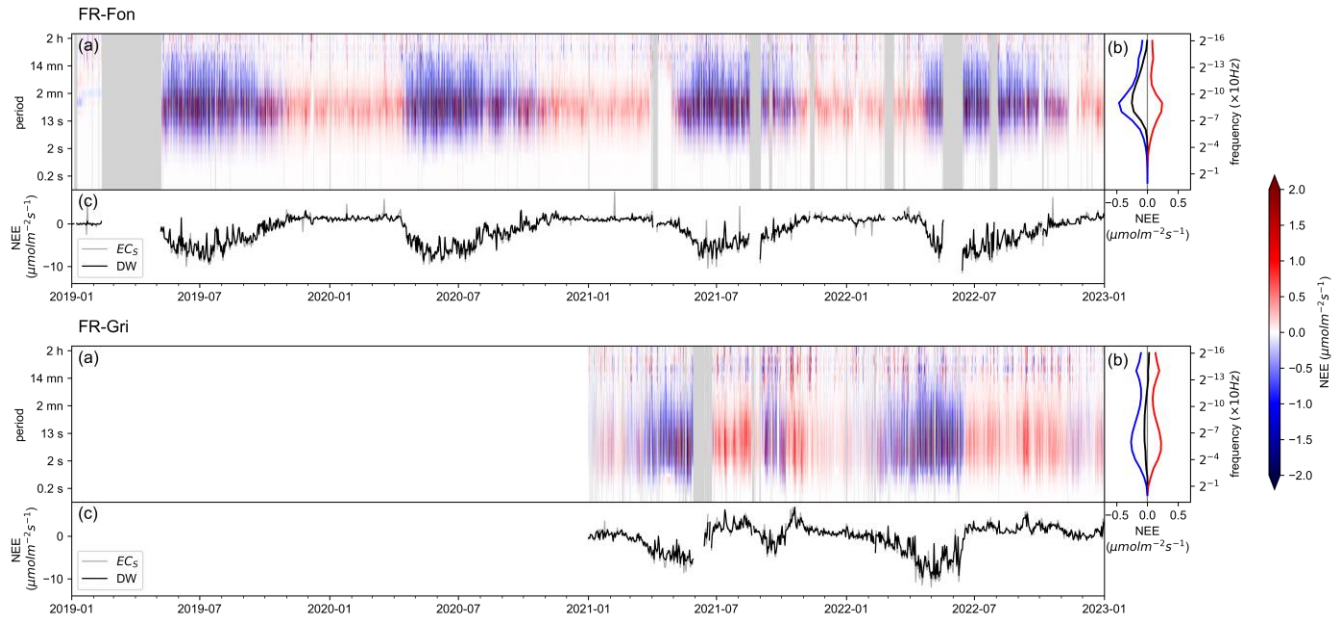

Figure 4.4: (a) NEE co-spectra derived by DW-EC and averaged half-hourly. Colours indicate NEE co-spectra and grey for missing data. (b) Average for NEE co-spectra (black), exclusively negative (blue) and positive (red) values of NEE. (c) The daily average NEE computed from the NEE co-spectra was integrated up 5.5e^{-4}Hz (30 minutes) (black, DW) and EC_S (grey).

Looking at NEE's co-spectra, we can see a peak of around 6 seconds ($0.16\ Hz$) frequency in FR-Gri and around 50 seconds ($0.02\ Hz$) in FR-Fon (Figure 4.4 b). The peak frequency is related to the measurement height, being higher on the 2 to 4-meter tower in FR-Gri than on the 37-meter tower FR-Fon (around 10 meters above the canopy). The measurement height affects the frequency contribution to the CO_2 flux because the height above ground constrains the size of the eddies. Indeed, the maximum co-spectral frequency is linearly dependent on height and modulated by the wind speed and the stability parameter z/L, where L is the Obukhov length (Kaimal and Finnigan, 1994). Indeed, the co-spectra calculated using equations in (Horst, 1997) peaks at the same 50 seconds (6 seconds) frequency for FR-Fon (FR-Gri). A secondary maximum of around 30 minutes can be seen in the positive and negative NEE co-spectra but disappears on the NEE. The co-spectra of NEE's positive (φ_c^+) and negative (φ_c^-) counterparts were overall mirrored with, however, slight differences: a higher contribution of higher frequencies on φ_c^+ and of lower frequencies on φ_c^- in FR-Fon, suggesting large coherent structures may contribute more to GPP (defined mainly by φ_c^-) than R_{eco} on average. This scale difference was not observed at the crop site.

Seasonally, NEE (φ_c) co-spectra aligned with theoretical estimations, displaying peaks near the expected frequencies (Figure S 4.3). During months with high carbon sequestration (from April to October in FR-Fon and February to June in FR-Gri) and under neutral or unstable stratification, the negative (φc-) portion of co-spectra exhibited lower-frequency peaks compared to the positive (φc+) portion. Conversely, stable conditions prompted the opposite pattern, albeit less pronounced in the crop site due to an unexpected secondary peak around 30 minutes, which softens the distribution on the higher frequencies. This secondary peak became most evident from

June (stable) and July (neutral and unstable) through November, coinciding with the post-harvest period after the primary crop cycle and before Winter sets in. No similar seasonality was seen in the theoretical co-spectra, which considers micrometeorology conditions.

Still looking at raw data, both methods show a clear daily and seasonal pattern for NEE expected for these ecosystems (Figure 4.5). Indeed, half-hourly DW- and EC_S-NEE were very close to each other (R^2= 0.98, Bias=0.14 µmol m−2 s−1, MAE=0.58 µmol m−2 s−1, ECs=1.08×DW linear fit, sites combined) when both were high-quality data, deteriorating when moving to medium and low-quality data (Figure S 4.2). In the forest site, during March and April, we can see peaks in the ECS-NEE 5th and 95th percentiles, which are lower in DW. These two months had the highest non-stationarity in the site, yielding 60% of the observations unreliable. The same ECS-NEE peaks are seen for the crop site but are less closely related to the stationarity flag. They could be related to night-time CO_2 spikes due to advection from the nearby animal barns (around 600 m west).

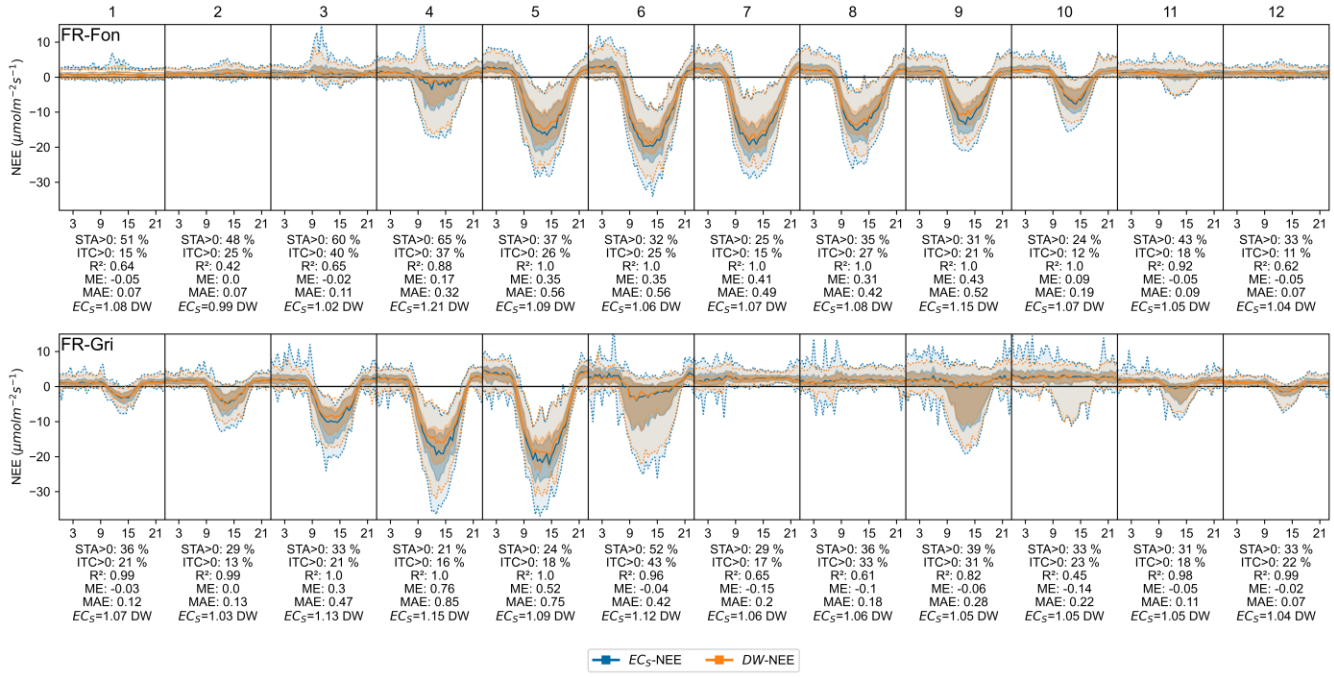

Figure 4.5. Half-hourly NEE estimated monthly using EC_S (blue) and DW (orange). The darker region indicates interquartile (25th and 75th percentile), and the lighter region with dotted lines indicates the 5th and 95th percentile. Below the curves, the monthly statistics are shown: the percentage of non-stationarity (STA>0) and low turbulence (ITC>0) data, the correlation coefficient (R^2), the mean error (ME, µmol m−2 s−1), the mean absolute error (MAE, µmol m−2 s−1) and the linear fit.

4.4.2 Effects of flux processing method on data coverage

In this section, we analyse the effect of flux processing methods on the number of data gaps. The quality control steps related to turbulence, namely the Integral Turbulence Characteristic (ITC) test and friction velocity threshold (u∗crit), unsurprisingly discarded the most during the night (Rg < 10 Wm^2) on both the forest (FR-Fon) and the crop site (FR-Gri) (Table 4.2). This higher nocturnal discard is expected since the surface cools during these periods, creating a stable layer near the surface and preventing turbulent mixing. $u*_{crit}$ impacted more DW-EC than EC_S because $u*_{crit}$ is

calculated at the end of the quality control; thus, for EC_S, all periods with co-occurrence between non-stationarity and low u∗ (u∗< $u*_{crit}$) had already been dropped.

The non-stationarity test flagged a significant amount of data during the day and night. However, considering the co-occurrence between flags, it impacted more day-time observations when turbulence is usually well-developed. The difference in the total amount of discarded data between methods reflects this. During night time, EC_S discarded around 17 % more than DW-EC and 20 to 30 % more during day-time (Table 4.2).

*Table 4.2: Cumulative percentages of discarded data at each quality control step for the CO_2 flux at the two sites. Medium and low-quality data are replaced. Symbol * means less than 1%.*

Quality control step	FR-Gri (2021-22)		FR-Fon (2019-22)	
	Night	Day	Night	Day
Missing data	5 %	5 %	10 %	10 %
Turbulence not fully developed (ITC medium or low)	28 %	14 %	17 %	6 %
Discrete Wavelet Transform (DW-EC)				
Friction velocity threshold ($u*_{crit}$ = 5^{th}/50^{th}/95^{th} percentile)	10 / 18 / 28 %	1 / 2 / 5 %	12 / 20 / 30 %	2 / 5 / 10 %
Total	**49 %**	**20 %**	**42 %**	**19 %**
Standard (EC_S)				
Non-stationarity (STA medium or low)	19 %	20 %	23 %	30 %
Friction velocity threshold ($u*_{crit}$ = 5^{th}/50^{th}/95^{th} percentile)	6 / 13 / 21 %	* / * / 3 %	5 / 11 / 19 %	* / 2 / 6 %
Total	**66 %**	**40 %**	**60 %**	**48 %**
Difference between DW-EC and EC_S	**17%**	**20%**	**18%**	**29%**

When looking at the length of the gaps (Table 4.3), we found a decrease in all gap lengths when using DW-EC compared to EC. With more observations and narrower gaps, we expect that the DW-EC method would improve the accuracy of any commonly used gap-filling methods (Moffat et al., 2007), improving the annual NEE accuracy.

Table 4.3: Occurrence of gaps by length for each site identified by EC and DW-EC. One occurrence is a period of 1 or many points of gap. In parentheses, the percentage of the data is concerned by the gap length over the total data length.

Gap length (record number)	FR-Gri		FR-Fon	
	EC_S	DW-EC	EC_S	DW-EC
1-2	2538 (9 %)	2084 (7 %)	5076 (9 %)	2192 (4 %)
3-5	592 (6 %)	424 (4 %)	1373 (7 %)	600 (3 %)
6 and above	711 (44 %)	535 (30 %)	1254 (40 %)	840 (29 %)

4.4.3 Effects of flux processing method on gap filling

In this section, NEE measurements using the standard EC (EC_S-NEE) were compared with the DW-EC (DW-NEE) method to assess the degree of their agreement, potential biases, and the reliability of the DW-EC method. Both methods were gap-filled using MDS; however, the gap-filling was performed on a different amount of data, as the quality control filtering shows, excluding more data in ECs than in DW (Table 4.2). Daily gap-filled DW- and EC_S-NEE agreed well (Figure 4.6.b), with only marginal differences from before gap-filling, suggesting gap-filling was unbiased over a day on these sites. Unexpectedly, gap-filled NEE in the forest site had an MAE 0.1 µmol m−2 s−1 higher than raw NEE. To understand the increase in MAE, we calculated the RMSE, which showed a decrease from 3.9 µmol m−2 s−1 (raw) to 1.9 µmol m−2 s−1 (gap-filled), suggesting MAE distribution got narrower, also confirmed by looking at the quartiles (not shown here). Despite these differences, MAE was the same magnitude on both sites as the mean random uncertainty (1.03 µmol m−2 s−1 in FR-Fon; 0.73 µmol m−2 s−1 in FR-Gri).

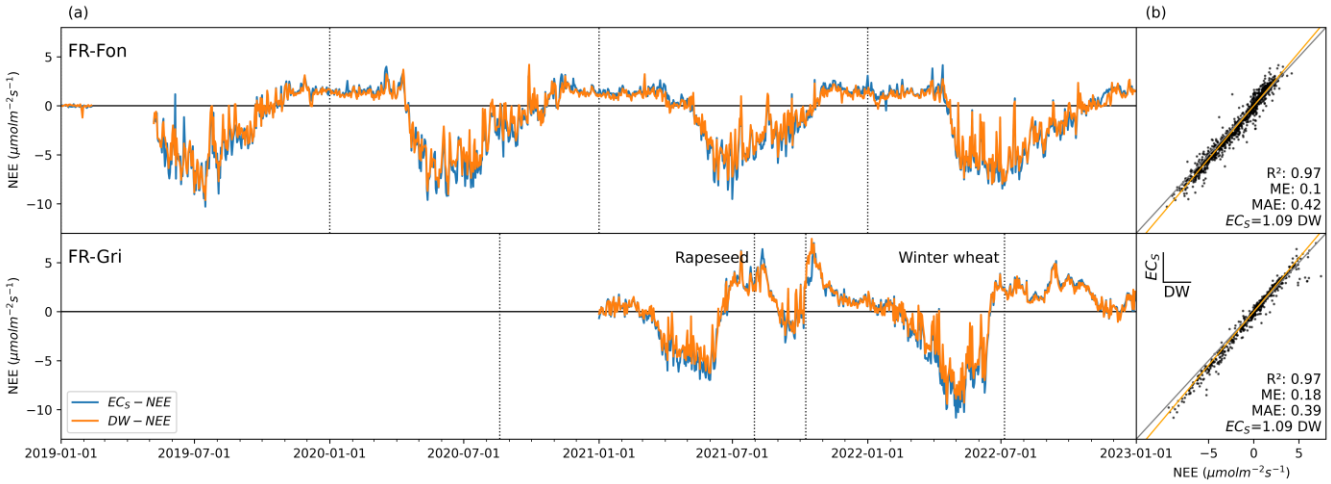

Figure 4.6. (a) Daily averaged NEE was calculated using EC_S (blue) and DW-EC (orange), both gap-filled with the MDS method. Dotted vertical lines show the start or end of the seasons (years for FR-Fon and crop season for FR-Gri). (b) Daily DW- and EC_S-NEE, in grey 1:1 line, in orange true linear relation. On the bottom, the correlation coefficient (R^2), the mean error (ME, µmol m−2 s−1), the mean absolute error (MAE, µmol m−2 s−1) and the linear fit.

Daily DW underestimated EC_S by 9 % and half-hourly by 4 % (8 %) in FR-Fon (FR-Gri). This underestimation is consistent with other flux studies using wavelets (Desjardins et al., 2018; Mauder et al., 2007; Metzger et al., 2013; Schaller et al., 2017), which found underestimations between 3% and 9%. Wavelet-based EC way of calculating instant deviation (*e.g.*, w' and CO_2') works as a low-frequency filter and detrends the signal instead of simply subtracting the mean as in standard EC. Detrending has been found to lead to an underestimation of around 2 % to 15 %, depending on the running mean filtering used (Rannik and Vesala, 1999), which would explain the observed underestimations.

To disentangle the differences due to gap-filling from those due to the flux computation, we gap-filled the DW-NEE with the DW gaps (DW as previously done) and with the gaps from EC_S (DW') (Figure S 4.9). The comparison between DW' and DW yields high correlation (R^2= 0.97 (0.98) for FR-Fon (FR-Gri)), small bias (ME=-0.01 (0.05) µmol m−2 s−1) and deviation (MAE=0.5 (0.2) µmol m−2 s−1). We can conclude that the gap-reduction effect was minor for these sites based on the small difference between DW (only discards underdeveloped turbulence) and DW' (discards underdeveloped turbulence and non-stationarity). Accounting for the non-stationary conditions would increase (decrease) the annual NEE by 0.01 (0.05) µmol m−2 s−1 or around 1 (2) % in FR-Fon (FR-Gri).

4.4.4 Effects of flux processing method on standard NEE partitioning

In this section, we examine whether the gaps in NEE obtained with EC_S- or DW-NEE impact the partitioning of NEE in GPP and R_{eco}. Half-hourly observations show that using EC_S- or DW-NEE yields similar GPP: R^2=0.94 (0.97), ME=-0.35 (0.4) µmol m−2 s−1, MAE= 1.0 (0.71) µmol m−2 s−1, ECS=1.07 (1.09)×DW, and similar R_{eco}: R^2=0.69 (0.74), ME=-0.24 (0.33) µmol m−2 s−1, MAE= 0.48 (0.85) µmol m−2 s−1, ECS=1.05 (1.05)×DW, for NT (DT) method (see daily mean statistics in Figure S 4.4). For all cases, DT yielded higher R^2 than NT; other statistics depended on the site and on which variable was considered (GPP or R_{eco}). For instance, NT yielded smaller ME and closer to 1 linear relation than DT in the forest site but the opposite in the crop site. R_{eco} estimations using the DT method on DW-NEE were higher than on EC_S (by 5 %), while the opposite is true for all the other cases.

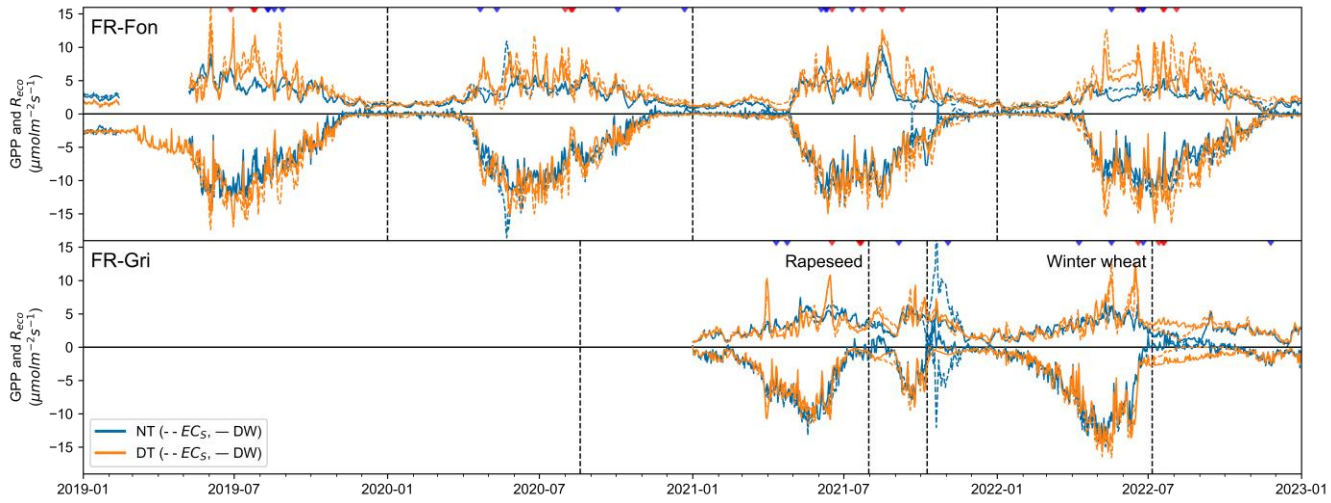

Figure 4.7. GPP and Reco daily average from January 2019 to December 2022 using night-time (blue) and day-time (orange) partitioning on EC_S (dashed) and DW-EC (solid). Note that positive values estimate R_{eco} and negative GPP. Dotted vertical lines do not influence the data; they assign the start or end of the season (years for FR-Fon forest and crop season for FR-Gri). Inverted triangles indicate daily temperature mean (red) or cumulated rain higher than the 99th percentile of that year.

We note that differences in DT and NT in FR-Fon in June 2022 happened during a several-week-long gap (see Figure 4.4) and should not be interpreted. While DT estimations show overall good agreement between EC_S and DW-EC, NT estimations using DW-NEE yield a smaller GPP and

R_{eco} than ECS in June 2020 (FR-Fon) and October 2021 (FR-Gri) (Figure 4.7). On both occasions, NT's R_{ref} parameter for EC_S was at its maximum (Figure S 4.5). At the end of October 2021, the FR-Gri intermediate crop was harvested, and some residues were left on the field. NT cannot distinguish the different carbon sources or calculate a single temperature response curve. The increase in R_{ref} increased R_{eco} exponentially with the warmer day-time temperatures, forcing a physically inconsistent positive GPP. Interestingly, NT estimations using DW-NEE were lower, and R_{ref} did seem to follow a smoother seasonal pattern (Figure S 4.5). In June 2020, a bias could emerge from moving from cloudy and rainy to sunny and warmer.

DT's light-response model avoids the positive GPP problem but produces more sensitive estimations to dynamic daytime conditions. Several occasions where DT estimations are higher than NT coincide with high day-time temperatures (Summer 2019, August 2021) or intense precipitations (June 2021).

4.4.5 Evaluation of the new wavelet-based method for direct flux partitioning

In this section, we compare the new DW-CS method with NT, and both were calculated using DW-NEE as the basis for comparing only the partitioning algorithm. NT was chosen as the reference method due to the relative complexity of interpreting DT's variance found in the previous section. However, the results would be similar to DT (see Figure S 4.6 for a comparison between all methods). Overall, the partitioning methods agreed well (Figure 4.8b) with a mean absolute daily error of 0.81 (0.65) µmol m^{-2} s^{-1} in FR-Fon (FR-Gri), lower than random uncertainty, 1.03 (0.73) µmol m^{-2} s^{-1} in FR-Fon (FR-Gri). Comparison between the DW-CS method using DW-NEE and NT method using EC_S-NEE (Figure S 4.6, sites combined) yields higher bias, absolute daily error, and an increase in the underestimation. This statistic worsens due to the differences between DW- and EC_S-NEE (see Figure 4.6).

Figure 4.8. (a) Daily averaged GPP and R_{eco} were calculated using standard night-time partitioning (NT, blue) and wavelet-based direct partitioning DW-CS (DW, orange), using DW-NEE as base data. Positive values show R_{eco}, and negative values show GPP. Dotted vertical lines show the start or end of the season (calendar years for forest site FR-Fon and cropping season for FR-Gri). (b) Daily NT versus DW GPP and R_{eco} (both on the same graph), in grey 1:1, in orange linear fit. On the bottom, statistics for GPP and R_{eco} combined the correlation

coefficient (R^2), the mean error (ME, µmol m−2 s−1), the mean absolute error (MAE, µmol m−2 s−1) and the linear fit.

In the forest site, differences between DW-CS and NT during Summer 2019 (particularly warm) and 2021 (particularly rainy) fall into periods with peak temperatures (June and July 2019, August 2021) or precipitation (August 2019, June 2021).

In the crop site, DW-CS Reco estimations were higher on a few occasions than NT, when NT estimated an erroneously positive GPP. In October 2021, this happened after the intermediate crop was harvested and herbicides were used, possibly generating a pulse in Reco that was captured by the direct partitioning method. On 26/07/2022, solid manure before barley seeding also generated erroneous positive GPP. In August 2021, a similar pulse was observed after crop harvesting.

Unsurprisingly, given the methods equation, half-hourly results showed different R_{eco} diel patterns between methods (Figure 4.9, DT included in Figure S 4.8). NT-R_{eco} increased smoothly with temperature; DW-CS- R_{eco} was flatter during the night, decreased during sunrise and sunset, and showed an inversed U-shape curve during the day. Depending on the developmental stage, the daytime R_{eco} can be larger (spring, peak season) or smaller (senescence, summer) than the night-time R_{eco}.

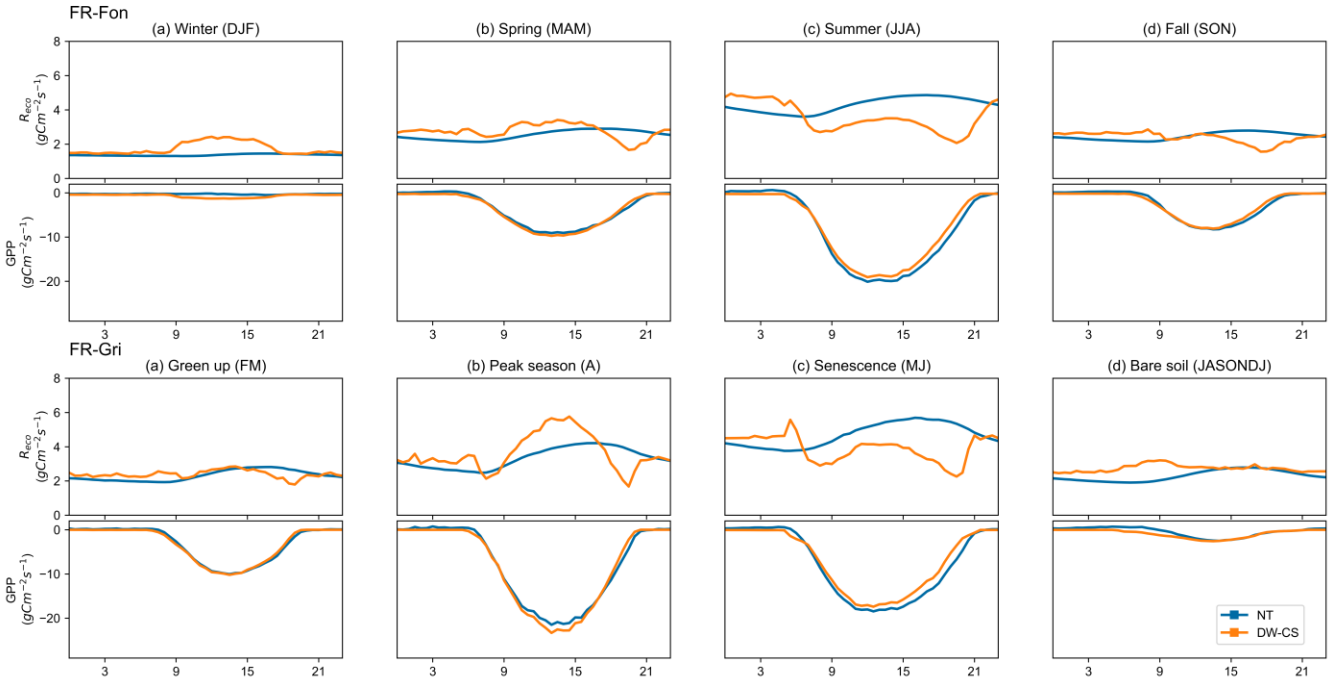

Figure 4.9. Diel patterns of R_{eco} and GPP estimated by wavelet-based conditional sampling (DWCS) and by standard night-time modelling (NT) during climatic seasons (FR-Fon) and the phenophases of green-up, peak season, senescence, and bare soil (excluding September 2021 due to intermediate crop), months are indicated by their first letter in parentheses. Note that R_{eco} and GPP are not on the same scale.

A closer inspection of φ_c components (Figure 4.10) reveals diel patterns resemblance between $\varphi_c^+|\varphi_v^+$ and soil respiration (R_{soil}) (daytime decrease during certain seasons), and $\varphi_c^+|\varphi_v^-$

and plant respiration (R_{plant}) (bimodal, with a maximum during daytime) found in (Järveoja et al., 2020). R_{soil} responds to soil temperature rather than air temperature and so follows the delayed warming and cooling pattern of the soil at the depth where respiration is maximum. We found here that the $\varphi_c^+|\varphi_v^+$ diel pattern follows well soil temperature around 20 cm depth (at 16 (30) cm depth for FR-Fon (FR-Gri) due to the difference in available measurement depths) while $\varphi_c^+|\varphi_v^-$ follows air temperature and incoming radiation.

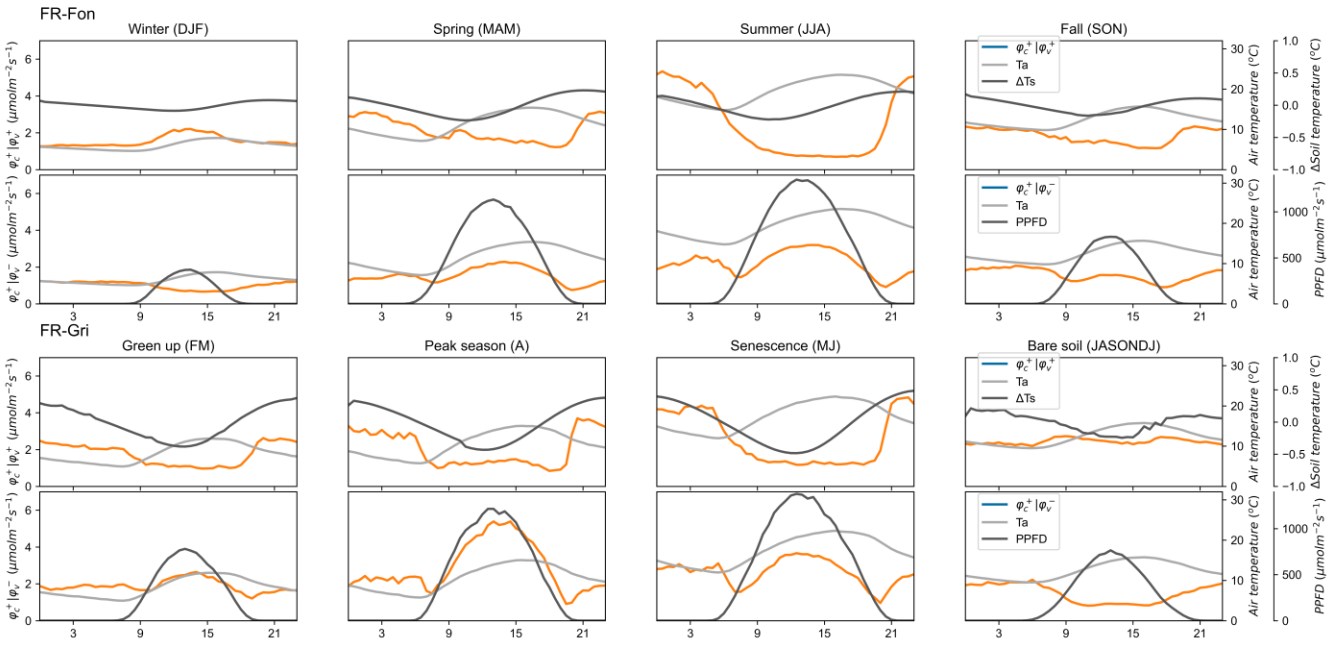

Figure 4.10. Diel patterns of $\varphi_c^+|\varphi_v^+$ (associated with heterotrophic respiration, Rh) and $\varphi_c^+|\varphi_v^-$ (associated to autotrophic respiration, Ra) and Rh's and Ra's main abiotic controls including air temperature (T_{air}), soil temperature at 16 (30) cm depth in FR-Fon (FR-Gri) (ΔT_{soil}, showed as deviation from the seasonal mean for readability), and photosynthetic photon flux density (PPFD) during climatic seasons (FR-Fon) and the phenophases of green-up, peak season, senescence, and bare soil, months indicated in parentheses. (cf. (Järveoja et al., 2020) Fig. 4)

4.5 Discussion

4.5.1 On the differences between standard- and DW-EC

Results suggest that the DW method successfully captures the NEE dynamics observed by standard EC on a half-hourly (Figure 4) and annually (Figure 4.6) basis, highlighting its potential as a reliable alternative for flux analyses. The proposed DW-EC method obtained around 20% more high-quality data by not requiring stationarity. Reducing the gap fillings to zero is impossible since a certain amount of gap filling will always be necessary, even without technical problems and insufficient turbulence. Still, gap-filling is essential for retrieving continuous data series, but its use should be limited to the strict necessity. Even largely employed methods, such as Marginal Distribution Sampling (MDS), have shown poorer performance during night-time due to fewer observations (Moffat et al., 2007) and higher latitudes due to a skewed radiation distribution (Vekuri et al., 2023). Part of this is because the standard EC method cannot handle non-stationary

CO_2 flux, flagging it as unreliable. Still, the increase in high-quality data can help improve the performance of gap-filling itself (Moffat et al., 2007), even if this benefit is irrelevant for our two sites.

The DW underestimation most probably emerges from the detrending nature of wavelet transform. The decomposition effectively disentangles each frequency, subtracting trends or fluctuations from the signal that span periods longer than the frequency under consideration. In this case, the low-frequency correction could help decrease the difference between EC and DW since, in other contexts, it has been shown to reduce the difference between EC calculated using different detrending strategies (including no detrending) to as low as 1 % (Mauder et al., 2021; Moncrieff et al., 2006; Rannik and Vesala, 1999). Differently, including DW's lower frequencies (> 30 minutes) is not as simple since although it requires making assumptions on the co-spectra in the low-frequency range, as well as that lower frequencies use more 'neighbour' data, making continuity of good quality data more of an issue.

To enforce comparison between methods, using the same pre-processing corrections was important. However, some relevant questions should be raised about this choice. Time lag and axis rotation corrections, in particular, transform w and CO_2, creating artificial breaking points between observations of two neighbour half-hours. Both corrections were built for EC_S, where each half-hour is separated from the other. Wavelet decomposition always uses neighbour values and assigns these breaks to corresponding frequencies. We employed the commonly used double rotation method for axis rotation, but planar fit, often recommended, should prevent these breaking points. Finnigan et al. (2003) have shown that 30-min double-rotation is equivalent to high pass filtering but may also add up part of the horizontal fluxes into the vertical flux, thereby biasing the measured flux.

The time lag may differ for different concentration fluctuation frequencies for sticky compounds such as ammonia (Ferrara et al., 2012) or VOCs (Loubet et al., 2022). Using the wavelet decomposition to retrieve frequency-dependent time lags may be tested, especially for ammonia, which has been shown to lead to systematic underestimation of eddy covariance fluxes and show asymmetrical correlation functions (Ferrara et al., 2012 Fig 5). In sum, further wavelet-based flux calculations may require revisiting some current pre-processing methods.

4.5.2 On the seasonal differences in the co-spectra

In peak and shape, NEE co-spectra matched reasonably well with standard-modelled co-spectra (Horst, 1997) (Figure S 4.3). The forest site showed low-frequency attenuation, less visible in the crop site. Positive (φ_c^+) and negative (φ_c^-) parts showed seasonal patterns not seen in the theoretical curve, suggesting it shall be explained by something different than micrometeorological factors (wind speed or Obukov length) and measuring height (for the agricultural site) obtained from the modelled co-spectra (Horst, 1997). Indeed, φ_c^- is expected to come mainly from the leaves, while φ_c^+ is from the ground and leaves brought up from in-canopy by injection. Intuitively, the second process moves eddies forward on the Kolmogorov cascade by encountering obstacles between the ground and canopy, while the first, coming from the top of the canopy, is less influenced by obstacles. This difference in eddy size transporting the signal would explain why, during photosynthetically active months, φ_c^- shows lower frequencies than φ_c^+

during neutral and unstable conditions (mostly daytime). The seasonality would thus come from the absence (presence) of leaves and crops, which leads to a reduced (increased) number of "obstacles". In stable conditions (mostly night), the same pattern is not seen because φ_c^- is expected to be minor, and indeed, at times, it differs significantly from the characteristic NEE co-spectra.

Of course, co-spectra analysis is neither a specificity of DW nor any frequency decomposed method; the Fourier transform may be used in post-processing spectral corrections. Wavelets remain, however, advantageous because they do not require stationarity. Wind-velocity coordinate rotations may, however, be performed over more extended periods than 30 minutes. Planar fit approaches should, therefore, be preferred.

4.5.3 On partitioning methods and possible sources of error

In standard practice, a modelled response of NEE to light, water, and temperature over days is used to split it into GPP and R_{eco}. The standard night-time method (NT) employs a nocturnal temperature response model to estimate R_{eco} (Reichstein et al., 2005), while day-time (DT) incorporates a light response curve to estimate both GPP and R_{eco} during day-time (Keenan et al., 2019; Lasslop et al., 2010). Given their similarity, we could expect little difference when comparing the same partitioning method on standard EC and wavelet-based fluxes (Figure 4.6).

However, in August 2021 in FR-Gri, when the increase in high-quality data in DW-NEE made NT's estimation undoubtedly more reasonable than its EC_S-NEE prediction (Figure 4.7). On this occasion, NT relying on EC_S projected an unrealistic rise in absolute GPP following intermediate crop harvest and herbicide application. Conversely, NT based on DW-EC showed the expected absolute GPP decrease, albeit with implausible positive GPP values (a known issue for the NT method). Nonetheless, standard model-based partitioning yielded somewhat different estimations at times (Figure 4.7) despite being informed by relatively similar input data (Figure 4.6), underscoring model-based uncertainty. In addition to that, by rendering partitioning contingent on distinct periods, spatial heterogeneity becomes an issue (Wehr et al., 2016). Direct partitioning methods are based on single 30-minute periods and are, therefore, relatively free from this issue, given that neighbourhood influence is limited.

Measuring directly GPP and R_{eco} at the ecosystem level poses challenges, yielding inconclusive comparative studies. A more direct way of measuring Reco is by using dark chambers (Järveoja et al., 2020) or using carbon isotopes (more precisely, the ratio between ^{13}C to ^{12}C) (Wehr et al., 2016). However, R_{eco} by NT partitioning was found to be 25% higher than isotopic-derived R_{eco} fluxes in a deciduous temperate forest during June-July (Wehr et al., 2016) and 16 % to 22 % higher than automatic dark chambers observations in a peatland (Järveoja et al., 2020). These differences are often attributed to models' limited capacity to replicate diel patterns (Wehr et al., 2016; Keenan et al., 2019; Griffis et al., 2004; Järveoja et al., 2020). In particular, the dynamics of the root-microbe-soil system are not well characterised. Some large-scale girdling experiments, however, show that soil respiration is highly correlated to photosynthate supply to roots: respiration was found to be reduced by 37 % within 5 days (54% in 1-2 months) after stopping the supply of photosynthates to roots (Högberg et al., 2001). ^{13}C labelling studies showed a 35-hour half-life of soil respiratory efflux in a forest (Högberg et al. 2008). NT's nocturnal calibration

on respiration does not account for photosynthate transfer processes. In addition, light's inhibition of leaf respiration is estimated to cause systematic overestimation of daytime ecosystem basal respiration estimated using NT (Wehr et al., 2016; Keenan et al., 2019). These references indicate that the respiration dial pattern may be much more complex than currently included in temperature response models.

In this study, we propose a new direct partitioning method, the discrete wavelet-based conditional sampling (DW-CS), based on the conditional sampling of frequency decomposed w and χ_{CO_2} product (Eq. **3.13**. Daily mean NT estimations were 12 (22) % higher than DW-CS for GPP (R_{eco}). Much noticeably, the DW-CS R_{eco} diel cycle unveils a bimodal trend (Figure 4.9), which, as previously observed by thorough chamber methods measurements (Järveoja et al., 2020) and on the $^{13}C/^{12}C$ derived estimations (Wehr et al., 2016). This diurnal variation was attributed by Wehr et al. (2016) to the inhibition of leaf respiration in light and by Järveoja et al. (2020) to the differential response of R_{eco} to soil temperature and air or plant temperature. Another noticeable result, shown in Figure 4.9, is that during the crop's peak growing season, DW-CS R_{eco} is much higher than NT R_{eco} during the day. An increase in autotrophic respiration concomitant with higher GPP from plant growth during that period may explain this increase. The NT method cannot capture this feature, which uses nocturnal calibration.

In Figure 4.10, the similarities between $\varphi_c^+|\varphi_v^+$ ($\varphi_c^+|\varphi_v^-$) and R_{soil} (R_{plant}) from Järveoja et al. (2020) indicate the potential to perform even further detailed partitioning. The similarities may relate to soil evaporation being higher than plant evaporation when a respiration signal (φ_c^+) is measured. Indeed, R_{plant} and GPP depend on stomata, so a cut in GPP, for instance, due to lower incoming radiation induced by cloud or shadowing, could cause stomatal closure or a decrease in plant surface temperature. Whether by physical constraint or condensation, during these moments, R_{plant} would come with a negative water flux ($\varphi_c^+|\varphi_v^-$). Evaluating the proposed partitioning method would require measuring R_{eco}, R_{soil} and R_{plant} at the field scale, which requires further research.

4.5.4 Perspectives on using wavelet-based EC for less gap-filling and direct partitioning

In this study, we have explored how including non-stationary fluxes, omitted by the standard EC method, modified the computed CO_2 flux and further gap-filling. These periods carry real information on the surface flux. For instance, dynamic light environments can trigger rapid but non-coordinated photosynthesis and stomatal response (McAusland et al., 2016), possibly leading to non-stationary NEE. When filtered out, those non-stationary events effectively "blinds" the gap-filling methods and final users from these transition events.

Similarly, non-homogeneous footprints are often encountered in ecosystem monitoring sites, although everything is done to minimise these conditions. Agricultural fields and sub-urban and urban areas are especially prone to source heterogeneity, mainly in the shape of a local intensive anthropogenic source (animal grazing on the field, animal barns, tractors, roads, chimneys) that may also lead to changes in CO_2 concentrations and fluxes with wind direction and hence non-stationarity in these components (Crawford and Christen, 2015). Thus, even if the impact is arguably small on monthly and annual net flux budgets on ecosystem towers, using DW-

EC becomes especially relevant in setups or situations with multiple local sources that are hard to isolate.

Intermittent turbulence was identified as the main problem for nocturnal EC, which leads to the u_* filtering approach (Aubinet, 2008). It is important to note that in some instances of such intermittent turbulence, a non-stationary flux may be delayed from the process that generated this flux. Indeed, when very low turbulence is followed by a burst of wind (ejections or sweeps), measured flux includes releasing accumulated stock (Katul et al., 2006; Kaimal and Finnigan, 1994). Consequently, including non-stationary fluxes retrieved by DW in the standard model-based partitioning methods, which do not consider these peaks as night-time delayed respiration, may lead to biased gap-filling. This bias, however, should affect less direct partitioning using DW-CS, which exclusively relies on data from the same snapshot of time.

The conditional sampling method presented here could be further developed to use soil and plant, heterotrophic and autotrophic or even biogenic and anthropogenic tracers like carbon and water isotopes to improve our understanding of carbon cycling in an ecosystem. Including co-produced gases can be the key to performing more elaborated attribution of fluxes to ecosystem compartments. Carbonyl sulphide (COS) is a known tracer of photosynthesis (Maseyk et al., 2014). Combining CO_2 flux with COS flux with H_2O would further partition GPP and Reco. In another context, carbon monoxide has been used to identify fossil fuel emissions (Super et al., 2017). Wavelet-based conditional sampling emerges as a promising framework for integrating such data, either directly as proposed here or through hybrid methods in which more elaborated models could be used to refine the partitioning method.

4.6 Conclusions

Discrete Wavelet-based Eddy Covariance (DW-EC) yielded around 17 % and 29 % fewer gaps than standard Eddy Covariance (EC_S) over four years of data in a forest site (FR-Fon) and two years in a crop site (FR-Gri) in the French Parisian region, respectively. We can expect even larger gap differences in perturbated environments (topography, inhomogeneous areas). The half-hour high-quality NEE (stationary and within well-developed turbulence) computed by wavelets were highly correlated to standard eddy covariance (R^2= 0.98 for both FR-Fon and FR-Gri), worsening for medium (0.73 and 0.52) and low-quality (0.03 and 0.0) data. At the daily scale, this correlation was kept (R^2= 0.97), but with a slight bias with DW around 9% lower than ECs (mean error = 0.1 and 0.18 µmol m s−1, mean absolute error = 0.42 and 0.39 µmol m^{-2} s^{-1}, ECs=1.09×DW by linear fitting for FR-Fon and FR-Gri). This effect is likely related to the detrending nature of wavelet decomposition, which leads to low-frequency attenuation of the flux. The supposed advantage of reduced gaps for DW-EC leads to sensibly similar NEE budgets: +2 (−1) % in FR-Fon (FR-Gri) when compared to DW-EC, forced to have the same gaps as EC_S. This small difference suggests that for standard sites (mostly homogeneous and flat), moving towards DW-EC would not significantly improve the annual budget. However, partitioning using EC_S- and DW-NEE yielded different GPP and R_{eco}, particularly for the night-time method (NT), where more high-quality observations made estimations arguably more credible in the crop site.

A new partitioning method is proposed, combining discrete wavelet transform and conditional sampling (DW-CS). The method splits positive and negative parts of the product of the wavelet decomposed vertical component of the wind, $w'(j)$, and a scalar, $\chi_s'(j)$. The underlying empirical assumption is that wavelet decomposition should allow the trap in each frequency of the positive and negative "gusts" mixed up in the original signal. Further including PPFD and $w' \chi_{H_2O}'$, attributing unrealistic CO_2 fluxes led to a method for estimating R_{eco} and GPP. Compared to DW-CS, Night-time partitioning (NT) showed better correlation and smaller errors than day-time methods. Mean absolute errors between NT and DW-CS (0.8 and 0.65 µmol m^{-2} s^{-1} in FR-Fon and FR-Gri) were lower than the NEE random uncertainty (1.03 and 0.73 µmol m^{-2} s^{-1} in FR-Fon and FR-Gri). However, most noticeably, DW-CS led to a different R_{eco} diel pattern compared to temperature-only driven models, with a daily respiration pattern that follows radiation (and hence GPP) and a night-time pattern that follows soil respiration. This diel pattern was already observed using chambers and has some ground to be more realistic than the standard NT and DT approaches: this pattern may reflect either a differentiated temperature response from soil and plants, a light inhibition response from plants, or a time shift between photosynthates production and their transport to roots. Field measurements of net flux components did not validate our DW-CS approach to confirm that this respiration pattern was happening in the observed sites. This study, however, strongly suggests further evaluating the R_{eco} diel pattern as it may strongly impact how the global CO_2 cycle is modelled. The DW-CS we present here should be further tested and refined as it has the benefit of integrating at the field scale without needing extra measurements, which also allows reprocessing of old data. We also note that DW-CS could be developed to incorporate other tracers like COS to partition the CO_2 fluxes between ecosystem compartments better.

Eddy covariance has improved observations and, indirectly, models for the last decades. This study shows that standardising wavelets for EC measurements can be operational using discrete wavelet decomposition. This use would be very beneficial as it includes non-stationary data, reduces gaps, and allows a look into the transitory process. The simplicity and flexibility of DW-EC also make it very easy to do (re)analysis. The method would be powerful for CH_4 and N_2O fluxes, which are highly non-stationary and difficult to gap-fill, and for urban setups for the same reasons. The new direct partitioning method shows great promise in providing fully observation-based partitioning at the field scale. However, partitioning methods, in general, and our new wavelet-based method, in particular, need further validation experiments across ecosystems and environmental conditions.

Acknowledgements

We acknowledge the ICOS ERIC for providing the FR-Gri and FR-Fon data. This project has received funding from the European Union's Horizon 2020 research and innovation programme under Grant Agreement No 101037319 (PAUL ICOS-Cities project).

Data availability

ICOS data for the FR-Gri site can be downloaded from the carbon portal: https://meta.icos-cp.eu/resources/stations/ES_FR-Gri. ICOS data for the FR-Fon site can be downloaded from the carbon portal: https://meta.icos-cp.eu/resources/stations/ES_FR-Fon.

Code

The code used in the analysis presented in this paper is available online and can be accessed at https://github.com/pedrohenriquecoimbra/coimbra-et-al-wavelet-based-partitioning

References

Arts, L. P. A. and van den Broek, E. L.: The fast continuous wavelet transformation (fCWT) for real-time, high-quality, noise-resistant time-frequency analysis, Nat. Comput. Sci., 2, 47–58, https://doi.org/10.1038/s43588-021-00183-z, 2022.

Aubinet, M.: Eddy Covariance Co2 Flux Measurements in Nocturnal Conditions: An Analysis of the Problem, Ecol. Appl., 18, 1368–1378, https://doi.org/10.1890/06-1336.1, 2008.

Aubinet, M., Grelle, A., Ibrom, A., Rannik, Ü., Moncrieff, J., Foken, T., Kowalski, A. S., Martin, P. H., Berbigier, P., Bernhofer, Ch., Clement, R., Elbers, J., Granier, A., Grünwald, T., Morgenstern, K., Pilegaard, K., Rebmann, C., Snijders, W., Valentini, R., and Vesala, T.: Estimates of the Annual Net Carbon and Water Exchange of Forests: The EUROFLUX Methodology, in: Advances in Ecological Research, vol. 30, edited by: Fitter, A. H. and Raffaelli, D. G., Academic Press, 113–175, https://doi.org/10.1016/S0065-2504(08)60018-5, 1999.

Aubinet, M., Heinesch, B., and Longdoz, B.: Estimation of the carbon sequestration by a heterogeneous forest: night flux corrections, heterogeneity of the site and inter-annual variability, Glob. Change Biol., 8, 1053–1071, https://doi.org/10.1046/j.1365-2486.2002.00529.x, 2002.

Aubinet, M., Berbigier, P., Bernhofer, Ch., Cescatti, A., Feigenwinter, C., Granier, A., Grünwald, Th., Havrankova, K., Heinesch, B., Longdoz, B., Marcolla, B., Montagnani, L., and Sedlak, P.: Comparing CO2 Storage and Advection Conditions at Night at Different Carboeuroflux Sites, Bound.-Layer Meteorol., 116, 63–93, https://doi.org/10.1007/s10546-004-7091-8, 2005.

Aubinet, M., Feigenwinter, C., Heinesch, B., Laffineur, Q., Papale, D., Reichstein, M., Rinne, J., and Van Gorsel, E.: Nighttime Flux Correction, in: Eddy Covariance: A Practical Guide to Measurement and Data Analysis, edited by: Aubinet, M., Vesala, T., and Papale, D., Springer Netherlands, Dordrecht, 133–157, https://doi.org/10.1007/978-94-007-2351-1_5, 2012.

Baldocchi, D. D.: Assessing the eddy covariance technique for evaluating carbon dioxide exchange rates of ecosystems: past, present and future, Glob. Change Biol., 9, 479–492, https://doi.org/10.1046/j.1365-2486.2003.00629.x, 2003.

Canadell, J. G., Monteiro, P. M. S., Costa, M. H., Cotrim da Cunha, L., Cox, P. M., Eliseev, A. V., Henson, S., Ishii, M., Jaccard, S., Koven, C., Lohila, A., Patra, P. K., Piao, S., Rogelj, J., Syampungani,

S., Zaehle, S., and Zickfeld, K.: Global Carbon and other Biogeochemical Cycles and Feedbacks, edited by: Masson-Delmotte, V., Zhai, P., Pirani, A., Connors, S. L., Péan, C., Berger, S., Caud, N., Chen, Y., Goldfarb, L., Gomis, M. I., Huang, M., Leitzell, K., Lonnoy, E., Matthews, J. B. R., Maycock, T. K., Waterfield, T., Yelekçi, O., Yu, R., and Zhou, B., Clim. Change 2021 Phys. Sci. Basis Contrib. Work. Group Sixth Assess. Rep. Intergov. Panel Clim. Change, 673–816, https://doi.org/10.1017/9781009157896.007, 2021.

Crawford, B. and Christen, A.: Spatial source attribution of measured urban eddy covariance CO2 fluxes, Theor Appl Climatol, 119, 733–755, https://doi.org/10.1007/s00704-014-1124-0, 2015.

Daubechies, I.: Orthonormal bases of compactly supported wavelets, Commun. Pure Appl. Math., 41, 909–996, https://doi.org/10.1002/cpa.3160410705, 1988.

Delpierre, N., Berveiller, D., Granda, E., and Dufrêne, E.: Wood phenology, not carbon input, controls the interannual variability of wood growth in a temperate oak forest, New Phytol., 210, 459–470, https://doi.org/10.1111/nph.13771, 2016.

Desjardins, R. L., Worth, D. E., Pattey, E., VanderZaag, A., Srinivasan, R., Mauder, M., Worthy, D., Sweeney, C., and Metzger, S.: The challenge of reconciling bottom-up agricultural methane emissions inventories with top-down measurements, Agric. For. Meteorol., 248, 48–59, https://doi.org/10.1016/j.agrformet.2017.09.003, 2018.

Du, Q., Liu, H., Feng, J., and Wang, L.: Effects of different gap filling methods and land surface energy balance closure on annual net ecosystem exchange in a semiarid area of China, Sci. China Earth Sci., 57, 1340–1351, https://doi.org/10.1007/s11430-013-4756-5, 2014.

Duffy, K. A., Schwalm, C. R., Arcus, V. L., Koch, G. W., Liang, L. L., and Schipper, L. A.: How close are we to the temperature tipping point of the terrestrial biosphere?, Sci. Adv., 7, eaay1052, https://doi.org/10.1126/sciadv.aay1052, 2021.

Falge, E., Baldocchi, D., Olson, R., Anthoni, P., Aubinet, M., Bernhofer, C., Burba, G., Ceulemans, R., Clement, R., Dolman, H., Granier, A., Gross, P., Grünwald, T., Hollinger, D., Jensen, N.-O., Katul, G., Keronen, P., Kowalski, A., Lai, C. T., Law, B. E., Meyers, T., Moncrieff, J., Moors, E., Munger, J. W., Pilegaard, K., Rannik, Ü., Rebmann, C., Suyker, A., Tenhunen, J., Tu, K., Verma, S., Vesala, T., Wilson, K., and Wofsy, S.: Gap filling strategies for defensible annual sums of net ecosystem exchange, Agric. For. Meteorol., 107, 43–69, https://doi.org/10.1016/S0168-1923(00)00225-2, 2001.

Farge, M.: Wavelet transforms and their applications to turbulence, Annu. Rev. Fluid Mech., 24, 395–458, 1992.

Farge, M. and Schneider, K.: Analysing and Computing Turbulent Flows Using Wavelets, in: New trends in turbulence Turbulence: nouveaux aspects: 31 July – 1 September 2000, edited by: Lesieur, M., Yaglom, A., and David, F., Springer, Berlin, Heidelberg, 449–504, https://doi.org/10.1007/3-540-45674-0_9, 2001.

Ferrara, R. M., Loubet, B., Di Tommasi, P., Bertolini, T., Magliulo, V., Cellier, P., Eugster, W., and Rana, G.: Eddy covariance measurement of ammonia fluxes: Comparison of high frequency correction

methodologies, Agric. For. Meteorol., 158–159, 30–42, https://doi.org/10.1016/j.agrformet.2012.02.001, 2012.

Finnigan, J. J., Clement, R., Malhi, Y., Leuning, R., and Cleugh, H. A.: A Re-Evaluation of Long-Term Flux Measurement Techniques Part I: Averaging and Coordinate Rotation, Bound.-Layer Meteorol., 107, 1–48, https://doi.org/10.1023/A:1021554900225, 2003.

Foken, T., Aubinet, M., and Leuning, R.: The Eddy Covariance Method, in: Eddy Covariance: A Practical Guide to Measurement and Data Analysis, edited by: Aubinet, M., Vesala, T., and Papale, D., Springer Netherlands, Dordrecht, 1–19, https://doi.org/10.1007/978-94-007-2351-1_1, 2012.

Foken, Th. and Wichura, B.: Tools for quality assessment of surface-based flux measurements, Agric. For. Meteorol., 78, 83–105, https://doi.org/10.1016/0168-1923(95)02248-1, 1996.

Fowler, D., Hargreaves, K., Skiba, U., Milne, R., Zahniser, M., Moncrieff, J., Beverland, I., and Gallagher, M.: Measurements of Ch4 and N2o Fluxes at the Landscape Scale Using Micrometeorological Methods, Philos. Trans. R. Soc. -Math. Phys. Eng. Sci., 351, 339–355, https://doi.org/10.1098/rsta.1995.0038, 1995.

Göckede, M., Kittler, F., and Schaller, C.: Quantifying the impact of emission outbursts and non-stationary flow on eddy-covariance CH_4 flux measurements using wavelet techniques, Biogeosciences, 16, 3113–3131, https://doi.org/10.5194/bg-16-3113-2019, 2019.

van Gorsel, E., Delpierre, N., Leuning, R., Black, A., Munger, J. W., Wofsy, S., Aubinet, M., Feigenwinter, C., Beringer, J., Bonal, D., Chen, B., Chen, J., Clement, R., Davis, K. J., Desai, A. R., Dragoni, D., Etzold, S., Grünwald, T., Gu, L., Heinesch, B., Hutyra, L. R., Jans, W. W. P., Kutsch, W., Law, B. E., Leclerc, M. Y., Mammarella, I., Montagnani, L., Noormets, A., Rebmann, C., and Wharton, S.: Estimating nocturnal ecosystem respiration from the vertical turbulent flux and change in storage of CO2, Agric. For. Meteorol., 149, 1919–1930, https://doi.org/10.1016/j.agrformet.2009.06.020, 2009.

Goulden, M. L., Munger, J. W., Fan, S.-M., Daube, B. C., and Wofsy, S. C.: Measurements of carbon sequestration by long-term eddy covariance: methods and a critical evaluation of accuracy, Glob. Change Biol., 2, 169–182, https://doi.org/10.1111/j.1365-2486.1996.tb00070.x, 1996.

Griffis, T. J., Black, T. A., Gaumont-Guay, D., Drewitt, G. B., Nesic, Z., Barr, A. G., Morgenstern, K., and Kljun, N.: Seasonal variation and partitioning of ecosystem respiration in a southern boreal aspen forest, Agric. For. Meteorol., 125, 207–223, https://doi.org/10.1016/j.agrformet.2004.04.006, 2004.

Gu, L., Falge, E. M., Boden, T., Baldocchi, D. D., Black, T. A., Saleska, S. R., Suni, T., Verma, S. B., Vesala, T., Wofsy, S. C., and Xu, L.: Objective threshold determination for nighttime eddy flux filtering, Agric. For. Meteorol., 128, 179–197, https://doi.org/10.1016/j.agrformet.2004.11.006, 2005.

Gu, L., Massman, W. J., Leuning, R., Pallardy, S. G., Meyers, T., Hanson, P. J., Riggs, J. S., Hosman, K. P., and Yang, B.: The fundamental equation of eddy covariance and its application in flux measurements, Agric. For. Meteorol., 152, 135–148, https://doi.org/10.1016/j.agrformet.2011.09.014, 2012.

Heskel, M. A., Atkin, O. K., Turnbull, M. H., and Griffin, K. L.: Bringing the Kok effect to light: A review on the integration of daytime respiration and net ecosystem exchange, Ecosphere, 4, art98, https://doi.org/10.1890/ES13-00120.1, 2013.

Högberg, P., Högberg, M. N., Göttlicher, S. G., Betson, N. R., Keel, S. G., Metcalfe, D. B., Campbell, C., Schindlbacher, A., Hurry, V., Lundmark, T., Linder, S., and Näsholm, T.: High temporal resolution tracing of photosynthate carbon from the tree canopy to forest soil microorganisms, New Phytologist, 177, 220–228, https://doi.org/10.1111/j.1469-8137.2007.02238.x, 2008.

Högberg, P., Nordgren, A., Buchmann, N., Taylor, A. F. S., Ekblad, A., Högberg, M. N., Nyberg, G., Ottosson-Löfvenius, M., and Read, D. J.: Large-scale forest girdling shows that current photosynthesis drives soil respiration, Nature, 411, 789–792, https://doi.org/10.1038/35081058, 2001.

Horst, T. W.: A simple formula for attenuation of eddy fluxes measured with first-order-response scalar sensors, Bound.-Layer Meteorol., 82, 219–233, https://doi.org/10.1023/A:1000229130034, 1997.

IPCC: Climate Change 2021: The Physical Science Basis. Contribution of Working Group I to the Sixth Assessment Report of the Intergovernmental Panel on Climate Change, , In Press, https://doi.org/10.1017/9781009157896, 2021.

IPCC: Climate Change 2022: Mitigation of Climate Change, , https://doi.org/10.1017/9781009157926, 2022a.

IPCC: Climate Change 2022: Impacts, Adaptation and Vulnerability, , https://doi.org/10.1017/9781009325844, 2022b.

Irvin, J., Zhou, S., McNicol, G., Lu, F., Liu, V., Fluet-Chouinard, E., Ouyang, Z., Knox, S. H., Lucas-Moffat, A., Trotta, C., Papale, D., Vitale, D., Mammarella, I., Alekseychik, P., Aurela, M., Avati, A., Baldocchi, D., Bansal, S., Bohrer, G., Campbell, D. I., Chen, J., Chu, H., Dalmagro, H. J., Delwiche, K. B., Desai, A. R., Euskirchen, E., Feron, S., Goeckede, M., Heimann, M., Helbig, M., Helfter, C., Hemes, K. S., Hirano, T., Iwata, H., Jurasinski, G., Kalhori, A., Kondrich, A., Lai, D. Y., Lohila, A., Malhotra, A., Merbold, L., Mitra, B., Ng, A., Nilsson, M. B., Noormets, A., Peichl, M., Rey-Sanchez, A. C., Richardson, A. D., Runkle, B. R., Schäfer, K. V., Sonnentag, O., Stuart-Haëntjens, E., Sturtevant, C., Ueyama, M., Valach, A. C., Vargas, R., Vourlitis, G. L., Ward, E. J., Wong, G. X., Zona, D., Alberto, Ma. C. R., Billesbach, D. P., Celis, G., Dolman, H., Friborg, T., Fuchs, K., Gogo, S., Gondwe, M. J., Goodrich, J. P., Gottschalk, P., Hörtnagl, L., Jacotot, A., Koebsch, F., Kasak, K., Maier, R., Morin, T. H., Nemitz, E., Oechel, W. C., Oikawa, P. Y., Ono, K., Sachs, T., Sakabe, A., Schuur, E. A., Shortt, R., Sullivan, R. C., Szutu, D. J., Tuittila, E.-S., Varlagin, A., Verfaillie, J. G., Wille, C., Windham-Myers, L., Poulter, B., and Jackson, R. B.: Gap-filling eddy covariance methane fluxes: Comparison of machine learning model predictions and uncertainties at FLUXNET-CH4 wetlands, Agric. For. Meteorol., 308–309, 108528, https://doi.org/10.1016/j.agrformet.2021.108528, 2021.

Järveoja, J., Nilsson, M. B., Crill, P. M., and Peichl, M.: Bimodal diel pattern in peatland ecosystem respiration rebuts uniform temperature response, Nat. Commun., 11, 4255, https://doi.org/10.1038/s41467-020-18027-1, 2020.

Jia, G., Shevliakova, E., Artaxo, P., De Noblet-Ducoudré, N., Houghton, R., House, J., Kitajima, K., Lennard, C., Popp, A., and Sirin, A.: Land–climate interactions, in: Climate Change and Land: an IPCC special report on climate change, desertification, land degradation, sustainable land management, food security, and greenhouse gas fluxes in terrestrial ecosystems, 2019.

Kaimal, J. C. and Finnigan, J. J.: Atmospheric Boundary Layer Flows: Their Structure and Measurement, Oxford University Press, 304 pp., 1994.

Kaimal, J. C., Wyngaard, J. C., Izumi, Y., and Coté, O. R.: Spectral characteristics of surface-layer turbulence, Q. J. R. Meteorol. Soc., 98, 563–589, https://doi.org/10.1002/qj.49709841707, 1972.

Katul, G., Porporato, A., Cava, D., and Siqueira, M.: An analysis of intermittency, scaling, and surface renewal in atmospheric surface layer turbulence, Physica D: Nonlinear Phenomena, 215, 117–126, https://doi.org/10.1016/j.physd.2006.02.004, 2006.

Keenan, T. F., Migliavacca, M., Papale, D., Baldocchi, D., Reichstein, M., Torn, M., and Wutzler, T.: Widespread inhibition of daytime ecosystem respiration, Nat. Ecol. Evol., 3, 407–415, https://doi.org/10.1038/s41559-019-0809-2, 2019.

Klosterhalfen, A., Graf, A., Brüggemann, N., Drüe, C., Esser, O., González-Dugo, M. P., Heinemann, G., Jacobs, C. M. J., Mauder, M., Moene, A. F., Ney, P., Pütz, T., Rebmann, C., Ramos Rodríguez, M., Scanlon, T. M., Schmidt, M., Steinbrecher, R., Thomas, C. K., Valler, V., Zeeman, M. J., and Vereecken, H.: Source partitioning of H_2O and CO_2 fluxes based on high-frequency eddy covariance data: a comparison between study sites, Biogeosciences, 16, 1111–1132, https://doi.org/10.5194/bg-16-1111-2019, 2019.

Kowalski, A. S. and Serrano-Ortiz, P.: On the relationship between the eddy covariance, the turbulent flux, and surface exchange for a trace gas such as CO2, Bound.-Layer Meteorol., 124, 129–141, https://doi.org/10.1007/s10546-007-9171-z, 2007.

Lasslop, G., Reichstein, M., Papale, D., Richardson, A. D., Arneth, A., Barr, A., Stoy, P., and Wohlfahrt, G.: Separation of net ecosystem exchange into assimilation and respiration using a light response curve approach: critical issues and global evaluation, Glob. Change Biol., 16, 187–208, https://doi.org/10.1111/j.1365-2486.2009.02041.x, 2010.

Lee, G. R., Gommers, R., Waselewski, F., Wohlfahrt, K., and O'Leary, A.: PyWavelets: A Python package for wavelet analysis, J. Open Source Softw., 4, 1237, https://doi.org/10.21105/joss.01237, 2019.

Lloyd, J. and Taylor, J. A.: On the Temperature Dependence of Soil Respiration, Funct. Ecol., 8, 315–323, https://doi.org/10.2307/2389824, 1994.

Loubet, B., Laville, P., Lehuger, S., Larmanou, E., Fléchard, C., Mascher, N., Genermont, S., Roche, R., Ferrara, R. M., Stella, P., Personne, E., Durand, B., Decuq, C., Flura, D., Masson, S., Fanucci, O., Rampon, J.-N., Siemens, J., Kindler, R., Gabrielle, B., Schrumpf, M., and Cellier, P.: Carbon, nitrogen and Greenhouse gases budgets over a four years crop rotation in northern France, Plant Soil, 343, 109, https://doi.org/10.1007/s11104-011-0751-9, 2011.

Loubet, B., Buysse, P., Gonzaga-Gomez, L., Lafouge, F., Ciuraru, R., Decuq, C., Kammer, J., Bsaibes, S., Boissard, C., Durand, B., Gueudet, J.-C., Fanucci, O., Zurfluh, O., Abis, L., Zannoni, N., Truong, F., Baisnée, D., Sarda-Estève, R., Staudt, M., and Gros, V.: Volatile organic compound fluxes over a winter wheat field by PTR-Qi-TOF-MS and eddy covariance, Atmospheric Chem. Phys., 22, 2817–2842, https://doi.org/10.5194/acp-22-2817-2022, 2022.

Lucas-Moffat, A. M., Schrader, F., Herbst, M., and Brümmer, C.: Multiple gap-filling for eddy covariance datasets, Agric. For. Meteorol., 325, 109114, https://doi.org/10.1016/j.agrformet.2022.109114, 2022.

Mallat, S. G.: A theory for multiresolution signal decomposition: the wavelet representation, IEEE Trans. Pattern Anal. Mach. Intell., 11, 674–693, https://doi.org/10.1109/34.192463, 1989.

Maseyk, K., Berry, J. A., Billesbach, D., Campbell, J. E., Torn, M. S., Zahniser, M., and Seibt, U.: Sources and sinks of carbonyl sulfide in an agricultural field in the Southern Great Plains, Proc. Natl. Acad. Sci., 111, 9064–9069, https://doi.org/10.1073/pnas.1319132111, 2014.

Massman, W. J. and Lee, X.: Eddy covariance flux corrections and uncertainties in long-term studies of carbon and energy exchanges, Agric. For. Meteorol., 113, 121–144, https://doi.org/10.1016/S0168-1923(02)00105-3, 2002.

Mauder, M. and Foken, T.: Documentation and Instruction Manual of the Eddy-Covariance Software Package TK3, 60, 2011.

Mauder, M., Foken, T., Aubinet, M., and Ibrom, A.: Eddy-Covariance Measurements, in: Springer Handbook of Atmospheric Measurements, edited by: Foken, T., Springer International Publishing, Cham, 1473–1504, https://doi.org/10.1007/978-3-030-52171-4_55, 2021.

Mauder, M., Desjardins, R. L., and MacPherson, I.: Scale analysis of airborne flux measurements over heterogeneous terrain in a boreal ecosystem, J. Geophys. Res. Atmospheres, 112, https://doi.org/10.1029/2006JD008133, 2007.

Mauder, M., Cuntz, M., Drüe, C., Graf, A., Rebmann, C., Schmid, H. P., Schmidt, M., and Steinbrecher, R.: A strategy for quality and uncertainty assessment of long-term eddy-covariance measurements, Agric. For. Meteorol., 169, 122–135, https://doi.org/10.1016/j.agrformet.2012.09.006, 2013.

Metzger, S.: Surface-atmosphere exchange in a box: Making the control volume a suitable representation for in-situ observations, Agric. For. Meteorol., 255, 68–80, https://doi.org/10.1016/j.agrformet.2017.08.037, 2018.

Metzger, S., Junkermann, W., Mauder, M., Butterbach-Bahl, K., Trancón y Widemann, B., Neidl, F., Schäfer, K., Wieneke, S., Zheng, X. H., Schmid, H. P., and Foken, T.: Spatially explicit regionalization of airborne flux measurements using environmental response functions, Biogeosciences, 10, 2193–2217, https://doi.org/10.5194/bg-10-2193-2013, 2013.

Mishurov, M. and Kiely, G.: Gap-filling techniques for the annual sums of nitrous oxide fluxes, Agric. For. Meteorol., 151, 1763–1767, https://doi.org/10.1016/j.agrformet.2011.07.014, 2011.

Moffat, A. M.: A new methodology to interpret high resolution measurements of net carbon fluxes between terrestrial ecosystems and the atmosphere, 2012.

Moffat, A. M., Papale, D., Reichstein, M., Hollinger, D. Y., Richardson, A. D., Barr, A. G., Beckstein, C., Braswell, B. H., Churkina, G., Desai, A. R., Falge, E., Gove, J. H., Heimann, M., Hui, D., Jarvis, A. J., Kattge, J., Noormets, A., and Stauch, V. J.: Comprehensive comparison of gap-filling techniques for eddy covariance net carbon fluxes, Agric. For. Meteorol., 147, 209–232, https://doi.org/10.1016/j.agrformet.2007.08.011, 2007.

Moncrieff, J., Clement, R., Finnigan, J., and Meyers, T.: Averaging, Detrending, and Filtering of Eddy Covariance Time Series, in: Handbook of Micrometeorology, Atmospheric and Oceanographic Sciences Library, vol. 29, 7–31, https://doi.org/10.1007/1-4020-2265-4_2, 2006.

Moncrieff, J. B., Massheder, J. M., de Bruin, H., Elbers, J., Friborg, T., Heusinkveld, B., Kabat, P., Scott, S., Soegaard, H., and Verhoef, A.: A system to measure surface fluxes of momentum, sensible heat, water vapour and carbon dioxide, J. Hydrol., 188–189, 589–611, https://doi.org/10.1016/S0022-1694(96)03194-0, 1997.

Papale, D. and Valentini, R.: A new assessment of European forests carbon exchanges by eddy fluxes and artificial neural network spatialization, Glob. Change Biol., 9, 525–535, https://doi.org/10.1046/j.1365-2486.2003.00609.x, 2003.

Papale, D., Reichstein, M., Aubinet, M., Canfora, E., Bernhofer, C., Kutsch, W., Longdoz, B., Rambal, S., Valentini, R., Vesala, T., and Yakir, D.: Towards a standardized processing of Net Ecosystem Exchange measured with eddy covariance technique: algorithms and uncertainty estimation, Biogeosciences, 3, 571–583, https://doi.org/10.5194/bg-3-571-2006, 2006.

Pastorello, G., Trotta, C., Canfora, E., Chu, H., Christianson, D., Cheah, Y.-W., Poindexter, C., Chen, J., Elbashandy, A., Humphrey, M., Isaac, P., Polidori, D., Reichstein, M., Ribeca, A., van Ingen, C., Vuichard, N., Zhang, L., Amiro, B., Ammann, C., Arain, M. A., Ardö, J., Arkebauer, T., Arndt, S. K., Arriga, N., Aubinet, M., Aurela, M., Baldocchi, D., Barr, A., Beamesderfer, E., Marchesini, L. B., Bergeron, O., Beringer, J., Bernhofer, C., Berveiller, D., Billesbach, D., Black, T. A., Blanken, P. D., Bohrer, G., Boike, J., Bolstad, P. V., Bonal, D., Bonnefond, J.-M., Bowling, D. R., Bracho, R., Brodeur, J., Brümmer, C., Buchmann, N., Burban, B., Burns, S. P., Buysse, P., Cale, P., Cavagna, M., Cellier, P., Chen, S., Chini, I., Christensen, T. R., Cleverly, J., Collalti, A., Consalvo, C., Cook, B. D., Cook, D., Coursolle, C., Cremonese, E., Curtis, P. S., D'Andrea, E., da Rocha, H., Dai, X., Davis, K. J., Cinti, B. D., Grandcourt, A. de, Ligne, A. D., De Oliveira, R. C., Delpierre, N., Desai, A. R., Di Bella, C. M., Tommasi, P. di, Dolman, H., Domingo, F., Dong, G., Dore, S., Duce, P., Dufrêne, E., Dunn, A., Dušek, J., Eamus, D., Eichelmann, U., ElKhidir, H. A. M., Eugster, W., Ewenz, C. M., Ewers, B., Famulari, D., Fares, S., Feigenwinter, I., Feitz, A., Fensholt, R., Filippa, G., Fischer, M., Frank, J., Galvagno, M., et al.: The FLUXNET2015 dataset and the ONEFlux processing pipeline for eddy covariance data, Sci. Data, 7, 225, https://doi.org/10.1038/s41597-020-0534-3, 2020.

Perez-Priego, O., Katul, G., Reichstein, M., El-Madany, T. S., Ahrens, B., Carrara, A., Scanlon, T. M., and Migliavacca, M.: Partitioning Eddy Covariance Water Flux Components Using Physiological

and Micrometeorological Approaches, J. Geophys. Res. Biogeosciences, 123, 3353–3370, https://doi.org/10.1029/2018JG004637, 2018.

Pohl, F., Rakovec, O., Rebmann, C., Hildebrandt, A., Boeing, F., Hermanns, F., Attinger, S., Samaniego, L., and Kumar, R.: Long-term daily hydrometeorological drought indices, soil moisture, and evapotranspiration for ICOS sites, Sci. Data, 10, 281, https://doi.org/10.1038/s41597-023-02192-1, 2023.

Rana, G., Palatella, L., Scanlon, T. M., Martinelli, N., and Ferrara, R. M.: CO2 and H2O flux partitioning in a Mediterranean cropping system, Agric. For. Meteorol., 260–261, 118–130, https://doi.org/10.1016/j.agrformet.2018.06.007, 2018.

Rannik, Ü. and Vesala, T.: Autoregressive filtering versus linear detrending in estimation of fluxes by the eddy covariance method, Bound.-Layer Meteorol., 91, 259–280, https://doi.org/10.1023/A:1001840416858, 1999.

Rebmann, C., Aubinet, M., Schmid, H., Arriga, N., Aurela, M., Burba, G., Clement, R., De Ligne, A., Fratini, G., Gielen, B., Grace, J., Graf, A., Gross, P., Haapanala, S., Herbst, M., Hörtnagl, L., Ibrom, A., Joly, L., Kljun, N., and Franz, D.: ICOS eddy covariance flux-station site setup: A review, Int. Agrophysics, 32, 471–494, https://doi.org/10.1515/intag-2017-0044, 2018.

Reichstein, M., Falge, E., Baldocchi, D., Papale, D., Aubinet, M., Berbigier, P., Bernhofer, C., Buchmann, N., Gilmanov, T., Granier, A., Grünwald, T., Havránková, K., Ilvesniemi, H., Janous, D., Knohl, A., Laurila, T., Lohila, A., Loustau, D., Matteucci, G., Meyers, T., Miglietta, F., Ourcival, J.-M., Pumpanen, J., Rambal, S., Rotenberg, E., Sanz, M., Tenhunen, J., Seufert, G., Vaccari, F., Vesala, T., Yakir, D., and Valentini, R.: On the separation of net ecosystem exchange into assimilation and ecosystem respiration: review and improved algorithm, Glob. Change Biol., 11, 1424–1439, https://doi.org/10.1111/j.1365-2486.2005.001002.x, 2005.

Reichstein, M., Stoy, P. C., Desai, A. R., Lasslop, G., and Richardson, A. D.: Partitioning of Net Fluxes, in: Eddy Covariance: A Practical Guide to Measurement and Data Analysis, edited by: Aubinet, M., Vesala, T., and Papale, D., Springer Netherlands, Dordrecht, 263–289, https://doi.org/10.1007/978-94-007-2351-1_9, 2012.

Sabbatini, S., Mammarella, I., Arriga, N., Fratini, G., Graf, A., Hörtnagl, L., Ibrom, A., Longdoz, B., Mauder, M., Merbold, L., Metzger, S., Montagnani, L., Pitacco, A., Rebmann, C., Sedlák, P., Šigut, L., Vitale, D., and Papale, D.: Eddy covariance raw data processing for CO2 and energy fluxes calculation at ICOS ecosystem stations, Int. Agrophysics, 32, 495–515, https://doi.org/10.1515/intag-2017-0043, 2018.

Scanlon, T. M. and Albertson, J. D.: Turbulent transport of carbon dioxide and water vapor within a vegetation canopy during unstable conditions: Identification of episodes using wavelet analysis, J. Geophys. Res. Atmospheres, 106, 7251–7262, https://doi.org/10.1029/2000JD900662, 2001.

Scanlon, T. M. and Kustas, W. P.: Partitioning carbon dioxide and water vapor fluxes using correlation analysis, Agric. For. Meteorol., 150, 89–99, https://doi.org/10.1016/j.agrformet.2009.09.005, 2010.

Scanlon, T. M. and Kustas, W. P.: Partitioning Evapotranspiration Using an Eddy Covariance-Based Technique: Improved Assessment of Soil Moisture and Land–Atmosphere Exchange Dynamics, Vadose Zone J., 11, vzj2012.0025, https://doi.org/10.2136/vzj2012.0025, 2012.

Scanlon, T. M. and Sahu, P.: On the correlation structure of water vapor and carbon dioxide in the atmospheric surface layer: A basis for flux partitioning, Water Resour. Res., 44, https://doi.org/10.1029/2008WR006932, 2008.

Scanlon, T. M., Schmidt, D. F., and Skaggs, T. H.: Correlation-based flux partitioning of water vapor and carbon dioxide fluxes: Method simplification and estimation of canopy water use efficiency, Agric. For. Meteorol., 279, 107732, https://doi.org/10.1016/j.agrformet.2019.107732, 2019.

Schaller, C., Göckede, M., and Foken, T.: Flux calculation of short turbulent events – comparison of three methods, Atmospheric Meas. Tech., 10, 869–880, https://doi.org/10.5194/amt-10-869-2017, 2017.

Sousa, P. M., Barriopedro, D., García-Herrera, R., Ordóñez, C., Soares, P. M. M., and Trigo, R. M.: Distinct influences of large-scale circulation and regional feedbacks in two exceptional 2019 European heatwaves, Commun. Earth Environ., 1, 1–13, https://doi.org/10.1038/s43247-020-00048-9, 2020.

Strunin, M. A. and Hiyama, T.: Applying wavelet transforms to analyse aircraft-measured turbulence and turbulent fluxes in the atmospheric boundary layer over eastern Siberia, Hydrological Processes, 18, 3081–3098, https://doi.org/10.1002/hyp.5750, 2004.

Sulman, B. N., Roman, D. T., Scanlon, T. M., Wang, L., and Novick, K. A.: Comparing methods for partitioning a decade of carbon dioxide and water vapor fluxes in a temperate forest, Agric. For. Meteorol., 226–227, 229–245, https://doi.org/10.1016/j.agrformet.2016.06.002, 2016.

Super, I., Denier van der Gon, H. A. C., Visschedijk, A. J. H., Moerman, M. M., Chen, H., van der Molen, M. K., and Peters, W.: Interpreting continuous in-situ observations of carbon dioxide and carbon monoxide in the urban port area of Rotterdam, Atmospheric Pollution Research, 8, 174–187, https://doi.org/10.1016/j.apr.2016.08.008, 2017.

Thomas, C. and Foken, T.: Re-evaluation of integral turbulence characteristics and their parameterisations, in: 15th Symposium on Boundary Layers and Turbulence, Boston, 129–132, 2002.

Thomas, C., Martin, J. G., Goeckede, M., Siqueira, M. B., Foken, T., Law, B. E., Loescher, H. W., and Katul, G.: Estimating daytime subcanopy respiration from conditional sampling methods applied to multi-scalar high frequency turbulence time series, Agric. For. Meteorol., 148, 1210–1229, https://doi.org/10.1016/j.agrformet.2008.03.002, 2008.

Torrence, C. and Compo, G. P.: A Practical Guide to Wavelet Analysis, Bull. Am. Meteorol. Soc., 79, 61–78, https://doi.org/10.1175/1520-0477(1998)079<0061:APGTWA>2.0.CO;2, 1998.

Twardosz, R., Walanus, A., and Guzik, I.: Warming in Europe: Recent Trends in Annual and Seasonal temperatures, Pure Appl. Geophys., 178, 4021–4032, https://doi.org/10.1007/s00024-021-02860-6, 2021.

Valentini, R., De ANGELIS, P., Matteucci, G., Monaco, R., Dore, S., and Mucnozza, G. E. S.: Seasonal net carbon dioxide exchange of a beech forest with the atmosphere, Glob. Change Biol., 2, 199–207, https://doi.org/10.1111/j.1365-2486.1996.tb00072.x, 1996.

Vekuri, H., Tuovinen, J.-P., Kulmala, L., Papale, D., Kolari, P., Aurela, M., Laurila, T., Liski, J., and Lohila, A.: A widely-used eddy covariance gap-filling method creates systematic bias in carbon balance estimates, Sci. Rep., 13, 1720, https://doi.org/10.1038/s41598-023-28827-2, 2023.

Wang, W., Smith, J. A., Ramamurthy, P., Baeck, M. L., Bou-Zeid, E., and Scanlon, T. M.: On the correlation of water vapor and CO2: Application to flux partitioning of evapotranspiration, Water Resour. Res., 52, 9452–9469, https://doi.org/10.1002/2015WR018161, 2016.

Warm Winter 2020 Team, & ICOS Ecosystem Thematic Centre: Warm Winter 2020 ecosystem eddy covariance flux product for 73 stations in FLUXNET-Archive format—release 2022-1 (Version 1.0), ICOS Carbon Portal, https://doi.org/10.18160/2G60-ZHAK, 2020.

Webb, E. K., Pearman, G. I., and Leuning, R.: Correction of flux measurements for density effects due to heat and water vapour transfer, Q. J. R. Meteorol. Soc., 106, 85–100, https://doi.org/10.1002/qj.49710644707, 1980.

Wehr, R., Munger, J. W., McManus, J. B., Nelson, D. D., Zahniser, M. S., Davidson, E. A., Wofsy, S. C., and Saleska, S. R.: Seasonality of temperate forest photosynthesis and daytime respiration, Nature, 534, 680–683, https://doi.org/10.1038/nature17966, 2016.

Wilczak, J. M., Oncley, S. P., and Stage, S. A.: Sonic Anemometer Tilt Correction Algorithms, Bound.-Layer Meteorol., 99, 127–150, https://doi.org/10.1023/A:1018966204465, 2001.

Wutzler, T., Lucas-Moffat, A., Migliavacca, M., Knauer, J., Sickel, K., Šigut, L., Menzer, O., and Reichstein, M.: Basic and extensible post-processing of eddy covariance flux data with REddyProc, Biogeosciences, 15, 5015–5030, https://doi.org/10.5194/bg-15-5015-2018, 2018.

Zahn, E., Bou-Zeid, E., Good, S. P., Katul, G. G., Thomas, C. K., Ghannam, K., Smith, J. A., Chamecki, M., Dias, N. L., Fuentes, J. D., Alfieri, J. G., Kwon, H., Caylor, K. K., Gao, Z., Soderberg, K., Bambach, N. E., Hipps, L. E., Prueger, J. H., and Kustas, W. P.: Direct partitioning of eddy-covariance water and carbon dioxide fluxes into ground and plant components, Agric. For. Meteorol., 315, 108790, https://doi.org/10.1016/j.agrformet.2021.108790, 2022.

Zeeman, M. J., Eugster, W., and Thomas, C. K.: Concurrency of Coherent Structures and Conditionally Sampled Daytime Sub-canopy Respiration, Bound.-Layer Meteorol., 146, 1–15, https://doi.org/10.1007/s10546-012-9745-2, 2013.

Supplementary materials for: Improvement of CO_2 flux quality through wavelet-based Eddy Covariance: a new method for partitioning respiration and photosynthesis

Pedro Henrique H. Coimbra[1*], Benjamin Loubet[1], Olivier Laurent[2], Matthias Mauder[3,4], Bernard Heinesch[5], Jonathan Bitton[5], Nicolas Delpierre[6,7], Jérémie Depuydt[1], Pauline Buysse[1]

[1] ECOSYS, INRAE, AgroParisTech, Université Paris-Saclay, Palaiseau, France
[2] Laboratoire des Sciences du Climat et de l'Environnement, CEA, CNRS, Université Paris-Saclay, Gif-sur-Yvette, France
[3] Institute of Meteorology and Climate Research - Atmospheric Environmental Research (IMK-IFU), Karlsruhe Institute of Technology, Garmisch-Partenkirchen, Germany
[4] Institute of Hydrology and Meteorology, Technische Universität Dresden, Dresden, Germany
[5] Faculté des Sciences Agronomiques de Gembloux, Unité de Physique, Gembloux, Belgium
[6] Ecologie Systématique Evolution, CNRS, AgroParisTech, Université Paris-Saclay, Gif-sur-Yvette, France
[7] Institut Universitaire de France, France

* corresponding author: pedro-henrique.herig-coimbra@inrae.fr

4.7 Appendix

4.7.1 A Demonstrating covariance can be calculated using decomposed signals

Assuming two time series variables, *x* and *y*, the sum of the $\overline{x'y'}(j)$ for all frequencies, *j* is not strictly equal to the covariance $\overline{x'y'}$. Indeed, we have:

$$\overline{x'y'} = \overline{\sum_{J=0}^{J} x'_J \sum_{J=0}^{J} y'_J} = \sum_{j=0}^{J} \overline{x'_j y'_j} + \sum_{k \neq j} \overline{x'_j y'_k} \qquad (A.1)$$

For discrete wavelet transform DWT, the orthogonality of the wavelet base implies independent frequencies, *i.e.* $\overline{x'_k y'_j} = 0$ for $k \neq j$, hence $\overline{x'y'} = \sum_{j=1}^{J} \overline{x'_j y'_j}$. For continuous wavelet transform CWT, a coefficient C_φ is introduced to ensure energy conservation and correct for cross-correlations of *x* and *y* between scales *j*, leading to:

$$\overline{x'y'} = C_\varphi \sum_j \overline{x'y'}(j) \qquad (A.2)$$

C_φ depends on the wavelet chosen (Table 3.1). Alternatively, a direct formulation of the covariance was proposed by (Torrence and Compo, 1998) based on $\tilde{f}_x(n,j)$ and $\tilde{f}_y(n,j)$ the wavelet coefficients for time series *x* and *y*:

$$\overline{x'y'} = \frac{\delta j \delta t}{C_\delta N} \sum_{n=0}^{N-1} \sum_{j=0}^{J} \tilde{f}_x(n,j) \overline{\tilde{f}_y}(n,j) \qquad (A.3)$$

Where C_δ is a scale-independent reconstruction factor depending on the chosen mother wavelet function (Table 3.1).

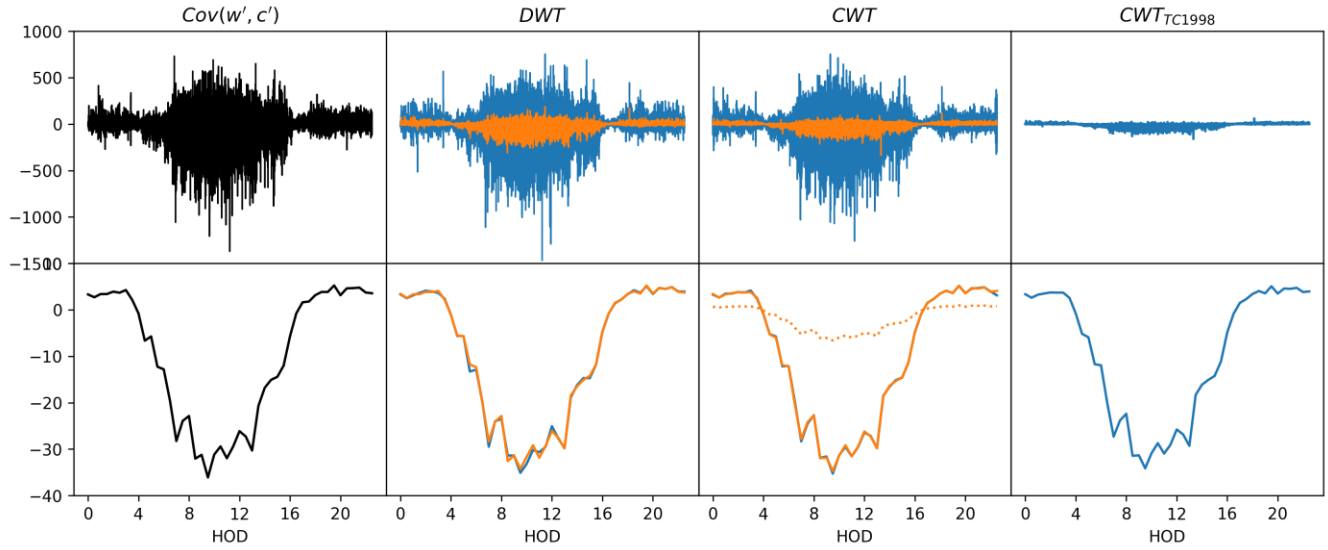

Figure S 4.1. Covariance is calculated using the standard equation ($\overline{\boldsymbol{w'c'}}$ in black), DWT considering cross-correlation ($\overline{\sum \boldsymbol{w_j'} \sum \boldsymbol{c_j'}}$ in blue), and ignoring it ($\sum \overline{\boldsymbol{w_j'} \boldsymbol{c_j'}}$ in orange), idem for CWT plus without C_φ (dotted orange), using covariance equation from Torrence and Compo (1998) (CWT_{TC1998}). Top 20 Hz data before time averaging, bottom half-hour average. Data for FR-Gri 03/05/2022.

4.7.2 Supplemental figures

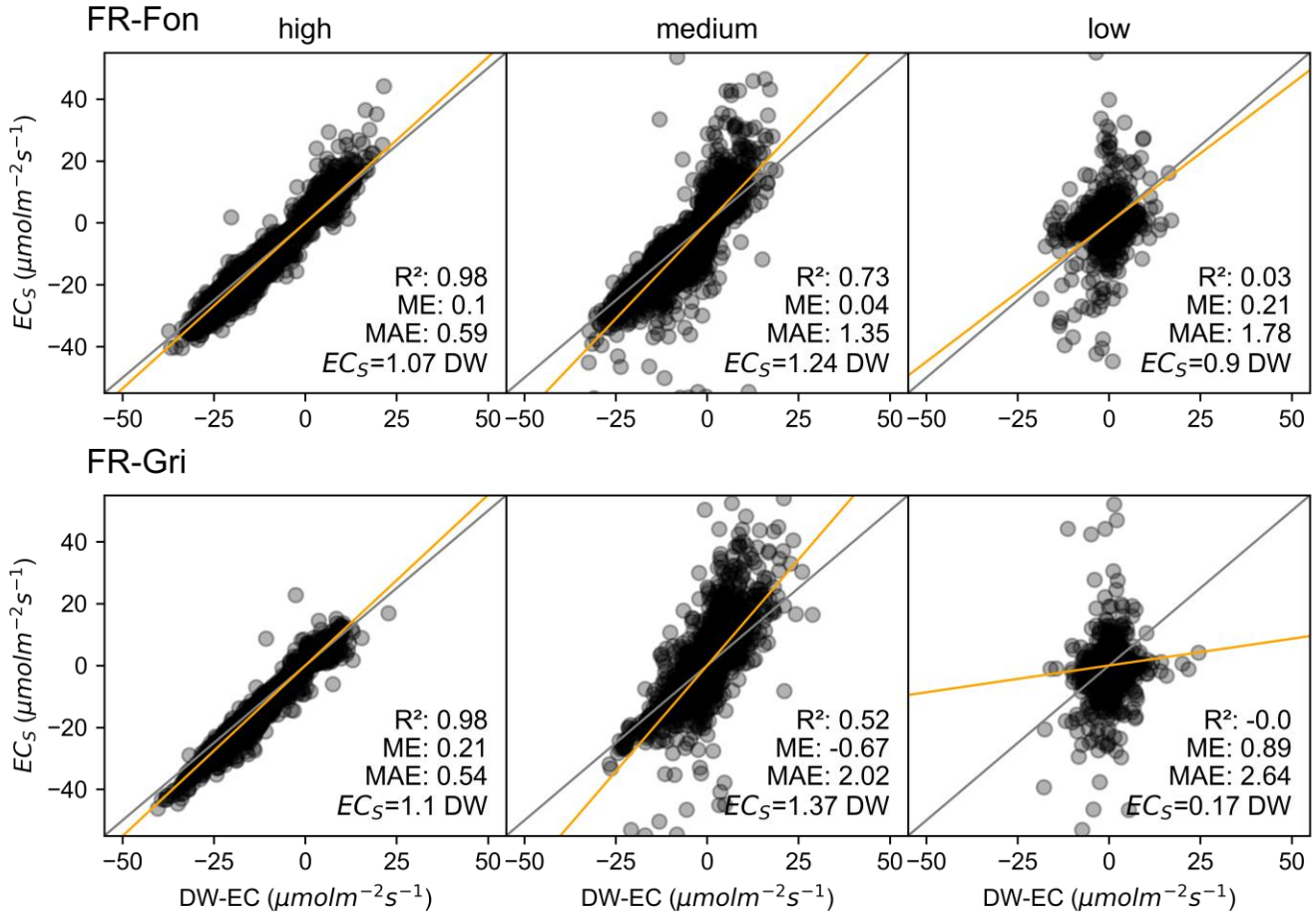

Figure S 4.2. Half-hourly NEE was calculated using ECS and DW-EC and grouped by quality flags. High: well-developed turbulence (ITC < 30 %) and stationary (STA < 30 %); medium: at least one of the tests higher than 30 % but both lower than 100%; low: at least one of the tests higher than 100 %. In grey, 1:1, and orange, linear relation. No gap-filling was used.

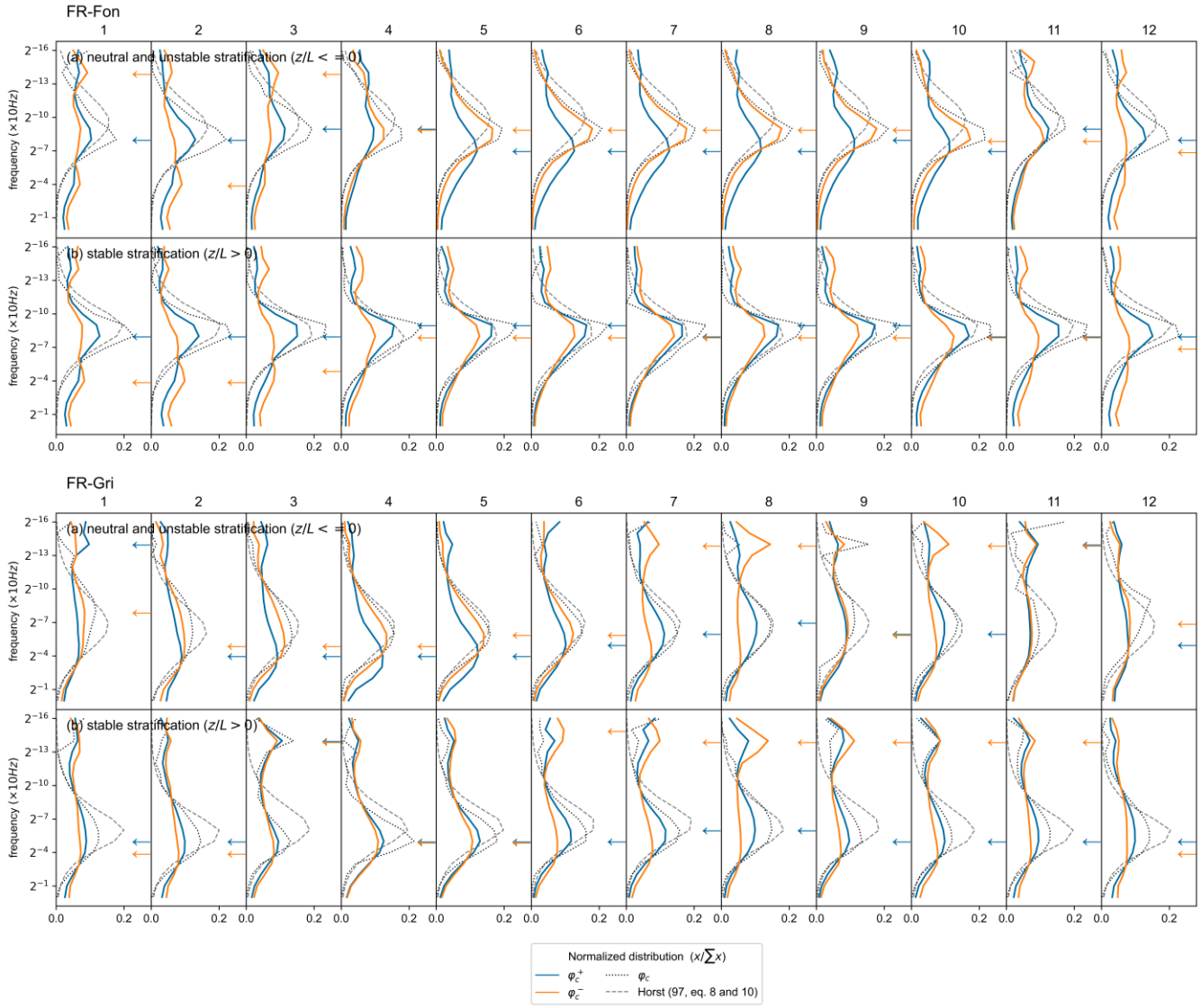

Figure S 4.3. Monthly mean co-spectra of w'CO_2' (φ_c), its positive and negative parts, and modelled co-spectra following Horst (1997) grouped by stratification status. Co-spectra curves sum to 1. Horst (1997) co-spectra are calculated using measured mean wind speed, displacement height and Obukhov length. Peak frequencies are shown with an arrow.

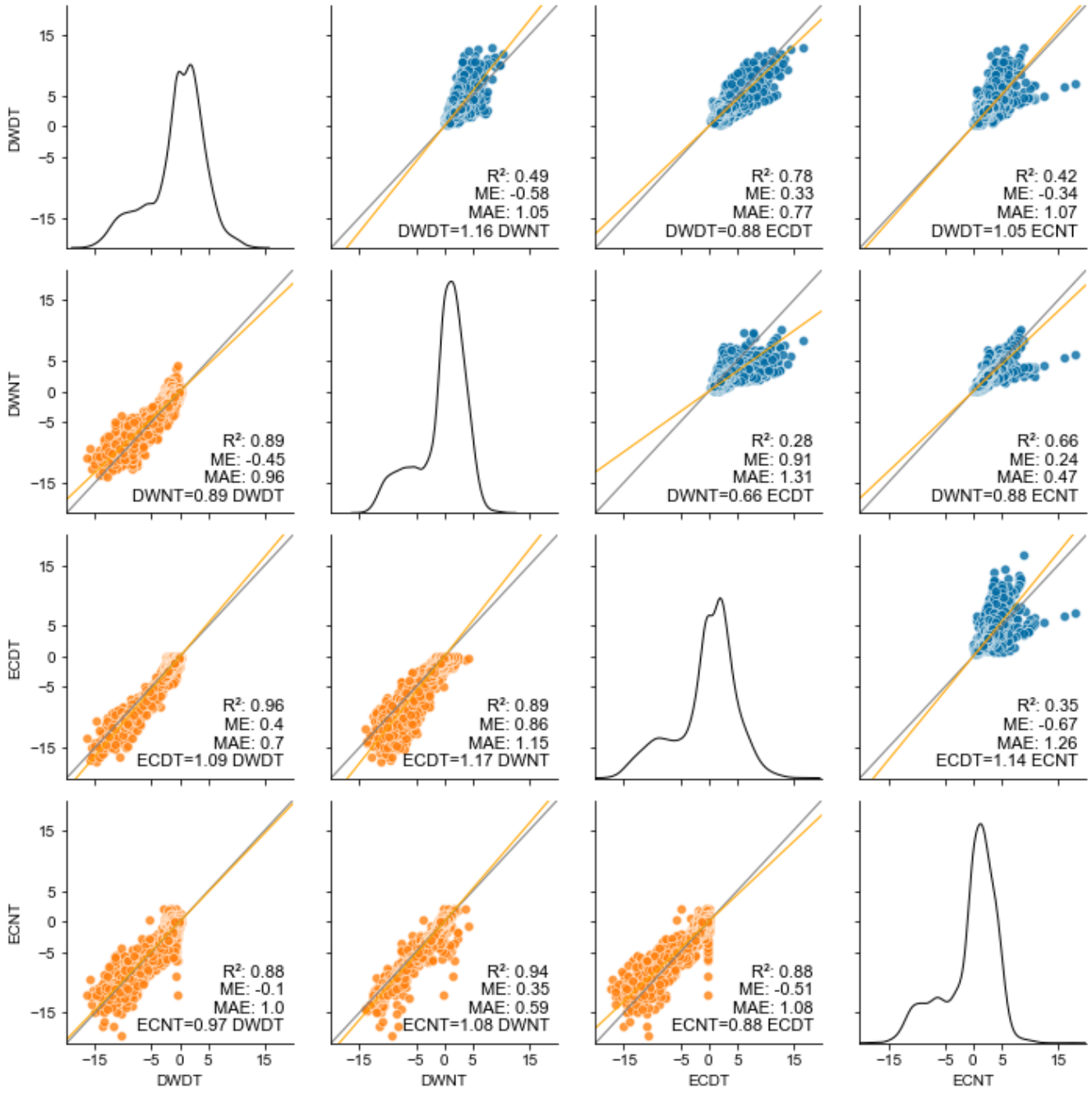

Figure S 4.4. Correlation Matrix for GPP (orange, bottom-left) and R_{eco} (blue, upper-right) estimations, sites combined. NT and DT partitioning methods were used, with NEE calculated using standard EC (ECNT and ECDT, respectively) and discrete wavelets (DWNT and DWDT).

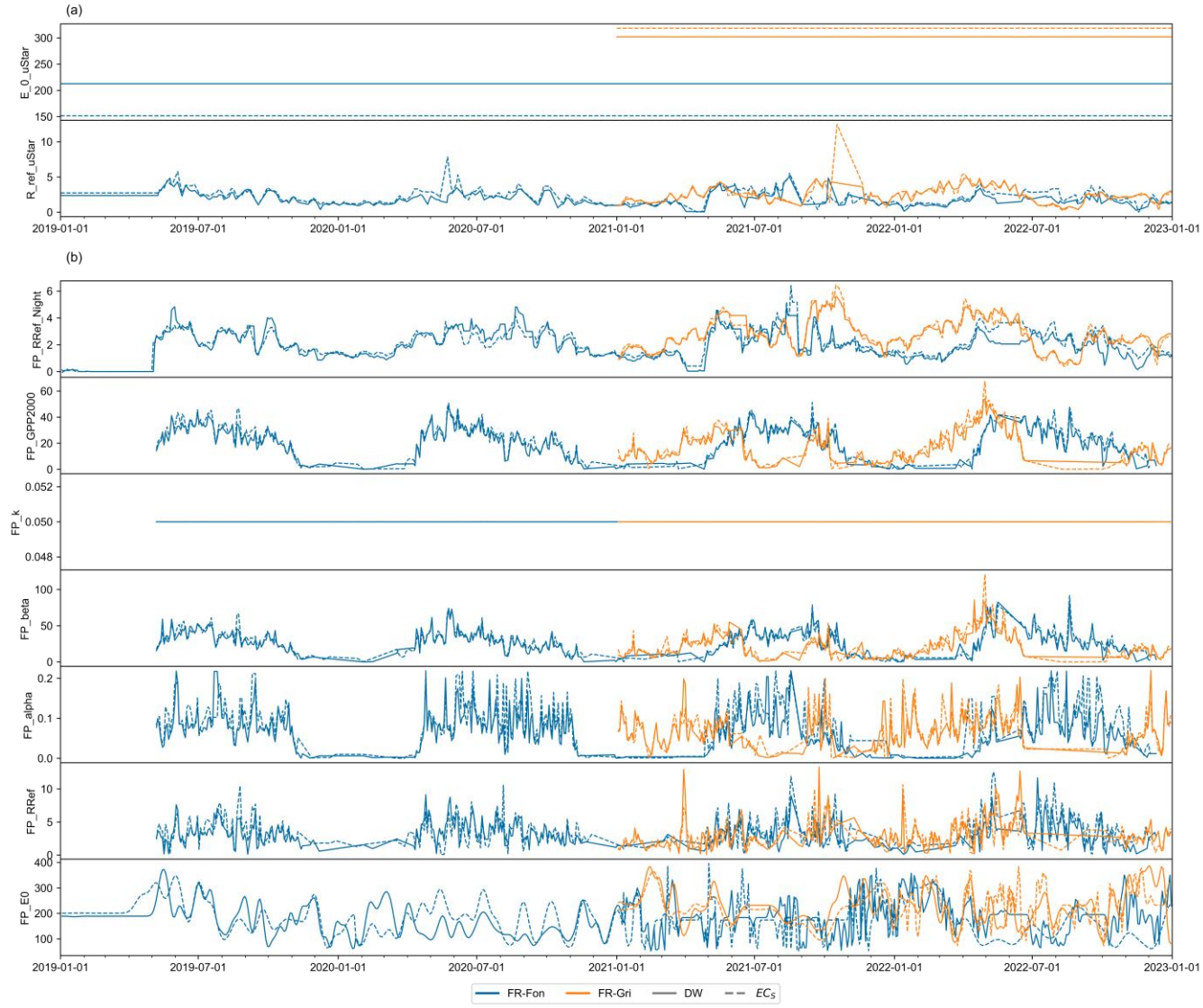

Figure S 4.5. (a) Parameters estimated for night-time partitioning method (NT). (a) Parameters estimated for day-time partitioning method (DT).

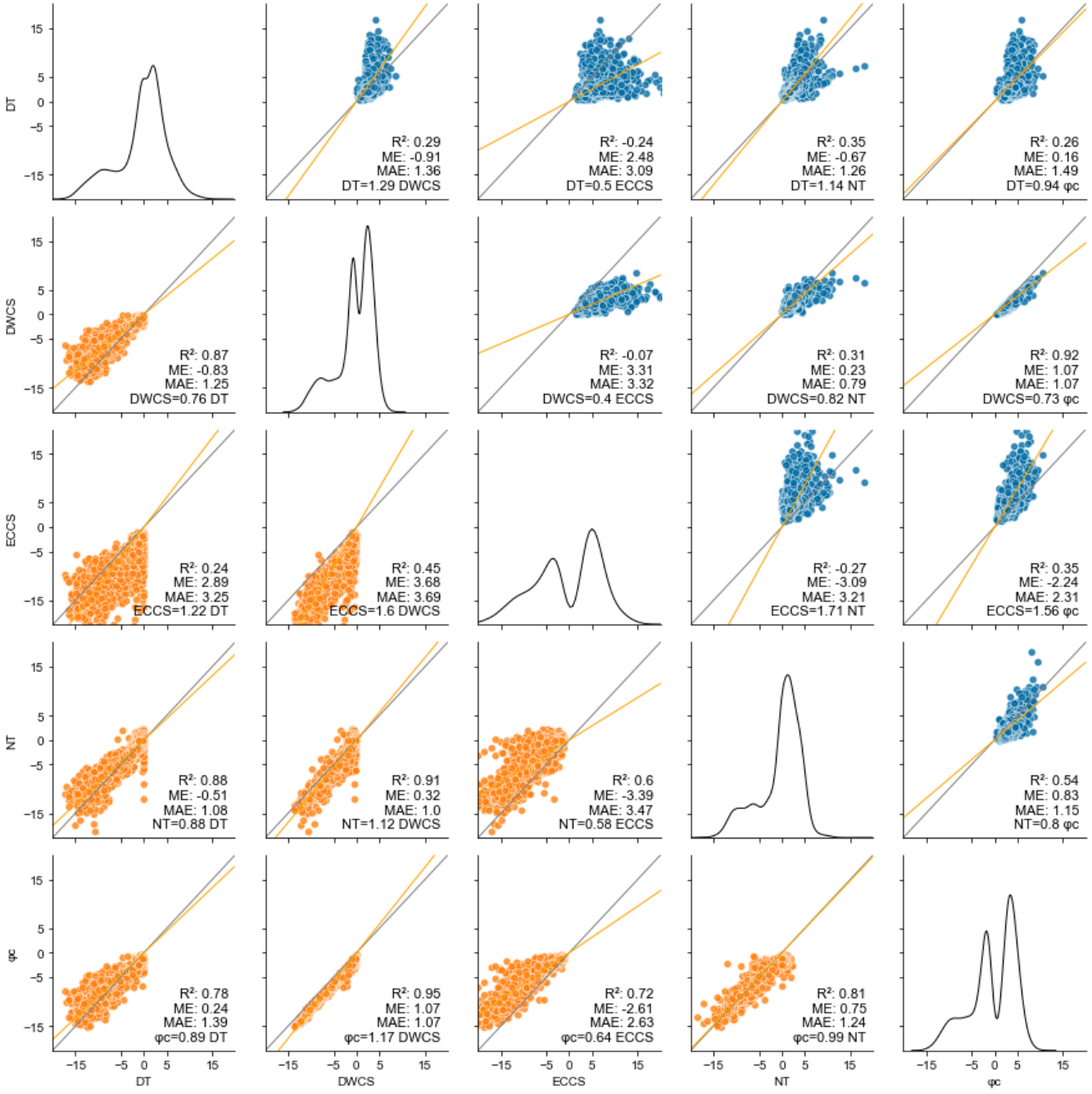

Figure S 4.6. Correlation Matrix for GPP (orange, bottom-left) and Reco (blue, upper-right) estimations, sites combined, using the following partitioning methods: NT, DT (with light inhibition), DW-CS (DWCS), φ_c, and ECCS (same partitioning as DWCS but used for $\boldsymbol{w'\chi_{co_2}}$' without wavelet decomposition). The diagonal shows flux distribution.

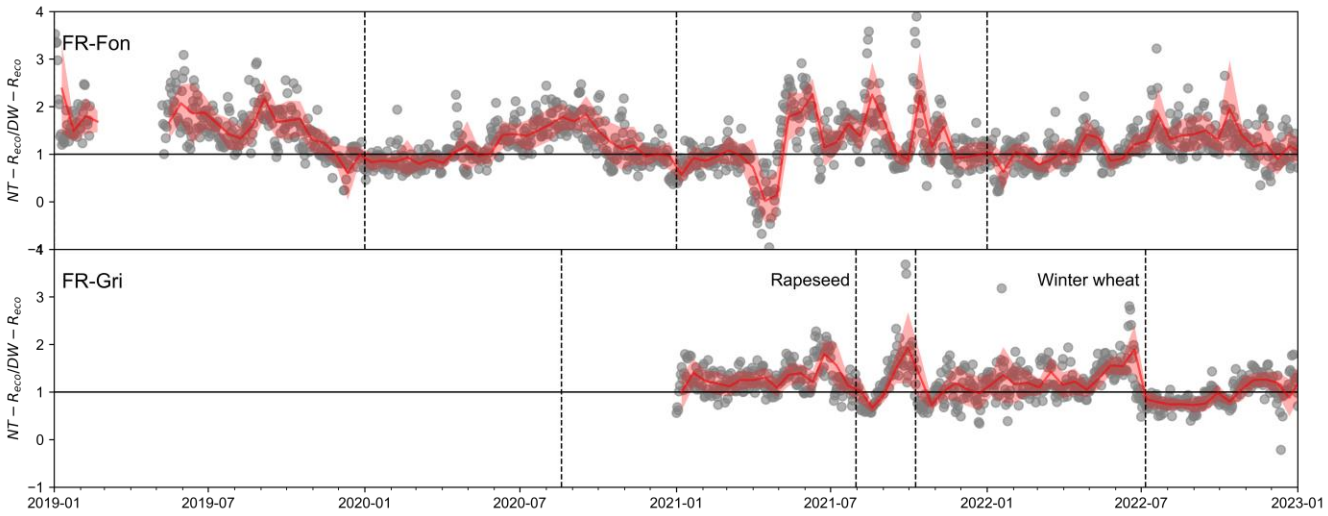

Figure S 4.7. Ratios of daily ecosystem respiration (R_{eco}) are estimated by a standard night-time modelling approach (NT) and measured by discrete wavelet conditional sampling (DW). Symbols indicate daily NT and DW ratios for 2019–2022; the red line represents the block average (window size = 14 days) with shaded bands indicating ±1 standard error. The horizontal line represents the unity of the ratio. Vertical dotted lines represent the start or end of the season (calendar years for forest site FR-Fon and crop season for FR-Gri).

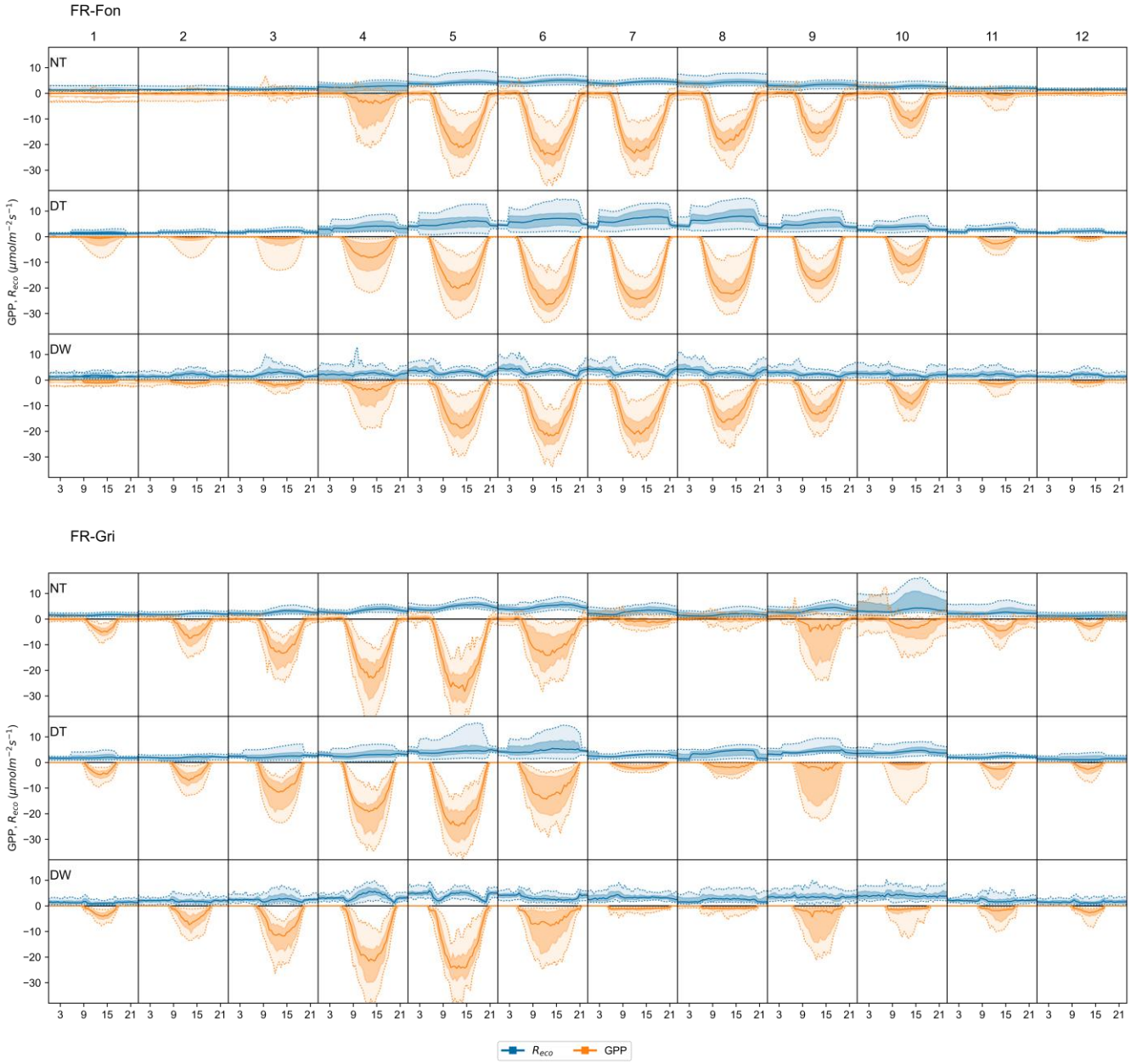

Figure S 4.8. Monthly averaged half-hourly GPP and R_{eco} estimations using NT, DT and DW methods. The darker region indicates interquartile (25th and 75th percentile), and the lighter region with dotted lines indicates the 5th and 95th percentile.

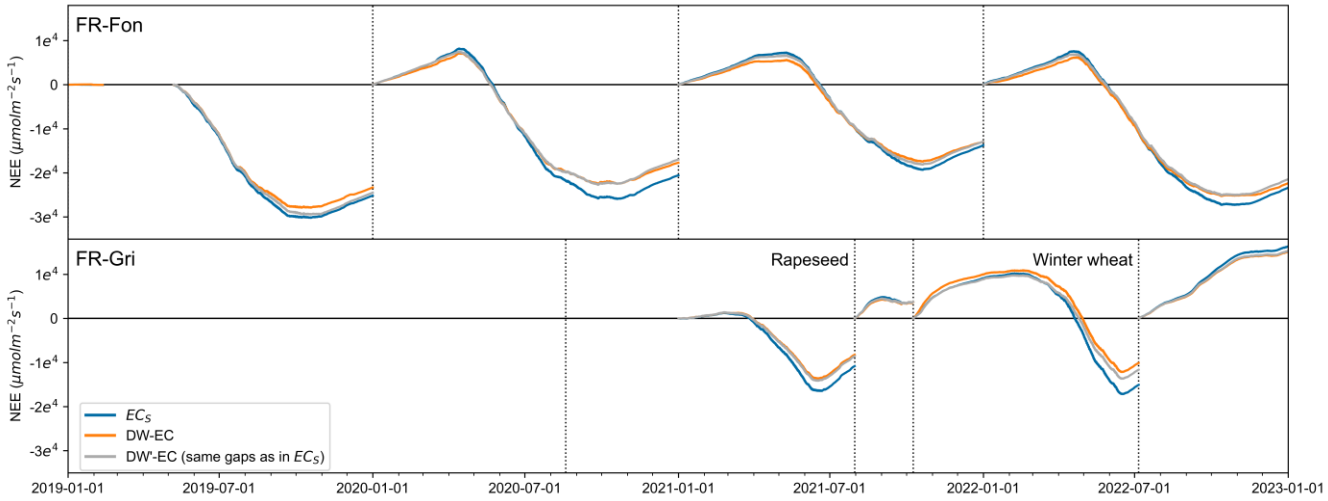

Figure S 4.9. The seasonally cumulated sum for NEE in Figure 4.6 (a) includes additional discrete-wavelet-based NEE forcing the same gaps as EC_S (DW'-EC).

5. MEASURING FLUX WITH SLOW-RESPONSE ANALYSERS ON TALL TOWERS

In atmospheric science, tall towers serve as crucial platforms for ground-based monitoring stations. They are instrumented with high-precision analysers that often measure more than one trace gas. Atmospheric and ecosystem measurements have developed worldwide networks, though mainly concentrated over the northern hemisphere. Tall towers, in particular, offer a promising middle ground as they can be used to measure both fluxes and background concentration. Leveraging the existing atmospheric networks for flux measurements has the advantage of geographically expanding the network and adding trace gases standardly measured in ICOS atmospheric towers, such as carbon monoxide (CO) and methane (CH_4).

CO and CH_4 can be used as tracers of fossil fuel combustion and effectively help monitor anthropogenic emissions. Indeed, partitioning in complex landscapes is complex due to mixed biogenic and anthropogenic fluxes and is challenging to disentangle. Atmospheric inversions, statistical models, and novel methods like wavelet-decomposed covariance and filters allow partitioning flux into biogenic and anthropogenic components. Repurposing such methods for urban settings may involve identifying gases with distinct signatures for different emissions sources, and here, these additional trace gases may play an important role (see next Chapter).

However, there are some technical challenges, particularly regarding the adaptation of equipment not initially designed for eddy covariance measurements, particularly employing a gas analyser with high precision but with a slower response time (~3 seconds) and long tubes (100 metres).

Chapter 4 delves into the synergy between atmospheric and ecosystem monitoring networks, leveraging instruments installed on an ICOS atmospheric tall tower in conjunction with a 3D anemometer. This Chapter evaluates the feasibility of this setup to compute surface fluxes evaluating it by comparing with standard eddy covariance setup at 100 meters on the ICOS FR-SAC atmospheric tower.

The fluxes computed in the Chapter will be used in Chapter 5 to compute partitioned CO_2 fluxes, Reco, GPP and anthropogenic sources and map the fluxes around the Saclay ICOS tower.

5.1 Article: Eddy-covariance with slow-response greenhouse gas analyser on tall towers: bridging atmospheric and ecosystem greenhouse gases networks

Citation: Herig Coimbra, P. H., Loubet, B., Laurent, O., Bignotti, L., Lozano, M., and Ramonet, M.: Eddy-covariance with slow-response greenhouse gas analyser on tall towers: bridging atmospheric and ecosystem greenhouse gases networks, Atmospheric Measurement Techniques Discussions, 1–44, https://doi.org/10.5194/amt-2024-71, 2024.

Submitted to Atmospheric Measurement Techniques on 19 April 2024.

Preprint available here: https://doi.org/10.5194/amt-2024-71, 13 May 2024.

Please note that the wavelet method described in this chapter follows the procedures outlined in 3. Any differences in nomenclature between the two may arise from variations in formalization but are duly addressed in the Materials and Methods section of the chapter. In doubt, please refer to the Materials and Methods section of the current chapter for clarification.

Eddy-covariance with slow-response greenhouse gas analyser on tall towers: bridging atmospheric and ecosystem greenhouse gases networks

Pedro Henrique H. Coimbra[1,2*], Benjamin Loubet[1], Olivier Laurent[2], Laura Bignotti[1], Mathis Lozano[2,] Michel Ramonet[2]

[1] ECOSYS, INRAE, AgroParisTech, Université Paris-Saclay, Palaiseau, France
[2] Laboratoire des Sciences du Climat et de l'Environnement, CEA, CNRS, Université Paris-Saclay, Gif-sur-Yvette, France

* corresponding author: pedro-henrique.herig-coimbra@inrae.fr

Abstract

Greenhouse gas monitoring is essential to ensure climate goals are being achieved. This study unveils the potential of using atmospheric tall towers in direct flux measurements, bridging the gap between atmospheric and ecosystem monitoring networks. The ICOS Cities (PAUL) project aims to monitor CO_2 emissions in urban areas, where concentrated emissions make them critical targets for climate change mitigation. Using the Eddy Covariance method, this study explores the synergy between ICOS atmospheric and ecosystem networks by utilizing slow-response analysers (~2 sec) on tall atmospheric towers for ecosystem studies. A standard setup with an ultrasonic anemometer and an infrared (IR) fast-response CO2 analyser was installed and compared with measurements from an existing cavity ring-down spectroscopy (CRDS) analyser measuring CO2, CO, and CH4. Deployed on the 100 m Saclay tower near Paris, covering a 43.9 km^2 80% footprint with heavy traffic roads, a nearby heating plant, and a forest, the setup addressed technical challenges and height-induced complexities. Corrections for flux attenuation by high-frequency losses were limited to <20% on average for all stabilities around 11% for unstable conditions. Wavelet-based eddy covariance allowed 18-34% more data exploitation than standard EC, enabling the analysis of non-stationary fluxes, particularly from a point source such as the case of a heating plant. The estimated storage term produced by atmospheric profiling measurements reported an expected increase at night, destocking during the first half of the day. Storage term represented at times more than half of the surface flux. Elevated mean fluxes for CO_2 (10

μmolm−2s−1) and CH_4 (200 nmolm−2s−1) were observed from the heating plant wind direction during December and January. Conversely, the forest direction exhibited the most substantial sink among all wind directions, with −4 μmolm−2s−1 during July and August. These results demonstrate the feasibility and versatility of utilizing atmospheric towers for urban emission monitoring, offering valuable insights for emission monitoring strategies worldwide.

5.2 Introduction

Global surface temperature is 1.6 °C warmer on land compared with the pre-industrial era (IPCC, 2021), and projections show more than 2°C warming in 2100 (IPCC, 2022). Warming results from the increase in greenhouse gas (GHG) concentration in the atmosphere, mainly driven by anthropogenic emissions (IPCC, 2021), of which 86% comes from fossil fuel CO_2 (Canadell et al., 2021). Agriculture, forestry and other land use (AFOLU) are a significant source of GHG (12.0 ± 2.9 GtCO2eq yr−1) while concurrently possessing the potential to remove CO_2 from the atmosphere (Jia et al., 2019).

Urban areas concentrate on human activities and represent a significant source of GHG emissions, consequently making it one of the targets for mitigating climate change. Many northern countries' cities have ambitious GHG emission reduction plans over the next 2 decades that consist of electrifying the energy grid, implementing car-free zones, and investing in insulation improvement. Consequently, an imperative for robust monitoring of urban areas' emissions reduction arises. Several works have tried to decompose eddy covariance measurements in (sub-)urban setups with different degrees of uncertainty (Velasco et al., 2009; Bergeron and Strachan, 2011; Ueyama and Takano, 2022). Currently, in Europe, the project ICOS Cities (PAUL) aims to advance technologies for monitoring CO2 concentrations in urban areas of three pilot cities of different sizes (Munich, Paris, and Zurich).

Monitoring GHG in the atmosphere, ocean, and ecosystem is the objective of world-distributed research infrastructures such as ICOS in Europe (Heiskanen et al., 2022). To that purpose, different methods are used on terrestrial sites. Ecosystem sites focus on local flux monitoring using high-frequency measurements, while atmospheric towers measure precisely the concentrations as an imprint of larger-scale fluxes. Ecosystem sites measure surface fluxes representing a specific biome determined by the tower's footprint. In contrast, atmospheric sites have a footprint spanning several hundreds of km^2 and may be used to identify anomalies in CO_2 surface fluxes based on concentration (Ramonet et al., 2020) or retrieve surface flux by inverse modelling, eventually using tracers (Ciais et al., 2011).

At the local scale, Eddy Covariance (EC) is the reference method for GHG monitoring. The method is praised for directly and continuously measuring surface turbulent flux and broadly applied since early measurements to different gases, including water vapour, CO_2, CH_4 and N_2O (Valentini et al., 1996; Moncrieff et al., 1996; Fowler et al., 1995). Standard measurements require fast-response instruments, a technical limitation for measuring specific compound concentrations. Long-term measurement sites are equipped with CO_2 and H_2O gas analysers, and some wet or agricultural sites with N_2O or CH_4 analysers (Nemitz et al. 2018). At larger scales, atmospheric concentration measurements are often used alongside meso-to-continental scale transport

models to solve surface flux (Lauvaux et al., 2012). Direct EC measurements often validate This top-down approach locally (Vuichard et al., 2016).

The differences between a typical atmospheric and a flux tower monitoring setup are that: (1) atmospheric towers are taller (above 100 meters height), whereas flux towers range from 2 to 40 meters height. This height difference is because atmospheric measurements are set to catch the seasonal and annual trend in atmospheric background concentrations at the regional scale, which requires limiting the impact of local sources (Yazidi et al., 2018); (2) atmospheric towers have more precise measurements but slower, not cadenced, sampling rate around a few seconds, whereas EC sample from 5 to 20 Hz. (3) ecosystem stations have ecosystem monitoring (vegetation and soil sampling), which are not measured in atmospheric stations, while these measure additional gaseous compounds (CH_4, N_2O, CO) (Hazan et al., 2016).

Using slow-response analysers to calculate flux by eddy covariance has been identified as a valuable strategy for expanding the flux networks to other compounds (Wohlfahrt et al., 2009). Atmospheric towers have high-precision analysers, which, if we can use them to compute Eddy-Covariance fluxes, would provide multi-species flux measurements that would expand the flux network. Integrating atmospheric towers as flux towers would require a fast 3D anemometer and continuous data logging at these sites. However, the constraints for concentration and flux measurements are different, so not all towers may be suitable. For any atmospheric tower, a couple of adversities must be addressed first. Discarding atmospheric stations on mountains that have unsuitable conditions for flux measurements, we focus on tall towers over reasonably flat landscapes:

- Firstly, measuring flux with a 3s-response time analyser is challenging. Indeed, fast-response analysers, typically with a 100 millisecond response time, are needed for flux measurements to capture the small and fast eddies (turbulent fluctuations) that carry most of the flux signal in the surface layer (Kaimal and Finnigan, 1994). Using slow-response analysers on short towers would mean losing most of the signal. For instance, the frequency with the highest contribution to the flux on a 4- and 37-meter tall tower was 0.16 Hz (6 s period) and 0.02 Hz (50 s period), respectively (Coimbra et al., 2023). Using a slow analyser in these towers would attenuate the flux by 65-80 % and 30-45 %, respectively, in unstable conditions with wind speeds from 3 to 7 m/s, and even more significant attenuation is expected in stable conditions. Fortunately, the contribution of higher frequencies to the EC flux is inversely proportional to height (Horst, 1997), and so for the same unstable conditions, measurements at 100 m would give a peak contribution between 0.002 and 0.009 Hz (8.3 and 1.85 minutes period) and the high-frequency attenuation would therefore be small (10-20%). High-frequency (HF) corrections based on predefined or experimental co-spectra profiles are well-established and routinely applied to correct for tube attenuations in ICOS and other flux networks (Horst, 1997; Massman and Lee, 2002; Ibrom et al., 2007; Fratini et al., 2012). We, therefore, expect sampling with slow-response analysers at tall towers to be suitable because the peak of the covariance co-spectrum would be well caught and could be corrected with standardised approaches (Massman, 2000).

- Secondly, the height also affects the source area. Taller towers have a bigger footprint and often higher heterogeneity, commonly including artificial and vegetated patches in the same wind sector. Heterogeneity and point sources can induce sudden shifts in the concentration due to wind direction changes, flagged as non-stationary by standard eddy covariance procedures. This quality filtering results in the loss of a significant amount of data for less stationary surface fluxes, such as CH_4 and N_2O (Irvin et al., 2021; Mishurov and Kiely, 2011). Whereas standard EC requires stationarity, wavelet-based EC does not (Torrence and Compo, 1998; Mallat, 1989; Farge, 1992; Farge and Schneider, 2001). Wavelet-based EC methods are sought in airborne campaigns when short-time resolution is needed (Strunin and Hiyama, 2004; Mauder et al., 2007; Desjardins et al., 2018; Metzger et al., 2013) and have been used to retrieve outbursts and non-stationary flux (Schaller et al., 2017; Göckede et al., 2019). By not requiring stationarity, they yield high-quality data with fewer gaps. In two ICOS ecosystem sites, Wavelet-based EC methods have increased the number of high-quality observations by 17% to 29 % (Coimbra et al., 2023). The number may even be greater in urban conditions where point source and denser landscape would enhance surface flux heterogeneity.

- Lastly, the height also requires accounting for storage fluxes below the EC measurement height and vertical advection fluxes components (Aubinet et al., 2005). Storage flux arises from the accumulation or release of the compound below the measurement height. Hence, the flux at the ground is the sum of the flux at the measurement height and the storage flux below. Positive storage flux may result from the decoupling of surface and atmospheric dynamics. Such decoupling may arise especially under a stably stratified surface layer, occurring at night above canopies and especially under radiative cooling conditions (Kaimal and Finnigan, 1994). Negative storage fluxes arise during the early morning when the atmospheric boundary layer rises and the stably stratified layer breaks down (Aubinet et al., 2005). At tall towers, the storage can be high and remain significant in the morning when the vegetation starts photosynthesizing, but the turbulence is still low (Haszpra et al., 2005). At very tall towers (300 m), the storage dominates the flux dynamics (up to 95% of the total flux, Winderlich et al. 2014). It should be noted that under ideal surface homogeneous conditions, the storage term is expected to tend to zero when averaged over a day and hence only affect the surface flux dynamics but not the integrated fluxes.

In atmospheric towers, ICOS routinely focuses on measuring not only CO2 but also CO and CH4 concentrations. Therefore, measuring fluxes on these towers potentially enables the measurement of CO and CH_4 fluxes in the surrounding areas of each tower.

On mid-latitudes in the northern hemisphere, most CO emissions (14,000 $TgCOyr^{-1}$, 54%) come from direct (fossil or bio) fuel combustion (Zheng et al., 2019). We expect this emission to increase during winter due to the diminished efficiency of fuel combustion induced by colder temperatures (Helfter et al., 2016). Additionally, a substantial contribution to CO levels stems from the chemical oxidation of CH_4 (900 $TgCOyr^{-1}$, 40%) and volatile organic compounds (VOCs) (300 $TgCOyr^{-1}$, 12%) (Zheng et al., 2019). This oxidation process makes vegetation an indirect CO emitter through the release of biogenic VOCs, but this production is not local and would not

appear as a flux from the surrounding of the tower. Soil also emits VOCs up to three orders of magnitude lower than canopy emissions under usual conditions (Peñuelas et al., 2014). On the contrary, soils are mainly recognized as CO sinks (15 times stronger than soil sources), primarily attributed to microbial oxidation processes (Inman et al., 1971; Conrad and Seiler, 1980; Conrad, 1996).

Globally for the 2008–2017 decade, the majority of CH_4 emissions arise predominantly from wetlands natural emissions (~24%), enteric fermentation and manure (~17%), and fossil fuels (~17%) (Saunois et al., 2020). Wetland emissions are concentrated in tropical and southern regions (< 30◦ N), while fossil fuels are the predominant source in mid-latitudes (30–60° N). Agricultural waste contributes significantly in tropical and mid-latitude areas (Saunois et al., 2020). In-situ observations showed considerable emissions from marshes (41±21 $gCm^{-2}yr^{-1}$), lakes (28±33 $gCm^{-2}yr^{-1}$), swamps (26±20 $gCm^{-2}yr^{-1}$), and fens (20±16 $gCm^{-2}yr^{-1}$) (Delwiche et al., 2021). The high emissions from marshes and high variability for lakes highlight the dependence of sediment for CH_4 emissions. In a high flux lake (JP-SwL, 67 $gCm^{-2}yr^{-1}$), emissions can vary from a monthly average of 0.1 $\mu molm^{-2}s^{-1}$ to 0.3 $\mu molm^{-2}s^{-1}$ from winter to summer (Iwata et al., 2020). Fossil fuels observations from a 190 m tall communications tower in the centre of London showed a mean annual CH_4 flux of 46.5 ± 5.6 g C m^{-2} yr^{-1}, increasing in the winter attributed to a seasonal increase in natural gas usage (Helfter et al., 2016). With that said, soils not only produce CH_4 but also consume it. Indeed, soil oxidation is the primary inland process for CH_4 consumption (Canadell et al., 2021), making upland soils a net sink (Dutaur et Verchot, 2007).

In this study, we evaluate the capability of using an atmospheric monitoring tower with a slow response analyser supplemented with a sonic anemometer to compute surface fluxes of CO_2, CH_4 and CO. To that purpose, we installed a standard eddy covariance setup for CO2 and H2O at 100 m at the ICOS FR-SAC atmospheric tower in the south of Paris, collecting 4 months of data from July 2023 until October 2023. The chosen site is a sub-urban site surrounded by agriculture, forest, wetlands, roads, and buildings. We then computed net CO_2 flux for slow and fast-response analysers and compared them. The high-frequency losses were determined, and the correction procedure was evaluated. The fluxes were calculated using the wavelet-based eddy covariance method detailed in Coimbra et al. (2023), while the storage flux was computed using three-point profile concentrations routinely measured at the ICOS tower. The seasonal variations with wind directions of the CO_2, CH_4 and CO fluxes were then discussed.

5.3 Material and methods

5.3.1 Site description

The study uses data from a 100-meter tall tower in the French Alternative Energies and Atomic Energy Commission (CEA) at a research campus in Saclay, 20 km southwest of Paris (Figure 5.1). The tower is part of the ICOS atmospheric network (FR-Sac) and participates in the ICOS Cities, Pilot Applications in Urban Landscapes (PAUL) project, which focuses on integrated city observatories for greenhouse gases. Climatically, the area is under oceanic influence with mild temperatures (11.5°C annual mean) and moderate precipitations (677-700 mm annual). The surrounding landscape is dominated by artificial (buildings, roads), agriculture (mainly cereal) and

forest. The region serves as a pathway for urban-to-suburban daily mobility, with more than 60 thousand vehicles every day in 2022, according to SIREDO in the national (N118) and regional (D306, D36, D128) roads.

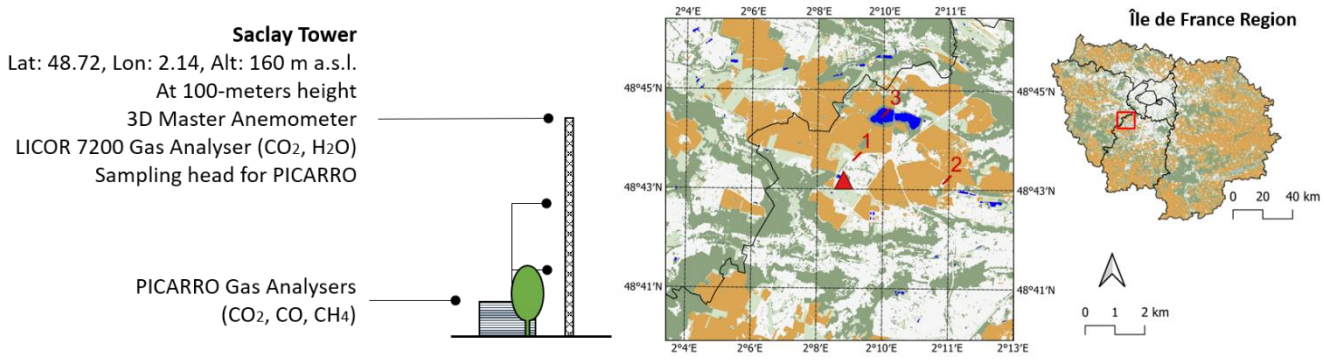

Figure 5.1. Site diagram showing tower and acquisition house with tree height for scale. On the right panel, site map and localisation in the region. Colours indicate land use: cropland (orange), grassland (light green), forest (dark green), water (light blue), and white (urban). For reference, (1) a heating plant, (2) a manure/composting plant, and (3) a lake.

Since 2011, the site has been equipped with high-precision cavity ring-down spectroscopy (CRDS) gas analysers (CO_2, CO, CH_4, G2401; Picarro Inc., Santa Clara, CA, USA) with a varying time response of a few seconds. The analyser is placed in a ground-level hut, connected to 3 sampling lines, 9.5 mm in internal diameter, collecting air at the 3 different heights of the tower (15, 60, and 100 meters above ground level) alternatively every 10 minutes. Since 2017, a second multi-gas analyser has been measuring continuously through a parallel sampling line connected to the top of the tower (100 meters above ground level).

The flow rate through the sampling lines is set around 12 L min^{-1} but with no control. At the bottom of all lines connected to the CRDS analyzer, the air is dried with Nafion (PermaPure, model MD-070-144S-4). The CRDS gas analysers followed the ICOS calibration procedure aiming for a precision higher than 50, 1 and 2 ppb for CO_2, CO and CH_4 (ICOS RI, 2020). From June to October 2023, we set up a complete Eddy Covariance system at 100 m, consisting of a closed-path infrared (IR) gas analyser (LI-7200; Li-Cor Inc., Lincoln, NE, USA), a 0.7 m heated tube with a flow rate set to 15 L min^{-1} and a three-dimensional sonic anemometer (Gill WindMaster; Gill Instruments Ltd, Lymington, Hampshire, UK). The tower is also equipped with pressure (Vaisala PTB200), humidity and temperature sensors (Vaisala HMP155) at 1.5, 60 and 100 m.

Half-hourly average dry CO_2 mixing ratio showed a high degree of comparability between instruments (R^2 0.97) and no bias (slope=1) (Figure 5.2). Nonetheless, we found an offset of 7.25 ppm and an average drift of -11 ppm yr^{-1}, which does not impact eddy covariance flux.

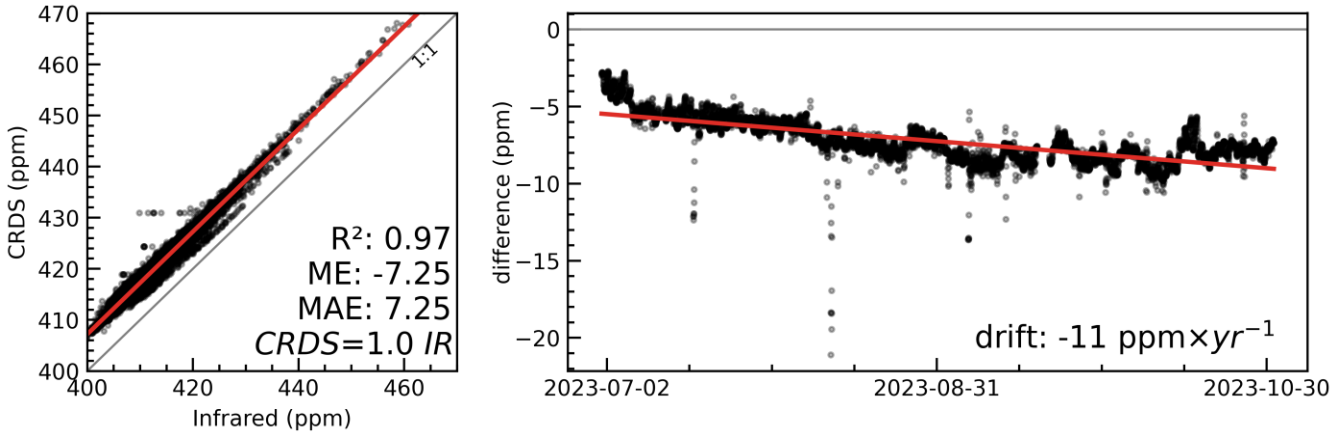

Figure 5.2. Comparison between dry CO_2 mixing ratio measured by the IR (LI-7200) and the CRDS (PICARRO G2401) analysers. Left panel: scatter plot. Right panel: mixing ratio difference (IR-CRDS) as a function of time. Dots are observations; the red line is a linear fit, and the grey line is a 1:1 line. The correlation coefficient (R^2), the mean error (ME, ppm), the mean absolute error (MAE, ppm), the linear fit and the drift.

Data was unavailable for most of November due to instrument maintenance. The IR (LI-7200) was set up unconventionally with the analyser horizontally, and the sampling tube vertically with a U-shaped head and a rain cap turned downwards. The choice was made based on the safety of maintenance on top of the tower. Unfortunately, the IR malfunctioned during the measurement campaign and prevented all analysers from running simultaneously for the whole period.

5.3.2 Data processing

The mass balance equation to compute surface flux includes storage, advection, and turbulent transport (Foken et al. 2012). For the scope and goals of this work, vertical and horizontal advection was considered negligible, assuming dynamic horizontal homogeneity of the surface. The vertical component of the wind (w) and the mixing ratio of a scalar s (χ_s) can then be used to calculate flux at the surface F_{eco}based on the turbulent covariance ($\overline{w'\chi_s'}$) measured at a certain height (h_m), and the storage term ($\int_0^{h_m} \frac{\partial \overline{\chi_s}}{\partial t} dz$, where t is time and z is the height). Here, overbars stand for time averaging. The surface flux F_{eco} (μmol m^{-2} s^{-1}) can be then expressed as a function of the molar volume of dry air $V_a = \frac{RT_a}{P-e}$, where P is atmospheric pressure (Pa), e is vapour pressure (Pa), R is the ideal gas law constant (8.31 J kg^{-1} K^{-1}), and T_a is air temperature (K):

$$F_{eco} = \left(\int_0^{h_m} V_a^{-1} \frac{\partial \overline{\chi_s}}{\partial t} dz + V_a^{-1} \overline{w'\chi_s'} \right) \quad (5.1)$$

Storage flux computation

The storage flux was computed as in Aubinet et al. (2005) as the derivative over time of scalar s contained in the column below the measurement height (100 m):

$$ST_s = \int_0^{h_m} V_a^{-1} \frac{\partial \overline{\chi_s}}{\partial t} dz \sim \frac{\Delta \sum_1^3 V_{a_i}^{-1} \overline{\chi_{s_i}} \Delta z_i}{\Delta t} \quad (5.2)$$

Where Δt is 30 min, index i stands for the three layers (0-15, 15-60, 60-100, and $\Delta z_i$is the layer depth. The scalars CO_2, CO and CH_4 were measured at 15, 60 and 100 m with the CRDS analysers. The dry air volume ratio was computed at each height based on measured air relative humidity and temperature. The storage was calculated using the three levels of measurements done by the same instrument alternating between the three heights for periods of 10 minutes. The 10-minute average measurements were linearly interpolated. The 30-minute average was computed, and the time derivative was calculated at that time step.

Turbulent flux calculation

The turbulent flux was calculated based on a covariance, thus the name of the method Eddy Covariance (EC). Pre-processing is required and was done using EddyPro 7.0.9, applying de-spiking (Mauder et al., 2013), covariance maximization for time lag, and double rotation (Wilczak et al., 2001). Time lag relates to the delay from sampling and measurement, and the maximization can lose reliability under noisy measurements (Langford et al. 2015). Typically, a default value and bounds are set individually for each gas and gas analyser. If an optimal value falls within the bounds, it is retained; otherwise, the default is chosen. Based on tube dimensions and flow rate, the LICOR 7200 analyser's lag time was set to 0.09 ± 0.35 s. For the PICARRO analysers with a 100 m line, the lag time was set to 60 ± 2 s based on comparison with the LICOR 7200 CO_2 concentration. This lag time is compatible with a ~12.6 L min−1 flow rate. The ± 2 s tolerance was included to account for the uncertainty over the precise travel time and possible seasonal changes linked to air viscosity dependency on temperature and filter dirtiness.

In addition to the standard EC calculated by EddyPro 7.0.9, we used a second flux processing method based on discrete wavelet transform (Coimbra et al., 2023) (Appendix A). This method decomposes a time series (x) into sub-series ($\tilde{x}$), each defined in a given frequency domain *j* :

$$x(t) = \sum_{j=0}^{J} \tilde{x}(t,j) \quad (5.3)$$

Where j is the scale level corresponding to a given frequency $f_j = s_0^{-1} 2^{-j\delta_j}$, for $j = 0, 1, \ldots J$, where s_0 is the sampling rate (0.1 s in this study) and δ_j the frequency resolution (1 for discrete wavelets). When using discrete wavelets, since frequencies are independent (Coimbra et al., 2023, appendix A), we can calculate the covariance of w and χ_s in each frequency band $\overline{\tilde{w}\tilde{\chi}_s}(j)$ by a simple multiplication of the decomposed sub-series $\tilde{w}(t,j)$ and $\tilde{\chi_s}(t,j)$:

$$\overline{\tilde{w}\tilde{\chi}_s}(j) = \overline{\tilde{w}(t,j) \times \tilde{\chi}_s(t,j)} = \int_{j-1}^{j} Co_{w\chi_s}(f) df \quad (5.4)$$

For continuous wavelets, a different formula (Farge, 1992; Torrence and Compo, 1998; Farge and Schneider, 2001) or an empirical wavelet-specific correction factor (Coimbra et al., 2023) should be applied. We note in eq. (4) that the frequency-resolved covariance $\overline{\widetilde{w}\widetilde{\chi}_s}(j)$ is also the integration of the co-spectrum of $Co_{w\chi_s}(f)$ in the frequency band j^{-1} to j, which EddyPro can compute. The sum of the wavelet-decomposed covariance then yields the covariance:

$$\overline{w'\chi_s'} \approx \sum_{j=1..J} \overline{\widetilde{w}\widetilde{\chi}_s}(j) \qquad (5.5)$$

A detailed description of the wavelet method, the wavelet transform, and the corresponding flux data processing can be found in Appendix A1 and in (Coimbra et al., 2023). In this study, we used a discrete Daubechies (k=6) wavelet (Daubechies, 1988), ensuring the influence cone was larger than the period selected. All fluxes were averaged every 30 minutes, integrating up to the closest available period (6.1×10^{-4} Hz or 27 min). Despiking (Mauder et al., 2013) was used on each frequency-decomposed sub-series ($\tilde{x}$) to eliminate any unrealistic values identified and replace them using a linear interpolation. For EC flux calculation, the slow-response analyser (PICARRO) was resampled to 10 Hz to synchronize with the sonic anemometer sampling rate. The resample was achieved by repeating each measured value until it changed.

Quality flags and stability classes

Quality flags were assigned using the standard 0-1-2 flag system from FLUXNET (Mauder and Foken, 2011), involving tests for stationarity and fully developed turbulence (Foken and Wichura, 1996). Stationarity is essential to equate ensemble and time averages, as turbulent fluctuation is formally defined as a deviation from the former rather than the latter. Standard eddy covariance (EC) cannot be used for non-stationary events, but wavelet decomposed series are stationary in each scale, eliminating the need to flag out these data.

The stationarity test (STA) measures the absolute relative deviation between 5 and 30-minute covariances, while the turbulence test (ITC) assesses the deviation between measured and modelled integral turbulent characteristics. Data is considered of high quality (< 30 %), medium (30 – 100 %), or low (>100 %), based on deviation percentages for each test (worst applicable result prevails). A detailed description of the quality flags can be found in Foken and Wichura (1996).

Stability classes were defined using the stability parameter $\zeta = (z - d) / L$, where z is the measurement height, d is the zero-plane displacement height, and L is the Obhukov length. We classified stability as unstable ($\zeta < -0.2$), near neutral ($-0.2 > \zeta > 0.2$), and stable ($\zeta > 0.2$).

5.3.3 High-frequency corrections on noisy measurements

Instruments have measurement limitations, which decreases their ability to produce a true value. Closed-path gas analysers require a gas sample to pass through a tube system, which includes filters. Longer tube lengths typically result in increased time lag and reduced high-frequency

signal. The signal degradation can be represented by a transfer function, TF, which attenuates the high-frequency (Ibrom et al., 2007) of the true co-spectrum of *w* and a compound *s*:

$$fSp_{s,measured}(f) = fSp_{s,true}(f) \times TF \quad (5.6)$$

Where *f* is the frequency (Hz), Sp_s is the spectrum between *w* and a scalar *s*. Note that we can consider the transfer function equal for the spectrum and co-spectrum, as we neglect the *w* transfer function and spatial sensor separation for the case of this tall tower (Massman, 2000). We assume the true covariance can be estimated by multiplying the measured covariance by a correction factor, *CF*:

$$\overline{w'\chi'_{s}}_{true} = CF \times \overline{w'\chi'_{s}}_{measured} \quad (5.7)$$

Acknowledging that the covariance is the integral over all frequencies of the co-spectra, the correction factor CF can be calculated from the transfer function TF and a true co-spectrum, which is usually taken to be wT_s (where T_s is the ultrasonic temperature). Indeed, we assume the similarity of scalars in the atmospheric boundary layer and use the (co)spectrum of T_s as a proxy of unattenuated co-spectrum, as T_s is collocated to *w* (Ibrom et al., 2007). This yields for *CF*:

$$CF = \frac{\int Co_{wT_s}(f)df}{\int Co_{wT_s}(f) \times TF(f|f_c)df} \quad (5.8)$$

Where TF can be calculated in different forms and account for low and high-frequency attenuation, experimental methods are recommended for high-frequency spectral correction (Ibrom et al., 2007; Fratini et al., 2012). We can approximate an empirical TF, explained further down, using a first-order system, as the product of a transfer function *H* accounting for a first-order filter's time constant, τ_c, representing the system response time (s), and a transfer function H_p accounting for a generic phase shift φ as (Massman, 2000):

$$TF = H \times H_p \quad (5.9)$$

$$H = \frac{1}{1 + (2\pi f \tau_c)^2} \quad (5.10)$$

$$H_p = cos\varphi - 2\pi f \tau_c sin\varphi \quad (5.11)$$

Note that the cut-off frequency, f_c equals $(2\pi\tau_c)^{-1}$. Ideally, *H* would be the measured-to-true spectra ratio for the scalar of interest. However, only the measured spectrum is known and so eq. (5.102.8 is fitted using the sonic temperature T_s as a proxy of the unattenuated spectrum (Ibrom et al., 2007; Fratini et al., 2012; Peltola et al., 2021):

$$H = \frac{Sp_s(f)}{Sp_{s,true}(f)} \approx F_n \frac{Sp_s(f)/\sigma_s}{Sp_{T_s}(f)/\sigma_{T_s}} \quad (5.12)$$

Where F_n is a normalisation factor that accounts for any inaccuracies in the variance.

Sometimes $TF = H$ is used, and H_p is not considered (Ibrom et al., 2007). However, not accounting for the phase shift (e.g., using cross-covariance maximisation for lag correction and solely *H* for co-spectra correction) can bias CF (Peltola et al., 2021). Fortunately, $H_p \approx 1/\sqrt{H}$ which leads to $TF = HH_p \sim \sqrt{H}$ (Peltola et al., 2021). In this work we use Fratini et al. (2012) where $TF = \sqrt{H}$.

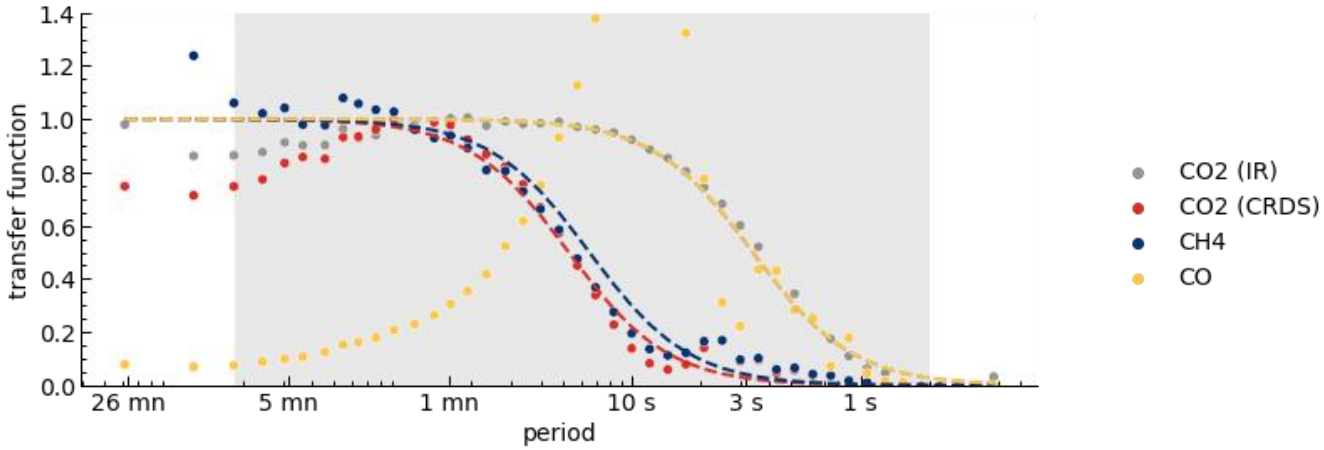

Figure 5.3. Transfer functions H (dotted lines) for each compound and analyser. The transfer function was fitted to the ratio of each compound's spectra to the sonic temperature spectra. All spectra are ensemble averages taken from EddyPro outputs, filtered for significant fluxes. Dots show the mean spectra per frequency band. The grey shaded area shows the frequency range (2 - 0.0018 Hz) over which transfer functions were fitted.

The spectra and co-spectra calculation were performed using EddyPro 7.0.9, following Fratini et al. (2012) described in equations 8-12. The transfer function *H*, accounting for the first-order filter's time constant τ_c, was estimated for each analyser and each compound through a least square minimisation approach of the spectra (Figure 5.3).

From the *H*, *TF* was computed as $\sqrt{H}$, and *CF* was calculated with eq. (5.8). For *TF* optimisation and *CF* calculation, only frequencies between 2 and 0.0018 Hz were used (see Figure 5.3). We assumed all compounds (CO_2, CH_4, CO) measured by CRDS (PICARRO G2401) suffered the same attenuation and used CO_2, the best-defined curve for all three analysers (Table 5.1). This assumption is grounded on the fact that measurements are done by the same instrument at the same acquisition rate sampled through the same line and is backed by the proximity between CH_4 and CO_2 spectra, while the CO signal noise can explain the unexpected CO spectra due to the lower signal-to-noise ratio. Indeed, the noise was already larger than the signal at periods longer than 5 minutes (Figure 5.3). Similarly, the small step increase of around 4 s for the CRDS analysers corresponds to the actual measurement interval.

Table 5.1. The transfer function parameters for each instrument account for high-frequency attenuation. Here $\boldsymbol{TF} = (\mathbf{1} + (\mathbf{2}\boldsymbol{\pi} \boldsymbol{f} \boldsymbol{\tau_c})^{\mathbf{2}})^{-\frac{\mathbf{1}}{\mathbf{2}}}$*, where* $\boldsymbol{\tau_c}$ *is the first-order filter's time constant. The cut-off frequency,* f_c*, equals* $(\mathbf{2}\boldsymbol{\pi}\boldsymbol{\tau_c})^{-\mathbf{1}}$*.* F_n *is a normalisation factor. The optimized values correspond to optimisations, as shown in Figure 3. The values used correspond to the optimised ones except for the CH4 and CO, for which the* CO_2 *parameters are used instead. See equations (8-12) and text for details.*

Instrument	Compound	Optimized			Used	
		τ_c (s)	f_c (Hz)	F_n (-)	τ_c (s)	f_c (Hz)
IR	CO_2	0.5	0.34	1.12	0.5	0.34
CRDS	CO_2	3.0	0.05	1.63	3.0	0.05
CRDS	CH_4	2.4	0.06	1.01	3.0	0.05
CRDS	CO	0.5	0.34	3.49	3.0	0.05

5.3.4 Spatial tools

For an analysis of the fluxes' footprint as a function of wind direction, we used a backward Lagrangian stochastic particle dispersion model (LPDM-B) for the footprint (Kljun et al. 2015), and computed vegetation indexes based on Sentinel 2 (ESA/Copernicus Data) and a French land use map (IGN, 2022).

Sentinel 2 data was collected using Google Earth Engine, a tool available at https://github.com/pedrohenriquecoimbra. To monitor vegetation, we calculated the enhanced vegetation index (EVI) using the following equation:

$$EVI = G\frac{NIR - Red}{NIR + C_1 Red - C_2 Blue + L} \quad (5.13)$$

Where NIR, Red, and Blue are surface reflectances centred in the 842, 665 and 490 nm wavelengths, band B8, B4 and B2 in Sentinel2, corrected for transfer through the atmosphere; L is the canopy background adjustment that addresses non-linear, differential NIR and red radiant transfer through a canopy, and C_1, C_2 are coefficients, G is a gain factor. We adopted the same coefficients as in the MODIS-EVI algorithm: L = 1, C1 = 6, C2 = 7.5, and G = 2.5. For all reflectance bands, we removed clouds using the Sentinel-2 Cloud Masking, *s2cloudless*, also available in Google Earth Engine. We classified clouds if the cloud probability was above 60 % and removed pixels considered cloud shadows based on a threshold of 0.15 for near-infrared and a maximum distance of 1 km from cloud edges. We also removed 50 m around the mask, assuming the cloud shadowing may still affect these pixels.

5.3.5 Performance measurements

Comparisons between instruments were carried out using mean bias and absolute error, defined as:

$$Mean\ Error\ (bias) = \frac{1}{N}\sum_{n=1}^{N}(X_{a,n} - X_{b,n}) \tag{5.14}$$

$$Mean\ Absolute\ Error = \frac{1}{N}\sum_{n=1}^{N}\left|X_{a,n} - X_{b,n}\right| \tag{5.15}$$

Where *N* equals the amount of data, *X* is the variable measured with instruments *a* and *b* at a time *n*.

In the figures, 95% confidence interval bands were calculated using the Seaborn module in Python. It uses random sampling with a replacement strategy, bootstrapping, to construct a confidence interval (Dragicevic, 2016).

If not declared otherwise, the squared loss, also named the ordinary least squares method, is used for linear fits. The method minimises the sum of the squares of the difference between the observed and predicted values. When robust or Huber loss is mentioned, we use a linear fit which minimizes the squared loss for the samples where the absolute difference between the observed, *y*, and predicted, *f*(*x*), values is smaller than δ and the absolute loss, sum of the absolute difference, otherwise. This feature makes it less sensitive to outliers than the squared error.

$$Huber\ loss = \begin{cases} \sum \frac{1}{2}\left(y_i - f(x_i)\right)^2, & |y_i - f(x_i)| \le \delta \\ \sum \delta(|y_i - f(x_i)| - \frac{1}{2}\delta), & otherwise \end{cases} \tag{5.16}$$

By default, we chose arbitrarily $\delta = 5$, noting that very low δ values may increase the number of values considered outliers.

5.4 Results

5.4.1 Mixing ratios of CO_2, CO and CH_4

In Figure 5.4, the diel pattern shows a peak in χ_{CO_2} during morning, 07:00 in July and moving towards 09:00 in October, and a clear valley around 15:00. The pattern disappears when moving towards winter months. CO and CH_4 show a similar peak in the morning autumn, although less marked. Only CO shows an afternoon peak in September, with the more apparent morning peaks for CH_4 and CO. Seasonally, CO_2, CO and CH_4 mixing ratio are the highest in winter, while H_2O is higher during summer. This difference may be explained by a larger biogenic CO_2 sink and H_2O source during the daytime in summer and a higher anthropogenic CO_2 emission in winter (heating on). The difference may also be explained by larger (smaller) boundary layer thickness during the summer (winter), which can effectively dilute (concentrate) the molecules emitted at the ground.

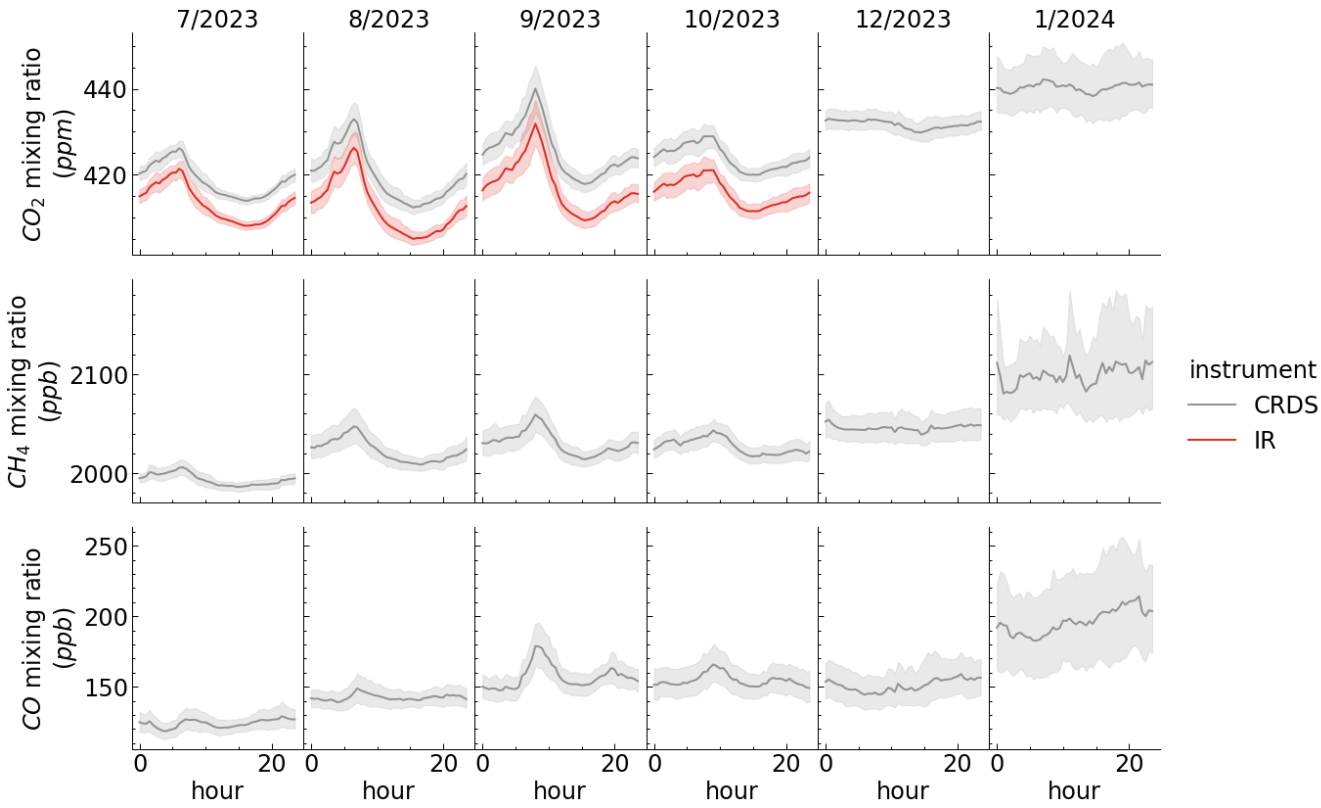

Figure 5.4. Monthly dry mixing ratios diel pattern for all measured gases (CO_2, H_2O, CH_4 and CO) for IR (LI-7200) and CRDS (PICARRO G2401). The solid line indicates the median, and the region shows a 95% confidence interval.

The mixing ratios vary with wind direction, which reveals some spatial patterns (Figure 5.5). During warmer months (July to October), the Westwind CO_2 mixing ratio was smaller than the median value, while for CH_4 and CO, we can notice a higher than the median value for the Northeast sector, especially clear for CO. In colder months (December and January), all mixing ratios were higher (also seen in Figure 5.4), with North-Easterly winds (0-180°) showing larger mixing ratios than in other directions. A peak in mixing ratios is observed for all three gases for winds coming from around 20°N, the direction from the heating plant. Interestingly, a smaller peak can be seen in the Northwest, in the direction of the lake (100 m afar), bare soil fields (around 500 m afar) and a regional road roundabout (around 1 km afar).

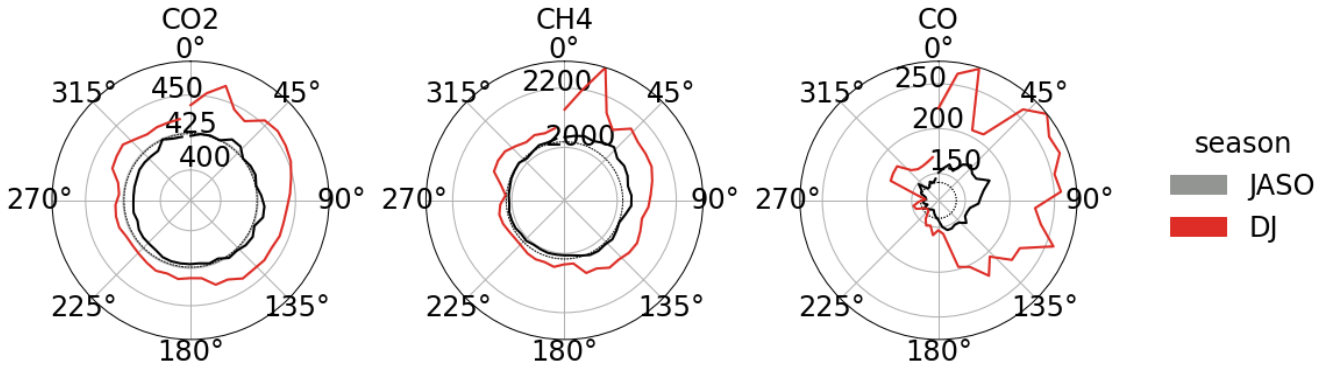

Figure 5.5. Average dry mixing ratios by wind direction. Warmer months (July to October) are in grey, and colder months (December and January) are in red. Extreme values in the left and right 0.1% tails were removed. See Figure S 5.1 for monthly observations. CO_2 is in ppm, while CH_4 and CO are in ppb.

5.4.2 Footprint and stationarity

Footprint analysis

A characterization of the site's flux footprint (Figure 5.6) shows a heterogeneous landscape composition comprising 25% urban, 23% agriculture, 21% forest, and 21% grassland areas. In the western part of the site (42% forest), there is a relatively dense woodland primarily featuring deciduous trees. To the south (41% grassland), the landscape includes a golf club near the CEA campus. In all directions, there are croplands, predominantly with cereal crops (winter wheat, barley, maize) and oilseeds (rapeseed), which are typical of the region. In the northeast (45% urban), the landscape aligns with the CEA campus's location, including a heating plant aligned to 20° N. The 43.9 km² 80% footprint encompasses a national road (N118) and several regional roads (D306, D36, D128) with a weekly traffic of 60 thousand vehicles on average (in 2022 according to SIREDO). Water ponds have a small contribution to the northwest to northeast sectors (2.3-2.6%). Two ponds are situated in these sectors, one approximately 100 meters from the tower (northwest) and a second larger farther away (around 2.4 km northeast, visible in the map Figure 5.6.a).

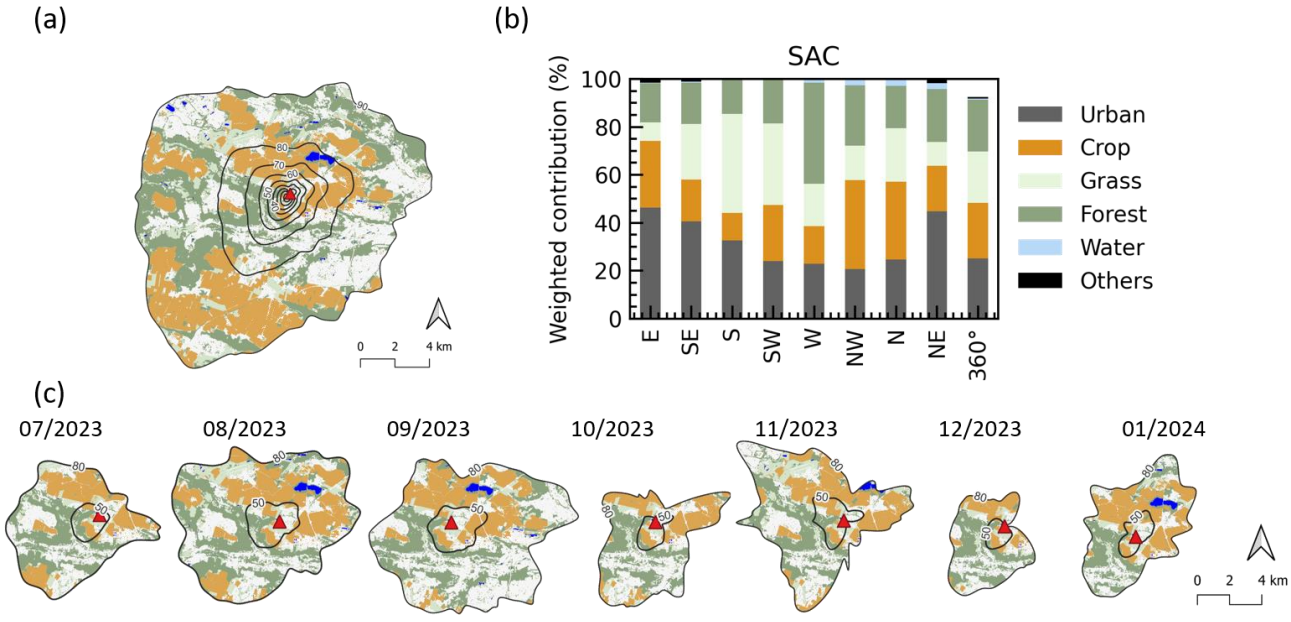

Figure 5.6. Flux footprint by land use group. (a) Footprint for all the periods, where lines indicate 10 to 90 (border) % level source area. (b) The contribution of each land use is weighted by footprint density. (c) Monthly footprint, where lines indicate 50 and 80 (border) % level source area. Note that for visual purposes, urban areas are coloured as white-grey on the map. Footprints were estimated using the model by Kljun et al. (2015).

In Figure 5.6.c, we can see that the monthly changes in composition and shape of the area contribute to the fluxes measured at the tower (the flux footprint). Some months have a larger

footprint (e.g. August and September), while others are narrower (e.g. December and January) related to changes in the dispersion conditions. This difference is explained by the most prominent occurrence of stable conditions during the summer, which leads to larger footprints than during the winter, which has mainly neutral conditions (shown by the stability ratio z / L) driven by stronger Winter winds, elevated friction velocity, and cloudy conditions (Figure 5.7). Note that the landscape is not homogeneous (Figure 5.6.b), so wind direction can also change the profile of sources and sinks, contributing to each compound flux measured at the tower. December, for instance, was the month with the least contribution from the most urban northeast sector.

The mixing and atmospheric boundary layers show clear diurnal and seasonal cycles (Figure 5.7). Warmer hours of the day and months show taller boundary layer heights, implying a larger volume of the developed layer in which the compounds can be diluted. During these warmer periods, the conditions are often unstable (z/L < 0.2), and friction velocity is high (> 0.4 ms−1). These conditions indicate a well-mixed layer and bigger eddy sizes. On the contrary, colder months (December and January) showed a relatively flat diel pattern, primarily due to a shorter photoperiod, leading to a much lower boundary layer height. We also noted that on-site fog was frequently observed during these periods. Concurrently, friction velocity increased on average during winter. We do not think strong winds in neutral conditions, especially medium winds in stable conditions, would favour horizontal advection. In the scope of the present work, however, it was not quantified due to a lack of measurements (horizontal gradients of concentration and fluxes).

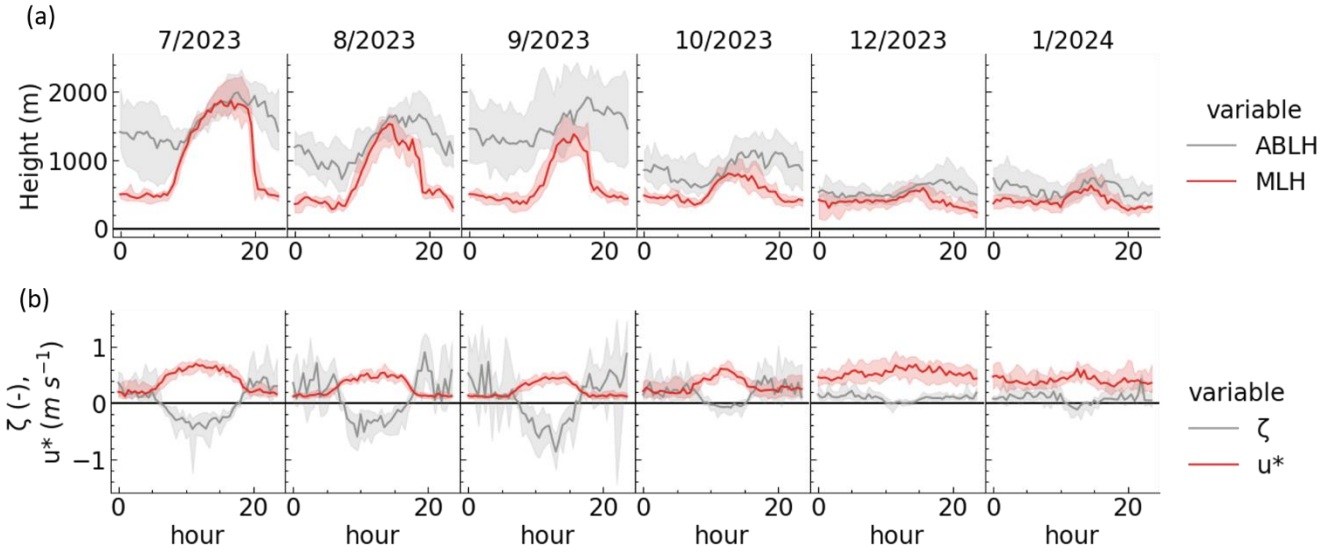

Figure 5.7. Boundary layer conditions. (a) The heights of the atmospheric boundary layer (ABLH) and the mixing layer (MLH) were measured by SIRTA in Palaiseau, 4.8 km from the tower. Data is available online (Kotthaus et al., 2023). (b) Stability parameters (ζ = (z - d) / L) and friction velocity (u_*) were measured at the FR-Sac tower. Absolute values of ζ bigger than 2 were ignored.

Stationarity and well-developed turbulence

Most of the data collected was under well-developed turbulence, 75% if only considering high-quality (flag 0) integral turbulence characteristics test (ITC), and 99 % including medium-

quality (flag 1). Around half of the data (41 %), with an ITC flag 0, was also considered stationary (stationary flag 0), increasing to 81 % if we include flag 1 on both tests. The stationarity test is required for standard EC but not for wavelets; thus, using the latter increases the data amount by 34 % in case only high-quality observations are used and 55 % in case medium-quality data is included (Figure 5.8). These savings happen more often during the day due to a higher coincidence of both flags at night. The percentages given are for the Licor (IR) fast analyser but are of the same order of magnitude as those for the PICARRO analyser (CRDS).

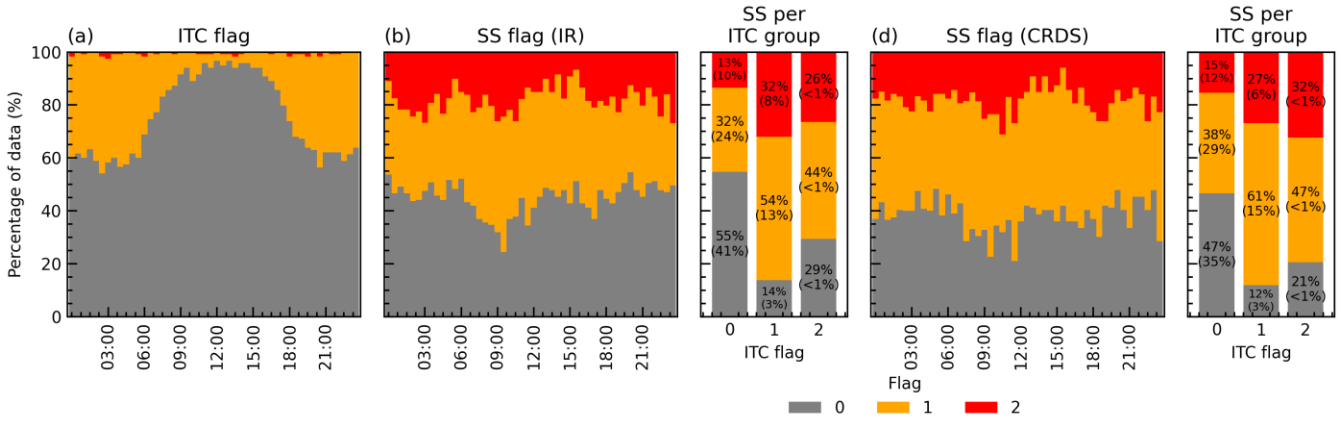

Figure 5.8. Quality control flags for turbulence (ITC) and CO_2 stationarity (SS). Flags follow a 0-1-2 system for high, medium and low quality. Percentage of (a) turbulence flagged data by hour of the day. Stationarity flagged CO_2 data by hour of the day for (b) the Licor instrument (IR) and (d) the PICARRO instrument (CRDS). Stationarity flags per ITC group are also given for the IR (b) and CRDS instrument (c). Percentages are summed to 100% in each group and overall data (in parentheses). See Figure S 5.2 for stationary tests for the three instruments.

5.4.3 Comparison of CO_2 flux between slow and fast-response analysers

High-frequency spectral correction

The CRDS analysers showed significantly more high-frequency attenuation of the flux than IR analysers (Table 5.2 and **Figure 5.9**), as expected due to the much longer sampling tube of the CRDS analyser (115 m) than the IR analyser (0.7 m), as well as the slower CRDS acquisition frequency (~3 s) compared to the IR (0.1 s). The difference was greater in (very) stable conditions, when higher frequencies contribute more to the flux than in (very) unstable conditions (**Figure 5.9**). On (very) unstable conditions, the contribution of low-frequencies to the flux increased, as shown by the fact that none of the ogive levels levelled at 1 for 30 minutes of integration time (ogive slope > 0). Surprisingly, CO (measured by CRDS) showed an atypical curve with stronger contribution from high frequencies, which after analysis was attributable to noise from this less sensitive instrument.

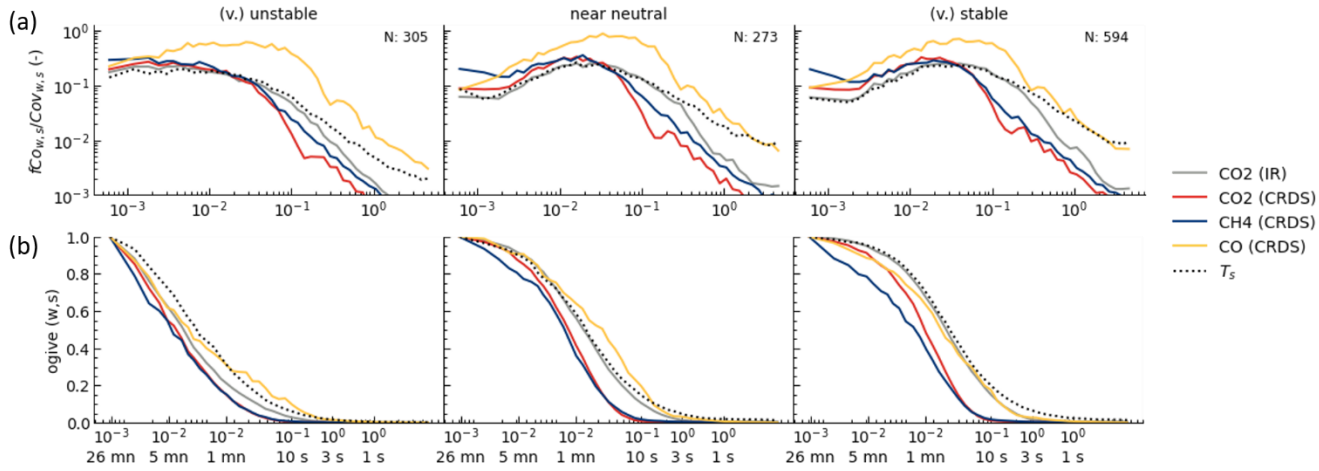

Figure 5.9. Normalised co-spectra (a) and ogives (b) of w and CO_2, CH_4, and CO covariances for gases measured by IR and CRDS and the reference sonic temperature, T_s. Median values from July to October 2023 grouped by stability classes: $\zeta < -0.2$ (unstable); $-0.2 > \zeta > 0.2$ (near neutral); $\zeta > 0.2$ (stable). N indicates the amount of half-hourly data in each class.

The high-frequency attenuation varied from 3 to 7% for the fast instrument (IR), while the CRDS instruments sampling at 100 m ranged from 11 to 19% (Table 5.2). We can expect more extensive corrections on stable conditions, characterized by a larger contribution of high frequencies to the flux, as observed for IR; contrarily, CRDS decreases compared to near-neutral conditions. It is worth noting that despite the 10 Hz acquisition frequency and 100 m height, the attenuation of the IR instrument was non-negligible. Additionally, the time response of the slow CRDS analysers, estimated based on the transfer function (3.62 s), matches the acquisition frequency (ranging between 3 s and 4 s), but it also matches the expected attenuation for a long tube (Figure 5.16).

Table 5.2. Percentage of high-frequency corrections of each instrument's CO_2, CH_4 and CO fluxes per stability class. Note that we used the CO_2 transfer function for all compounds in the CRDS, assuming the damping in the sampling line was a dominant attenuating process.

Instrument (compound)	Stability class (very) unstable	near-neutral	(very) stable
IR (CO_2)	2.7%	5.5%	6.6%
CRDS (CO_2, CH_4, CO)	11%	19%	17%

Comparing CO_2 flux measured by slow and fast-response analysers

The CO_2 fluxes computed from the IR (LI-7200) and the CRDS (PICARRO) analysers were well correlated with an underestimation of 13% of the CRDS for uncorrected fluxes that was diminished to 3% after high-frequency corrections (Figure 5.10). High-frequency correction decreased the bias, ME, by 0.04 $\mu molm^{-2}s^{-1}$ with no effect on absolute error (MAE) or the correlation coefficient (R^2). Moreover, the CRDS-corrected fluxes tended to underestimate the CO_2 fluxes slightly under stable conditions (Figure S 5.3).

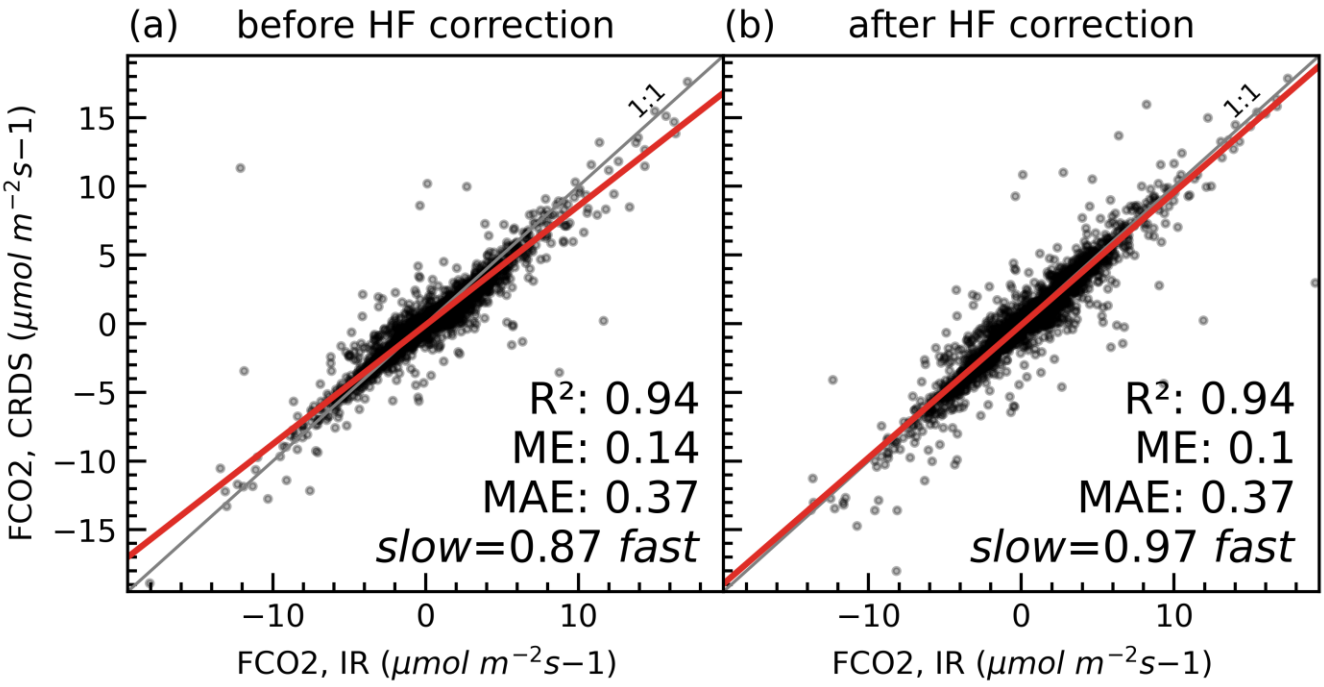

Figure 5.10. Comparison of CO_2 flux computed with the IR (LI-7200) and the CRDS (PICARRO G2401) analysers, (a) before and (b) after high-frequency loss corrections. Dots are observations; the red line is a robust linear relation, and the grey line is the 1:1 line. The correlation coefficient (R^2), the mean error (ME, $\mu molm^{-2}s^{-1}$), and the mean absolute error (MAE, $\mu molm^{-2}s^{-1}$) are shown in the bottom right. Statistics are calculated by ignoring outliers from robust linear regression.

5.4.4 Surface flux dynamics

Turbulent fluxes

We observed a well-defined summer pattern for the CO_2 flux with emissions at night and sequestration during the day (Figure 5.11). From summer to winter, the sink shortens in time and decreases in magnitude up to the point that during winter, the site behaves on average as a source all day. We note that the concentration morning peak observed in Figure 5.4 does not correspond to a peak in the flux. Following the seasonal pattern of CO_2, the evapotranspiration (as shown by the latent heat flux) decreased towards colder months. The similarity between CO_2 and H_2O trends indicates that photosynthetic activity slowed down. Indeed, in September, several crops were senescent or harvested, and the deciduous trees in the surrounding started to lose their leaves, as shown by the EVI maps (Figure S 5.5).

The CH_4 fluxes showed a marked daily pattern from July to September, with higher emissions in the morning than in the afternoon. Seasonally, the emissions in January were 10 times larger than in the previous months. The CO flux shows a marked increase in November and January but not in December, despite similar temperatures and traffic. In January, winds were relatively well distributed, while in December, the most urban NE sector was rarely in the footprint, which may explain the difference between the three months.

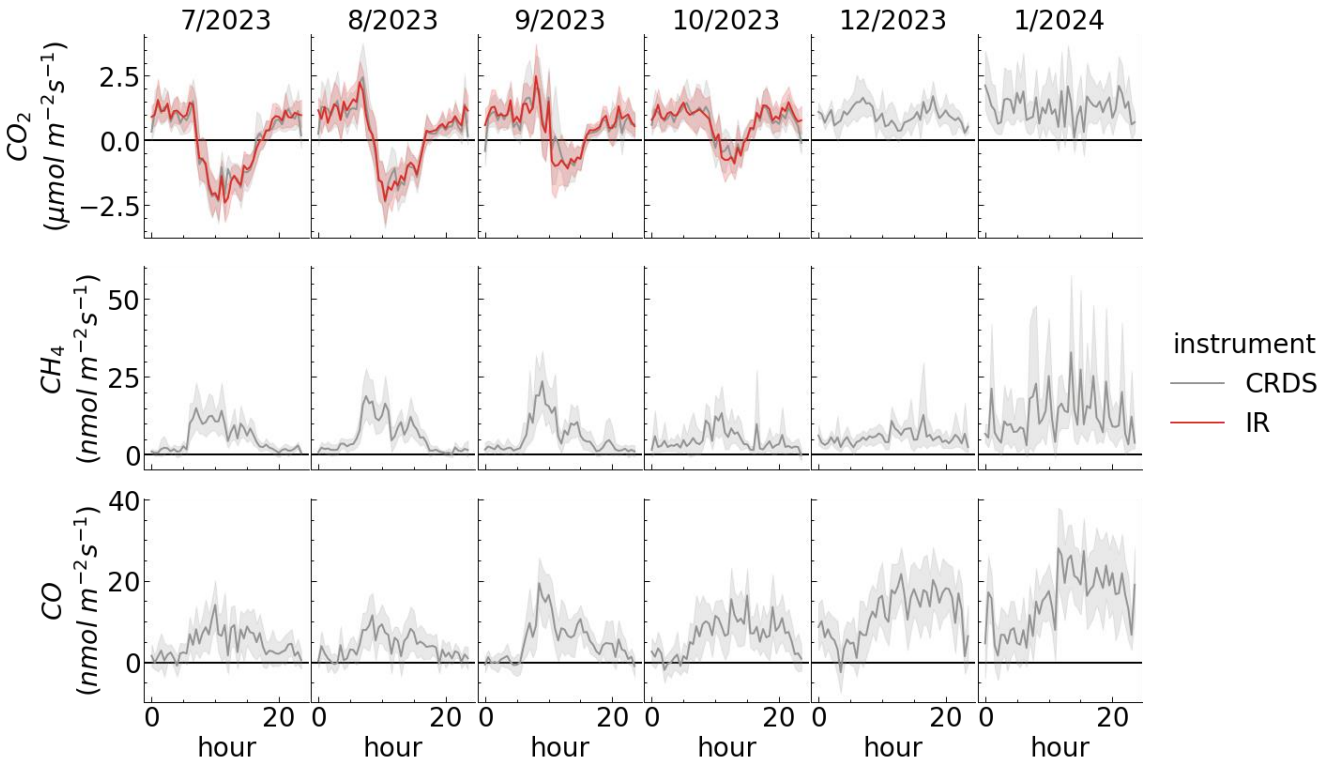

Figure 5.11. Monthly mean turbulent fluxes diel pattern of CO_2, CH_4 and CO for IR (LI-7200, only CO_2) and CRDS (PICARRO G2401) gas analysers. Fluxes showed after spectral correction. Data points falling within the extreme 1% tail of the distribution were removed.

Storage and surface fluxes

The CO_2 storage fluxes were the same magnitude as the turbulent fluxes (Figure 5.11) and showed diurnal patterns with positive values at night, early peaks of negative values during sunset, and a following increase towards positive values throughout the day (Figure 5.12).

The storage fluxes represented night-time emissions and daytime CO_2 and CH_4 absorption. In warmer months, when storage was significant, we observed the appearance of destocking (negative storage term) at the same time as the rise in mixing layer height (Figure 5.7). Both started in the early hours during sunrise when the surface heated, causing instability and forming turbulence. During these early events, nearly all the ecosystem flux was measured through CO_2 storage flux. Over the months, we have observed a decrease in the CO_2 storage term as atmospheric stratification progressively becomes neutral, and the boundary layer height stays unchanged throughout the day. We also noted a decrease in CH4 over time; however, in January, we can see negative values in the middle of the day, as observed for CO and CO_2. CO showed little storage during the vacation months (June and July) or in December, with the wind coming from the vegetated sector. CO storage increased during rush hours in September and October.

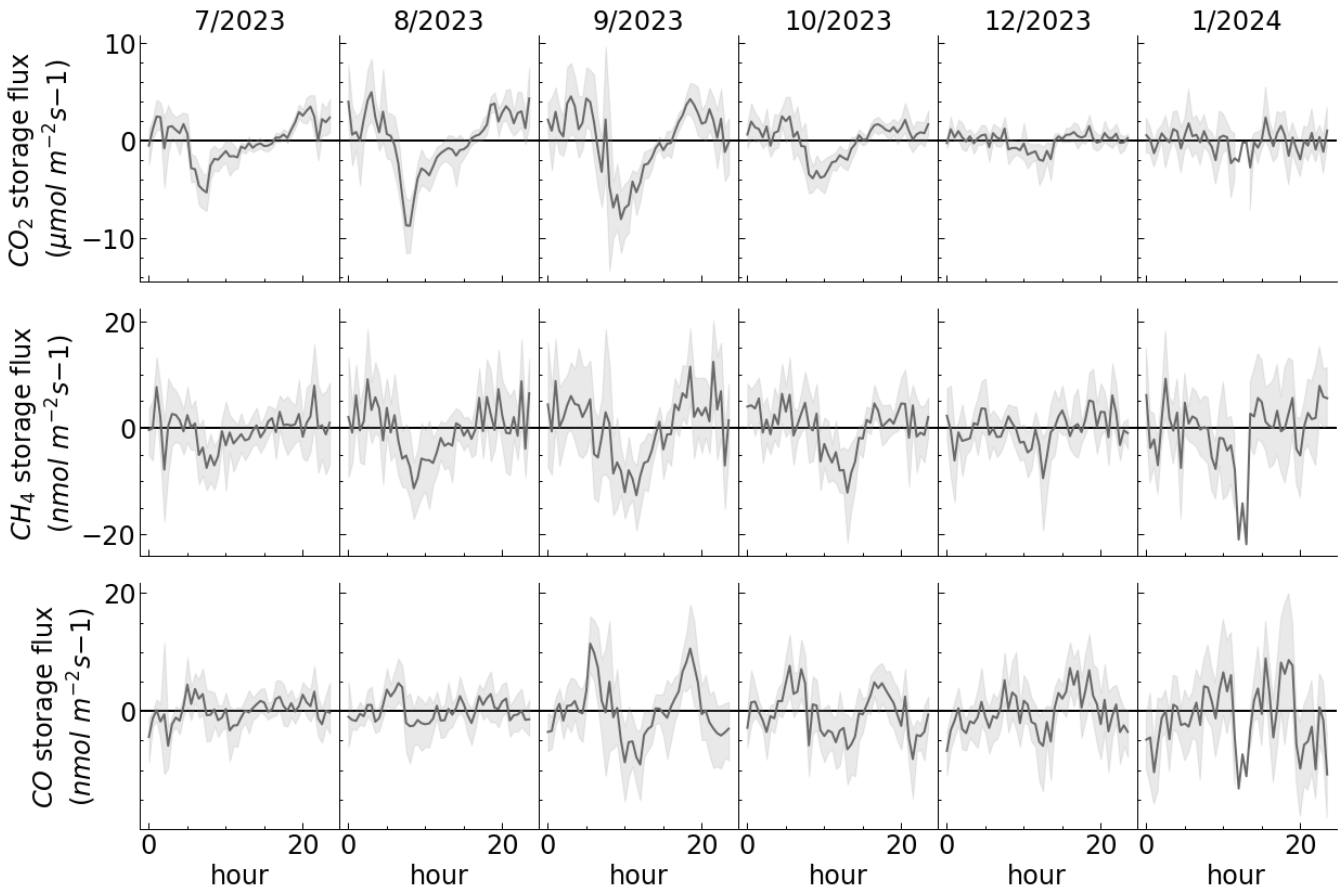

Figure 5.12. Monthly mean storage fluxes diel pattern of CO_2, CH_4 and CO computed using mixing ratios measured by the CRDS (PICARRO G2401) gas analyser on three levels (15, 60 and 100 m). Data points falling within the extreme 1% tail of the distribution were removed.

5.4.5 A look into the flux spatial heterogeneity

Fluxes categorized by wind direction and separated for day and night reveal spatial patterns (Figure 5.13). During daytime in warmer months (January to October), most directions exhibited a CO_2 sink. The most pronounced CO_2 sink was observed from the west, in the direction of the forest, where some emissions of CH_4 were observed, but notably, smaller emissions of CO. Colder months revealed stronger southeast CO_2 emissions echoed in CH_4 and CO fluxes. In the northeast sector, CO emissions were strong, increasing in colder months, possibly due to the alignment with the national road N118, ~50°. Peaks in CO emissions during nights align with directions with higher emissions during the day and maybe turbulent fluxes from particularly windy nights. Additionally, the wind direction spanning 10-45°, the direction of the local heating plant, exhibited CO_2 and CH_4 fluxes significantly higher than those observed in other directions during both daytime and night-time periods.

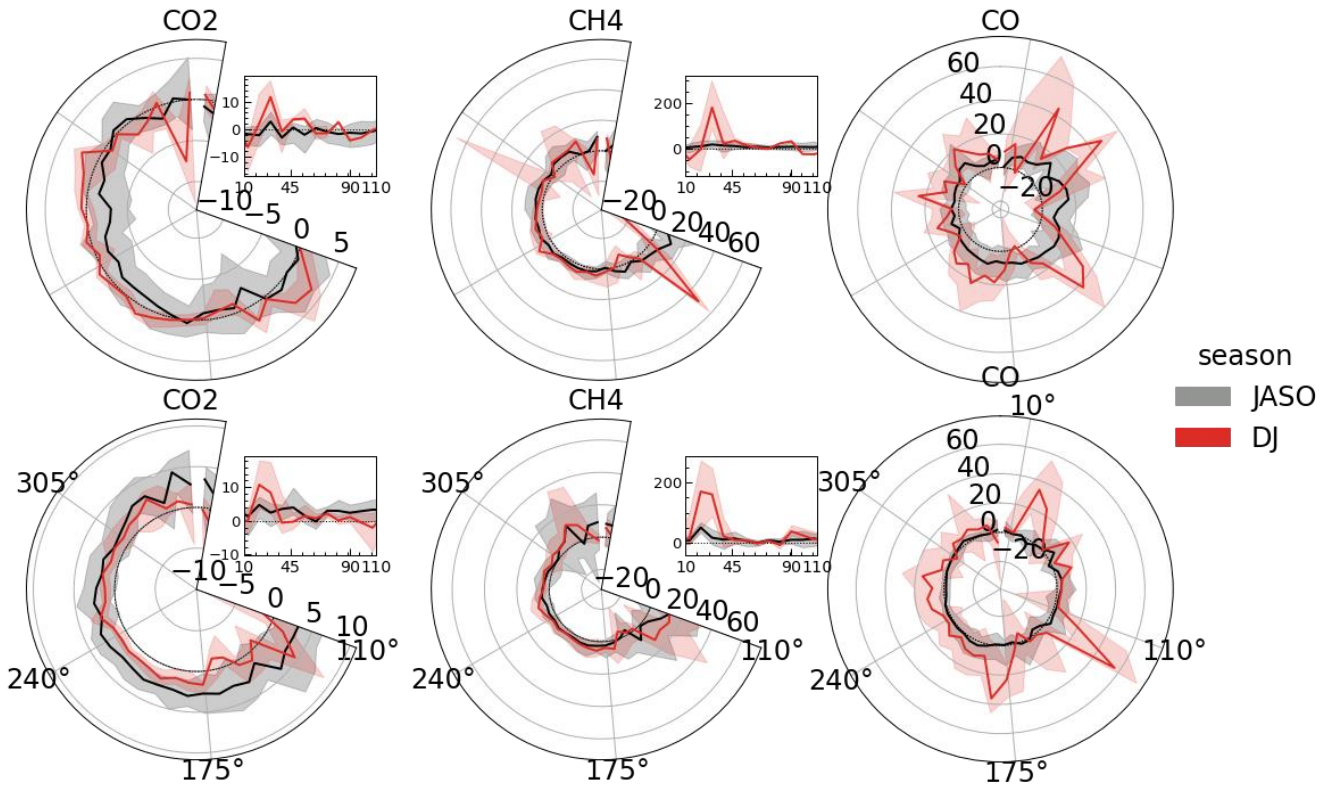

Figure 5.13. Surface fluxes by wind direction, daytime in the top panel and night-time in the bottom panel. Surface fluxes include turbulent and storage terms. The values presented are the median with the interquartile range; 0.1% extreme values were removed. Wind directions bins with less than 10 observations were added to the next bin clockwise. CO_2 fluxes are in µmol m^{-2} s^{-1}, and fluxes of CH_4 and CO are in nmol m^{-2} s^{-1}. Note for CO_2 and CH_4, 10-110° were plotted separately for visual purposes.

The NW CO_2 flux also showed a shift from a source in warmer months to a small sink during winter. This shift is expected when considering the crop field in this wind direction: bare soil in July (Figure 5.14) and green in January (Figure 5.15). Greenness can be identified by a higher leaf density, which is why the Enhanced Vegetation Index (EVI) is a proxy.

In July, west wind fluxes show a recognizable CO_2 diel pattern with carbon sequestration during the day when the wind comes from the vegetated direction (W and SW) (Figure 5.14.b). The high EVI indicates that the forest and grassland had fully green leaves this month. On the 17th of July, we can spot a positive CO_2 peak at the end of the day coming from the W direction, which is not found in CH_4 or CO. The peak is atypical for a forest ecosystem at this magnitude and may be a signal from the road or other activity. CH_4 was found to be more elevated for W winds. CO did not show a marked pattern when the wind came from a vegetated direction. For the period when wind came from the CEA campus (10-100°), the three gases showed very similar patterns, with a peak in the middle of the day.

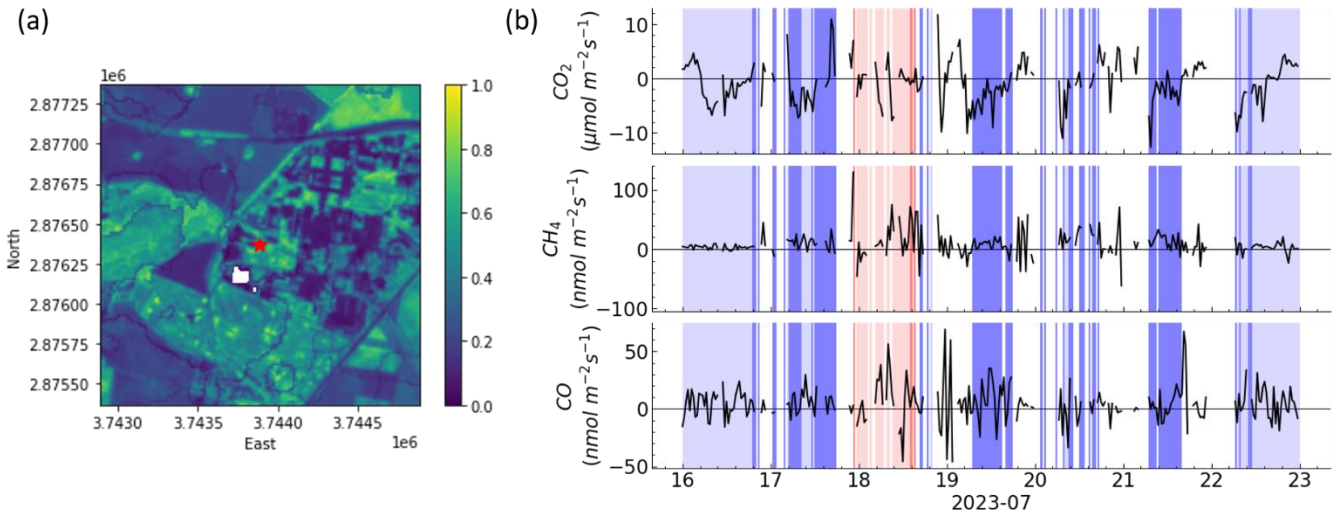

Figure 5.14. Zoom into a summer week. (a) EVI mean mosaic from July (2nd, 7th, 12th, 14th, 17th, 24th) using Sentinel2 data. (b) Surface fluxes, turbulent and storage term, with background colours per wind directions, W in blue, SW in light blue, 10-30° in red, 30-100° in light red.

In January, when the heating plant was operational, and the wind came from its direction, we can distinctly observe the contribution of the heating plant to the CO_2 and CH_4 fluxes (Figure 5.15). CO fluxes were also higher when the wind came from the heating plant, but the difference compared to the vegetated wind direction was less striking. The mean (and 90th percentile) for CO_2, CH_4 and CO fluxes from the NE were 8.2 (25) µmol m^{-2} s^{-1}, 214 (801) nmol m^{-2} s^{-1}, and 27 (71) nmol m^{-2} s^{-1}, respectively. While W and SW values were 1 (2.3), 4.8 (12) and 12 (40) µmol m^{-2} s^{-1} smaller.

Apart from the heat plant's fluxes, Wintertime fluxes were notably smaller than summer (Figure 5.14), as expected by the lower biological activity during that period. The green areas exhibited lower EVI, indicating the loss of leaves during this season.

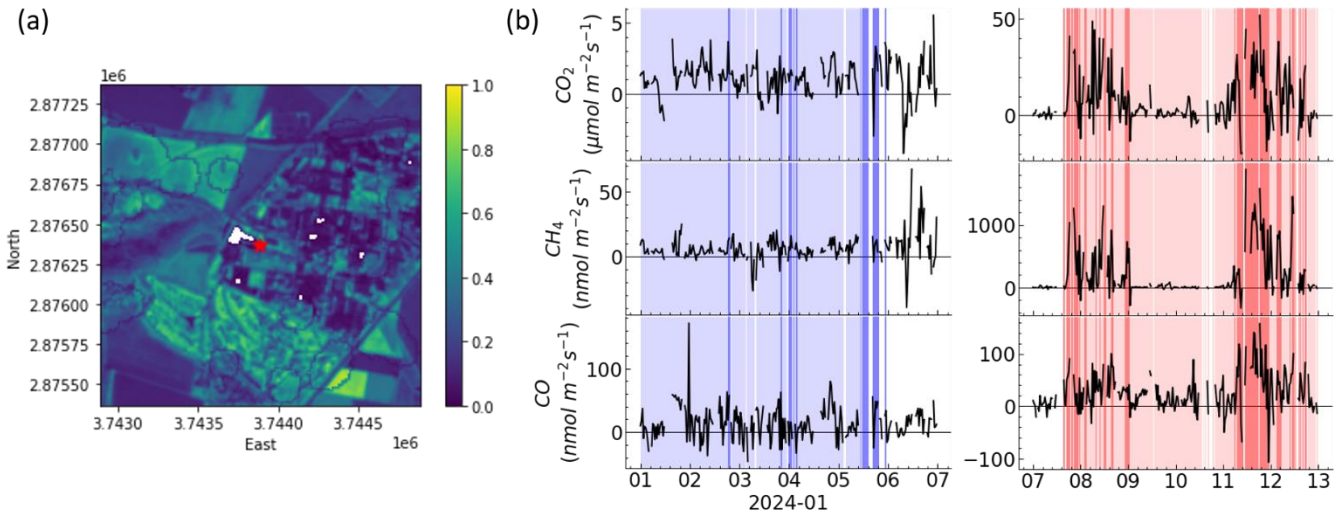

Figure 5.15. Zoom into a winter week. (a) EVI mean mosaic from January (5th, 18th, 20th) using Sentinel2 data. (b) Surface fluxes, turbulent and storage term, with background colours per wind directions, W in blue, SW in light blue, 10-30° in red, 30-100° in light red.

5.5 Discussion

5.5.1 Challenges of measuring on a tall tower with slow-response analysers

High-frequency loss corrections on the atmospheric tower configuration

Our findings revealed that an ICOS atmospheric tower configuration utilizing a CRDS gas analyser with an acquisition frequency of approximately 0.3 Hz and a tube length of 100 m exhibited a high-frequency loss correction of approximately 20%. This correction was around three times more than the conventional ecosystem flux measurement setup, which employed an IR gas analyser with a 10 Hz acquisition frequency and a tube length of 0.7 m, positioned at the top of the tower. The observed transfer function (TF) for the CRDS setup closely matched the theoretical attenuation expected, as depicted in Figure 5.16Figure 5.16. Indeed, the tube and sensor attenuation together leads to a first-order time constant around 3s, as we observed for the CRDS setup (Table 1). This outcome suggests that only a limited attenuation reduction can be expected even with a faster measurement system or a smaller tube attenuation. In order to substantially decrease the high-frequency attenuation of the flux, both an increase of the acquisition frequency and a decrease in tube attenuation (decrease in tube length or increase in flow rate) would be required.

Since the tube attenuation is higher when flow inside the tube is laminar (Lenschow and Raupach, 1991), ensuring a Reynolds number larger than ~2300 is key to minimize attenuation. We can define $Re = \frac{2Q}{\pi r v}$, where Re is Reynolds number (-), r is tube radius (m), Q is the volumetric flow rate ($m^3 s^{-1}$), and v is the kinematic viscosity of air. We find that for the tube in place with 9.5 mm of internal diameter, pumping ~14-17 L min^{-1} is necessary to achieve a turbulent flow. Under these conditions, the cut-off frequency would increase to more than 0.6 Hz, but the pressure would drop from -6 mbar to -47 mbar.

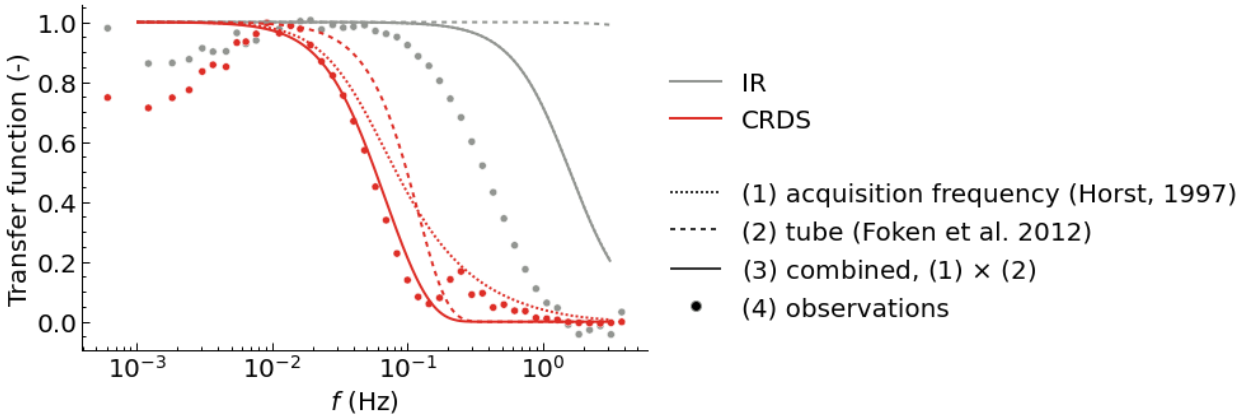

Figure 5.16. Transfer functions were computed for the tube (TF_{tube}, Leuning and Moncrieff, 1990; Foken et al., 2012), the sensors acquisition frequencies (TF_{acq}, Horst, 1997) and observed for CO_2 for the two setups at the tower. The Saclay atmospheric setup (CRDS) consists of a 100 m sampling line with a 9.5 mm diameter, acquisition frequency ~0.3 Hz and flow rate of 12.7 L min−1. Conventional ecosystem setup (IR) consists of a 0.7 m sampling line with a 5.33 mm diameter, acquisition frequency of 10Hz and flow rate of 15 L min−1. Note that curves (1) and (3) are superposed for the IR setup.

It is worth mentioning that in our study, we used a first-order filter fitted on in-situ data as a transfer function, following Fratini et al. (2012) and shared by other studies (Ibrom et al., 2007; Peltola et al., 2021). In the atmospheric tower configuration where the main attenuation arises from the tube length, the transfer function may take an exponential shape, as proposed by Leuning and Moncrieff (1990) and Foken et al. (2012), and the fitting may not be perfect, as depicted in Figure 5.16. However, the effect on the correction factor was evaluated to be negligible.

For the same transfer function, attenuation may change based on the co-spectra dependence on measuring height, wind speed, and stability parameter (z/L). Specifically, increases in wind speed and stability parameters, or decreases in measuring height, are expected to shift a co-spectrum towards higher frequencies, thereby enhancing attenuation for a given transfer function (Horst, 1997). Theoretical expectations of the attenuation factor from Horst et al. (1997) based on empirical co-spectra agree very well with our measurements under unstable to near-neutral conditions but do not entirely align with our observations for neutral and stable conditions (Figure 5.17). Indeed, surprisingly, we found that the attenuation remained stable or slightly decreased for z/L values over 0.2 in the case of IR and CRDS, respectively. This finding contrasts with the prediction by Horst et al. (1997), which suggested an increase by a factor of 5 under very stable conditions. This difference needs further investigation.

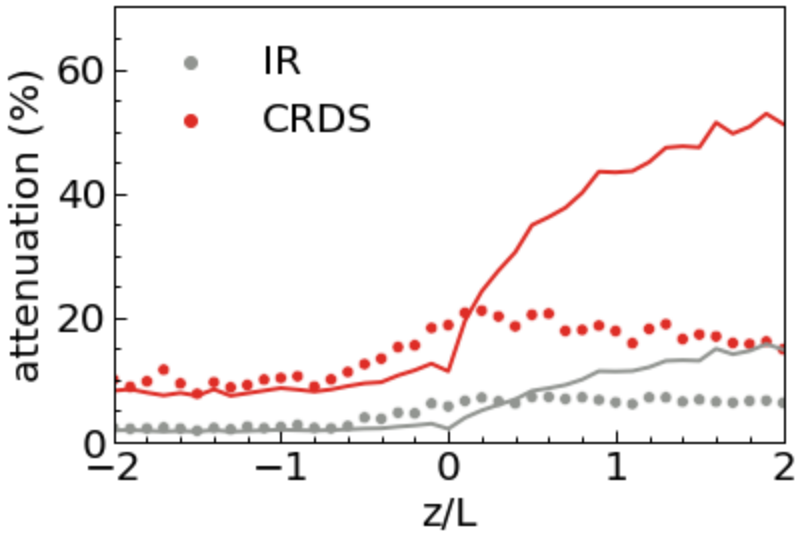

Figure 5.17. Flux attenuation is due to high-frequency losses, theoretical as lines and measured as points. The theoretical losses are computed from Horst (1997, eq. 11), using the measured first-order time constant τ_c for the IR (0.5 s) and the CRDS (3s)

More surprising is the HF losses found for CO_2 measured by the IR (LI-7200). On this supposedly conventional ecosystem setup (0.7 m heated tube, 5.33 inner diameter, 15 $Lmin^{-1}$ flow rate, 7 µm filter), attenuation and the transfer function were expected to be much smaller. The time constant of 0.5 s is equal to the cutting frequency (0.32 Hz) reported by Ibrom et al. (2007) for CO_2 with a 50 m long tube, 8 mm diameter, and a flow rate of 20 L min^{-1}. We do not have strong evidence to explain this substantial attenuation, and we are bound to speculate that this may be due to the inlet filter. Indeed, we observed a considerable HF loss for H_2O with a τ_c ranging from 0.7 s for RH < 30% to 5 s at 70% RH and 50 s for RH larger than 80% (data not shown). Such a loss during wetter conditions indicates that the inlet accumulated water vapour, probably on the filter holding hygroscopic aerosols. Since CO_2 dissolves in water, the microscopic water accumulated in the tube may have buffered the CO_2, leading to a significant attenuation.

The CRDS setup, however, exhibited relatively small attenuation. Wintjen et al. (2020) reported a 16-22% damping factor for a 48 m tube with a 6 mm diameter, measuring reactive nitrogen at 10 Hz. Despite the longer tube length and slower analysers in our study compared to Wintjen et al., their slower flow rate (2.1 L min−1) and the expected stronger air-wall interactions for reactive nitrogen compounds may have contributed to the higher damping factor in their study. Correcting for high-frequency losses resulted in agreement between the IR and CRDS methods within 3%, maintaining the elevated R^2 of 0.94 (Figure 5.10). This match demonstrates that the high-frequency correction was able to correct for the losses.

Storage and advection

Storage fluxes amplitude were of the same magnitude as the turbulent fluxes, as Haszpra et al. (2005) observed. These values mean the storage term must be included when looking into the

diel surface flux pattern. In particular, we observe a negative storage flux in the morning during the summer months that may account for the early onset of photosynthesis and the expansion of the mixed layer (Figure 5.7).

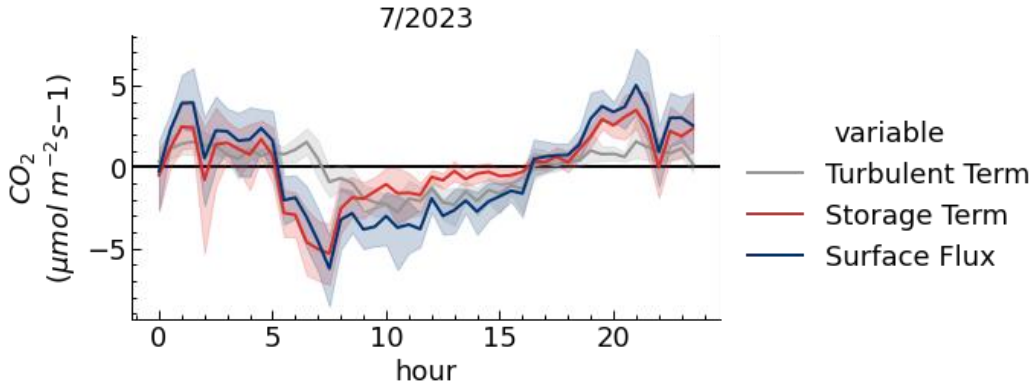

Figure 5.18. Diel mean for July 2023 for CO_2 surface flux and turbulent and storage terms. Values for the CRDS (PICARRO G2401). Data points falling within the extreme 1% tail of the distribution were removed.

Similarly, we observe a quite strong night-time respiration component after sunset that is not captured by the turbulent flux. Storage flux would therefore be essential to consider when partitioning CO_2 fluxes into biological uptake (photosynthesis) and emissions, which included both biological emission as respiration and anthropogenic emissions (Stoy et al. 2006; Tramontana et al. 2020; Coimbra et al. 2023).

In this work, horizontal and vertical advection were assumed to be negligible, but they may not be. Indeed, daily mean storage in the site gravitates around zero during July but shows a non-negligible variability for CO_2 in August and September and for all gases in January (Figure S 5.6). In ideal conditions, the storage flux should average 0 over 24 hours since what is stored at night should be released during the day. Non-zero daily storage may indicate horizontal advection.

Additionally, the chimney of the heating plant, ~600 m away from the tower, situated at a certain height, may bias the storage fluxes, which rely on gradient profiles along the tower. Indeed, if the plume from the heating plant emissions is measured intermittently due to changes in wind directions, we may attribute or ignore storage fluxes where lateral advection occurs. Correctly identifying such a process would require tracking the chimney plume with a 3D dispersion model and half-hourly resolution, which was out of the scope of the present work.

Vertical advection may also exist but is challenging to estimate and may even lead to erroneous corrections and implausible fluxes, as Haszpra et al. (2005) observed. Vertical advection would even be neglected for very tall towers, as Davis et al. (2003) proposed, based on the assumption that synoptic scale processes should counterbalance vertical advection in the long term.

5.5.2 Plausibility of the measured fluxes

Winds originating from the deciduous forest (West) exhibit expected seasonal variations, with CO_2 acting as a sink and CO emissions being negligible in warmer months, transitioning to

CO_2 and CO emissions in winter. Comparison with a mixed deciduous forest site at 50 km SE (FR-Fon ICOS site, e.g. Delpierre et al., 2016) shows a similar seasonality of the CO_2 fluxes, a storage term being slightly larger in FR-Sac than in FR-Fon, and a turbulent term notably smaller in FR-Sac (Figure S 5.7). To explain the difference, we cannot exclude the possibility that the forests may behave differently simply because they are different ecosystems; however, some aspects deserve to be mentioned. The surface flux in FR-Sac is expected to be smaller since the forest only represents ~40% of the footprint. Moreover, ~20% of the footprint is urban or traffic, which may add a positive component to the flux, decreasing its amplitude during the day (Figure 5.6). Advection could also play an additional role in reducing surface fluxes in FR-Sac, and storage may have been underestimated because of the reduced number of sampling heights. Furthermore, while this paper primarily examines the high-frequency aspect of the signal, it is essential to note that the 30-minute integration period did not allow to capture entirely the low frequencies of the fluxes, especially under unstable conditions as can be seen by the co-ogives, slope being non-zero at the lowest frequencies (**Figure 5.9**). A recent study on tall urban towers also reported low-frequency contributions to kinematic heat and CO_2, indicating the importance of low-frequency corrections (Lan et al., 2024).

CO emissions during colder months may suggest contributions from activities beyond the forest, including traffic and nearby village heating such as Villiers-le-Bâcle. We cannot exclude the possibility of indirect CO emissions from the forest through the oxidation of CH_4 and biogenic volatile organic compounds (BVOCs), though this should be limited since the trees lost their leaves. Additionally, soil microorganisms consume CO (Conrad, 1996), which makes CO a tracer that distinguishes soil respiration from anthropogenic emissions in the CO_2 emissions.

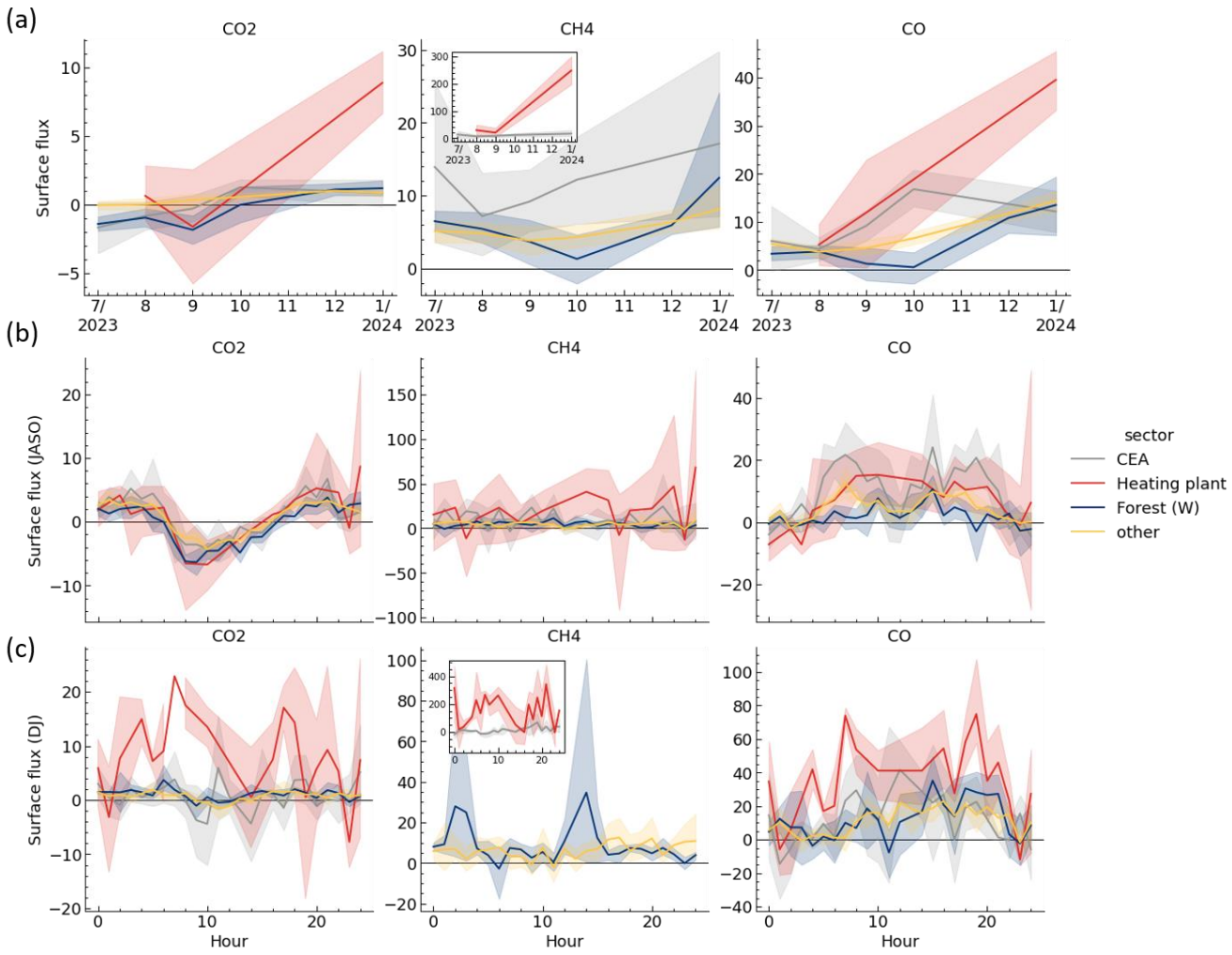

Figure 5.19. Mean surface fluxes for CO_2 ($\mu molm^{-2}s^{-1}$), CH_4 ($nmolm^{-2}s^{-1}$) and CO ($nmolm^{-2}s^{-1}$) by identified sectors. Monthly averages (a) and hourly mean for warmer JASO (b) and colder months DJ (c). Surface fluxes include turbulent and storage terms. Wind sectors are CEA (10°-100° without heating plant), Heating plant (20°-40°), and Forest (247.5°-292.5°). Note in (a) November is interpolated.

The emissions from the heating plant were distinct, with significantly higher levels of CO_2 and CH_4 observed from ~30° wind direction compared to other directions (Figure 5.18, Figure 5.19). The high fluxes from point sources like the heating plant can induce non-stationarity. Using wavelets allows us to measure these non-stationary fluxes effectively. The CO_2, CH_4, and CO emissions from the heating plant wind sector increased to a maximum of 10000, 250 and 40 nmol m^{-2} s^{-1}, respectively, in January (Figure 5.18a), while they were not different from the other directions during the warmer months (Figure 5.18b). The CO_2 and CH_4 emissions show a similar diel pattern during the colder month with two minima at 0h and 16h. The emission ratios computed from these data are CO_2/CH_4 ~ 40 and CO_2/CO ~250, indicating a significant methane loss.

Interestingly, the diel pattern of CO during colder months followed expected traffic patterns, while this trend was observed for the CEA wind direction during warmer months.

5.5.3 Recommendations for atmospheric sites concerned with such a method

Currently, the ICOS network comprises 38 atmospheric sites, with 17 classified as class 1 and the remainder as class 2. The ecosystem centre is more extensive, encompassing 99 sites, including 18 class 1, 31 class 2, and the remaining associated sites. This count may further rise when other regional networks are taken into consideration.

Not all atmospheric sites are adapted for flux measurements. EC towers prioritize flat surfaces, slim towers and homogeneity, whilst atmospheric towers may prioritize locations based on grid redundancy to improve atmospheric inversions. Slim towers with limited topography around them are recommended for reliable measurements. Atmospheric measurements conducted close to large structures (e.g., just above domes) or in mountainous regions can introduce disturbances in the turbulence signal. These disturbances can lead to unreliable tilt angle correction and surface flux assessments. In some cases, flagging wind sectors that are not appropriate for EC measurements can be a straightforward solution. With that said, eddy covariance has successfully been used in mountainous landscapes using appropriate tilt corrections (Matthews et al. 2017).

For atmospheric tower candidates interested in measuring flux, we recommend:

- Selecting at least one height for calculating fluxes through Eddy Covariance. A footprint estimation (Kljun et al., 2015) may be relevant to this decision.
- Including a high-frequency 3D anemometer at the chosen height(s).
- Evaluating the first-order filter time for tube and sensors, as shown here, to verify that high-frequency attenuation is below an acceptable threshold, ~20%.
- Performing continuous mixing ratio measurements on the chosen height(s), limiting profile measurements to specific hours or using a separate set of instruments. The continuity ensures a low-frequency signal for eddy covariance, and the profile can prioritise transition periods when fluxes may exhibit non-stationary behaviour or low turbulence.
- Evaluating the flow regime in the sampling tube, if possible, increasing the flow rate to guarantee turbulence ($Re > 2300$).
- Additional meteorological data (e.g., precipitation, short and longwave incoming and outgoing radiation) and metadata (e.g., forest type, crops, transport counting) pertinent for flux interpretation should also be collected.

Ensuring continuous measurements is crucial for wavelets, given that their frequency resolution depends on the quantity of continuous data points. Indeed, profile measurements are often contemplated and doubling the instruments may not be feasible. Therefore, we recommended restricting profile measurements to specific hours when the development of the boundary layer may overshadow the relevance of measuring flux close to the tower. These moments, typically during sunrise and sunset, provide valuable insights from atmospheric and ecosystem (storage) perspectives. Furthermore, standard covariance would typically flag and

disregard measurements during these moments, although to a lesser extent for wavelet-based eddy covariance, as depicted in Figure 5.8.

5.6 Conclusions

This study is a proof of concept for leveraging existing atmospheric towers to measure fluxes by adding a 3D anemometer. While eddy covariance on tall towers introduces challenges related to heterogeneity and storage effects, it mitigates concerns such as high-frequency attenuation. Comparing slow-response analysers with fast-response ones revealed very similar net fluxes across all stability conditions (R^2>0.94), indicating the viability of using slower instruments in this case.

It is important to note that our results focus solely on passive gases, as water was not considered due to air drying before measurement in the CRDS. We could expect more significant attenuation linked to tube length for water, as air-wall interactions of absorption and desorption are much stronger in water vapour (Massman and Ibrom, 2008). Similarly, we would not recommend measuring reactive gases, as their residence time might be too long (~60 s) for accurate eddy covariance measurements to be made. We also recommend using wavelet-based eddy covariance, as it enabled the exploitation of 18-34% more data compared to conventional EC, allowing for the analysis of non-stationary fluxes, particularly evident in the case of a point source, such as a heating plant.

While many attenuation variables are not under the researcher's control, limited choices remain for measurement height, tube dimensions, flow rate, and acquisition frequency. We recommend that continuous gas measurements be systematically done with a high-frequency 3D anemometer and a sufficiently large flow rate to ensure turbulent flows in the sampling tube.

To calculate the surface flux, we estimated the storage term. Although the storage term calculated using three heights provided useful estimations, caution is warranted due to potential biases from not measuring height simultaneously and the limited number of heights sampled. Our results underscore the significance of the storage term, which was as large as the turbulent flux at the measurement height.

Analysing fluxes by wind direction revealed distinct patterns, particularly between the forest (W) and campus site (NE). Notably, emissions from a heating plant significantly influenced CO_2 and CH_4 fluxes in colder months, highlighting the importance of considering local sources. While our findings align with anticipated patterns across various land uses, accurately attributing fluxes to land uses would necessitate additional modelling efforts, which were beyond the scope of this study.

This study demonstrates the potential of expanding flux measurements through a relatively inexpensive instrumentation addition, offering valuable insights for ecosystem and atmospheric research. It further shows that the Eddy Covariance method has sufficiently matured to use less-than-ideal instrumentation.

Acknowledgements

The authors would like to thank ICOS, the ICOS Cities EU H2020 project (Grant No 101037319), for supporting this study. We thank Rainer Hilland for the support in hosting the Saclay data. We also thank the SIRTA team, namely Simone Kotthaus, for their comments on the lidar data.

Financial support

This project has received funding from the European Union's Horizon 2020 research and innovation programme under Grant Agreement No 101037319 (PAUL ICOS-Cities project).

Data availability

ICOS data for FR-Sac and FR-Fon (forest site used for reference) can be downloaded from the carbon portal: data.icos-cp.eu/portal.

Code

The code used in the analysis presented in this paper is available online and can be accessed at https://github.com/pedrohenriquecoimbra

References

Aslan, T., Peltola, O., Ibrom, A., Nemitz, E., Rannik, Ü., and Mammarella, I.: The high-frequency response correction of eddy covariance fluxes – Part 2: An experimental approach for analysing noisy measurements of small fluxes, Atmospheric Meas. Tech., 14, 5089–5106, https://doi.org/10.5194/amt-14-5089-2021, 2021.

Aubinet, M., Berbigier, P., Bernhofer, Ch., Cescatti, A., Feigenwinter, C., Granier, A., Grünwald, Th., Havrankova, K., Heinesch, B., Longdoz, B., Marcolla, B., Montagnani, L., and Sedlak, P.: Comparing CO_2 Storage and Advection Conditions at Night at Different Carboeuroflux Sites, Bound.-Layer Meteorol., 116, 63–93, https://doi.org/10.1007/s10546-004-7091-8, 2005.

Bergeron, O. and Strachan, I. B.: CO_2 sources and sinks in urban and suburban areas of a northern mid-latitude city, Atmos. Environ., 45, 1564–1573, https://doi.org/10.1016/j.atmosenv.2010.12.043, 2011.

Canadell, J. G., Monteiro, P. M. S., Costa, M. H., Cotrim da Cunha, L., Cox, P. M., Eliseev, A. V., Henson, S., Ishii, M., Jaccard, S., Koven, C., Lohila, A., Patra, P. K., Piao, S., Rogelj, J., Syampungani, S., Zaehle, S., and Zickfeld, K.: Global Carbon and other Biogeochemical Cycles and Feedbacks, edited by: Masson-Delmotte, V., Zhai, P., Pirani, A., Connors, S. L., Péan, C., Berger, S., Caud, N., Chen, Y., Goldfarb, L., Gomis, M. I., Huang, M., Leitzell, K., Lonnoy, E., Matthews, J. B. R., Maycock, T. K., Waterfield, T., Yelekçi, O., Yu, R., and Zhou, B., Clim. Change 2021 Phys. Sci. Basis Contrib. Work. Group Sixth Assess. Rep. Intergov. Panel Clim. Change, 673–816, https://doi.org/10.1017/9781009157896.007, 2021.

Ciais, P., Rayner, P., Chevallier, F., Bousquet, P., Logan, M., Peylin, P., and Ramonet, M.: Atmospheric inversions for estimating CO_2 fluxes: methods and perspectives, in: Greenhouse Gas Inventories: Dealing With Uncertainty, edited by: Jonas, M., Nahorski, Z., Nilsson, S., and Whiter, T., Springer Netherlands, Dordrecht, 69–92, https://doi.org/10.1007/978-94-007-1670-4_6, 2011.

Covey, K. R. and Megonigal, J. P.: Methane production and emissions in trees and forests, New Phytologist, 222, 35–51, https://doi.org/10.1111/nph.15624, 2019.

Coimbra, P. H. H., Loubet, B., Laurent, O., Mauder, M., Heinesch, B., Bitton, J., Delpierre, N., Depuydt, J., and Buysse, P.: Improvement of Co2 Flux Quality Through Wavelet-Based Eddy Covariance: A New Method for Partitioning Respiration and Photosynthesis, https://doi.org/10.2139/ssrn.4642939, 24 November 2023.

Conrad, R.: Soil microorganisms as controllers of atmospheric trace gases (H2, CO, CH4, OCS, N2O, and NO), Microbiol. Rev., 60, 609–640, https://doi.org/10.1128/mr.60.4.609-640.1996, 1996.

Conrad, R. and Seiler, W.: Role of microorganisms in the consumption and production of atmospheric carbon monoxide by soil, Appl. Environ. Microbiol., 40, 437–445, https://doi.org/10.1128/aem.40.3.437-445.1980, 1980.

Crawford, B. and Christen, A.: Spatial source attribution of measured urban eddy covariance CO2 fluxes, Theor. Appl. Climatol., 119, 733–755, https://doi.org/10.1007/s00704-014-1124-0, 2015.

Daubechies, I.: Orthonormal bases of compactly supported wavelets, Commun. Pure Appl. Math., 41, 909–996, https://doi.org/10.1002/cpa.3160410705, 1988.

Davis, K. J., Bakwin, P. S., Yi, C., Berger, B. W., Zhao, C., Teclaw, R. M., and Isebrands, J. G.: The annual cycles of CO2 and H2O exchange over a northern mixed forest as observed from a very tall tower, Global Change Biology, 9, 1278–1293, https://doi.org/10.1046/j.1365-2486.2003.00672.x, 2003.

Delpierre, N., Berveiller, D., Granda, E., and Dufrêne, E.: Wood phenology, not carbon input, controls the interannual variability of wood growth in a temperate oak forest, New Phytol., 210, 459–470, https://doi.org/10.1111/nph.13771, 2016.

Delwiche, K. B., Knox, S. H., Malhotra, A., Fluet-Chouinard, E., McNicol, G., Feron, S., Ouyang, Z., Papale, D., Trotta, C., Canfora, E., Cheah, Y.-W., Christianson, D., Alberto, M. C. R., Alekseychik, P., Aurela, M., Baldocchi, D., Bansal, S., Billesbach, D. P., Bohrer, G., Bracho, R., Buchmann, N., Campbell, D. I., Celis, G., Chen, J., Chen, W., Chu, H., Dalmagro, H. J., Dengel, S., Desai, A. R., Detto, M., Dolman, H., Eichelmann, E., Euskirchen, E., Famulari, D., Fuchs, K., Goeckede, M., Gogo, S., Gondwe, M. J., Goodrich, J. P., Gottschalk, P., Graham, S. L., Heimann, M., Helbig, M., Helfter, C., Hemes, K. S., Hirano, T., Hollinger, D., Hörtnagl, L., Iwata, H., Jacotot, A., Jurasinski, G., Kang, M., Kasak, K., King, J., Klatt, J., Koebsch, F., Krauss, K. W., Lai, D. Y. F., Lohila, A., Mammarella, I., Belelli Marchesini, L., Manca, G., Matthes, J. H., Maximov, T., Merbold, L., Mitra, B., Morin, T. H., Nemitz, E., Nilsson, M. B., Niu, S., Oechel, W. C., Oikawa, P. Y., Ono, K., Peichl, M., Peltola, O., Reba, M. L., Richardson, A. D., Riley, W., Runkle, B. R. K., Ryu, Y., Sachs, T., Sakabe, A., Sanchez, C. R., Schuur, E. A., Schäfer, K. V. R., Sonnentag, O., Sparks, J. P., Stuart-Haëntjens, E., Sturtevant, C., Sullivan, R. C., Szutu, D. J., Thom, J. E., Torn, M. S., Tuittila, E.-S., Turner, J., Ueyama, M., Valach, A. C., Vargas, R.,

Varlagin, A., et al.: FLUXNET-CH_4: a global, multi-ecosystem dataset and analysis of methane seasonality from freshwater wetlands, Earth System Science Data, 13, 3607–3689, https://doi.org/10.5194/essd-13-3607-2021, 2021.

Desjardins, R. L., Worth, D. E., Pattey, E., VanderZaag, A., Srinivasan, R., Mauder, M., Worthy, D., Sweeney, C., and Metzger, S.: The challenge of reconciling bottom-up agricultural methane emissions inventories with top-down measurements, Agric. For. Meteorol., 248, 48–59, https://doi.org/10.1016/j.agrformet.2017.09.003, 2018.

Dragicevic, P.: Fair Statistical Communication in HCI, in: Modern Statistical Methods for HCI, edited by: Robertson, J. and Kaptein, M., Springer International Publishing, Cham, 291–330, https://doi.org/10.1007/978-3-319-26633-6_13, 2016.

Dutaur, L. and Verchot, L. V.: A global inventory of the soil CH4 sink, Global Biogeochemical Cycles, 21, https://doi.org/10.1029/2006GB002734, 2007.

El Yazidi, A., Ramonet, M., Ciais, P., Broquet, G., Pison, I., Abbaris, A., Brunner, D., Conil, S., Delmotte, M., Gheusi, F., Guerin, F., Hazan, L., Kachroudi, N., Kouvarakis, G., Mihalopoulos, N., Rivier, L., and Serça, D.: Identification of spikes associated with local sources in continuous time series of atmospheric CO, CO_2 and CH_4, Atmospheric Measurement Techniques, 11, 1599–1614, https://doi.org/10.5194/amt-11-1599-2018, 2018.

Farge, M.: Wavelet transforms and their applications to turbulence, Annu. Rev. Fluid Mech., 24, 395–458, 1992.

Farge, M. and Schneider, K.: Analysing and Computing Turbulent Flows Using Wavelets, in: New trends in turbulence Turbulence: nouveaux aspects: 31 July – 1 September 2000, edited by: Lesieur, M., Yaglom, A., and David, F., Springer, Berlin, Heidelberg, 449–504, https://doi.org/10.1007/3-540-45674-0_9, 2001.

Foken, T. and Wichura, B.: Tools for quality assessment of surface-based flux measurements, Agric. For. Meteorol., 78, 83–105, https://doi.org/10.1016/0168-1923(95)02248-1, 1996.

Foken, T., Aubinet, M., and Leuning, R.: The Eddy Covariance Method, in: Eddy Covariance: A Practical Guide to Measurement and Data Analysis, edited by: Aubinet, M., Vesala, T., and Papale, D., Springer Netherlands, Dordrecht, 1–19, https://doi.org/10.1007/978-94-007-2351-1_1, 2012.

Fowler, D., Hargreaves, K., Skiba, U., Milne, R., Zahniser, M., Moncrieff, J., Beverland, I., and Gallagher, M.: Measurements of Ch4 and N2o Fluxes at the Landscape Scale Using Micrometeorological Methods, Philos. Trans. R. Soc. -Math. Phys. Eng. Sci., 351, 339–355, https://doi.org/10.1098/rsta.1995.0038, 1995.

Fratini, G., Ibrom, A., Arriga, N., Burba, G., and Papale, D.: Relative humidity effects on water vapour fluxes measured with closed-path eddy-covariance systems with short sampling lines, Agric. For. Meteorol., 165, 53–63, https://doi.org/10.1016/j.agrformet.2012.05.018, 2012

Göckede, M., Kittler, F., and Schaller, C.: Quantifying the impact of emission outbursts and non-stationary flow on eddy-covariance CH4 flux measurements using wavelet techniques, Biogeosciences, 16, 3113–3131, https://doi.org/10.5194/bg-16-3113-2019, 2019.

Haszpra, L., Barcza, Z., Davis, K. J., and Tarczay, K.: Long-term tall tower carbon dioxide flux monitoring over an area of mixed vegetation, Agric. For. Meteorol., 132, 58–77, https://doi.org/10.1016/j.agrformet.2005.07.002, 2005.

Hazan, L., Tarniewicz, J., Ramonet, M., Laurent, O., and Abbaris, A.: Automatic processing of atmospheric CO_2 and CH_4 mole fractions at the ICOS Atmosphere Thematic Centre, Atmospheric Measurement Techniques, 9, 4719–4736, https://doi.org/10.5194/amt-9-4719-2016, 2016.

Heiskanen, J., Brümmer, C., Buchmann, N., Calfapietra, C., Chen, H., Gielen, B., Gkritzalis, T., Hammer, S., Hartman, S., Herbst, M., Janssens, I. A., Jordan, A., Juurola, E., Karstens, U., Kasurinen, V., Kruijt, B., Lankreijer, H., Levin, I., Linderson, M.-L., Loustau, D., Merbold, L., Myhre, C. L., Papale, D., Pavelka, M., Pilegaard, K., Ramonet, M., Rebmann, C., Rinne, J., Rivier, L., Saltikoff, E., Sanders, R., Steinbacher, M., Steinhoff, T., Watson, A., Vermeulen, A. T., Vesala, T., Vítková, G., and Kutsch, W.: The Integrated Carbon Observation System in Europe, Bulletin of the American Meteorological Society, 103, E855–E872, https://doi.org/10.1175/BAMS-D-19-0364.1, 2022.

Helfter, C., Tremper, A. H., Halios, C. H., Kotthaus, S., Bjorkegren, A., Grimmond, C. S. B., Barlow, J. F., and Nemitz, E.: Spatial and temporal variability of urban fluxes of methane, carbon monoxide and carbon dioxide above London, UK, Atmospheric Chem. Phys., 16, 10543–10557, https://doi.org/10.5194/acp-16-10543-2016, 2016.

Horst, T. W.: A simple formula for attenuation of eddy fluxes measured with first-order-response scalar sensors, Bound.-Layer Meteorol., 82, 219–233, https://doi.org/10.1023/A:1000229130034, 1997.

Ibrom, A., Dellwik, E., Flyvbjerg, H., Jensen, N. O., and Pilegaard, K.: Strong low-pass filtering effects on water vapour flux measurements with closed-path eddy correlation systems, Agric. For. Meteorol., 147, 140–156, https://doi.org/10.1016/j.agrformet.2007.07.007, 2007.

ICOS RI: ICOS Atmosphere Station Specifications V2.0 (editor: O. Laurent), 2734778, https://doi.org/10.18160/GK28-2188, 2020.

Inman, R. E., Ingersoll, R. B., and Levy, E. A.: Soil: a natural sink for carbon monoxide, Science, 172, 1229–1231, https://doi.org/10.1126/science.172.3989.1229, 1971.

IPCC: Climate Change 2021: The Physical Science Basis. Contribution of Working Group I to the Sixth Assessment Report of the Intergovernmental Panel on Climate Change, , In Press, https://doi.org/10.1017/9781009157896, 2021.

IPCC: Climate Change 2022: Mitigation of Climate Change, , https://doi.org/10.1017/9781009157926, 2022.

Irvin, J., Zhou, S., McNicol, G., Lu, F., Liu, V., Fluet-Chouinard, E., Ouyang, Z., Knox, S. H., Lucas-Moffat, A., Trotta, C., Papale, D., Vitale, D., Mammarella, I., Alekseychik, P., Aurela, M., Avati, A.,

Baldocchi, D., Bansal, S., Bohrer, G., Campbell, D. I., Chen, J., Chu, H., Dalmagro, H. J., Delwiche, K. B., Desai, A. R., Euskirchen, E., Feron, S., Goeckede, M., Heimann, M., Helbig, M., Helfter, C., Hemes, K. S., Hirano, T., Iwata, H., Jurasinski, G., Kalhori, A., Kondrich, A., Lai, D. Y., Lohila, A., Malhotra, A., Merbold, L., Mitra, B., Ng, A., Nilsson, M. B., Noormets, A., Peichl, M., Rey-Sanchez, A. C., Richardson, A. D., Runkle, B. R., Schäfer, K. V., Sonnentag, O., Stuart-Haëntjens, E., Sturtevant, C., Ueyama, M., Valach, A. C., Vargas, R., Vourlitis, G. L., Ward, E. J., Wong, G. X., Zona, D., Alberto, Ma. C. R., Billesbach, D. P., Celis, G., Dolman, H., Friborg, T., Fuchs, K., Gogo, S., Gondwe, M. J., Goodrich, J. P., Gottschalk, P., Hörtnagl, L., Jacotot, A., Koebsch, F., Kasak, K., Maier, R., Morin, T. H., Nemitz, E., Oechel, W. C., Oikawa, P. Y., Ono, K., Sachs, T., Sakabe, A., Schuur, E. A., Shortt, R., Sullivan, R. C., Szutu, D. J., Tuittila, E.-S., Varlagin, A., Verfaillie, J. G., Wille, C., Windham-Myers, L., Poulter, B., and Jackson, R. B.: Gap-filling eddy covariance methane fluxes: Comparison of machine learning model predictions and uncertainties at FLUXNET-CH4 wetlands, Agric. For. Meteorol., 308–309, 108528, https://doi.org/10.1016/j.agrformet.2021.108528, 2021.

Iwata, H., Nakazawa, K., Sato, H., Itoh, M., Miyabara, Y., Hirata, R., Takahashi, Y., Tokida, T., and Endo, R.: Temporal and spatial variations in methane emissions from the littoral zone of a shallow mid-latitude lake with steady methane bubble emission areas, Agricultural and Forest Meteorology, 295, 108184, https://doi.org/10.1016/j.agrformet.2020.108184, 2020.

Jia, G., Shevliakova, E., Artaxo, P., De Noblet-Ducoudré, N., Houghton, R., House, J., Kitajima, K., Lennard, C., Popp, A., and Sirin, A.: Land–climate interactions, in: Climate Change and Land: an IPCC special report on climate change, desertification, land degradation, sustainable land management, food security, and greenhouse gas fluxes in terrestrial ecosystems, 2019.

Kadygrov, N., Broquet, G., Chevallier, F., Rivier, L., Gerbig, C., and Ciais, P.: On the potential of the ICOS atmospheric CO_2 measurement network for estimating the biogenic CO_2 budget of Europe, Atmospheric Chem. Phys., 15, 12765–12787, https://doi.org/10.5194/acp-15-12765-2015, 2015.

Kaimal, J. C. and Finnigan, J. J.: Atmospheric Boundary Layer Flows: Their Structure and Measurement, Oxford University Press, 304 pp., 1994.

Kljun, N., Calanca, P., Rotach, M. W., and Schmid, H. P.: A simple two-dimensional parameterisation for Flux Footprint Prediction (FFP), Geosci. Model Dev., 8, 3695–3713, https://doi.org/10.5194/gmd-8-3695-2015, 2015.

Kotthaus, S., Bravo-Aranda, J. A., Collaud Coen, M., Guerrero-Rascado, J. L., Costa, M. J., Cimini, D., O'Connor, E. J., Hervo, M., Alados-Arboledas, L., Jiménez-Portaz, M., Mona, L., Ruffieux, D., Illingworth, A., and Haeffelin, M.: Atmospheric boundary layer height from ground-based remote sensing: a review of capabilities and limitations, Atmospheric Meas. Tech., 16, 433–479, https://doi.org/10.5194/amt-16-433-2023, 2023.

Lauvaux, T., Schuh, A. E., Uliasz, M., Richardson, S., Miles, N., Andrews, A. E., Sweeney, C., Diaz, L. I., Martins, D., Shepson, P. B., and Davis, K. J.: Constraining the CO_2 budget of the corn belt: exploring uncertainties from the assumptions in a mesoscale inverse system, Atmospheric Chem. Phys., 12, 337–354, https://doi.org/10.5194/acp-12-337-2012, 2012.

Lan, C., Mauder, M., Stagakis, S., Loubet, B., D'Onofrio, C., Metzger, S., Durden, D., and Herig-Coimbra, P.-H.: Inter-comparison of Eddy-Covariance Software for Urban Tall Tower Sites, EGUsphere, 1–25, https://doi.org/10.5194/egusphere-2024-35, 2024.

Langford, B., Acton, W., Ammann, C., Valach, A., and Nemitz, E.: Eddy-covariance data with low signal-to-noise ratio: time-lag determination, uncertainties and limit of detection, Atmospheric Measurement Techniques, 8, 4197–4213, https://doi.org/10.5194/amt-8-4197-2015, 2015.

Lenschow, D. H. and Raupach, M. R.: The attenuation of fluctuations in scalar concentrations through sampling tubes, Journal of Geophysical Research: Atmospheres, 96, 15259–15268, https://doi.org/10.1029/91JD01437, 1991.

Leuning, R. and Moncrieff, J.: Eddy-covariance CO2 flux measurements using open- and closed-path CO2 analysers: Corrections for analyser water vapour sensitivity and damping of fluctuations in air sampling tubes, Boundary-Layer Meteorol, 53, 63–76, https://doi.org/10.1007/BF00122463, 1990.

Mallat, S. G.: A theory for multiresolution signal decomposition: the wavelet representation, IEEE Trans. Pattern Anal. Mach. Intell., 11, 674–693, https://doi.org/10.1109/34.192463, 1989.

Massman, W. J.: A simple method for estimating frequency response corrections for eddy covariance systems, Agric. For. Meteorol., 104, 185–198, https://doi.org/10.1016/S0168-1923(00)00164-7, 2000.

Massman, W. J. and Ibrom, A.: Attenuation of concentration fluctuations of water vapor and other trace gases in turbulent tube flow, Atmospheric Chemistry and Physics, 8, 6245–6259, https://doi.org/10.5194/acp-8-6245-2008, 2008.

Massman, W. J. and Lee, X.: Eddy covariance flux corrections and uncertainties in long-term studies of carbon and energy exchanges, Agric. For. Meteorol., 113, 121–144, https://doi.org/10.1016/S0168-1923(02)00105-3, 2002.

Matthews, B., Mayer, M., Katzensteiner, K., Godbold, D. L., and Schume, H.: Turbulent energy and carbon dioxide exchange along an early-successional windthrow chronosequence in the European Alps, Agricultural and Forest Meteorology, 232, 576–594, https://doi.org/10.1016/j.agrformet.2016.10.011, 2017.

Mauder, M. and Foken, T.: Documentation and Instruction Manual of the Eddy-Covariance Software Package TK3, 60, 2011.

Mauder, M., Desjardins, R. L., and MacPherson, I.: Scale analysis of airborne flux measurements over heterogeneous terrain in a boreal ecosystem, J. Geophys. Res. Atmospheres, 112, https://doi.org/10.1029/2006JD008133, 2007.

Mauder, M., Cuntz, M., Drüe, C., Graf, A., Rebmann, C., Schmid, H. P., Schmidt, M., and Steinbrecher, R.: A strategy for quality and uncertainty assessment of long-term eddy-covariance measurements, Agric. For. Meteorol., 169, 122–135, https://doi.org/10.1016/j.agrformet.2012.09.006, 2013.

Metzger, S., Junkermann, W., Mauder, M., Butterbach-Bahl, K., Trancón y Widemann, B., Neidl, F., Schäfer, K., Wieneke, S., Zheng, X. H., Schmid, H. P., and Foken, T.: Spatially explicit regionalization of airborne flux measurements using environmental response functions, Biogeosciences, 10, 2193–2217, https://doi.org/10.5194/bg-10-2193-2013, 2013.

Mishurov, M. and Kiely, G.: Gap-filling techniques for the annual sums of nitrous oxide fluxes, Agric. For. Meteorol., 151, 1763–1767, https://doi.org/10.1016/j.agrformet.2011.07.014, 2011.

Moncrieff, J. b., Malhi, Y., and Leuning, R.: The propagation of errors in long-term measurements of land-atmosphere fluxes of carbon and water, Glob. Change Biol., 2, 231–240, https://doi.org/10.1111/j.1365-2486.1996.tb00075.x, 1996.

Moore, C. J.: Frequency response corrections for eddy correlation systems, Boundary-Layer Meteorol, 37, 17–35, https://doi.org/10.1007/BF00122754, 1986.

Moran, D., Kanemoto, K., Jiborn, M., Wood, R., Többen, J., and Seto, K. C.: Carbon footprints of 13 000 cities, Environ. Res. Lett., 13, 064041, https://doi.org/10.1088/1748-9326/aac72a, 2018.

Nemitz, E., Mammarella, I., Ibrom, A., Aurela, M., Burba, G. G., Dengel, S., Gielen, B., Grelle, A., Heinesch, B., Herbst, M., Hörtnagl, L., Klemedtsson, L., Lindroth, A., Lohila, A., McDermitt, D. K., Meier, P., Merbold, L., Nelson, D., Nicolini, G., Nilsson, M. B., Peltola, O., Rinne, J., and Zahniser, M.: Standardisation of eddy-covariance flux measurements of methane and nitrous oxide, International Agrophysics, 32, 517–549, https://doi.org/10.1515/intag-2017-0042, 2018.

Nordbo, A. and Katul, G.: A Wavelet-Based Correction Method for Eddy-Covariance High-Frequency Losses in Scalar Concentration Measurements, Bound.-Layer Meteorol., 146, 81–102, https://doi.org/10.1007/s10546-012-9759-9, 2013.

Peltola, O., Aslan, T., Ibrom, A., Nemitz, E., Rannik, Ü., and Mammarella, I.: The high-frequency response correction of eddy covariance fluxes – Part 1: An experimental approach and its interdependence with the time-lag estimation, Atmospheric Meas. Tech., 14, 5071–5088, https://doi.org/10.5194/amt-14-5071-2021, 2021.

Peñuelas, J., Asensio, D., Tholl, D., Wenke, K., Rosenkranz, M., Piechulla, B., and Schnitzler, J. p.: Biogenic volatile emissions from the soil, Plant Cell Environ., 37, 1866–1891, https://doi.org/10.1111/pce.12340, 2014.

Ramonet, M., Ciais, P., Apadula, F., Bartyzel, J., Bastos, A., Bergamaschi, P., Blanc, P. E., Brunner, D., Caracciolo di Torchiarolo, L., Calzolari, F., Chen, H., Chmura, L., Colomb, A., Conil, S., Cristofanelli, P., Cuevas, E., Curcoll, R., Delmotte, M., di Sarra, A., Emmenegger, L., Forster, G., Frumau, A., Gerbig, C., Gheusi, F., Hammer, S., Haszpra, L., Hatakka, J., Hazan, L., Heliasz, M., Henne, S., Hensen, A., Hermansen, O., Keronen, P., Kivi, R., Komínková, K., Kubistin, D., Laurent, O., Laurila, T., Lavric, J. V., Lehner, I., Lehtinen, K. E. J., Leskinen, A., Leuenberger, M., Levin, I., Lindauer, M., Lopez, M., Myhre, C. L., Mammarella, I., Manca, G., Manning, A., Marek, M. V., Marklund, P., Martin, D., Meinhardt, F., Mihalopoulos, N., Mölder, M., Morgui, J. A., Necki, J., O'Doherty, S., O'Dowd, C., Ottosson, M., Philippon, C., Piacentino, S., Pichon, J. M., Plass-Duelmer, C., Resovsky, A., Rivier, L., Rodó, X., Sha, M. K., Scheeren, H. A., Sferlazzo, D., Spain, T. G., Stanley, K. M., Steinbacher, M., Trisolino, P.,

Vermeulen, A., Vítková, G., Weyrauch, D., Xueref-Remy, I., Yala, K., and Yver Kwok, C.: The fingerprint of the summer 2018 drought in Europe on ground-based atmospheric CO2 measurements, Philos. Trans. R. Soc. Lond. B. Biol. Sci., 375, 20190513, https://doi.org/10.1098/rstb.2019.0513, 2020.

Sabbatini, S., Mammarella, I., Arriga, N., Fratini, G., Graf, A., Hörtnagl, L., Ibrom, A., Longdoz, B., Mauder, M., Merbold, L., Metzger, S., Montagnani, L., Pitacco, A., Rebmann, C., Sedlák, P., Šigut, L., Vitale, D., and Papale, D.: Eddy covariance raw data processing for CO2 and energy fluxes calculation at ICOS ecosystem stations, Int. Agrophysics, 32, 495–515, https://doi.org/10.1515/intag-2017-0043, 2018.

Saunois, M., Stavert, A. R., Poulter, B., Bousquet, P., Canadell, J. G., Jackson, R. B., Raymond, P. A., Dlugokencky, E. J., Houweling, S., Patra, P. K., Ciais, P., Arora, V. K., Bastviken, D., Bergamaschi, P., Blake, D. R., Brailsford, G., Bruhwiler, L., Carlson, K. M., Carrol, M., Castaldi, S., Chandra, N., Crevoisier, C., Crill, P. M., Covey, K., Curry, C. L., Etiope, G., Frankenberg, C., Gedney, N., Hegglin, M. I., Höglund-Isaksson, L., Hugelius, G., Ishizawa, M., Ito, A., Janssens-Maenhout, G., Jensen, K. M., Joos, F., Kleinen, T., Krummel, P. B., Langenfelds, R. L., Laruelle, G. G., Liu, L., Machida, T., Maksyutov, S., McDonald, K. C., McNorton, J., Miller, P. A., Melton, J. R., Morino, I., Müller, J., Murguia-Flores, F., Naik, V., Niwa, Y., Noce, S., O'Doherty, S., Parker, R. J., Peng, C., Peng, S., Peters, G. P., Prigent, C., Prinn, R., Ramonet, M., Regnier, P., Riley, W. J., Rosentreter, J. A., Segers, A., Simpson, I. J., Shi, H., Smith, S. J., Steele, L. P., Thornton, B. F., Tian, H., Tohjima, Y., Tubiello, F. N., Tsuruta, A., Viovy, N., Voulgarakis, A., Weber, T. S., van Weele, M., van der Werf, G. R., Weiss, R. F., Worthy, D., Wunch, D., Yin, Y., Yoshida, Y., Zhang, W., Zhang, Z., Zhao, Y., Zheng, B., Zhu, Q., Zhu, Q., and Zhuang, Q.: The Global Methane Budget 2000–2017, Earth System Science Data, 12, 1561–1623, https://doi.org/10.5194/essd-12-1561-2020, 2020.

Schaller, C., Göckede, M., and Foken, T.: Flux calculation of short turbulent events: comparison of three methods, Atmospheric Meas. Tech., 10, 869–880, https://doi.org/10.5194/amt-10-869-2017, 2017.

Stoy, P. C., Katul, G. G., Siqueira, M. B. S., Juang, J.-Y., Novick, K. A., Uebelherr, J. M., and Oren, R.: An evaluation of models for partitioning eddy covariance-measured net ecosystem exchange into photosynthesis and respiration, Agricultural and Forest Meteorology, 141, 2–18, https://doi.org/10.1016/j.agrformet.2006.09.001, 2006.

Strunin, M. A. and Hiyama, T.: Applying wavelet transforms to analyse aircraft-measured turbulence and turbulent fluxes in the atmospheric boundary layer over eastern Siberia, Hydrol. Process., 18, 3081–3098, https://doi.org/10.1002/hyp.5750, 2004.

Torrence, C. and Compo, G. P.: A Practical Guide to Wavelet Analysis, Bull. Am. Meteorol. Soc., 79, 61–78, https://doi.org/10.1175/1520-0477(1998)079<0061:APGTWA>2.0.CO;2, 1998.

Tramontana, G., Migliavacca, M., Jung, M., Reichstein, M., Keenan, T. F., Camps-Valls, G., Ogee, J., Verrelst, J., and Papale, D.: Partitioning net carbon dioxide fluxes into photosynthesis and respiration using neural networks, Global Change Biology, 26, 5235–5253, https://doi.org/10.1111/gcb.15203, 2020.

Ueyama, M. and Takano, T.: A decade of CO2 flux measured by the eddy covariance method including the COVID-19 pandemic period in an urban center in Sakai, Japan, Environ. Pollut., 304, 119210, https://doi.org/10.1016/j.envpol.2022.119210, 2022.

Valentini, R., De ANGELIS, P., Matteucci, G., Monaco, R., Dore, S., and Mucnozza, G. E. S.: Seasonal net carbon dioxide exchange of a beech forest with the atmosphere, Glob. Change Biol., 2, 199–207, https://doi.org/10.1111/j.1365-2486.1996.tb00072.x, 1996.

Velasco, E., Pressley, S., Grivicke, R., Allwine, E., Coons, T., Foster, W., Jobson, B. T., Westberg, H., Ramos, R., Hernández, F., Molina, L. T., and Lamb, B.: Eddy covariance flux measurements of pollutant gases in urban Mexico City, Atmospheric Chem. Phys., 9, 7325–7342, https://doi.org/10.5194/acp-9-7325-2009, 2009.

Vuichard, N., Ciais, P., Viovy, N., Li, L., Ceschia, E., Wattenbach, M., Bernhofer, C., Emmel, C., Grünwald, T., Jans, W., Loubet, B., and Wu, X.: Simulating the net ecosystem CO2 exchange and its components over winter wheat cultivation sites across a large climate gradient in Europe using the ORCHIDEE-STICS generic model, Agric. Ecosyst. Environ., 226, 1–17, https://doi.org/10.1016/j.agee.2016.04.017, 2016.

Wilczak, J. M., Oncley, S. P., and Stage, S. A.: Sonic Anemometer Tilt Correction Algorithms, Bound.-Layer Meteorol., 99, 127–150, https://doi.org/10.1023/A:1018966204465, 2001.

Winderlich, J., Gerbig, C., Kolle, O. and Heimann, M., 2014. Inferences from CO2 and CH4 concentration profiles at the Zotino Tall Tower Observatory (ZOTTO) on regional summertime ecosystem fluxes. Biogeosciences, 11(7): 2055-2068. 10.5194/bg-11-2055-2014

Wintjen, P., Ammann, C., Schrader, F., and Brümmer, C.: Correcting high-frequency losses of reactive nitrogen flux measurements, Atmospheric Measurement Techniques, 13, 2923–2948, https://doi.org/10.5194/amt-13-2923-2020, 2020.

Wohlfahrt, G., Hörtnagl, L., Hammerle, A., Graus, M., and Hansel, A.: Measuring eddy covariance fluxes of ozone with a slow-response analyser, Atmos. Environ., 43, 4570–4576, https://doi.org/10.1016/j.atmosenv.2009.06.031, 2009.

Zheng, B., Chevallier, F., Yin, Y., Ciais, P., Fortems-Cheiney, A., Deeter, M. N., Parker, R. J., Wang, Y., Worden, H. M., and Zhao, Y.: Global atmospheric carbon monoxide budget 2000–2017 inferred from multi-species atmospheric inversions, Earth Syst. Sci. Data, 11, 1411–1436, https://doi.org/10.5194/essd-11-1411-2019, 2019.

5.7 Appendix

5.7.1 Theoretical high-frequency attenuation

The theoretical approach for high-frequency loss corrections requires defining a transfer function, TF, for each of the relevant origins of frequency losses, *i*, and multiplying them to find the total transfer function, TF_{total} (Moore, 1996):

$$TF_{total}(f) = \prod TF_i(f) \tag{A 1}$$

Note that TFs range between 0 and 1, so the TF_{ws} is driven by the most restrictive function for each frequency. Considering only the attenuation from the air transport in the tube (TF_{tube}, Leuning and Moncrieff, 1990; Foken et al., 2012) and acquisition rate (TF_{acq}, Horst, 1997):

$$TF_{tube} = \begin{cases} \exp\left\{-160Re^{-\frac{1}{8}}\dfrac{\pi^2 r^5 f^2 L}{Q}\right\}, & Re < 2300 \\ \exp\left\{-\dfrac{\pi^3 r^4 f^2 L}{6 D_s Q}\right\}, & Re \geq 2300 \end{cases} \tag{A 2}$$

$$TF_{acq} = [1 + (2\,\pi f \tau_w)^2]^{-1/2} \times [1 + (2\,\pi f \tau_s)^2]^{-1/2} \tag{A 3}$$

Where Re is Reynolds number (-), *r* is tube radius (m), *f* is the frequency (Hz), L is tube length (m), Q is the volumetric flow rate ($m^3 s^{-1}$), and τ is the first-order filter's time constant (s) where $\tau = \left(2\,\pi f_{acq}\right)^{-1}$ and f_{acq} is the acquisition frequency (Hz) for vertical wind speed or scalar. Reynolds number is defined as $Re = \frac{2Q}{\pi r v}$, where *v* is the kinematic viscosity.

Attenuation also depends on the co-spectra. A theoretical approach is proposed by Horst (1997, eq. 11), where

$$\frac{\overline{w'c'}_{measured}}{\overline{w'c'}_{true}} = 1 + (2\pi\, n_{max} \tau_c \bar{u}/z)^{-\alpha} \tag{A 4}$$

Where $\bar{u}$ is the mean wind speed at height *z*, n_{max} is 0.085 in case $z/L < 0$ else $2 - 1.915/(1 + 0.5z/L)$, and α is 7/8 for $z/L < 0$ else 1.

5.7.2 Supplemental figures

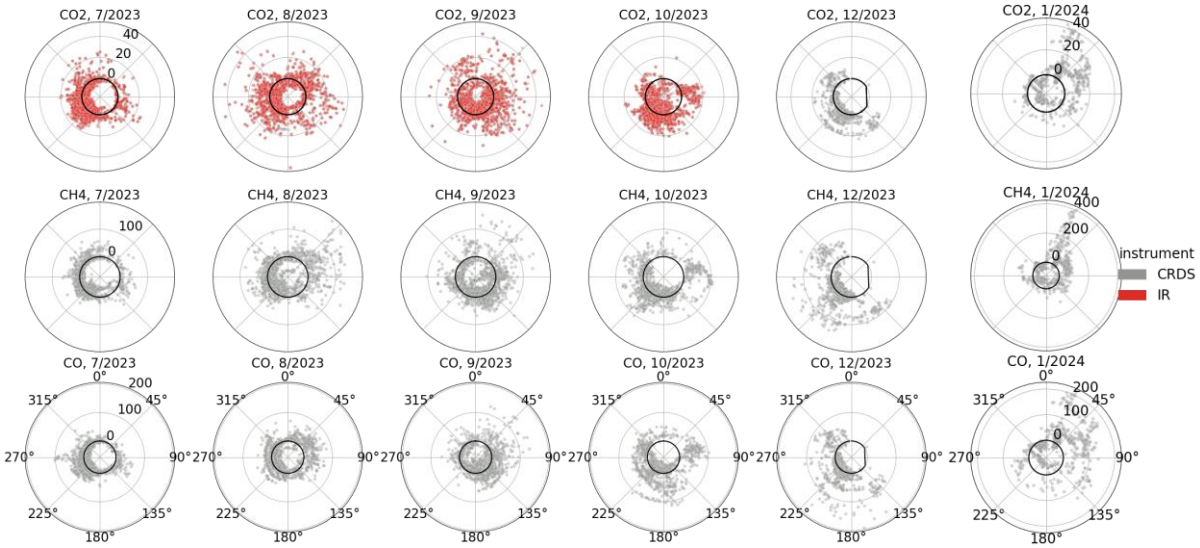

Figure S 5.1. Concentration by wind direction. Values differ from the monthly median (the black line is 0). Extreme values in the left and right 0.1% tails were removed. Note that January has a different scale.

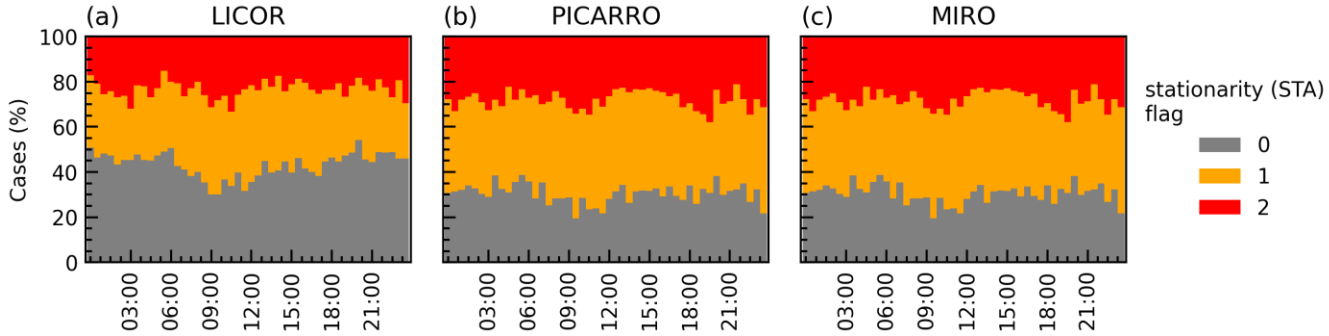

Figure S 5.2. Quality control flags for CO_2 flux stationarity for the three gas analysers. Flags follow a 0-1-2 system for high, medium and low quality.

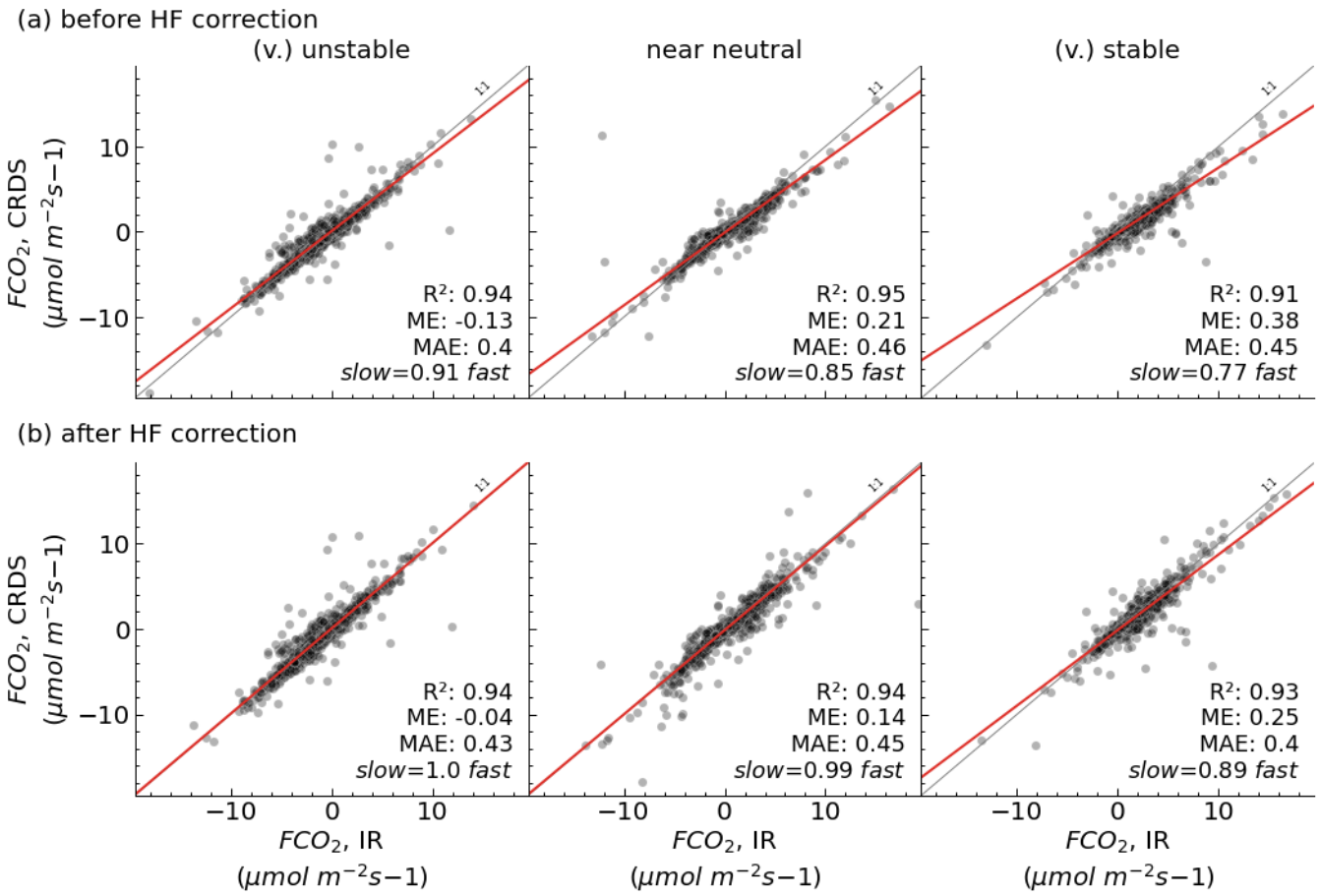

Figure S 5.3. Comparison of CO_2 flux using IR (LI-7200) and CRDS (PICARRO G2401) per stability condition. Dots are observations; the red line is a true linear relation, and the grey line is a 1:1 line. The correlation coefficient (R^2), the mean error (ME, $\mu molm^{-2}s^{-1}$), the mean absolute error (MAE, $\mu molm^{-2}s^{-1}$) and the linear fit.

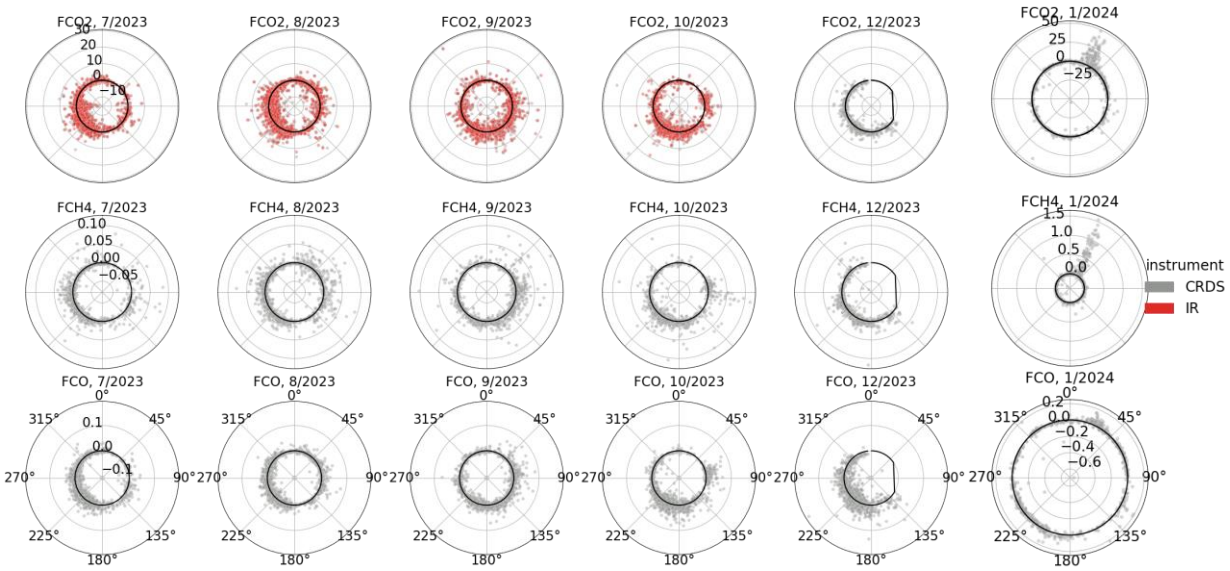

Figure S 5.4. Turbulent fluxes by wind direction. Values differ from the monthly media; 0.1% of extreme values dropped. Note that January has a different scale.

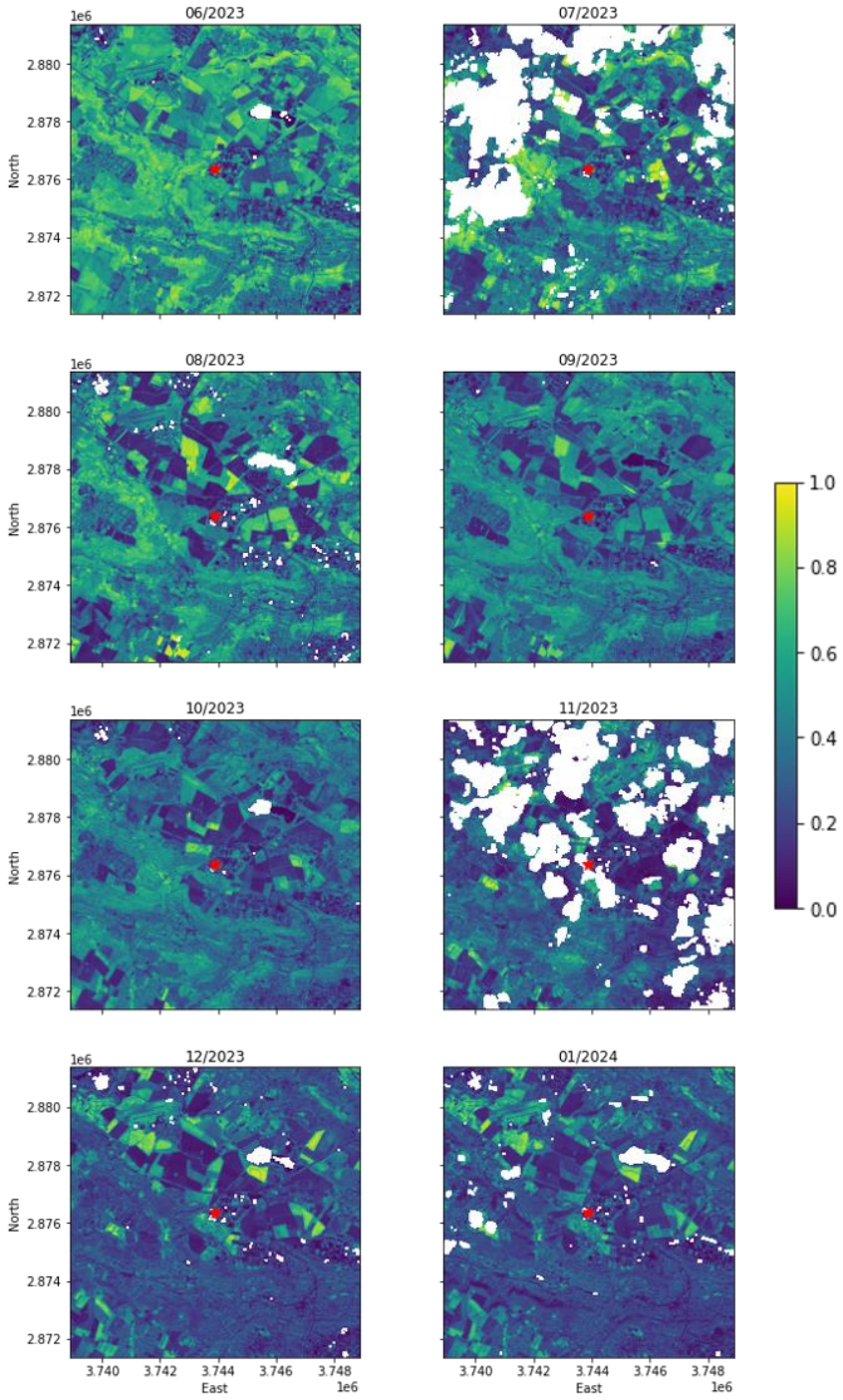

Figure S 5.5. The monthly average EVI is a 10x10 km grid centred in the Saclay tower (red star). Pixels with no data are represented in white.

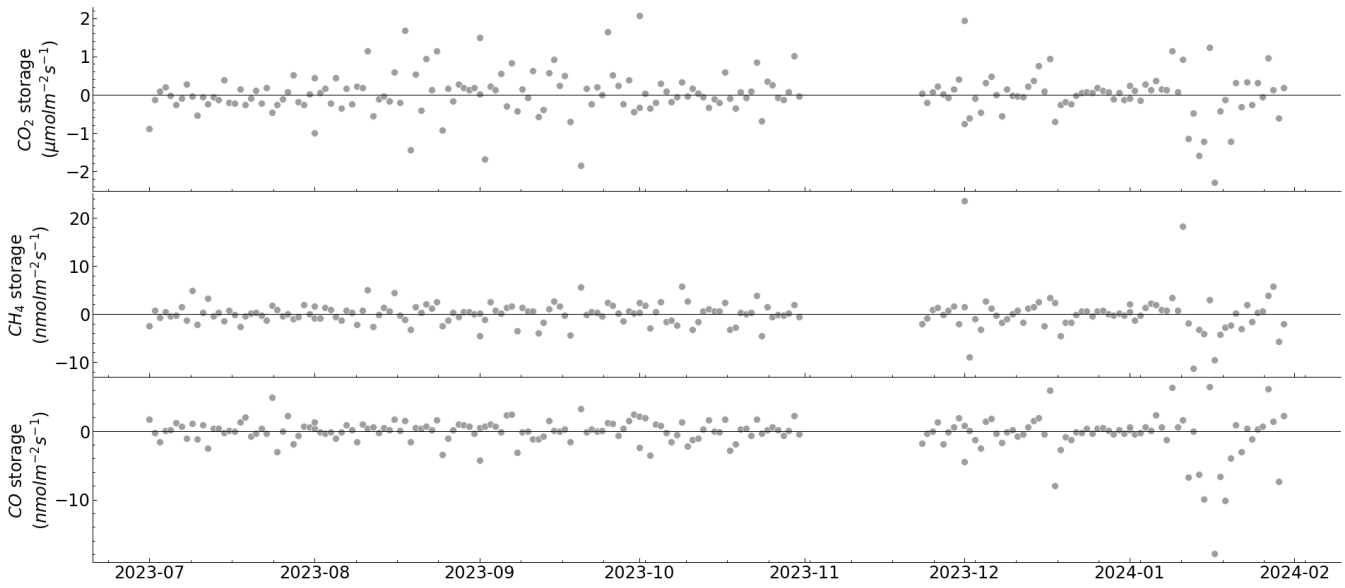

Figure S 5.6. Daily storage fluxes of CO2, CH4 and CO using measurements of a single CRDS (PICARRO G2401) gas analyser at 3 levels (15, 60, 100 m). Daily storage flux should be zero in ideal conditions since stocking and destocking should compensate for each other.

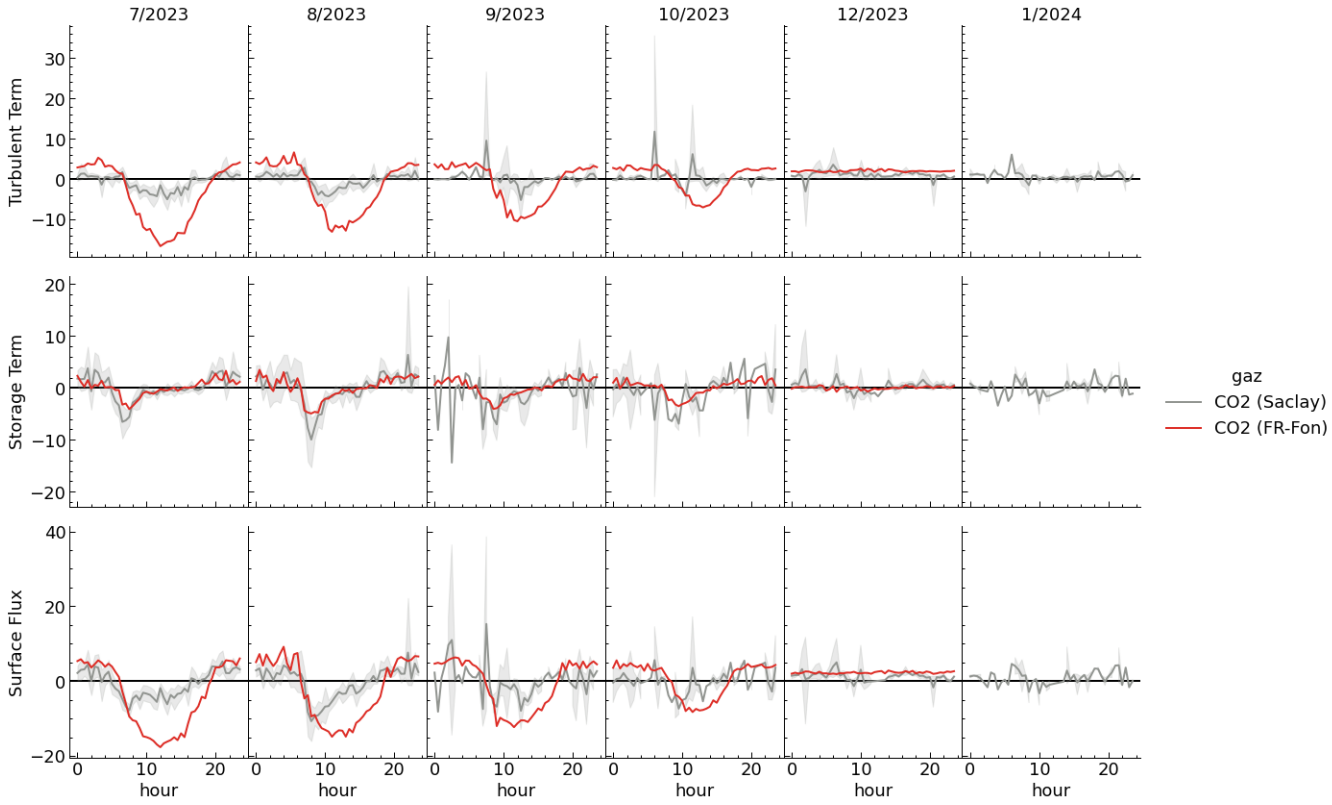

Figure S 5.7. Comparison with forest site (FR-Fon). Data is available at the ICOS Data Portal (https://meta.icos-cp.eu/objects/lCyv5rk_qnaaexfXx1skb2mV).

6. MAPPING PARTITIONED FLUXES OVER HETEROGENEOUS LANDSCAPES

Mapping partitioned fluxes across heterogeneous landscapes is a complex yet crucial task in studying gas exchanges at the landscape scale. Considering their heterogeneity, this approach aims to spatially represent the distribution of gas fluxes among different land cover types. By assimilating in-situ measurement with estimations from surface models, we can produce detailed maps of surface fluxes over heterogeneous landscapes. This mapping can help better understand the spatial distribution of greenhouse gas emissions and absorptions.

The real flux at a certain height depends on the surface flux, which is continuous in time and space, and on transport. During real-world calculations, both observations and models have uncertainties. Space and time are discretized, instruments introduce noise, and models are imperfect. The Bayesian approach provides a good framework for estimating surface fluxes while considering these uncertainties.

In this Chapter, we estimate a flux map and its uncertainty based on in-situ flux measurements and a footprint model coupled with a surface model. There is no conventional partitioning method for partitioning CO_2 fluxes containing anthropogenic fluxes. We, thus, used the method in further detail in Chapter 2 and demonstrated its applicability in Chapter 3. The advantage of this method is its flexibility and minimum requirements, which only require what is already needed for flux calculation. We thus use data from the atmospheric measurement setup tested for flux measurements in Chapter 4, partitioning CO_2 fluxes into GPP, Reco and aCO_2, using CO and CH_4 as tracers for the last one.

6.1 Mapping partitioned fluxes over heterogeneous landscapes: a framework for eddy covariance tower

Pedro Henrique H. Coimbra[1,2*], Benjamin Loubet[1], Olivier Laurent[2], Mathis Lozano[2,] Michel Ramonet[2], Olivier Perrussel[3]

[1] ECOSYS, INRAE, AgroParisTech, Université Paris-Saclay, Palaiseau, France
[2] Laboratoire des Sciences du Climat et de l'Environnement, CEA, CNRS, Université Paris-Saclay, Gif-sur-Yvette, France

* corresponding author: pedro-henrique.herig-coimbra@inrae.fr

Mapping partitioned fluxes over heterogeneous landscapes: a framework for eddy covariance tall towers

Pedro Henrique H. Coimbra[1,2*], Benjamin Loubet[1], Olivier Laurent[2], Mathis Lozano[2,] Michel Ramonet[2], Olivier Perrussel[3]

[1] ECOSYS, INRAE, AgroParisTech, Université Paris-Saclay, Palaiseau, France

[2] Laboratoire des Sciences du Climat et de l'Environnement, CEA, CNRS, Université Paris-Saclay, Gif-sur-Yvette, France
[3] AIRPARIF Surveillance de la Qualité de l'Air en Île-de-France, Paris, France

* corresponding author: pedro-henrique.herig-coimbra@inrae.fr

Abstract

Monitoring greenhouse gases is crucial to verifying projections and confirming that public policy is aligned with their expectations. With advancements in satellite technology offering resolutions smaller than a tower's footprint, coupled with the power of data assimilation, models can now estimate processes and assimilate data at exceptionally fine scales.

This study explores the potential of assimilating tall tower eddy covariance fluxes to calibrate a surface model of CO_2 exchange over a heterogeneous landscape intricating biogenic and anthropogenic sources and sinks. Additionally, it extends the previous work on wavelet-based direct partitioning and proposes a modified version to account for anthropogenic sources, using carbon monoxide and methane as a distinctive combustion tracer. The study focuses on a landscape of 8×8 km^2 around the Saclay ICOS tower FR-Sac in Palaiseau, including a local heating plant in the tower footprint, being a potential strong point source of CO_2 and methane.

Our findings affirm the interest of this approach, yielding coherent results on biogenic fluxes and a potential to retrieve the emissions from the local heating plant. However, the partitioning method artificially increased biogenic uptake as a compensation artefact when the CO_2 flux coming from the heating plant was high. Our results suggest splitting into biogenic and anthropogenic, which may still be possible using a different rule for partitioning. Further refinement in partitioning strategies is required to ensure robust flux attribution across diverse environmental contexts. Further studies should also focus on the validation of the mapped fluxes.

6.2 Introduction

Local gas exchanges play a crucial role on larger scales by regulating atmospheric composition, influencing climate change, and notably driving climate change through the greenhouse effect. Global surface temperatures are already surging by 1.6°C compared to pre-industrial levels, and further escalation is projected by 2100 (Canadell et al., 2021). Identifying and quantifying sources and sinks of greenhouse gases (GHGs) has become increasingly urgent for mitigating the drivers of this warming.

While agriculture, forestry, and other land use (AFOLU) activities are significant contributors to GHG emissions, they also possess the potential to act as carbon sinks, mitigating atmospheric CO_2 levels (Jia et al., 2019). However, urban areas are major GHG emitters due to their population denseness. Initiatives such as electrifying energy grids, implementing car-free zones, and enhancing insulation represent vital steps in reducing urban emissions. Yet, measuring and monitoring GHG fluxes in urban environments present unique challenges due to the fluxes' heterogeneity and point sources' presence. Addressing these complexities is essential for accurately assessing and guiding efforts to mitigate urban emissions and combat climate change

effectively. Urban observational networks have been used to address emissions in different cities (Newman et al., 2016; Gurney et al., 2012; Kim et al., 2018). In Europe, the ICOS Cities (PAUL) project, which seeks to advance monitoring technologies in piloting the cities of Munich, Paris, and Zurich, exemplifies the importance of innovative approaches in this endeavour.

At larger scales, monitoring GHG emissions is often done by integrating atmospheric concentration measurements with transport models to estimate surface fluxes (Bousquet et al., 2000; Chevallier et al., 2010). As they are based on very high-quality but few atmospheric measurements, they are good at providing emission estimates over vast areas. However, their accuracy at the resolution of a few kilometres remains low. The advancement of geospatial data resolution has facilitated the direct utilisation of flux measurements for creating high-resolution flux maps, allowing for detailed insights into flux dynamics at resolutions as fine as a few meters (Crawford and Christen, 2015). These methods promise to improve local and larger-scale estimations, potentially serving as valuable tools for cross-validating atmospheric inversions as their accuracy improves.

Flux monitoring sites were chosen based on surface homogeneity in their local footprint. Tall towers are exceptions and can have footprints spreading over a few kilometres, with different land uses contributing to the flux measured (Barcza et al., 2009). While tall towers meant for atmospheric background measurements may not adhere to all conventional technical specifications for a flux tower, notably fast-response gas analysers, we have shown that they can be used to compute fluxes of CO_2, methane and CO, with the addition of a sonic anemometer (Coimbra et al., 2024).

It is often essential to break down the net CO_2 flux into sources and sinks, a process known as partitioning. The partitioned fluxes can, in particular, help constrain the calibration of satellite-driven CO2 exchange models (Bazzi et al. 2024) compared to using the net flux where compensations happen. In fully vegetated ecosystems, gross primary productivity (GPP) and ecosystem respiration (R_{eco}), components of the net flux or net ecosystem exchange (NEE), exhibit distinct dynamics and respond to different environmental factors (Lloyd and Taylor, 1994; Farquhar et al., 1980). In (sub-)urban environments, direct anthropogenic emissions become an important component of the net flux. In these settings, NEE can sometimes be replaced by the term "net urban exchange" (NUE) to emphasize the distinction compared to fully vegetated ecosystems. Despite the marked differences in biogenic and anthropogenic emissions, the net flux partitioning between these components remains challenging.

While conventional methods for partitioning vegetation fluxes exist, no established method for distinguishing between biogenic and anthropogenic fluxes exists. From possible partitioning methods, direct ones combine the flexibility of being free from a model with the accuracy of direct measurements. These approaches rely on the same principle: an air parcel coming from the surface is not entirely mixed when reaching the EC sensors so that it retains some features of the leaf-scale and soil-scale exchange processes. This same principle is the basis for Scanlon et al. (2019), Thomas et al. (2008) and Coimbra et al. (2023). In Coimbra et al. (2023), over two sites, a forest and cropland, the authors reported a good comparison (R^2>0.94) between the proposed direct method and conventional model-based methods for partitioning CO_2.

The partitioning between gross primary productivity (GPP) and ecosystem respiration (R_{eco}) is a relatively straightforward task compared to when anthropogenic emissions come into play. While GPP and R_{eco} have different directions, uptake and release, respectively, when anthropogenic emissions are significant, R_{eco} and anthropogenic emissions are both emitters, making it challenging to differentiate between the two sources. The R_{eco} and anthropogenic emissions may, however, be correlated differently to other tracer gases. In particular, combustion tracers such as CO and CH_4 may be good candidates. NO and NO_2, as very reactive compounds, may not be suitable.

In mid-latitudes in the northern hemisphere, emissions of CO are mainly related to direct (fossil or bio) fuel combustion (Zheng et al., 2019), particularly during colder months with diminished efficiency of fuel combustion (Helfter et al., 2016). Methane and volatile organic compounds (VOCs) oxidation are also relatively small CO sources (Zheng et al., 2019). On the contrary, the soil is recognized as a CO sink, primarily attributed to microbial oxidation processes (Inman et al., 1971; Conrad and Seiler, 1980; Conrad, 1996). For methane (CH_4), wet environments are a known source alongside combustion and livestock (Canadell et al., 2021). Over inland, however, soil oxidation makes the land a sink of CH_4. Therefore, CH_4 and CO may be good candidates for decoupling anthropogenic and biogenic CO_2 sources in dry soils.

Surface models provide information on the spatial distribution of flux exchanges. The Vegetation Photosynthesis and Respiration Model (VPRM) is a simple yet powerful tool for estimating high-resolution biogenic flux maps (Bazzi et al., 2024). To compare with observations, conventional footprint models (Kljun et al., 2015) are needed to estimate what a tower would measure, given a flux map.

Data assimilation techniques offer a sophisticated approach to calibrating surface models and generating accurate flux maps. The Bayesian framework is extensively employed to estimate surface fluxes based on assimilating atmospheric mixing ratio measurements into prior estimations on global (Bousquet et al., 2000; Chevallier et al., 2010), continental (Kountouris et al., 2018) and regional (Lauvaux et al., 2012) scales. The priors and target estimation are the same objects in these studies: the CO_2 flux map. However, the Bayesian approach can be employed to find the parameters of a surface model used to generate the CO_2 flux map. A surface model adds another layer of constraints as estimations are derived from a biophysically meaningful model.

In this study, we evaluate a method combining CO_2 flux partitioning and Bayesian assimilation to compute the surface fluxes in an 8×8 km^2 area surrounding a tall tower flux measurement setup. For that, we:

- Partition the CO2 flux into gross primary production (GPP), ecosystem respiration (R_{eco}) and anthropogenic emissions (aCO_2), using the wavelet-based direct partitioning method of Coimbra et al. (2023), modified to include CO and CH_4 as a tracer of combustion. Wavelet-based eddy covariance is used for partitioning but also because it allows the analysis of non-stationary fluxes to yield more exploitable data, particularly from an intense local point source (Coimbra et al., 2024).

- Assimilate the CO_2 partitioned data into a flux map model. We use the VPRM model for biogenic sources and the AIRPARIF inventories for anthropogenic sources (traffic, residential heating and industries). The Kljun et al. (2015) footprint model transports the surface fluxes to the tower location, and Bayesian inference accounts for prior knowledge and uncertainties. We use the prior standard parameters in global studies (Mahadevan et al., 2008).

The method is evaluated using the dataset of 6 months of flux measurements at 100 m height at the Saclay tower, FR-SAC, part of ICOS atmospheric centre, from July 2023 until January 2024 (Coimbra et al., 2024). The dataset includes fluxes from a low-response analyser with a 100-m tube for CO_2, CH_4, and CO. The chosen site is a sub-urban site surrounded by agriculture, forest, roads, and buildings, providing a good playground that intermixes anthropogenic and biogenic sources. The inferred parameters and maps are discussed, and the biogenic fluxes are compared with those of nearby ICOS ecosystem sites.

6.3 Site and observations

6.3.1 Net surface flux

The flux measurements used as observations in the inversion system are eddy covariance measurements in µmol $m^{-2}s^{-1}$, collected at the FR-Sac ICOS tall tower. The study uses 6 monthly flux datasets from the 100-meter Saclay tower, FR-SAC, part of the ICOS Atmospheric Centre (Figure 6.1). The site is located at a university and research campus 20 km southwest of Paris. The site has two high-precision cavity ring-down spectroscopy (CRDS) gas analysers (CO_2, CO, CH_4, G2401; Picarro Inc., Santa Clara, CA, USA) on a ground-level shelf. One analyser continuously measures at 100 m above ground level, the other at 3 heights (15, 60, and 100 meters above ground level) alternating every 10 minutes (for more details, see 5.3.1).

The site had an ultrasonic anemometer (Gill WindMasterPro) and a Licor7200 CO_2/H_2O IRGA located at 100 m. The turbulent fluxes were computed by eddy covariance using the sonic anemometer and the CRDS analysers for CO_2, CO and CH_4. The turbulent fluxes were corrected for high-frequency losses due to the long tube and low CRDS sampling frequency. The surface fluxes were computed as the sum of the turbulent and storage fluxes computed from the vertical profile. For further description of the setup and methods, please refer to section 5.3.1.

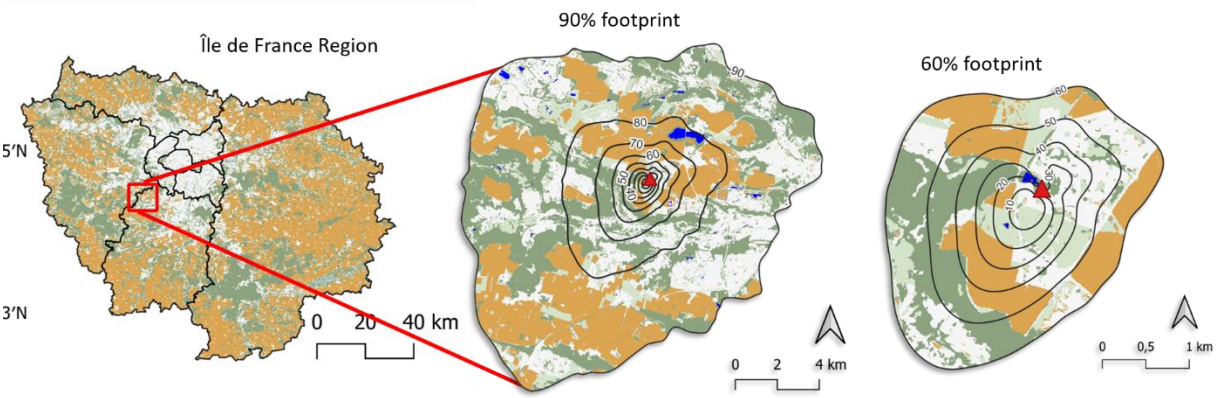

Figure 6.1. Site location. In the left panel, the Ile de France region with reference sites marked. In the middle and right panels, 90% and 60% footprint contour with the tower location red triangle. Colours indicate land use: cropland (orange), grassland (light green), forest (dark green), water (light blue), and white (urban).

In this work, we use wavelet-based eddy covariance. This choice is justified given that it allowed 18-34% more data exploitation than conventional EC and enabled the analysis of non-stationary fluxes, which is particularly prone due to a vigorous point source heating plant situated in the tower flux footprint. Finally, wavelets were also required for the direct partitioning method proposed by Coimbra et al. (2023) and used here.

A fully developed turbulence test was calculated following Foken and Wichura (1996) to guarantee the quality of the data for analysis and assimilation. In this study, we only used good and medium-quality data for the turbulence test, < 100%, following the flag system from FLUXNET (Mauder and Foken, 2011). Random uncertainties were computed to provide observational uncertainties in the assimilation framework. The random uncertainty was arbitrarily multiplied by 2 to account for the storage term uncertainty, which in a 3-point profile setup over 100 m may not be negligible.

6.3.2 Partitioning net flux

Partitioned fluxes are commonly used to help constrain model calibration. We use a wavelet-based direct partitioned method due to its flexibility and not requiring any previous calibration. In this method, variables are decomposed in the time *t* and frequency *j* domains, and their product (e.g.: $\widetilde{w}\widetilde{\chi}_s(t,j)$) is separated into groups, such as positive (emitter) and negative (sinks) (Figure 6.2). Here $\sim$ stands for decomposed variables, *w* is vertical velocity, and χ_s is the scalar dry mixing ratio. This separation into groups is also known as conditional sampling. The method is flexible and allows employing any variable split into positive and negative (or above and below a threshold). The processing steps described above are illustrated in Figure 6.2.

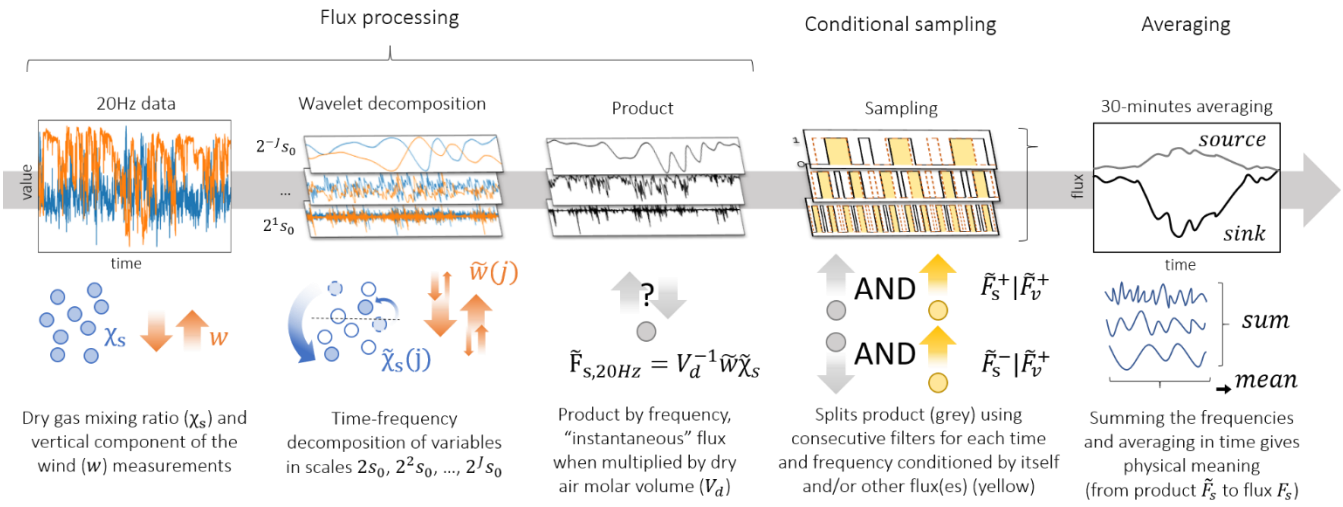

Figure 6.2: Conceptual scheme showing the main wavelet-based eddy covariance processing steps: time and frequency decomposition; the product of instantaneous deviation; partitioning by conditional sampling, and finally, frequency integration and time averaging. Where w is the vertical component of the wind velocity, χ_s is the mixing ratio of a gas, j represents the frequency scale, bars are for averaging and quotation marks are deviations from the mean.

We follow the same framework as in Coimbra et al. (2023), but here, we use CO and CH_4 as tracers to distinguish biogenic and anthropogenic sources. The underlying empirical assumption is that wavelet decomposition, in time and frequency, should capture positive and negative "gusts", which are mixed up in the original signal. These gusts must relate to relevant plausible fluxes, which for CO_2 and CH_4 are conceptualised in Figure 6.3. CO is not shown, but we assume it mostly comes from combustion.

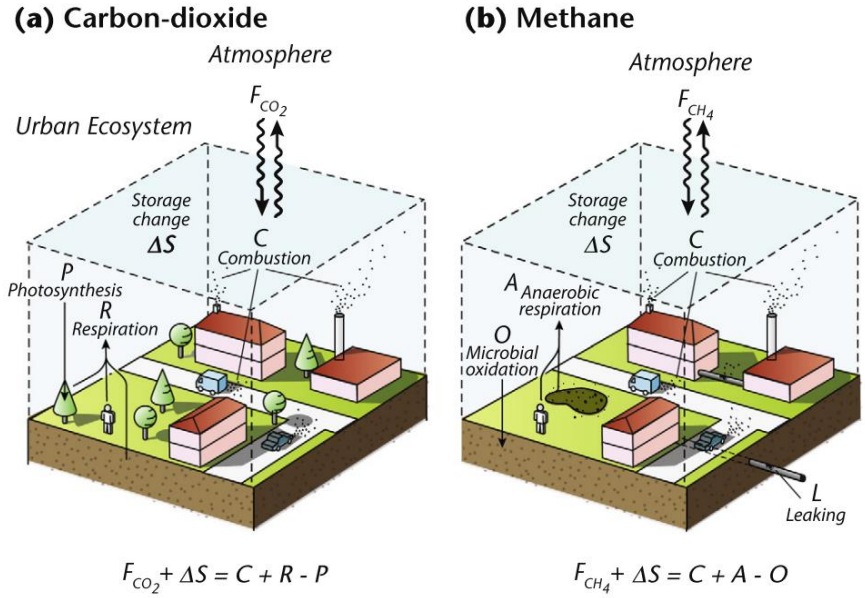

Figure 6.3. Conceptual representation of the mass fluxes of (a) carbon dioxide and (b) methane between a city and the atmosphere. The equations show mass balances for the volume encompassing the airspace in the

urban canopy layer and above up to a height where the atmosphere is well mixed. In the box, all emissions and uptake processes take place. In all three cases, ΔS is the change in mixing ratio in the canopy air volume. Chemical reactions in the atmosphere are neglected. Source: (Christen, 2014)

In this study, we take advantage of CO and CH_4 as tracers to attribute the partitioned CO_2 flux to gross primary productivity, or photosynthesis (GPP), ecosystem respiration, which includes leaves and soil (Reco), and anthropogenic emissions (aCO_2) (Figure 3.4).

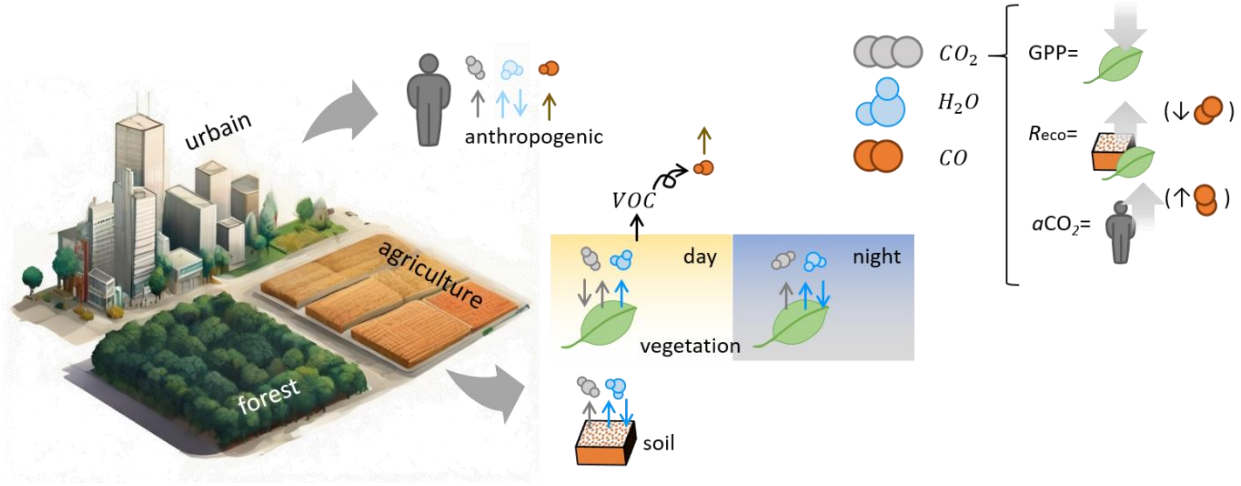

Figure 6.4. Conceptual schemes of correlations between CO2, H2O, and CO flux directions are based on the physical source or sink. GPP is gross primary productivity (photosynthesis); Reco is ecosystem respiration, which includes leaves and soil. aCO_2 is an anthropogenic emission. VOC stands for volatile organic compounds, which are sources of CO. The figure was partially generated using artificial intelligence (DALL-E3).

Air was dried in the tube before measurement, so water vapour could not be used, and the approach from Coimbra et al. (2023) had to be simplified. Thus, we computed GPP simply as the negative data points of the product $\widetilde{w}\tilde{\chi}_{CO_2}$:

$$\widetilde{w}\tilde{\chi}_{CO_2}^{GPP} = \widetilde{w}\tilde{\chi}_{CO_2}^{-} \quad 6.1$$

We used CO and CH_4 as a tracer of fossil fuel emissions to split R_{eco} and aCO_2, both CO_2 emitters. Indeed, mid-latitude soils are mostly CO-sink, and the same applies to CH_4 and dry soils (see section 2.1.3), while fuel combustion emits both. The Reco and $aCO2$ terms were computed as:

$$\widetilde{w}\tilde{\chi}_{CO_2}^{Reco} = \widetilde{w}\tilde{\chi}_{CO_2}^{+}|\widetilde{w}\tilde{\chi}_{CO}^{-} \quad 6.2$$

$$\widetilde{w}\tilde{\chi}_{CO_2}^{ffCO_2} = \widetilde{w}\tilde{\chi}_{CO_2}^{+}|\widetilde{w}\tilde{\chi}_{CO}^{+} \quad 6.3$$

Where $\tilde{\chi}_v$ is the mixing ratio of another gas (e.g.: H_2O, CH_4, CO) and $x|y$ stands for sampling x when y is true.

Distributing the storage term into each partitioned flux is not trivial. We subjectively opted for distributing the storage flux on the partitioned fluxes with $\alpha_{Reco} = \alpha_{aCO2} = \frac{1}{2}\alpha_{GPP} = 1/4$. Also a factor V_a was introduced to set the storage flux in the same units as the covariances, leading to $GPP = \sum_{j=0}^{J} \overline{\widetilde{w}\widetilde{\chi}_{CO_2}^{GPP}} + \alpha_{GPP} V_a ST_{CO_2}$, $R_{eco} = \sum_{j=0}^{J} \overline{\widetilde{w}\widetilde{\chi}_{CO_2}^{Reco}} + \alpha_{Reco} V_a ST_{CO_2}$ and $aCO_2 = \sum_{j=0}^{J} \overline{\widetilde{w}\widetilde{\chi}_{CO_2}^{aCO_2}} + \alpha_{aCO_2} V_a ST_{CO_2}$.

Note that we should have a closure of our system where $NEE = GPP + R_{eco} + aCO_2$ as the replacement is done using 0. In Coimbra et al. (2023), the authors took advantage of GPP's light dependency to only attribute GPP during the day. This forcing was unsatisfactory and may lead to unrealistic dynamics of GPP and Reco during the sunset and sunrise periods. In this study, we, therefore, did not add this constraint.

6.4 Inversion method

6.4.1 Inversion system

The variations of CO_2 surface fluxes are inferred from the direct flux measurements by the inversion scheme, which combines them with a footprint model and a surface model containing pre-existing information about the fluxes within a Bayesian framework. Following the usual terminology, the "prior" refers to information before inversion, and "posterior", or analysis, refers to the information about the fluxes after the inversion (Bousquet et al., 1999). The basic framework, Bayesian Inversion, consists of building a cost function:

$$F = \frac{1}{2}\left[\left(x - x^b\right)^T B^{-1}\left(x - x^b\right) + (Hx - y)^T R^{-1}(Hx - y)\right] \quad 6.4$$

Where x^b is a set of free parameters for the model *H*, composed of two layers: a surface model, *SURF*, and a subsequent footprint model, *FP*. The free parameters only affect *SURF*, so that $Hx = FP(SURF(x))$. The model *H* transforms parameters, *x*, in estimated fluxes measured by the tower, which are comparable with flux observations, *y* (Figure 6.5). From Tarantola (2005), we obtain the maximum likelihood vector, or analysis state x^a, which corresponds to the optimized model parameters as:

$$x^a = x^b + K(y - Hx^b) \quad 6.5$$

Where $K = BH^T(HBH^T + R)^{-1}$. Note x^a is found by adding an innovation term weighted by a relaxation term, *K*, to the prior estimations. The relaxation term, *K*, can be further decomposed using the Sherman-Morrison-Woodbury formula and considering $B = SS^T$:

$$K = S(HS)^T\,(R^{-1} - R^{-1}HS[I + (HS)^T R^{-1}(HS)]^{-1}(HS)^T R^{-1}) \quad 6.6$$

From Tarantola (2005), the covariance matrix of the approximated Gaussian probability, or simply speaking, the posterior covariance operator A, which provides the uncertainty on the posterior estimations, is given by:

$$A = (I - KH)B \qquad 6.7$$

We assimilated GPP and Reco separately. The individual inversion was possible because we used a partitioning technique. We assumed the AIRPARIF inventory data was correct but further questioned this by comparing posterior with measured fluxes.

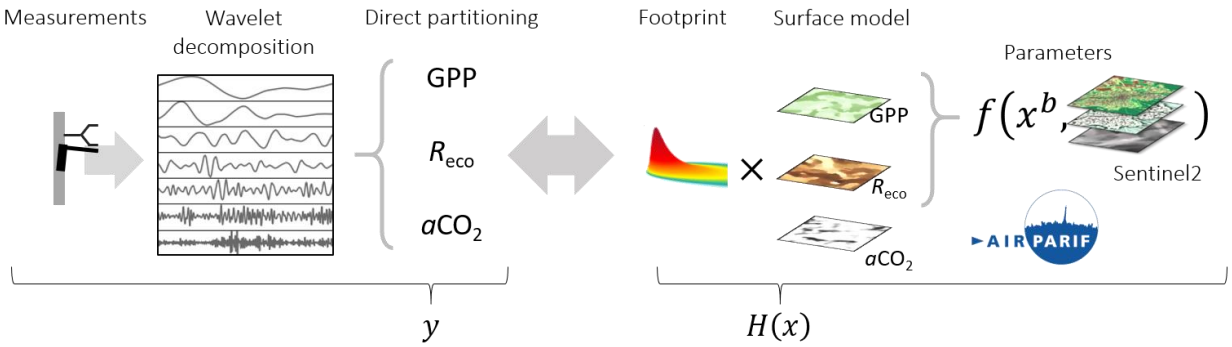

Figure 6.5. Illustration over the inversion's observations space. On the left, from left to right, eddy flux measurements, wavelet decomposition and direct partitioning follow the method modified from Coimbra et al. (2023). On the right, from right to left, model inputs, surface model maps, and footprint.

6.4.2 Assimilated observations

We cleaned the partitioned fluxes, GPP, Reco and aCO2 for the inversion. Eddy covariance (EC) measurements are a reliable tool for surface flux assessments and are the most certain element in the inversion. However, to ensure comparability with the simplistic models used for estimation, we filtered data before inversion to keep the most representative data and to avoid biases.

Firstly, we filter the data based on the mixing layer height, ensuring it is above 200 meters, which is twice the tower's height. This criterion helps minimize the impact of periods when the tower flux is decoupled from the surface, ensuring the measurements represent surface fluxes at that moment. However, it also results in the elimination of a significant portion of the nocturnal data. Additionally, we apply individual filters to the fluxes to remove outliers and unrealistic values: GPP values are constrained between -30 and 0, and Reco values between 0 and 10. These filters help ensure that only representative and physically plausible fluxes are included in the inversion analysis.

After cleaning the data to be more representative, we kept around 1250 half-hours for R_{eco} and 812 for GPP.

6.4.3 Models

Our prior fluxes are derived from a surface model, *SURF*, which is parameter-dependent, and a footprint model, a transport model. The footprint model, *F*, provides a density map that serves as

a weight for integrating the spatial dimension of the flux map such that *FP*(*SURF(x)*) is comparable to *y*. The grid resolution was 10×10 m, based on the Sentinel 2 data resolution.

To compute *FP*, we use the conventional footprint model as in Kljun et al. (2015), which consists of a backward Lagrangian Stochastic Particle Dispersion Model, LPDM-B. It is presented as well-suited for long-time series within the boundary layer and remains valid across different boundary layer conditions and measurement heights. In this model, surface heterogeneity is not considered. The footprint is symmetric in the crosswind direction, changing shape according to boundary layer height, wind shear and lateral wind variance.

Prior fluxes are calculated using a combination of the Vegetation Photosynthesis and Respiration Model (VPRM, Mahadevan et al., 2008) for biogenic fluxes and inventory data for the Ile de France region provided by AirParif:

$$NEE = \underbrace{GPP + R_{eco}}_{VPRM} + aCO2 \tag{6.8}$$

The anthropogenic CO_2 flux, aCO_2, comprises annual estimations for 2021 at 500m×500m resolution and daily, weekly and annual profiles. Emissions were grouped into three categories: road transport, stationary combustion, and others comprising fugitive, industry and other fluxes estimated as less important on the site. In recent years, higher-resolution inventories were unavailable when the present study was done, but they should be available in 2024.

The biogenic CO_2 flux, *b*CO2, can be expressed as the sum of ecosystem respiration, R_{eco}, and gross primary productivity, GPP. In a simplified model, GPP is influenced by light availability, leaf density, and stressors related to temperature, phenology, and water availability. Respiration, on the other hand, is directly influenced by temperature. Thus, in this study, the VPRM model was used where *b*CO2 was represented as follows:

$$bCO2 = \underbrace{-\lambda\, P_{scale}\, W_{scale}\, T_{scale}\, EVI\, \frac{1}{1+\frac{PAR}{PAR_0}}\, PAR}_{GPP} + \underbrace{\alpha T + \beta}_{Reco} \tag{6.9}$$

Where λ, α, β, and PAR_0 are fitting parameters, corresponding to, respectively, maximum light-use efficiency factor (µmol CO_2 m^{-2} s^{-1} / µmol PAR m^{-2} s^{-1}), temperature sensitivity of respiration (µmol m^{-2} s^{-1} $°C^{-1}$), baseline respiration (µmol m^{-2} s^{-1}) and half-saturation constant for photosynthetically active radiation (µmol m^{-2} s^{-1}). Photosynthetically active radiation (PAR, µmol m^{-2} s^{-1}) and air temperature (T, °C) are meteorological variables. T_{scale}, P_{scale} and W_{scale} are stress factors, ranging between 0 and 1, for temperature, phenology and water, respectively. These scaling factors range between 0 and 1 and constrain the potential GPP.

$$T_{scale} = \frac{(T - T_{min})(T - T_{max})}{(T - T_{min})(T - T_{max}) - \left(T - T_{opt}\right)^2} \tag{6.10}$$

$$P_{scale} = \frac{1 + LSWI}{2} \quad 6.11$$

$$W_{scale} = \frac{1 + LSWI}{1 + LSWI_{max}} \quad 6.12$$

Where T_{min}, T_{max}, and T_{opt} are minimum, maximum, and optimal temperatures (°C) for photosynthesis, respectively, and $LSWI_{max}$ is the maximum LSWI within the plant-growing season for each site (or pixel). All the model parameters were taken from a European-wide calibration Gerbig (2021).

The EVI and LSWI parameters were computed from Sentinel 2 data over an 8×8 km^2 square surrounding the FR-Sac tower. The meteorological variables T and PAR were taken from FR-Fon, an ICOS site ~50 km southeast km away.

6.4.4 Validation Method

Independent Observations

The ICOS database served for indirect comparison. This database comprises publicly available CO_2 flux measurements obtained through eddy covariance across Europe. We specifically compared the forest data we inferred in this study around the Saclay tower site with a mixed forest site, FR-Fon, located ~50 km southeast. It is important to note that since the measurements began in July, towards the end of the growing season, our focus was not on comparing with crop sites. Additionally, direct validation through independent data was not feasible, as there were no available data from overlapping experiments within the 40 km^2 80% footprint during the measurement campaign.

6.4.5 Performance measurements

Comparisons between instruments were carried out using mean bias and absolute error, defined as:

$$Mean\ Error\ (bias) = \frac{1}{N}\sum_{n=1}^{N}(X_{a,n} - X_{b,n}) \quad 6.13$$

$$Mean\ Absolute\ Error = \frac{1}{N}\sum_{n=1}^{N}\left|X_{a,n} - X_{b,n}\right| \quad 6.14$$

Where *N* equals the amount of data, *X* is the variable measured with instruments *a* and *b* at a time *n*.

Estimations in figures come with 95% confidence interval bands calculated using the Seaborn module in Python. It uses random sampling with a replacement strategy, bootstrapping, to construct a confidence interval (Dragicevic, 2016).

6.5 Results and discussion

6.5.1 Spatial variability and temporal variability of observations (vegetation index and CO_2 fluxes)

The satellite-derived vegetation index data revealed a well-defined seasonal change in plant activity (Figure 6.6.a). High vegetation indices reflected denser and greener leaves during summer. The high vegetation coincided with increased CO_2 sequestration during the day and emissions at night (Figure 6.6.b), as expected from active photosynthesis. However, as seasons shifted towards winter, the vegetation indices decreased, indicating a decline in photosynthetic activity. This decrease was accompanied by a corresponding decrease in CO_2 sequestration, suggesting a slowdown in plant metabolism. We thus define three periods: growing season, from July to September; transition, in October; cold, in December and January. Note that June and November were not considered, as no flux data was available.

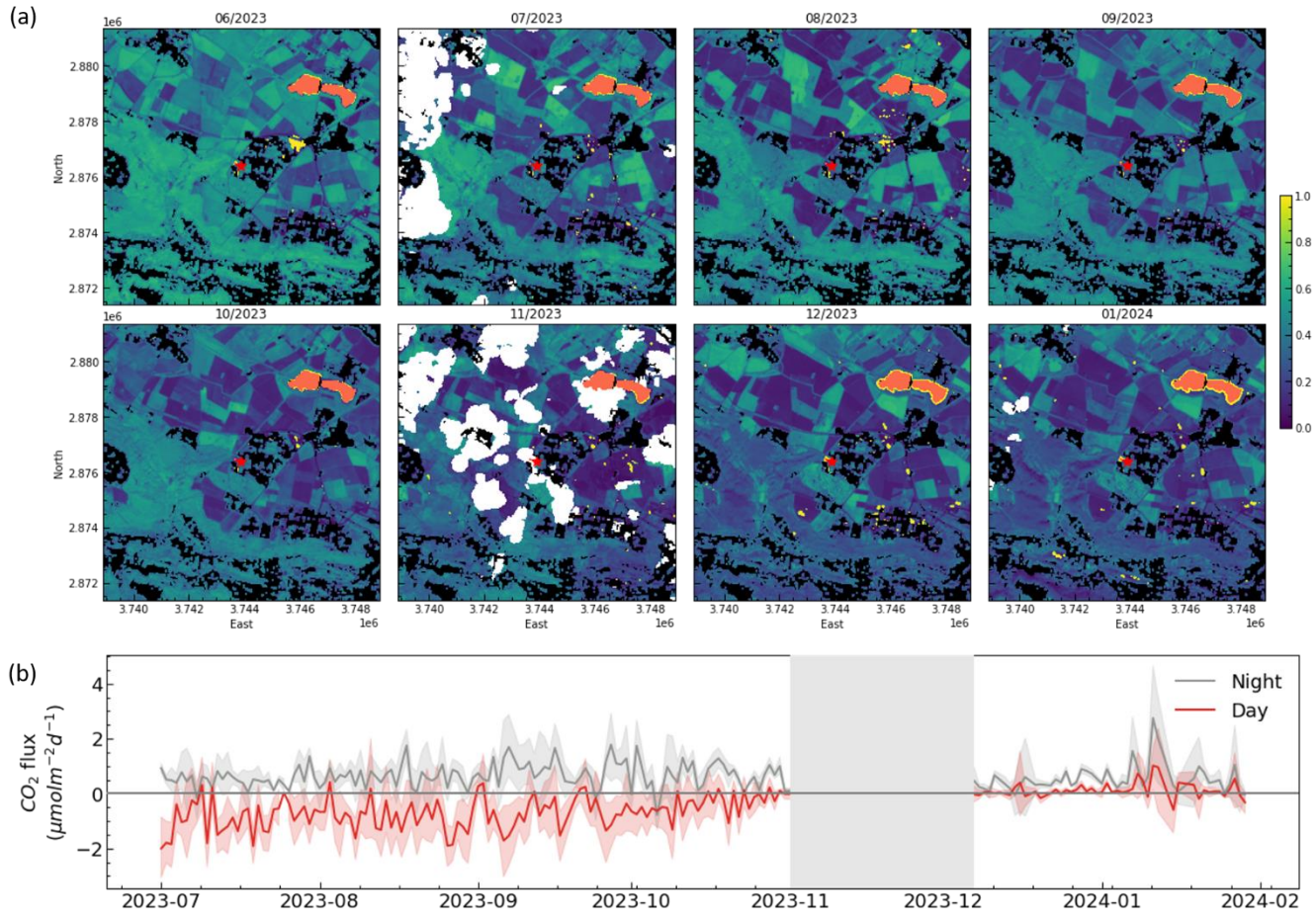

Figure 6.6. Seasonal evolution of (a) vegetation index (NDVI) around the site and (b) net flux measured at the FR-Sac tower. In (a), monthly averaged NDVI 8×8 km grid centred in Saclay tower (red star). The scale goes

from 0 to 1 for no vegetation to highly vegetated. The pixels in black are urban, salmon are lake, and there is no data in white. In (b) daily net fluxes in $\mu molm^{-2}d^{-1}$*. Note that only fluxes with well-developed turbulence were considered, and data was not gap-filled.*

In December and January, the biogenic contribution to the flux is anticipated to be minimal due to lower temperatures and reduced vegetation, with deciduous forests shedding leaves and summer crops being harvested. Despite these similarities between the two months, the net flux significantly differs. This variation is attributed to wind direction, with wind rarely coming from the northeast region in December, the direction of the local heating plant. However, wind from this direction in January becomes more prevalent, significantly influencing the measured flux.

6.5.2 A look at the spatial variability of partitioned CO_2 fluxes

Net and partitioned CO_2 fluxes exhibited distinct seasonal and spatial patterns (Figure 6.7). During warmer months (July to September), the site was, on average, a sink during the day (Figure 6.7.a), most notably in the west direction, pointing towards the forest. Contrarily, colder months revealed closer to zero net flux from the forest direction. The southeast direction, where the urban contribution from a roundabout, the campus, and an urban centre is present, shows net emissions all year long, which are stronger during daytime and increasing for colder months. Partitioned fluxes corroborate with this analysis. GPP and Reco estimations have shown reasonable values for warmer months. For periods where the wind is coming from the forest, GPP was stronger and anthropogenic *a*CO2 fluxes were small. We can also note the more significant *a*CO2 emissions from the southeast.

The partitioning, however, showed unclear results regarding different wind directions, times of day, and years. Some compensation seems to take place, in particular for the northeast direction where the heating plant is located. For this direction, all partitioned fluxes show a more substantial flux during colder months when the heating is on. While a high *a*CO2 is expected, the high GPP and Reco are most certainly an artefact from the partitioning in this direction. Note unrealistic estimations for nocturnal GPP fluxes for the southwest or during colder months. The reasons for these artefacts are unclear, although we could think of a possible mixing between sources and sinks in a 30-minute period.

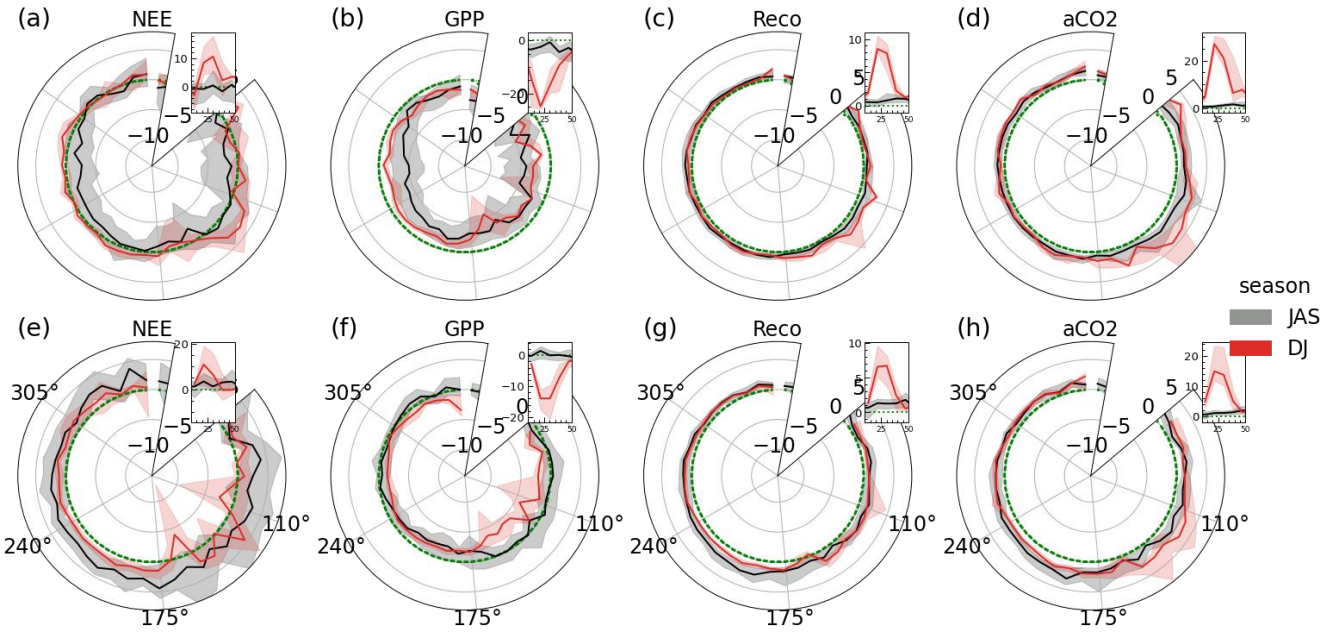

Figure 6.7. Net and partitioned fluxes are grouped by wind direction and grouped by daytime (a-d) and nighttime (e-h). Units are in µmol m-2 s-1, and values are the median with the interquartile range. Extreme 0.1% values were removed. Wind directions bins with less than 10 observations were added to the next bin clockwise. Note 10-50° were plotted separately for visual purposes. The zero line is shown in dashed green.

With that in mind, the site can be primarily separated into the west sector, driven by biogenic exchange; the east sector, comprehending mixing fluxes with anthropogenic driven fluxes during colder months; and at last, the 10°-40° range, where the heating plant drives fluxes during colder months.

6.5.3 Data assimilation

Analysis step

Assimilating west-sector daytime GPP during warmer months yielded stronger flux estimations than the model parametrised for Europe (Table 5.2). Indeed, the λ parameter, a multiplier of the GPP in the VPRM model, was multiplied by more than 2 for grassland and around 1.2 for forest.

Table 6.1. Parameters λ, α, β for the VPRM model per plant functional type (PFT) before and after inversion. Prior follows (Gerbig, 2021), and standard deviation was arbitrarily chosen as 20% of prior and reported in parentheses.

	Prior			*Posterior*		
PFT	λ	α	β	λ	α	β
DBF	0.181 (0.036)	0.127 (0.026)	1.140 (0.228)	0.212 (0.011)	0.124 (0.019)	0.838 (0.113)
GRA	0.170 (0.034)	0.086 (0.018)	0.363 (0.072)	0.386 (0.009)	0.107 (0.012)	0.331 (0.069)

The assimilation process ultimately led to a stronger CO_2 sink in the posterior than in the prior (Figure 6.8).

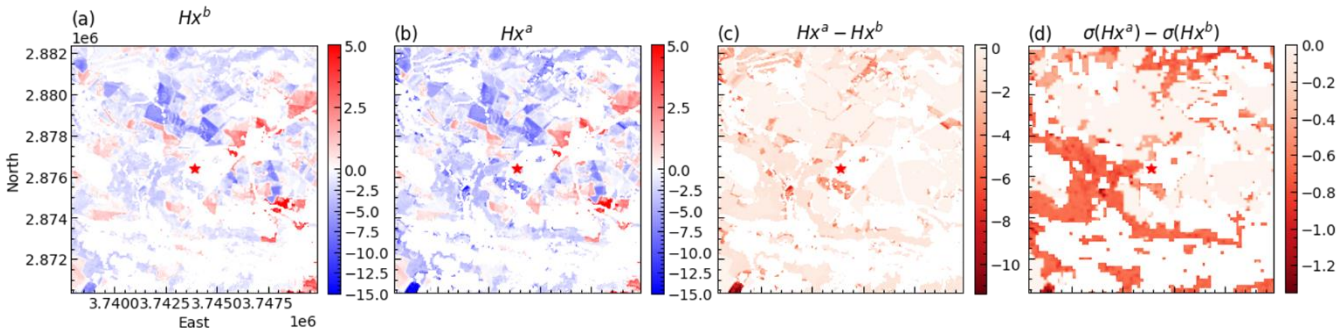

Figure 6.8. The contribution of data assimilation on surface flux estimations in July. In (a) prior, (b) analysis, (c) difference between (b) and (a), and (d) difference between the standard deviation of 100 repetitions using Gaussian distributed parameters. Units are in $\mu molm^{-2}s^{-1}$. The tower location is marked with a red star at the centre. Note that standard deviations (d) were calculated using a coarser resolution to allow for more repetitions.

The posterior map yielded coherent fluxes with the measured fluxes (Figure 6.9). Considering the smoothing effect caused by simplifications in surface and transport models, the estimated fluxes remained compatible with the measurements. Biogenic fluxes, part of the inversion process, are aligned closely with observations, as GPP shows. However, measured net flux and GPP showed a smaller sink than estimated by the inversion, particularly during the second half of the day. In addition to that, aCO_2 from the tower showed greater emissions compared to inventory data. It is important to note that we did not assimilate data in the inventory; in other words, the posterior here shows the inventory as it was.

It is worth noting that measurements from tall towers tend to be more erratic compared to shorter towers. This variability can be attributed to surface heterogeneity and the ever-changing source area, which brings a different mix of fluxes each time and a lower signal intensity at these heights.

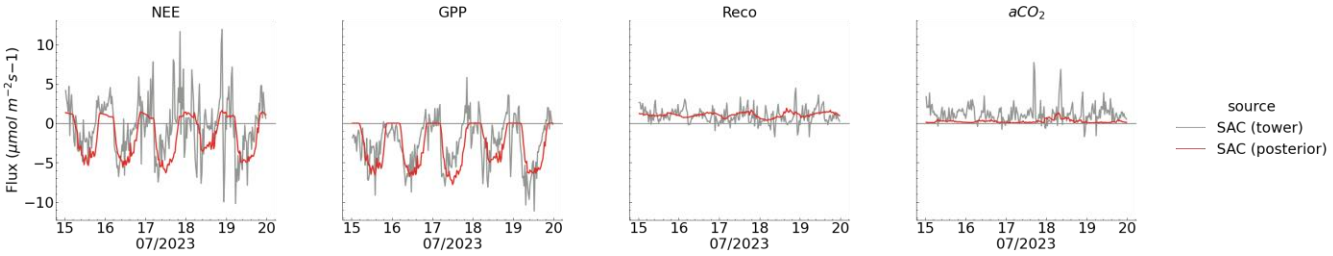

Figure 6.9. Net and partitioned fluxes, measured at the tower and posterior, estimated by footprint and flux map after inversion. Data shows that on July 15-20, wind mostly comes from the west. Note that GPP and Reco come from VPRM estimations, while aCO_2 comes from inventory data.

The estimation of NEE for the forest pixels had, on average, a smaller flux than a reference forest site (FR-Fon, ~50 km southeast) (Figure 6.10). During the middle of the day, fluxes at the SAC forest were estimated at −6 $\mu molm^{-2}s^{-1}$, while for FON, flux was around 10 $\mu molm^{-2}s^{-1}$ greater. It shows a much better agreement for a few days at the beginning of August, but this only lasts a few days, and the difference increases in July (not shown here).

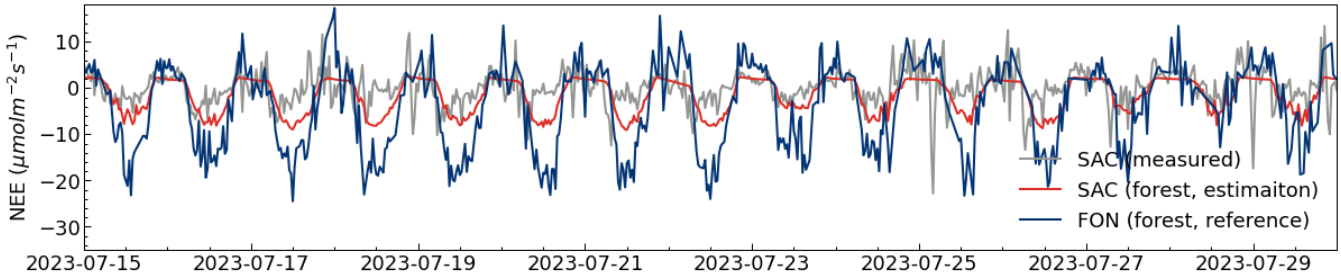

Figure 6.10. Forest net fluxes from late July were estimated from pixels on the surrounding tower and compared with FR-Fon as a reference.

This difference may be due to ecological reasons; the forests may have different species, ages, and root extractable water, which may lead to Fontainebleau having a 2 to 3 times larger NEE than the Palaiseau forest. Indeed, the Fontainebleau forest is known to have above-expected root extractable water (Maysonnave et al., 2022).

However, some other aspects may be invoked to explain the difference: Figure 6.9 shows that assimilated GPP in the map for all land uses mixed is smaller than the −15 to −20 $\mu molm^{-2}s^{-1}$ sink in FR-Fon. A hypothesis is that the longer transport time implies more mixing and potentially less well-defined "gusts". This mixing would imply an underestimation of the decomposed flux when using the direct partitioning method. However, if this is the case and considering the similarity between the partitioned fluxes, we could also expect the assimilated Reco and aCO_2 to be underestimated. The underestimation seems unlikely as aCO_2 is already higher than estimations coming from the inventory (Figure 6.9). Another possibility is that horizontal advection may effectively divert the forest flux. At last, storage flux in the SAC tower is somewhat uncertain as it

was measured using only 3-point measurements. Quantifying either fluxes, however, requires measurements that are not available at the moment of the study.

6.5.4 Estimating the flux from the heating plant

We estimated January fluxes using the same parameters (Table 6.1) and found assimilating months with biogenic-driven fluxes (July to September). The effect of the heating plant was apparent. First, the presence of the heating plant is very much visible as measured CO_2 fluxes are several orders of magnitude greater than estimations (Figure 6.11). Otherwise, aCO_2 fluxes seem to be better represented by the inventory compared to July's estimations.

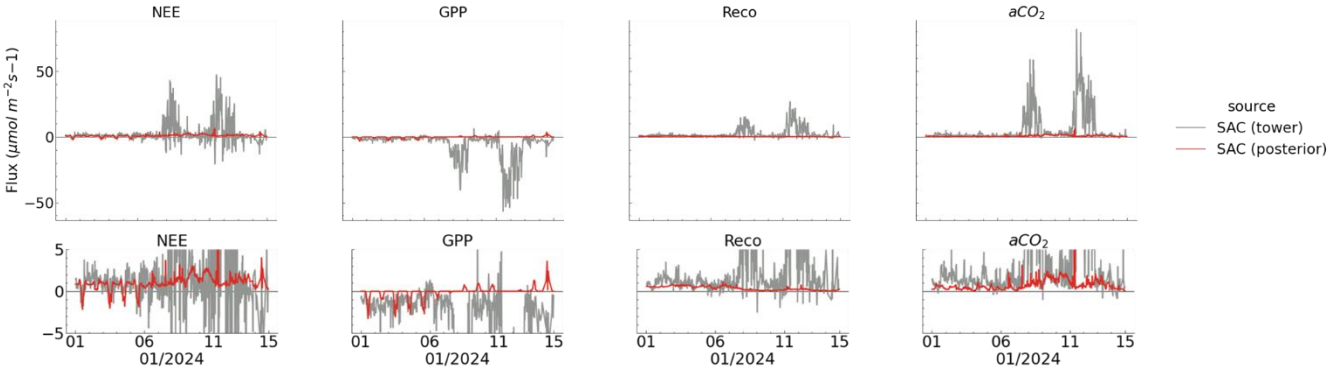

Figure 6.11. Net and partitioned fluxes were measured at the tower and posterior, estimated by footprint and flux map after inversion. The bottom panel replicates the top panel with a zoom focusing on values between -5 and 5 μmolm−2s−1. The dataset covers the period from the 1st to the 15th of January 2024, when wind blows from the heating plant.

6.5.5 Analysing the influence of the heating plant on direct partitioning

Important GPP and Reco fluxes were observed when the wind originated from the heating plant, suggesting a potential bias in the direct partitioning method (Figure 6.12). However, it is noteworthy that the net flux also exhibited erratic behaviour during these periods. The fluctuations observed in the net flux from one half-hour to another are unlikely to be solely attributed to the operation of the heating plant. A more plausible explanation is the influence of the plume emitted by the heating plant on the covariance measurements.

When the plume from the heating plant intersects with the tower's location, downwind measurements may capture air parcels enriched in CO_2, potentially biasing the measurements and introducing artefacts in the partitioning process (Figure 6.12.a). This phenomenon is attributed to the heating plant's intense and localized emissions and possible buoyancy effects that may lead to plume meandering because of the hot gases ejected through a tall chimney (~15 m).

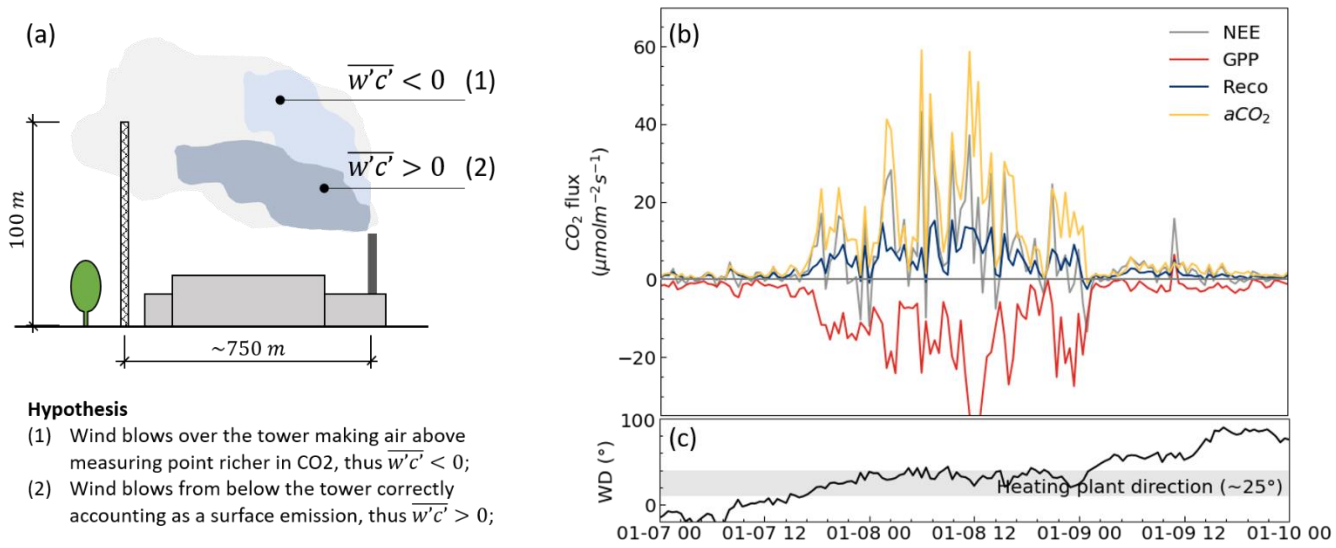

Figure 6.12. Fluxes and conceptual illustration on the effect of heating plant plume in the measurements. In (a), a conceptual illustration shows a hypothesis to explain unrealistic GPP from the wind direction coming from the heating plant. In (b) net and partitioned fluxes, in µmolm^{-2}s^{-1}, and (c) wind direction with heating plant direction (~25°) highlighted. Data for the period between the 7th and 10th of January.

Conditional sampling using CO or CH_4 resulted in very similar results (Figure 6.13). Typically, negative CO_2 fluxes are considered as GPP. For the particular situation when the wind came from the heating plant, though, doing so resulted in unrealistic GPP and Reco estimations (Figure 6.7). A better option for this situation may be to attribute it to *a*CO_2 fluxes when CH_4 or CO fluxes are positive and to biogenic CO_2 otherwise (Figure 6.13.c, d). In this new configuration, fluxes are more realistic (Figure 6.13c-d).

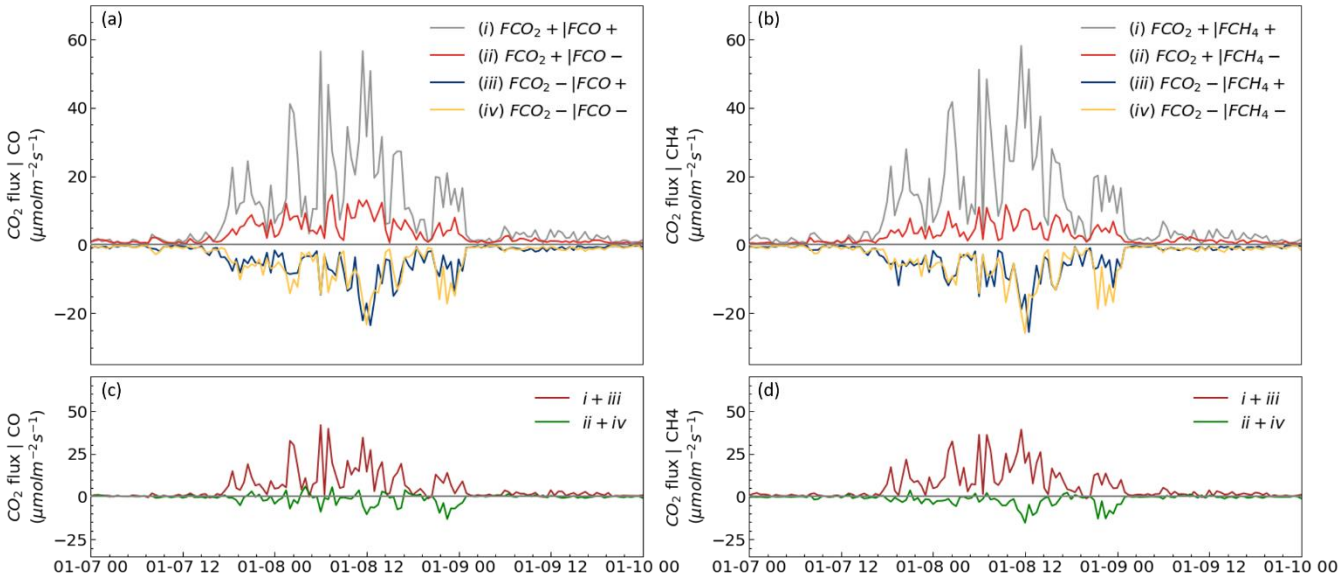

Figure 6.13. CO_2 fluxes conditioned by CO (a, c) and CH_4 (b, d) from 7th to 10th January. All four cases (a, b) and a sum based on the sign of the conditioned flux (c, d). In this latter case, i+iii would represent anthropogenic and ii+iv biogenic.

The partitioning requires an order of priority. So far, CO_2 flux and GPP have taken priority in partitioning as negative CO2 fluxes were considered GPP without further consideration, which is a reasonable assumption for biogenic-driven fluxes. For strong point sources, this might not be true anymore.

6.5.6 Foreseen improvement in the wavelet-based-partitioning-assimilation framework

On the observation side

Partitioning results yielded mixed outcomes. The expected values for GPP, in particular, are shown below. During the extreme case when the wind direction came from the heating plant, the partition yielded high values for GPP and Reco. It is considered compensation, and in this particular case, anthropogenic and biogenic sources might be better separated if CO or CH_4 covariance signs take priority so that when they are positive, the flux is attributed to anthropogenic independently of the CO_2 covariance sign. Applying this may not be appropriate for the whole year and all directions, indicating a need for further rule developments in the partitioning so that stronger fluxes take priority.

On the estimation side

In this work, we used the simple Vegetation Photosynthesis and Respiration Model (VPRM) introduced by Mahadevan et al. (2008). It initially provided a simplistic approach to calculating ecosystem respiration. However, subsequent versions of the VPRM have undergone significant modifications to enhance accuracy and capture more nuanced ecosystem processes. The simplistic approach to calculating ecosystem respiration, particularly in Mahadevan et al. (2008), may oversimplify the complex interactions within ecosystems. For this reason, recent studies by Gourdji et al. (2022) and Bazzi et al. (2024) have proposed several enhancements to the model equations. Modifications primarily focussed on the Reco and included additional data to account for soil temperature variations and soil moisture-induced water stress factors directly with soil measurements or by using precipitation as a proxy (Migliavacca et al., 2011). These additional processes result in a more comprehensive representation of ecosystem dynamics. Further improvements to the VPRM could incorporate additional factors such as crop management practices, biomass maps, and disturbance maps to represent ecosystem dynamics better.

Additionally, uncertainties on prior have been arbitrarily set and would require to be evaluated more thoroughly in particular uncertainties related to the simplified footprint model used.

On the validation side

Direct validation using multiple towers with overlapping footprints is ideal for validating the inversion at high resolution.

Benchmarking exercises and validation against independent observations are crucial steps in evaluating the performance of these algorithms. Ideally, benchmarking exercises should be conducted to evaluate the performance of inversion algorithms against known reference datasets or independent observations, such as local short-eddy-covariance towers in the tall-tower

footprint. Degrading the inversion can serve as a way to compare the additionality of model features or observational periods.

1.1. Conclusions

Eddy Covariance method provides direct, continuous, and reliable flux measurements. With advancements in satellite technology offering resolutions smaller than a tower's footprint, coupled with the power of data assimilation, models can now estimate processes and assimilate data at exceptionally fine scales. Leveraging tall-tower flux measurements presents distinct advantages, as flux footprints are much smaller than concentration ones and no background measurements are needed. Coupling these in a Bayesian inversion framework is promising.

Our findings affirm the viability of this framework, yielding coherent results over an area of 8×8 km^2. However, partitioning outcomes revealed nuances, with Gross Primary Productivity (GPP) and forest net fluxes exhibiting lower-than-expected values and instances of compensation between anthropogenic and biogenic fluxes under specific wind conditions. Further refinement in partitioning strategies is expected to ensure robust flux attribution across diverse environmental contexts.

Acknowledgements

The authors thank the ICOS Cities EU H2020 project (Grant No 101037319) for supporting this study. We thank Rainer Hilland for the support in hosting the Saclay data. We also thank the SIRTA team, namely Simone Kotthaus, for their comments on the lidar.

Financial support

This project has received funding from the European Union's Horizon 2020 research and innovation programme under Grant Agreement No 101037319 (PAUL ICOS-Cities project).

Data availability

ICOS data for the FR-Sac site can be downloaded from the carbon portal: https://meta.icos-cp.eu/resources/stations/AS_SAC.

Code

The code used in the analysis presented in this paper is available online and can be accessed at https://github.com/pedrohenriquecoimbra

References

Barcza, Z., Kern, A., Haszpra, L., and Kljun, N.: Spatial representativeness of tall tower eddy covariance measurements using remote sensing and footprint analysis, Agric. For. Meteorol., 149, 795–807, https://doi.org/10.1016/j.agrformet.2008.10.021, 2009.

Bazzi, H., Ciais, P., Abbessi, E., Makowski, D., Santaren, D., Ceschia, E., Brut, A., Tallec, T., Buchmann, N., Maier, R., Acosta, M., Loubet, B., Buysse, P., Léonard, J., Bornet, F., Fayad, I., Lian, J., Baghdadi, N., Segura Barrero, R., Brümmer, C., Schmidt, M., Heinesch, B., Mauder, M., and Gruenwald, T.: Assimilating Sentinel-2 data in a modified vegetation photosynthesis and respiration model (VPRM) to improve the simulation of croplands CO2 fluxes in Europe, Int. J. Appl. Earth Obs. Geoinformation, 127, 103666, https://doi.org/10.1016/j.jag.2024.103666, 2024.

Bousquet, P., Ciais, P., Peylin, P., Ramonet, M., and Monfray, P.: Inverse modeling of annual atmospheric CO2 sources and sinks: 1. Method and control inversion, J. Geophys. Res. Atmospheres, 104, 26161–26178, https://doi.org/10.1029/1999JD900342, 1999.

Bousquet, P., Peylin, P., Ciais, P., Le Quéré, C., Friedlingstein, P., and Tans, P. P.: Regional Changes in Carbon Dioxide Fluxes of Land and Oceans Since 1980, Science, 290, 1342–1346, https://doi.org/10.1126/science.290.5495.1342, 2000.

Canadell, J. G., Monteiro, P. M. S., Costa, M. H., Cotrim da Cunha, L., Cox, P. M., Eliseev, A. V., Henson, S., Ishii, M., Jaccard, S., Koven, C., Lohila, A., Patra, P. K., Piao, S., Rogelj, J., Syampungani, S., Zaehle, S., and Zickfeld, K.: Global Carbon and other Biogeochemical Cycles and Feedbacks, edited by: Masson-Delmotte, V., Zhai, P., Pirani, A., Connors, S. L., Péan, C., Berger, S., Caud, N., Chen, Y., Goldfarb, L., Gomis, M. I., Huang, M., Leitzell, K., Lonnoy, E., Matthews, J. B. R., Maycock, T. K., Waterfield, T., Yelekçi, O., Yu, R., and Zhou, B., Clim. Change 2021 Phys. Sci. Basis Contrib. Work. Group Sixth Assess. Rep. Intergov. Panel Clim. Change, 673–816, https://doi.org/10.1017/9781009157896.007, 2021.

Chevallier, F., Ciais, P., Conway, T. J., Aalto, T., Anderson, B. E., Bousquet, P., Brunke, E. G., Ciattaglia, L., Esaki, Y., Fröhlich, M., Gomez, A., Gomez-Pelaez, A. J., Haszpra, L., Krummel, P. B., Langenfelds, R. L., Leuenberger, M., Machida, T., Maignan, F., Matsueda, H., Morguí, J. A., Mukai, H., Nakazawa, T., Peylin, P., Ramonet, M., Rivier, L., Sawa, Y., Schmidt, M., Steele, L. P., Vay, S. A., Vermeulen, A. T., Wofsy, S., and Worthy, D.: CO2 surface fluxes at grid point scale estimated from a global 21 year reanalysis of atmospheric measurements, J. Geophys. Res. Atmospheres, 115, https://doi.org/10.1029/2010JD013887, 2010.

Christen, A.: Atmospheric measurement techniques to quantify greenhouse gas emissions from cities, Urban Clim., 10, 241–260, https://doi.org/10.1016/j.uclim.2014.04.006, 2014.

Coimbra, P. H. H., Loubet, B., Laurent, O., Mauder, M., Heinesch, B., Bitton, J., Delpierre, N., Depuydt, J., and Buysse, P.: Improvement of CO_2 Flux Quality Through Wavelet-Based Eddy Covariance: A New Method for Partitioning Respiration and Photosynthesis, https://doi.org/10.2139/ssrn.4642939, 24 November 2023.

Coimbra, P. H. H., Loubet, B., Laurent, O., Bignotti, L., Lozano, M., and Ramonet, M.: Eddy-covariance with slow-response greenhouse gas analyser on tall towers: bridging atmospheric and ecosystem greenhouse gases networks, Be Submitt., 2024.

Conrad, R.: Soil microorganisms as controllers of atmospheric trace gases (H2, CO, CH4, OCS, N2O, and NO), Microbiol. Rev., 60, 609–640, https://doi.org/10.1128/mr.60.4.609-640.1996, 1996.

Conrad, R. and Seiler, W.: Role of microorganisms in the consumption and production of atmospheric carbon monoxide by soil, Appl. Environ. Microbiol., 40, 437–445, https://doi.org/10.1128/aem.40.3.437-445.1980, 1980.

Crawford, B. and Christen, A.: Spatial source attribution of measured urban eddy covariance CO2 fluxes, Theor. Appl. Climatol., 119, 733–755, https://doi.org/10.1007/s00704-014-1124-0, 2015.

Farquhar, G. D., von Caemmerer, S., and Berry, J. A.: A biochemical model of photosynthetic CO2 assimilation in leaves of C3 species, Planta, 149, 78–90, https://doi.org/10.1007/BF00386231, 1980.

Foken, Th. and Wichura, B.: Tools for quality assessment of surface-based flux measurements, Agric. For. Meteorol., 78, 83–105, https://doi.org/10.1016/0168-1923(95)02248-1, 1996.

Gerbig, C.: Parameters for the Vegetation Photosynthesis and Respiration Model VPRM, https://doi.org/10.18160/R9X0-BW7T, 2021.

Gourdji, S. M., Karion, A., Lopez-Coto, I., Ghosh, S., Mueller, K. L., Zhou, Y., Williams, C. A., Baker, I. T., Haynes, K. D., and Whetstone, J. R.: A Modified Vegetation Photosynthesis and Respiration Model (VPRM) for the Eastern USA and Canada, Evaluated With Comparison to Atmospheric Observations and Other Biospheric Models, J. Geophys. Res. Biogeosciences, 127, e2021JG006290, https://doi.org/10.1029/2021JG006290, 2022.

Gurney, K. R., Razlivanov, I., Song, Y., Zhou, Y., Benes, B., and Abdul-Massih, M.: Quantification of Fossil Fuel CO2 Emissions on the Building/Street Scale for a Large U.S. City, Environ. Sci. Technol., 46, 12194–12202, https://doi.org/10.1021/es3011282, 2012.

Helfter, C., Tremper, A. H., Halios, C. H., Kotthaus, S., Bjorkegren, A., Grimmond, C. S. B., Barlow, J. F., and Nemitz, E.: Spatial and temporal variability of urban fluxes of methane, carbon monoxide and carbon dioxide above London, UK, Atmospheric Chem. Phys., 16, 10543–10557, https://doi.org/10.5194/acp-16-10543-2016, 2016.

Inman, R. E., Ingersoll, R. B., and Levy, E. A.: Soil: a natural sink for carbon monoxide, Science, 172, 1229–1231, https://doi.org/10.1126/science.172.3989.1229, 1971.

Jia, G., Shevliakova, E., Artaxo, P., De Noblet-Ducoudré, N., Houghton, R., House, J., Kitajima, K., Lennard, C., Popp, A., and Sirin, A.: Land–climate interactions, in: Climate Change and Land: an IPCC special report on climate change, desertification, land degradation, sustainable land management, food security, and greenhouse gas fluxes in terrestrial ecosystems, 2019.

Kim, J., Shusterman, A. A., Lieschke, K. J., Newman, C., and Cohen, R. C.: The BErkeley Atmospheric CO_2 Observation Network: field calibration and evaluation of low-cost air quality sensors, Atmospheric Meas. Tech., 11, 1937–1946, https://doi.org/10.5194/amt-11-1937-2018, 2018.

Kljun, N., Calanca, P., Rotach, M. W., and Schmid, H. P.: A simple two-dimensional parameterisation for Flux Footprint Prediction (FFP), Geosci. Model Dev., 8, 3695–3713, https://doi.org/10.5194/gmd-8-3695-2015, 2015.

Kountouris, P., Gerbig, C., Rödenbeck, C., Karstens, U., Koch, T. F., and Heimann, M.: Atmospheric CO_2 inversions on the mesoscale using data-driven prior uncertainties: quantification of the European terrestrial CO_2 fluxes, Atmospheric Chem. Phys., 18, 3047–3064, https://doi.org/10.5194/acp-18-3047-2018, 2018.

Lauvaux, T., Schuh, A. E., Uliasz, M., Richardson, S., Miles, N., Andrews, A. E., Sweeney, C., Diaz, L. I., Martins, D., Shepson, P. B., and Davis, K. J.: Constraining the CO_2 budget of the corn belt: exploring uncertainties from the assumptions in a mesoscale inverse system, Atmospheric Chem. Phys., 12, 337–354, https://doi.org/10.5194/acp-12-337-2012, 2012.

Lloyd, J. and Taylor, J. A.: On the Temperature Dependence of Soil Respiration, Funct. Ecol., 8, 315–323, https://doi.org/10.2307/2389824, 1994.

Mahadevan, P., Wofsy, S. C., Matross, D. M., Xiao, X., Dunn, A. L., Lin, J. C., Gerbig, C., Munger, J. W., Chow, V. Y., and Gottlieb, E. W.: A satellite-based biosphere parameterization for net ecosystem CO2 exchange: Vegetation Photosynthesis and Respiration Model (VPRM), Glob. Biogeochem. Cycles, 22, https://doi.org/10.1029/2006GB002735, 2008.

Mauder, M. and Foken, T.: Documentation and Instruction Manual of the Eddy-Covariance Software Package TK3, 60, 2011.

Migliavacca, M., Reichstein, M., Richardson, A. D., Colombo, R., Sutton, M. A., Lasslop, G., Tomelleri, E., Wohlfahrt, G., Carvalhais, N., Cescatti, A., Mahecha, M. D., Montagnani, L., Papale, D., Zaehle, S., Arain, A., Arneth, A., Black, T. A., Carrara, A., Dore, S., Gianelle, D., Helfter, C., Hollinger, D., Kutsch, W. L., Lafleur, P. M., Nouvellon, Y., Rebmann, C., Da ROCHA, H. R., Rodeghiero, M., Roupsard, O., Sebastià, M.-T., Seufert, G., Soussana, J.-F., and Van Der MOLEN, M. K.: Semiempirical modeling of abiotic and biotic factors controlling ecosystem respiration across eddy covariance sites, Glob. Change Biol., 17, 390–409, https://doi.org/10.1111/j.1365-2486.2010.02243.x, 2011.

Newman, S., Xu, X., Gurney, K. R., Hsu, Y. K., Li, K. F., Jiang, X., Keeling, R., Feng, S., O'Keefe, D., Patarasuk, R., Wong, K. W., Rao, P., Fischer, M. L., and Yung, Y. L.: Toward consistency between trends in bottom-up CO_2 emissions and top-down atmospheric measurements in the Los Angeles megacity, Atmospheric Chem. Phys., 16, 3843–3863, https://doi.org/10.5194/acp-16-3843-2016, 2016.

Pastorello, G., Trotta, C., Canfora, E., Chu, H., Christianson, D., Cheah, Y.-W., Poindexter, C., Chen, J., Elbashandy, A., Humphrey, M., Isaac, P., Polidori, D., Reichstein, M., Ribeca, A., van Ingen, C., Vuichard, N., Zhang, L., Amiro, B., Ammann, C., Arain, M. A., Ardö, J., Arkebauer, T., Arndt, S. K., Arriga, N., Aubinet, M., Aurela, M., Baldocchi, D., Barr, A., Beamesderfer, E., Marchesini, L. B., Bergeron, O., Beringer, J., Bernhofer, C., Berveiller, D., Billesbach, D., Black, T. A., Blanken, P. D., Bohrer, G., Boike, J., Bolstad, P. V., Bonal, D., Bonnefond, J.-M., Bowling, D. R., Bracho, R., Brodeur, J., Brümmer, C., Buchmann, N., Burban, B., Burns, S. P., Buysse, P., Cale, P., Cavagna, M., Cellier, P., Chen, S., Chini, I., Christensen, T. R., Cleverly, J., Collalti, A., Consalvo, C., Cook, B. D., Cook, D., Coursolle, C., Cremonese, E., Curtis, P. S., D'Andrea, E., da Rocha, H., Dai, X., Davis, K. J., Cinti, B. D., Grandcourt, A. de, Ligne, A. D., De Oliveira, R. C., Delpierre, N., Desai, A. R., Di Bella, C. M., Tommasi, P. di, Dolman, H., Domingo, F., Dong, G., Dore, S., Duce, P., Dufrêne, E., Dunn, A., Dušek, J., Eamus,

D., Eichelmann, U., ElKhidir, H. A. M., Eugster, W., Ewenz, C. M., Ewers, B., Famulari, D., Fares, S., Feigenwinter, I., Feitz, A., Fensholt, R., Filippa, G., Fischer, M., Frank, J., Galvagno, M., et al.: The FLUXNET2015 dataset and the ONEFlux processing pipeline for eddy covariance data, Sci. Data, 7, 225, https://doi.org/10.1038/s41597-020-0534-3, 2020.

Sabbatini, S., Mammarella, I., Arriga, N., Fratini, G., Graf, A., Hörtnagl, L., Ibrom, A., Longdoz, B., Mauder, M., Merbold, L., Metzger, S., Montagnani, L., Pitacco, A., Rebmann, C., Sedlák, P., Šigut, L., Vitale, D., and Papale, D.: Eddy covariance raw data processing for CO2 and energy fluxes calculation at ICOS ecosystem stations, Int. Agrophysics, 32, 495–515, https://doi.org/10.1515/intag-2017-0043, 2018.

Scanlon, T. M., Schmidt, D. F., and Skaggs, T. H.: Correlation-based flux partitioning of water vapor and carbon dioxide fluxes: Method simplification and estimation of canopy water use efficiency, Agric. For. Meteorol., 279, 107732, https://doi.org/10.1016/j.agrformet.2019.107732, 2019.

Tarantola, A.: Inverse Problem Theory and Methods for Model Parameter Estimation, Society for Industrial and Applied Mathematics, 348 pp., https://doi.org/10.1137/1.9780898717921, 2005.

Thomas, C., Martin, J. G., Goeckede, M., Siqueira, M. B., Foken, T., Law, B. E., Loescher, H. W., and Katul, G.: Estimating daytime subcanopy respiration from conditional sampling methods applied to multi-scalar high frequency turbulence time series, Agric. For. Meteorol., 148, 1210–1229, https://doi.org/10.1016/j.agrformet.2008.03.002, 2008.

Zheng, B., Chevallier, F., Yin, Y., Ciais, P., Fortems-Cheiney, A., Deeter, M. N., Parker, R. J., Wang, Y., Worden, H. M., and Zhao, Y.: Global atmospheric carbon monoxide budget 2000–2017 inferred from multi-species atmospheric inversions, Earth Syst. Sci. Data, 11, 1411–1436, https://doi.org/10.5194/essd-11-1411-2019, 2019.

CONCLUSION AND PERSPECTIVES

Direct flux measurements are pivotal in monitoring greenhouse gases, offering valuable insights into ecosystem dynamics and contributing to our understanding of climate change (Chapter 1). Traditionally, measurements were conducted in homogeneous fields, with each tower characterizing and monitoring a specific ecosystem type. The eddy covariance method has been continuously developed over the last decades. Our results show that moving the covariance calculation towards a wavelet-based framework can be beneficial to keep non-stationary data exploitable, reduce gaps, and allow for monitoring transitory processes. The simplicity and flexibility of the framework proposed (Chapters 2 and 3) make it very easy to deploy and allow for (re)analysis of existing datasets.

However, wavelet eddy covariance has the potential to bring much more information than only non-stationary process monitoring. Taking advantage of the time and frequency decomposition, we have shown that wavelets can partition CO_2 fluxes over a homogeneous ecosystem into photosynthesis and respiration by conditionally sampling up and down fluxes (Chapter 3). Although this new partitioning method must be evaluated and validated over a more extensive set of sites, it brings a conceptually rich framework that may be expanded to partition surface fluxes based on activity tracers (Chapter 5).

Tall towers for eddy covariance are interesting as they integrate over larger scales. However, they systematically measure over heterogeneous patches of land. This shift towards broader spatial coverage brings complexity but allows for a more representative sampling of emissions on a landscape. It also opens the door to closer collaboration between atmospheric and ecosystemic communities. We have shown that with the minimal addition of a 3D anemometer, an atmospheric setup including high precision but slow response analysers produced turbulent fluxes of CO_2 with reasonable corrections on high-frequency losses (Chapter 4). The computation of storage fluxes was essential for evaluating diurnal patterns.

Simultaneously, advancements in satellite technology have facilitated the development of large-scale models capable of estimating surface fluxes at fine resolutions. This greater spatial resolution, smaller than a tower's footprint, has created a valuable middle ground for comparing tall-tower-based and model-based fluxes. The comparison is important as both models and inventories need validation from direct measurements. Creating high-resolution flux maps from direct measurements represents an alternative way of having high-confidence maps at a fine scale that can be used to analyse the contribution of different land uses and validate larger-scale models and inventories (Chapter 5).

We preconise that the creation of high-resolution flux maps from single-tower measurements would require to fulfil a few criteria:

- Firstly, turbulent and storage fluxes must be measured. Further partitioning the fluxes is required for gases with important sinks and sources, such as CO2. Large footprints can average many surface processes, whether they are anthropogenic or biogenic, and thus, partitioned fluxes can help constrain the attribution of surface

fluxes to biospheric and anthropogenic origins. A complementary approach to be tested would be to use shorter averaging times to diminish the footprint area.

- Secondly, we need to relate time measurements of fluxes to the source area. A so-called footprint, or transport, model is needed to relate flux measurements to their respective source area. In addition to that, surface flux estimations by models and inventories should be used to help constrain estimations. Indeed, without some prior knowledge of the surface fluxes, the naïve approach of projecting the measurements into space using a footprint may not yield a satisfactory result. Larger and smaller emitters in the same wind direction may average out.

- Finally, a framework is needed to address the divergence between observed, y, and estimated fluxes, f(x). The typical approach minimises a cost function that increases with divergence, $f(x) - y$. The data assimilation Bayesian inference framework is well adapted to this problem as it provides surface flux estimations and their uncertainties. It indeed includes in the cost function the divergence of a state x, from its prior, x^b, and weight both divergence of x and y by their respective uncertainties.

This thesis represents a significant advancement in our understanding of direct flux measurements at the landscape scale through the exploration of new methods and setups. Our findings promise to enhance the reliability of landscape-scale monitoring efforts, providing valuable insights for science-driven development policies. Decision-makers require information with spatial and temporal resolutions tailored to the territory's specific needs, enabling informed decision-making and democratic participation. By delivering information on the consequences of policy actions at this scale, we can foster a culture of progressive change and encourage sustainable decision-making practices.